



HAL
open science

Identification of the local stiffness reduction of a damaged composite plate using the virtual fields method

Jin-Hwan Kim

► **To cite this version:**

Jin-Hwan Kim. Identification of the local stiffness reduction of a damaged composite plate using the virtual fields method. Mechanics [physics.med-ph]. Arts et Métiers ParisTech, 2008. English. NNT : 2008ENAM0026 . tel-00351689

HAL Id: tel-00351689

<https://pastel.hal.science/tel-00351689>

Submitted on 9 Jan 2009

HAL is a multi-disciplinary open access archive for the deposit and dissemination of scientific research documents, whether they are published or not. The documents may come from teaching and research institutions in France or abroad, or from public or private research centers.

L'archive ouverte pluridisciplinaire **HAL**, est destinée au dépôt et à la diffusion de documents scientifiques de niveau recherche, publiés ou non, émanant des établissements d'enseignement et de recherche français ou étrangers, des laboratoires publics ou privés.

École doctorale n° 432 : Sciences des Métiers de l'Ingénieur

THÈSE

pour obtenir le grade de

DOCTEUR

de

L'École Nationale Supérieure d'Arts et Métiers

Spécialité : Mécanique

présentée et soutenue publiquement

par

Jin-Hwan KIM

le 12 novembre 2008

<p>IDENTIFICATION DE CARTES D'ENDOMMAGEMENT DE PLAQUES COMPOSITES IMPACTÉES PAR LA MÉTHODE DES CHAMPS VIRTUELS</p>

Directeur de thèse : Fabrice PIERRON

Jury :

M. Michel GRÉDIAC	Professeur, Université de Blaise Pascal de Clermont-Ferrand	Président
M. Alain VAUTRIN	Professeur, Ecole des Mines de St-Etienne	Rapporteur
M. Laurent GUILLAUMAT	Professeur, ISAT, Nevers	Rapporteur
M. Stéphane AVRIL	Maître assistant, Ecole des Mines de St-Etienne	Examinateur
M. Michael WISNOM	Professeur, Université de Bristol (GB)	Examinateur
M. Fabrice PIERRON	Professeur, ENSAM, Châlons-en-Champagne	Examinateur

Laboratoire de Mécanique et Procédés de Fabrication

ENSAM, CER de Châlons-en-Champagne

École doctorale n° 432 : Sciences des Métiers de l'Ingénieur

Ph.D. THESIS

to obtain the grade of

DOCTOR

of the

L'École Nationale Supérieure d'Arts et Métiers

Speciality: Mechanics

presented by

Jin-Hwan KIM

November the 12th 2008

<p>IDENTIFICATION OF THE LOCAL STIFFNESS REDUCTION OF DAMAGED COMPOSITE PLATES USING THE VIRTUAL FIELDS METHOD</p>

Ph.D. Advisor : Fabrice PIERRON

Jury :

Dr. Michel GRÉDIAC	Professor, Blaise Pascal University, Clermont-Ferrand	Chairman
Dr. Alain VAUTRIN	Professor, Ecole des Mines, St-Etienne	Referee
Dr. Laurent GUILLAUMAT	Professor, ISAT, Nevers	Referee
Dr. Stéphane AVRIL	Assistant Professor, Ecole des Mines, St-Etienne	Examiner
Dr. Michael WISNOM	Professor, University of Bristol (GB)	Examiner
Dr. Fabrice PIERRON	Professor, ENSAM, Châlons-en-Champagne	Examiner

Mechanical Engineering and Manufacturing Research Group

ENSAM, CER de Châlons-en-Champagne

*For the purpose of
returning to Earth*

*And I do not call one a Brahmana
on account of his birth or of his origin from (a particular) mother;
(but) the one who is possessed of nothing and seizes upon nothing,
him I call a Brahmana.*

*The man who is free from anger,
endowed with (holy) works, virtuous, without desire, subdued,
and wearing the last body (antimasarira),
him I call a Brahmana.*

*The man who is not hostile amongst the hostile,
who is peaceful amongst the violent,
not seizing (upon anything) amongst those that seize (upon everything),
him I call a Brahmana.*

*Whosoever has passed over this quagmire difficult to pass,
(who has passed over) revolution (samsara) and folly,
who has crossed over, who has reached the other shore,
who is meditative, free from desire and doubt,
calm without seizing (upon anything),
him I call a Brahmana.*

Sutta Nipata, Book 3, Chapter 9

Acknowledgements

This thesis is the record of my four years' exploration into a new world and myself.

I owe my most sincere gratitude to my supervisor Professor Fabrice Pierron for his detailed and constructive comments, and for his important support throughout this work. This study would never have been done without his understanding, encouraging and thoughtful guidance. In addition, I am deeply indebted to Prof. Michael Wisnom for attracting me to Europe and giving me the opportunity to pursue my course of study. Without his great teaching, stimulating suggestions and encouragement, it might not have been possible for me to come up to this level.

A special thank goes to Prof. Michel Grédiac for his insights having remarkable influence on my research. Also, I warmly thank Dr. Stéphane Avril for his valuable advice and friendly help. His extensive discussions around my work and interesting explorations have been very helpful for this study. Looking backward, I wish to express my warm and sincere thanks to my Master supervisor, Professor Hsin-Piao Chen, who first brought me into the world of research and with whom I began to open my eye to the mechanics of materials.

I am indebted to many colleagues, but I am especially grateful to Mike Jones, Dr. Kevin Potter of Bristol University and Kashif Syed-Muhamad of Blaise Pascal University and Dr. Alain Giraudeau, Dr. René Rotinat, Raphaël Moulart, Dr. Patrick Ghidossi, Cédric Person, Benjamin Favre, Vinh Tran, Baoqiao Guo, José Xavier in the LMPF group. In addition, I would like to thank my friend Lee Engdahl for his essential assistance in reading my manuscript and providing me with valuable comments and encouragement. On a personal note, I would also like to express my gratitude to Mrs. Anne Pierron who provided assistance in numerous ways in France. Without the encouragement and understanding of my wife, it would have been impossible for me to finish this work.

Lastly, I would like to give my special thanks to my parents. They have always supported and encouraged me to do my best in all matters of life. To them I dedicate this thesis.

Résumé étendu en français

Introduction

Les matériaux composites stratifiés à fibres longues et matrices polymères occupent désormais une place de choix dans les matériaux de l'ingénieur comme en attestent leurs nombreuses applications dans le domaine des transports aériens, de l'espace, des sports et loisirs pour ne citer que quelques exemples. Néanmoins, un de leurs points faibles les plus critiques reste leur capacité à résister à des chargements de type impact (chute d'outils, impacts d'oiseaux en vol *etc.*). En effet, leur faible résistance interlaminaire (*i.e.*, entre les plis) implique que l'absorption de l'énergie d'impact se fait préférentiellement par délaminage (*i.e.*, fissure se propageant à l'interface entre les plis du stratifié). Ces endommagements sont souvent considérés comme critiques pour deux raisons. D'abord, les impacts peuvent ne laisser que peu de traces en surfaces alors même qu'à l'intérieur du stratifié, des délaminages significatifs peuvent exister. Ceci rend l'inspection visuelle inefficace (mode d'inspection classique dans l'aéronautique civil). Ensuite, ces délaminages réduisent fortement la résistance en compression du stratifié (mode de rupture en flambement). C'est d'ailleurs la raison pour laquelle l'essai de compression après impact est l'un des tests standards de l'industrie aéronautique. Il est donc très important de pouvoir évaluer les endommagements liés aux impacts à la fois, bien sur, pour la mise en place de procédures de contrôle non destructif mais aussi pour fournir des outils de validation expérimentale de simulation d'impact. Le présent travail est une contribution à ce sujet.

Il existent de très nombreuses techniques pour localiser un endommagement de type délaminage au sein d'un panneau stratifié (techniques ultrasonores, thermographie infrarouge, shearographie *etc.*) mais aucune ne fournit d'information quantitative quant à la perte locale de performance mécanique. Pour apporter une réponse à cette question, deux voies principales sont été explorées. La première concerne la mesure de la résistance résiduelle de la structure. C'est l'idée de l'essai de compression après impact. Néanmoins, si ce type d'essai est très sensible à un affaiblissement local du matériau, son problème principal est qu'il est destructif. L'alternative principale consiste à utiliser la rigidité de

la structure comme marqueur de son endommagement. De nombreuses techniques basées sur les fréquences propres du panneau ont été proposées mais le problème principal est que cette grandeur globale est peu sensible à une perte locale de rigidité. Pour contourner ce problème, il est possible de découper des éprouvettes de traction à différents niveaux de la zone endommagée mais on perd l'intérêt du côté non destructif de l'étude des rigidités. Le présent travail est une contribution à la mise au point d'une procédure expérimentale visant à déterminer de manière non destructive la perte locale de rigidité d'un panneau composite impacté. Pour cela, des mesures optiques de champs cinématiques sont utilisées afin de fournir une information expérimentale suffisamment riche pour traiter ce problème difficile. Ces mesures sont ensuite traitées avec une procédure d'identification inverse adaptée car le problème à résoudre n'admet pas de solution analytique. Pour cela, une méthode dédiée au traitement des mesures de champs est adoptée: la méthode des champs virtuels (MCV). Néanmoins, l'état de l'art de la MCV ne permettait pas au début de la thèse de traiter directement ce problème et une adaptation a été nécessaire. L'ensemble de la procédure a été testée sur des mesures simulées puis expérimentales afin de bien en cerner les performances. Il est important d'avertir le lecteur que cette étude consiste en un travail de défrichage dans la mesure où ce problème n'avais jamais été abordé au démarrage de cette thèse. Entre temps, une étude similaire mais avec d'autres outils a été lancée au sein du centre des composites d'Imperial College à Londres, soulignant l'actualité de ce sujet.

Le mémoire est organisé en six chapitres. Le premier présente une vue d'ensemble des différentes techniques de mesures de champs en insistant sur celles capables d'être utilisées en flexion. La technique de déflectométrie choisie pour ce travail est ensuite détaillée. Le chapitre 2 présente la méthode des champs virtuels et détaille son application aux chargements de flexion. Il est ensuite montré comment adapter la méthode pour identifier une variation spatiale de rigidité. Le chapitre 3 est dédié à la présentation du montage expérimental et à l'identification des rigidités d'une plaque orthotrope non endommagée. Le chapitre 4 passe en revue les différents modes d'endommagement des plaques stratifiées et les techniques pour les détecter. Les chapitres 5 et 6 présentent l'ensemble des résultats sur plaques endommagées. Le chapitre 5 étudie en détail les performances de la méthode avec différents paramétrages et le chapitre 6 donne les principaux résultats expérimentaux.

Chapitre 1

Ce chapitre est principalement dédié à la présentation de la méthode de déflectométrie utilisée dans ce travail. Après une brève évocation de quelques techniques alternatives pour mesurer des déformations de flexion sur des plaques minces (interférométrie de speckle,

shearographie, moiré d'ombres, stéréocorrélation), le principe de la déflectométrie est rappelé. Il s'agit de tirer partie des lois de la réflexion spéculaire en observant l'image d'une grille croisée à la surface d'une plaque réfléchissante. Une déformation de flexion de la plaque résultera en un changement local de pente en tout point de sa surface qui affectera la composante spéculaire de la lumière réfléchie. Ainsi, pour une plaque présentant une réflexion principalement spéculaire, en un point particulier de la plaque, l'image de cette partie de la grille sera translatée. Dans le montage habituel où la grille de référence est positionnée en face de la plaque testée (Fig. 1.1), la pente locale de la plaque testée est reliée de manière très simple à la phase locale de l'image de la grille (décrivant la position de chaque période de la grille), voir Eq. 1.2. En utilisant un algorithme de décalage de phase spatial de type transformée de Fourier fenêtrée (Eq. 1.22), couplé à un algorithme de séparation des informations selon les deux directions de la grille croisée (Fig. 1.4), on peut calculer le champ de pente dû à la déformation de la plaque en prenant une image de la grille réfléchie aux états initial et déformé (après l'utilisation d'un algorithme de redressement de phase approprié [12]). Le chapitre se termine en décrivant deux aspects pratiques importants : la procédure de lissage par interpolation polynomiale au sens des moindres carrés utilisée pour filtrer le bruit de mesure haute fréquence spatiale en vue de calculer les champs de courbure par différentiation numérique, et le positionnement latéral de la caméra afin d'éviter la perte d'information due à l'image du trou dans la grille de référence (Fig. 1.8).

Chapitre 2

Ce chapitre est consacré à la présentation détaillée de la méthode d'identification utilisée dans ce travail: la méthode des champs virtuels. Dans un premier temps, le principe de base de la MCV est rappelé: il s'agit d'utiliser la forme faible de l'équation d'équilibre (principe des travaux virtuels ou PTV) avec des champs virtuels particuliers puis de substituer le tenseur des contraintes via la loi de comportement. En élasticité homogène, ceci mène à un système d'équations linéaires faisant intervenir des intégrales pondérées des différentes composantes du tenseur des déformations. Ces intégrales peuvent être évaluées expérimentalement dans le cas où des mesures de champs sont disponibles. Néanmoins, comme les mesures ne sont obtenues qu'en surface, il est nécessaire de faire une hypothèse cinématique dans l'épaisseur. Ici, les hypothèses de la théorie classique des plaques minces (Love-Kirchhoff) sont retenues. On présente alors la MCV adaptée à ce cas de figure, avec une intégration directe selon z menant au PTV adapté à la formulation des plaques minces. Un résumé de la procédure de choix de champs virtuels optimaux est aussi donné. L'originalité du travail est alors introduite. Il s'agit d'adapter la formulation

du problème au cas des matériaux hétérogènes. Dans ce cas, les rigidités à identifier ne peuvent plus être sorties des intégrales et une paramétrisation est nécessaire. Plusieurs cas de figure ont été testés. D’abord, un paramétrage de type ‘endommagement isotrope’ (Eq. 2.37) où l’inconnue devient la fonction $p(x,y)$, distribution spatiale de réduction de rigidité. Ce modèle est dit ‘isotrope’ car, bien que la matériau de base soit orthotrope, on suppose que toutes les composantes de la matrice de raideur en flexion sont affectées par le même facteur de réduction. Ceci permet de limiter le nombre d’inconnues à identifier (première étape). Cette fonction $p(x,y)$ peut être soit continue (ici, une formulation polynomiale a été retenue) soit discrète (fonction constante par morceaux). On a ensuite essayé d’identifier directement les quatre rigidités orthotropes dans chaque zone de la plaque (endommagée et vierge). On a alors un problème à 8 inconnues si on considère une zone endommagée unique, problème se traitant avec la MCV classique dans ce cas. Des simulations numériques sont présentées au chapitre 5 pour évaluer les performances de chaque approche.

Chapitre 3

Le chapitre 3 est consacré à la présentation de la méthodologie expérimentale utilisée pour identifier les rigidités des plaques composites saines (non endommagées). En effet, certains paramétrages donnés au chapitre 2 nécessitent la connaissance *a priori* des rigidités initiales du matériau. Cela permet de détailler ici la procédure de revêtement des plaques par une fine couche de ‘gel coat’ (résine) menant à une surface bien plane et possédant de bonnes propriétés de réflexion spéculaire. L’incidence du lissage des mesures est également évalué rapidement (degré de l’interpolation polynomiale). Des résultats sont ensuite présentés sur une plaque de carbone époxyde unidirectionnel T300/914, avec les deux montages de déflectométrie (caméra en face et de biais). Les résultats sont très proches et dans un intervalle de quelques pour cents par rapport aux valeurs typique de ce matériau bien connu.

Chapitre 4

Avant de passer à l’identification sur des plaques endommagées, il a été jugé utile de faire quelques rappels sur les modes d’endommagement des plaques composites ainsi que sur les différentes techniques disponibles actuellement pour évaluer ces endommagements. Pour le premier point, on montre l’importance des délaminages (séparation de strates au sein d’un stratifié) en raison de l’absence de renforcement dans la direction de l’épaisseur. Ce mode d’endommagement peut ensuite conduire à des ruines prématurées des panneaux

par flambement (réduction de l'épaisseur, qui influence fortement les charges critiques de flambement). C'est la raison pour laquelle les chapitres suivants se focalisent principalement sur ce type d'endommagement. En ce qui concerne les techniques de contrôle non destructif, on montre que s'il en existent de nombreuses (ultrasons, thermographie IR shearographie *etc.*), elles sont limitées à une détection de localisation d'un endommagement car aucune ne permet de quantifier la perte de performance mécanique liée à la présence de ce dommage. C'est l'objectif de ce travail que de proposer une alternative permettant cette quantification.

Chapitre 5

Les deux derniers chapitres contiennent l'ensemble des résultats sur panneaux endommagés. Dans un premier temps, les performances de la méthode sont évaluées à partir de simulation numériques. C'est l'objectif de ce chapitre.

Endommagement intralaminare

Différents aspects de la procédure numérique ont été étudiés. Tout d'abord, dans le cas de l'endommagement isotrope, la paramétrisation polynomiale a été évaluée. Le cas test est celui d'une plaque composite possédant un endommagement de forme carrée représentant environ 10% de la surface totale, avec un contraste de rigidité de flexion de 30%. Ceci est représenté numériquement par une stratification avec des plis dont la rigidité est réduite à presque zéro. On montre qu'un polynôme de degré 8 est un bon compromis pour représenter ce défaut. En cas de défaut inconnu, on pourra essayer plusieurs degrés. Plus le degré est bas, plus la procédure pourra détecter de faibles contrastes sur des zones étendues et plus il est élevé, plus de petits défauts pourront être localisés mais avec des contrastes plus élevés. L'ajout de bruit aux données simulées dégrade les performances, comme on s'y attendait. On voit en particulier apparaître des 'faux positifs' (défauts fantômes, en regard du vrai défaut et d'amplitude plus faible). Le type de chargement a aussi été étudié. Deux configurations d'essais ont été simulés, avec différentes positions du défaut. Peu de différences ont été trouvées entre les configurations, même si certaines semblent légèrement meilleures. On montre aussi que plus l'effort de flexion est élevé, plus les résultats sont de bonne qualité car le niveau de bruit est fixe donc si l'amplitude du signal augmente, le rapport signal sur bruit augmente. Néanmoins, il faut veiller à ce que la flèche ne dépasse pas l'épaisseur pour rester dans une configuration de petites perturbations. Une étude de sensibilité est ensuite mise en œuvre en faisant varier conjointement la taille du défaut et le contraste de rigidité. Pour une charge de 10 N, on détecte l'endommagement

jusqu'à une taille de 1.3% et un contraste de 7%. C'est résultats seront confirmés au chapitre 6 avec la plaque impactée. L'effet de la résolution spatiale de la mesure a aussi été explorée en simulant numériquement la déformation de la grille à partir des pentes calculées par éléments finis. On voit qu'une grille de référence de 2 mm de pas (1 mm sur l'image) est bien adaptée au problème. Des résultats expérimentaux convaincants tiennent souvent à une somme de petits détails. La simulation et l'analyse des effets de différents détails de la procédure expérimentale, présentés ensuite dans ce chapitre, en apportent une démonstration sans appel. Les points étudiés ont été:

- l'ajout de bruit;
- la perte de données sur les bords;
- la perte de données sur le trou (image du trou d'accès de la caméra sur la grille de référence);
- présence de deux trous lorsque cette image se déplace significativement entre l'état initial et déformé;
- perte d'information due aux fixations de la plaque.

La dégradation des résultats est spectaculaire lorsqu'on ajoute ces problèmes les uns après les autres. C'est la raison pour laquelle la procédure expérimentale a été graduellement raffinée pour prendre en compte ces effets : déplacement de la caméra (plus de trou), modification des fixations (plus de données perdues) et augmentation au maximum de l'effort appliqué (maximisation du rapport signal sur bruit). Une deuxième partie de cette section a été dédiée à l'évaluation des performances de la techniques pour un paramétrage par morceau (endommagement isotrope). On s'aperçoit que très vite (quatre morceaux dans la zone dégradée), en présence de bruit, la procédure devient instable. Ceci n'est pas surprenant dans la mesure où un gradient de rigidité est équivalent à un gradient de déformation, soit une dérivée seconde du signal (troisième, même, en cas de mesure de flèche). On voit ici tout le bénéfice de la régularisation apportée par le paramétrage polynomial. On pourrait bien sûr mettre en œuvre une régularisation plus locale pour obtenir des performances intermédiaires en termes de rapport résolution - résolution spatiale, mais ceci n'a pas été entrepris ici. Enfin, l'identification d'un endommagement anisotrope a été exploré. Le principal problème est que pour un essai donné, la zone endommagée ne contient pas assez de richesse spatiale pour identifier correctement l'ensemble des rigidités orthotropes. Il faudrait combiner plusieurs cas de chargement pour y arriver. Une petite étude de sensibilité a d'ailleurs permis de donner des idées quant à la position optimale de l'effort à appliquer pour identifier chaque composante. Néanmoins, cet aspect n'a pas été poussé plus avant.

Endommagement interlaminaire

Une première tentative de validation à partir d'un modèle par éléments finis d'un délaminage sur la surface moyenne se solde par un échec, même pour des données non bruitées. Même si la localisation est à peu près assurée, ni la forme (polynomiale ici) de $p(x,y)$, ni son amplitude ne correspondent à ce qui est attendu. L'analyse détaillée de ce point est effectuée au chapitre suivant en s'aidant des résultats expérimentaux.

Chapitre 6

Le dernier chapitre présente les résultats expérimentaux pour différents types d'endommagements introduits *a priori* dans des panneaux unidirectionnel et croisé, ainsi que pour une plaque impactée (endommagement se rapprochant d'un cas réel). Le premier cas consiste à enlever deux plis en surface d'une plaque de carbone époxyde unidirectionnelle, sur une surface carrée d'environ 8% de la surface totale de la plaque. Les mesures sont effectuées sur la face vierge selon le protocole détaillé au chapitre 3. Les résultats obtenus avec la paramétrisation polynomiale isotrope sont très satisfaisants. L'endommagement est correctement localisé et son amplitude correspond à celle attendue. En se servant de ce premier résultat, on peut utiliser un critère pour définir une zone endommagée (par exemple, le carré contenant les points ayant tous plus de 30% de réduction de rigidité. On peut ensuite identifier $p(x,y)$ par morceaux. Pour un seul morceau, la réduction attendue est bien récupérée (ce qui est logique au vu du critère utilisé), mais lorsqu'on passe à quatre morceaux, la solution devient instable pour la raison déjà invoquée au chapitre précédent. On peut aussi essayer d'identifier directement les quatre rigidités orthotropes dans les zones vierge et endommagée (définie avec le critère précédent). Les premières sont correctement identifiées (ce qui permet de s'affranchir de la connaissance *a priori* de ces valeurs) mais pour les secondes, seul D_{22} , et dans une moindre mesure, D_{11} , sont correctement identifiés. Le fait que D_{66} ne soit pas correctement obtenu dans cette zone reste une question ouverte (c'est *a priori* la grandeur la mieux identifiable après D_{22} pour ce cas de chargement, et cela fonctionnait très bien sur les données simulées, même avec bruit). Ce point devra faire l'objet de compléments d'investigation. Le deuxième endommagement étudié est un délaminage artificiellement introduit dans une plaque de carbone époxyde croisée sous la forme de films de PTFE insérés sur la face inférieure des deux derniers plis, sur une surface identique à celle du cas précédent. Après cuisson, la plaque possède sur la face arrière, au niveau des délaminages, une légère cloque suggérant qu'en chargement, ces deux derniers plis ne supporteront pas (ou très peu) de chargement (cas identique à un flambement local). Ceci est confirmé par les résultats très proches du cas précédent,

quel que soit le paramétrage utilisé (y compris le mystère de la rigidité de cisaillement dans la zone délaminée). Néanmoins, l'ensemble de ces résultats, parfaitement originaux à notre connaissance, reste très satisfaisant, surtout si on considère le faible contraste de rigidité mis en jeu. Le troisième cas considéré est celui d'un délaminage unique sur le plan moyen du panneau, introduit en pratique via un film PTFE comme précédemment. Le résultat avec le paramétrage isotrope polynomial est identique à celui obtenu avec des données simulées. En fait, la procédure ne fonctionne pas correctement en raison du fait que la distribution des déformations dans l'épaisseur s'éloigne ici beaucoup de la linéarité supposée lors de l'écriture du PTV. Une modélisation par éléments finis montre d'ailleurs que les résultats obtenus sont cohérents avec le champ de pente observé en surface. Il faut néanmoins modérer la portée pratique de cette mise en échec de la procédure par les deux points suivants. Tout d'abord, même si le champ d'endommagement a une forme plus difficile à interpréter, la procédure détecte qu'il se passe quelque chose de significatif. Peut-être serait-il possible de mettre en place une procédure adaptée à ce cas de figure. Ensuite, ce type de délaminage unique sur le plan moyen est très loin de la réalité d'un endommagement par impact où des délaminages sont répartis sur différents plis à travers l'épaisseur. Il faudra bien sûr tester ce type d'endommagement mais le présent travail s'est concentré sur des cas simple afin de défricher le problème et d'identifier les difficultés potentielles. A ce titre, cette thèse a rempli pleinement son objectif. Enfin, et afin de démontrer une faisabilité sur cas réel, une plaque de carbone époxyde croisée a été impactée avec un dispositif assez rudimentaire : une pièce métallique contondante (simulant un outil) a été lâchée au dessus d'une plaque encastree aux bords par un montage réalisé au laboratoire. L'énergie d'impact est de 20 J pour une vitesse d'impact d'à peu près 2 m/s. Sur la surface impactée, on peut voir une légère indentation mais rien de très significatif. Par contre, sur la face arrière, on observe bien le flambement local des plis extérieurs. Ceci correspond bien à un impact de type BVID (barely visible impact damage) qui est un souci pour la maintenance aéronautique (pas d'endommagement visible en surface mais un endommagement qui peut être important dans l'épaisseur du panneau). A noter qu'ici, la zone endommagée est de taille plus faible que celle utilisée pour valider la procédure (2 à 3% de la surface de la plaque seulement). Néanmoins, le paramétrage polynomial isotrope détecte une chute d'environ 10% de la rigidité sur une surface correspondant à peu près à l'emplacement visualisé sur la face arrière. On note cependant que la carte d'endommagement est très bruitée. Quoi qu'il en soit, ce premier résultat est très prometteur au vu du très faible contraste de rigidité et de la petite taille de la zone endommagée. Il faut dire aussi que ce résultat doit beaucoup à la grande qualité des mesures obtenues par la déflectométrie qui est une technique très sensible.

Conclusion et perspectives

Le travail faisant l'objet de cette thèse est de nature exploratoire, car personne, à notre connaissance, n'a jamais entrepris ce type de d'étude. En conséquence, il a fallu explorer les différentes pistes et dégager des conclusions partielles permettant de poursuivre dans cette voie dans le futur. On peut d'ores et déjà tirer les conclusions suivantes.

- Il est possible d'adapter la méthode des champs virtuels à l'identification de champs d'endommagement de plaques composites impactées, dans l'hypothèse des plaques minces, avec mesures de champs en surface. Ici, des champs de pentes obtenues par déflectométrie permettent d'obtenir les déformations en une seule dérivation spatiale (au lieu de deux en cas de mesure des flèches).
- La procédure fonctionne bien lorsque la distribution spatiale des grandeurs mécaniques est bien linéaire dans l'épaisseur. A ce titre, elle est partiellement mise en défaut dans le cas d'un délaminage unique sur le plan moyen de la plaque.
- Un premier résultat prometteur a été obtenu sur une plaque avec un endommagement d'impact réel.

Ce travail apporte néanmoins plus de questions que de réponses. En particulier, pour fiabiliser la procédure, il faudra:

- pouvoir combiner des cas de chargement afin d'identifier convenablement un endommagement anisotrope;
- mettre en œuvre une technique de régularisation pour améliorer les performances du paramétrage constant par morceaux;
- appliquer la procédure à divers plaques ayant subi des impacts réels, avec observation microscopique des endommagements et validation par modèles éléments finis.

Enfin, il est clair que cette procédure a pour vocation d'être adaptée à des structures réelles, non planes et non réfléchissantes (avec difficulté voir impossibilité de revêtements), comme par exemple des aubes de moteurs d'avion en composites. Il faudra donc mettre en œuvre une autre technique de mesure de champs. L'interférométrie de speckle est un bon candidat pour des mesures sur pièce non plane et diffusante, avec la sensibilité requise pour une mesure directe des déplacements plans. L'alternative est la shearographie (ou interférométrie différentielle), variante de la technique précédente mais peu sensible aux vibrations parasites et donnant directement les pentes à la surface. Néanmoins, la shearographie quantitative est peu répandue et il faudra travailler en collaboration avec un laboratoire spécialisé pour en montrer la faisabilité dans ce cas précis.

Contents

Résumé étendu en français	I
General Introduction	XXIII
1 Full-Field Measurement Technique	1
1.1 Introduction	1
1.1.1 Out-of-plane measurement techniques	3
1.1.1.1 Electronic Speckle Pattern Interferometry (ESPI)	3
1.1.1.2 Shearography	4
1.1.1.3 Shadow moiré	5
1.2 Deflectometry	5
1.2.1 Principle	6
1.2.2 Sensitivity, resolution and spatial resolution	8
1.2.3 Fringe Analysis	9
1.2.3.1 Phase detection	11
1.2.3.2 Spatial phase stepping	12
1.2.3.2.1 Windowed-DFT Algorithm	15
1.2.3.3 Unwrapping	16
1.2.3.4 Numerical differentiation to obtain curvatures from the slope fields	17
1.2.3.4.1 Spatial smoothing	17
1.2.3.4.2 Numerical differentiation after spatial smoothing	18
1.2.3.4.3 Numerical differentiation without spatial smoothing	18
1.2.3.5 Effects of camera position	20
1.2.3.5.1 Calibration for camera position	20
1.3 Conclusion	21
2 The Virtual Fields Method	23

2.1	The Virtual Fields Method	23
2.1.1	Application of the VFM to thin plate bending	25
2.1.1.1	Kirchhoff thin plate theory and Mindlin plate theory	25
2.1.1.1.1	Mindlin plate theory	26
2.1.1.1.2	Kirchhoff plate theory	28
2.1.1.1.3	Classical lamination theory	29
2.1.1.2	The Virtual Fields Method in the case of plate bending	31
2.1.1.3	Special virtual fields method	33
2.1.1.4	Construction of the special virtual fields	34
2.1.1.5	Optimization of special virtual fields	36
2.2	The Adapted Virtual Fields Method	37
2.2.1	Continuous parameterization	38
2.2.1.1	Isotropic damage	38
2.2.1.2	Anisotropic damage	39
2.2.2	Discrete parameterization	40
2.2.2.1	Isotropic damage	41
2.2.2.2	Anisotropic damage	42
2.3	Conclusion	42
3	Identification of undamaged plate bending stiffnesses	45
3.1	Introduction	45
3.1.1	Bending stiffness identification using the VFM	46
3.2	Results and discussion	47
3.2.1	Validation on FE simulated data without noise	47
3.2.1.1	FE modeling	47
3.2.1.2	Validation from FE curvature data	48
3.2.2	Validation on FE simulated data with noise	50
3.2.3	Experimental identification results	52
3.2.3.1	Specimen preparation with resin coating	53
3.2.3.2	Experimental Set-up	56
3.2.3.3	Data processing	58
3.2.3.4	Comparison between FE data and experimental data (slopes, strains)	58
3.2.3.5	Identification results with original camera position (with spatial smoothing)	60
3.2.3.6	Identification results with offset camera position (without spatial smoothing)	61

3.3	Conclusion	62
4	Review of damage process and detection techniques for composite plates	63
4.1	Introduction	63
4.2	Damage in composites	64
4.2.1	Delamination	65
4.2.1.1	Initiation and propagation	66
4.2.1.1.1	Strength analysis	67
4.2.1.1.2	Fracture mechanics approach	67
4.2.1.2	Buckling	69
4.2.2	Impact damage	71
4.2.2.1	Low / High velocity impact	71
4.2.2.2	Damage mechanisms in low velocity impact	72
4.2.2.2.1	Matrix damage	72
4.2.2.2.2	Delamination	72
4.2.2.2.3	Fibre failure	73
4.3	Effects of damage on mechanical performance	73
4.3.1	Residual strength	74
4.3.1.1	Residual tensile strength	74
4.3.1.2	Residual compressive strength	75
4.3.1.3	Residual flexural strength	76
4.3.2	Residual stiffness	77
4.3.2.1	Residual in-plane stiffness	77
4.3.2.1.1	Stiffness reduction due to matrix cracking	77
4.3.2.1.1.1	Shear-lag approach	77
4.3.2.1.1.2	Variational approach	78
4.3.2.1.2	Stiffness reduction due to delamination induced by matrix cracking	78
4.3.2.1.3	Stiffness reduction due to impact damage	79
4.3.2.2	Residual flexural stiffness	80
4.4	Damage detection methods	80
4.4.1	Visual inspection	81
4.4.2	Ultrasonic inspection	81
4.4.3	Eddy current	82
4.4.4	Acoustic emission	82
4.4.5	Radiography	82
4.4.6	Thermography	82

4.4.7	Lamb waves	83
4.4.8	Optical methods	83
4.4.9	Vibration-based analysis using eigenfrequency and mode shapes	84
4.5	Conclusion	84
5	Identification of the local stiffness reduction Part I: simulation	87
5.1	Introduction	87
5.1.1	Modeling scale levels	88
5.1.2	Finite element (FE) approach	89
5.1.2.1	3D/2D	89
5.1.2.2	Damage modeling	90
5.1.2.2.1	Intralaminar damage	90
5.1.2.2.2	Interlaminar damage	91
5.1.3	Plate theory approach	92
5.2	Results and discussion (Intralaminar damage)	92
5.2.1	Polynomial parameterization	93
5.2.1.1	Validation on FE simulated data for isotropic damage	93
5.2.1.1.1	FE model	93
5.2.1.1.2	Validation from FE curvature data	94
5.2.1.2	Sensitivity study for isotropic damage	97
5.2.1.2.1	Effect of the smoothing of the slope field	97
5.2.1.2.2	Effect of boundary conditions	98
5.2.1.2.3	Effect of load magnitude	100
5.2.1.2.4	Threshold of damage detection	101
5.2.1.2.5	Effect of spatial resolution	104
5.2.1.2.6	Effect of experimental conditions	105
5.2.1.2.7	Unsymmetrical damage	109
5.2.1.3	Validation on FE simulated data for anisotropic damage (without noise)	110
5.2.2	Discrete parameterization	113
5.2.2.1	Isotropic damage	114
5.2.2.2	Anisotropic damage	115
5.2.2.2.1	Validation on FE simulated data without noise	115
5.2.2.2.2	Validation on FE simulated data with noise	117
5.2.2.2.2.1	Effect of force location	117
5.3	Results and discussion (Interlaminar damage)	119
5.3.1	Polynomial parameterization	120

5.3.1.1	Validation on FE simulated data	120
5.3.1.1.1	FE model	120
5.3.1.1.2	Validation from FE curvature data	122
5.4	Conclusion	123
6	Identification of the local stiffness reduction Part II: experiment	125
6.1	Introduction	125
6.2	Identification of stiffness reduction on artificial damage	126
6.2.1	Removal of plies	126
6.2.1.1	Polynomial parameterization	128
6.2.1.2	Discrete parameterization	129
6.2.1.2.1	Isotropic damage	129
6.2.1.2.2	Anisotropic damage	130
6.2.2	Near-the-surface delamination	133
6.2.2.1	Polynomial parameterization	134
6.2.2.2	Discrete parameterization	135
6.2.3	Mid-plane delamination	137
6.2.3.1	Polynomial parameterization	137
6.2.3.2	Stress fields	140
6.2.3.3	Slope fields	142
6.2.3.4	Discussion on the current methodology	143
6.3	Identification of stiffness reduction on real impact damage	147
6.3.1	Impact test	147
6.3.2	Polynomial parameterization	150
6.4	Conclusion	151
	General conclusions and perspectives	153
	References	157

List of Tables

3.1	Identification results depending on the polynomial degrees (R.D.: Relative Difference).	49
3.2	Comparison between polynomial and piecewise methods.	50
3.3	Identification results with noisy data.	53
3.4	Identified stiffness components for the carbon epoxy plate (a) with original camera position (spatial smoothing, 9 th order) (b) with offset camera position (without spatial smoothing, before calibration) (c) with offset camera position (without spatial smoothing, after calibration).	61
4.1	Damage statistics in metallic and composite structures taken from the MONITOR end-user surveys [52].	64
5.1	Conditions used in the parametric study.	107
5.2	Stiffness reduction depending on the lay-up (R.D.: Relative Difference). . .	111
5.3	Comparison of results between type 1 and type 3 (D^u : stiffness for undamaged area, D^d : stiffness for damaged area, units for D : Nm ²).	116
5.4	Sensitivity values for each stiffness in type 1 and type 3.	116
5.5	Comparison of results between type 1 and type 3 (Units for D : Nm ²). . . .	117
6.1	Comparison of results from exact damage location and identified damage location (D^u : stiffness for undamaged area, D^d : stiffness for damaged area, R.D.: Relative Difference, units for D : Nm ²).	131
6.2	Sensitivity values for each stiffness in exact and identified damage location ($(\frac{\eta}{D})^u$: for undamaged area, $(\frac{\eta}{D})^d$: for damaged area).	131
6.3	Identified stiffness components for a THR160/EH84 UD plate (a) with original camera position (spatial smoothing) (b) with offset camera position (without spatial smoothing, after calibration).	133

6.4	Comparison of results from exact damage location (a) with original camera position (spatial smoothing) (b) with offset camera position (without spatial smoothing) (D^u : stiffness for undamaged area, D^d : stiffness for damaged area, units for D : Nm^2).	136
6.5	Sensitivity values for each stiffness in exact damage location (a) with original camera position (spatial smoothing) (b) with offset camera position (without spatial smoothing).	136

List of Figures

1.1	Principle of deflectometry.	6
1.2	Fringe analysis in phase x (a) Intensity pattern (b) Phase field x (c) Corresponding wrapped phase (d) Unwrapped phase (e) Loading and boundary conditions.	10
1.3	Fringe analysis in phase y (a) Intensity pattern (b) Phase field y (c) Corresponding wrapped phase (d) Unwrapped phase.	11
1.4	Removing of the periodic horizontal or vertical information by period-wise averaging [11].	13
1.5	Ideal intensity profile.	13
1.6	Experimental intensity profile.	16
1.7	Curvatures fields obtained from slope fields (a) with polynomial spatial smoothing (b) without spatial smoothing	19
1.8	Camera position (a) behind the grid (b) beside the grid	20
2.1	Displacement field through-the-thickness in Kirchhoff plate theory.	26
2.2	Displacement field through-the-thickness in Mindlin plate theory.	27
3.1	Geometry and test configuration of the plate.	48
3.2	Bending stresses in a thin plate [43].	48
3.3	Residual values depending on the polynomial degree.	52
3.4	A procedure for producing reflective coatings.	54
3.5	A procedure for producing reflective coatings (Cont'd).	55
3.6	Comparison of surfaces with and without coating (image of a ceiling light)	56
3.7	Deflectometry set-up.	57
3.8	Comparison of slope fields between (a) FEA and (b) experiment.	59
3.9	Comparison of strain fields between (a) FEA and (b) experiment, with original camera position (spatial smoothing, 9 th order) and (c) experiment, with offset camera position (without spatial smoothing).	60
3.10	The 2D distribution of sensitivity.	62

4.1	Types of delaminations: (a) internal (b) near-surface [57].	66
4.2	Three basic modes of crack tip deformation: (a) Mode I (tension, opening) (b) Mode II (in-plane shear, sliding) (c) Mode III (out-of-plane shear, tearing) [68].	68
4.3	Basic fracture mechanics tests: (a) DCB test (b) ENF test [69]	69
4.4	Three types of buckling mode shapes: (a) Local buckling mode (b) Mixed buckling mode (c) Global buckling mode [74].	70
4.5	Optical micrograph of virgin and failed sample: (a) Rich resin interface between two layers (b) Delamination propagation for a $[90_2/0_2]_s$ specimen [90].	73
4.6	Characteristic residual strength versus impact energy curve [48].	75
4.7	Residual flexural properties as a function of absorbed impact energy [97].	76
4.8	Shearography image of delamination [114].	84
5.1	FE model of DCB experiment [124].	90
5.2	Geometry and test configuration of the damaged plate.	94
5.3	Detection results as a function of the degree of the polynomial parameterization.	95
5.4	Example of identification of the stiffness reduction for different modulus contrast (simulated curvatures).	96
5.5	Damage description by a polynomial function.	96
5.6	Detection results as a function of the degree of the slope curve fitting polynomials.	97
5.7	Four test configurations for the noise sensitivity test.	98
5.8	Damage identification figures in noise sensitivity test.	99
5.9	Relative difference of curvatures between undamaged and damaged plate in each configuration.	100
5.10	Effect of the magnitude of the applied force on damage detection.	101
5.11	Detection results for different combinations of the size of the damaged area and the stiffness reduction (Applied force: 5 N).	102
5.12	Detection results for different combinations of the size of the damaged area and the stiffness reduction (Applied force: 10 N).	103
5.13	The undeformed and deformed grid images.	105
5.14	Damage detection results depending on various grid pitch sizes.	106
5.15	Damage detection results depending on the conditions in Tab. 5.1	108
5.16	Point grips for bending test (a) previous grips (b) new grips.	109

5.17	Comparison of detection results between (a) symmetric damage, and (b) unsymmetrical damage.	110
5.18	Comparison of detection results between (a) isotropic damage (type A) and (b) anisotropic damage (type B) in cross-ply laminates.	111
5.19	Force locations.	112
5.20	Corresponding stiffness reduction of D_{66} depending on force location. . . .	113
5.21	Detection results depending on the mesh size (a) 6×4 , (b) 12×8 , (c) 19×14	114
5.22	Comparison between (a) polynomial and (b) discrete parameterization. . . .	114
5.23	Identification results with noisy data depending on the mesh size (a) 1×1 , (b) 2×2 , (c) 3×3 (the number in parenthesis means relative difference from the reference).	115
5.24	Force locations used for each criterion (a) $\frac{\eta}{D} \times$ maximum deflection and $\frac{\eta}{D} \times$ maximum von Mises strain; (b) minimum standard deviation.	119
5.25	Optimal force location depending on each criterion: (a) $\frac{\eta}{D} \times$ maximum deflection; (b) $\frac{\eta}{D} \times$ maximum von Mises strain; (c) minimum standard deviation (the point in each figure indicates the optimal position).	120
5.26	Two different delamination models.	122
5.27	Stiffness reduction due to mid-plane delamination (a) with adjusted scale (b) with original scale (including exact location of delamination).	123
6.1	Geometry and test configuration of the damaged plate.	126
6.2	Experimental slope field data.	127
6.3	Experimental strain field data.	127
6.4	First experimental result for a damaged composite plate.	128
6.5	Damaged area (left: exact damaged area, right: chosen damaged area). . . .	129
6.6	Stiffness identification results with 1 piece (left: exact damaged area (0.73), right: identified damaged area (0.79)).	130
6.7	Stiffness identification results with 4 pieces (left: exact damaged area (0.65, 0.82, 0.68, 0.81, from lower left corner, clockwise direction), right: identified damaged area (0.71, 0.97, 0.64, 0.86)).	132
6.8	Stiffness identification results with 9 pieces.	132
6.9	Comparison of strain fields between the cases (a) with original camera position (spatial smoothing, 14th order) (b) with offset camera position (without spatial smoothing).	134

6.10	Identification of the stiffness reduction on the near-the-surface delamination with (a) original camera position (spatial smoothing) including exact damaged area (b) offset camera position (without spatial smoothing) including exact damaged area.	135
6.11	Comparison of curvature fields between (a) FEA and (b) the experiment, without spatial smoothing and (c) the experiment, with spatial smoothing (14th order).	138
6.12	Comparison of stiffness reduction results between (a) experiment, and (b) FEA, using curvatures from strains, and (c) FEA, using curvatures from slopes.	139
6.13	Stress distribution in the x direction within each layer (FEA).	141
6.14	Comparison of stress fields in the x direction between several damage types (FEA, BSR: bending stiffness reduction).	142
6.15	Experimental slope field in the x direction of mid-plane delamination.	143
6.16	Comparison of slope fields in the x direction between several damage types (FEA, BSR: bending stiffness reduction).	144
6.17	Through-the-thickness strain distributions in the mid-plane delamination.	145
6.18	Identification of the stiffness reduction on the half layers removal (FE simulation).	146
6.19	Through-the-thickness strain distributions in the half layers removal.	146
6.20	Support fixture and impactor.	147
6.21	Small indent and bulge zone.	148
6.22	Image distortion on the impacted area.	149
6.23	Phase field (a) x and (b) y	149
6.24	Identification of the stiffness reduction on the impact damage (a) with original scale (including exact location of impact damage, the location of the bulge zone was measured with a tape measure) and (b) with adjusted scale.	150

General Introduction

Composite materials offer many advantages over conventional metallic counterparts such as high specific stiffness, strength and excellent fatigue and corrosion resistance. Laminated composite plates fabricated by stacking unidirectional plies exhibit directional properties which can be adopted very efficiently under various structural loading conditions. However, their inherent anisotropy and the brittle characteristics of fibres and resin result in failure mechanisms that are very different from those of homogeneous metallic ones. While ductile metallic components can yield and absorb kinetic energy via plasticity, brittle composites can only dissipate energy by a variety of damage modes. Particularly, the lack of through-the-thickness reinforcement of most of the prepreg-based laminates develops a unique type of damage as a form of discontinuity between layers. Accordingly, the damage modes in composite laminates involve not only intralaminar damage (matrix cracking, fiber breakage) but also interlaminar damage (delamination).

Delamination is the most dangerous failure mechanism in composite laminates. Delamination damage is caused by large interlaminar stresses resulting from low-velocity impact (maintenance tool, bird strike, *etc.*), the structure's free edge effect, or faulty manufacturing processes. If a laminated plate with delamination is under tensile loading, delamination does not affect load carrying capability much. On the contrary, under compressive or bending load, delamination can be critical. Under compressive load, each sublaminar in the delaminated region should resist its own buckling load. Owing to the reduced thickness of each sublaminar, the flexural stiffness decreases. Consequently, the critical buckling load is much lower than that of the virgin laminate. In bending case, the presence of delamination can reduce the bending rigidity drastically as the second moment of area decreases with the third power of thickness. In addition, the load carrying capability from the undamaged part to the damaged part is seriously impaired because the delaminated part loses its ability to transfer interlaminar shear stress.

The strength and stiffness of composite laminates are significantly impaired in the presence of delaminations, therefore evaluation of the residual properties and prognosis of the remaining service life of the structure have been of great interest. The evaluation

of residual strength and stiffness in a quantitative sense would be a good choice for the assessment of reliability in composite structures. Nevertheless, measurement of residual strength during damage development is not practical because the destruction of the test specimens is involved. On the other hand, measurement of residual stiffness can be done repeatedly and continuously during damage development without destruction of the specimen. Damage state in laminates may evolve from matrix cracking to delamination under service loading. Gradual stiffness reduction due to damage evolution can also be measured since the measurement does not disturb the damage development. Accordingly, residual stiffness can be a very promising parameter which can be used for the evaluation of structural reliability non-destructively. However, the global stiffness is not very sensitive to local damage. The most important parameter which needs to be considered is the local stiffness reduction. The local instability induced by local stiffness reduction plays an important role in the failure mechanism of composite laminates through stress redistribution. Therefore, accurate evaluation of the actual state of damage and prediction of the final failure require the identification of local stiffness reduction of the damaged zone rather than the global stiffness reduction.

Although various damage detection techniques have been developed, most of them provide limited and mostly qualitative information regarding damage modes and distributions. The evaluation of the local loss of stiffness remains an open problem. Classical measurement techniques such as strain gages may be applied to the measurement of local stiffness reduction. However, the contact procedure inevitably induces deviation in measurement and it is very difficult to measure large area with a small number of sensors, if not impossible. Therefore, it is of primary importance to develop analytical tools which can assess whether the detected damage is critical or not for the life of the component. In order to effectively diagnose the reliability of the damaged structure, both qualitative and quantitative information concerning the damage should be addressed.

The present study aims at taking advantage of the availability of non-contact full-field measurements and adapted inverse identification procedures in order to not only locate the damage but also to identify the local stiffness reduction of the panel. To do so, full-field heterogeneous slope fields are measured through a deflectometry technique. The interest of slope compared to deflection is that only one differentiation is required to obtain the curvatures which directly relate to the strains in the framework of Love-Kirchhoff thin plate theory. The virtual fields method (VFM) is used as an inverse procedure to process curvatures for the identification of the local loss of stiffness. The VFM is based on a relevant use of the equilibrium equations through the principle of virtual work. It has been adapted to the case of a plate with stiffnesses varying with the space variables.

The present thesis is organized into six chapters. The first chapter is focused on full-field measurement techniques to extract kinematic information from experiment. In the first part, several optical techniques are reviewed. The principles and characteristics of some techniques which can measure out-of-plane deformation are introduced. In the second part, the deflectometry technique which will be used in this study is discussed in detail. The principle, basic properties for optical performance and the procedure of fringe analysis are presented. Finally, some issues related to the spatial smoothing for differentiation are introduced and a new configuration for deflectometry is developed.

Chapter 2 discusses the principles of the VFM and its application to the present problem. In the case of plate bending, the VFM utilizes the kinematic assumptions of plate theories. Kirchhoff and Mindlin plate theories are reviewed and the application of the classical lamination theory (CLT) to the VFM is discussed. Next, the identification procedure with the VFM for a specimen whose stiffnesses do not change inside the solid is given. However, in the case of a plate with stiffnesses varying within the material, the VFM should be adapted. It is necessary to find some ‘parameterization’ to solve the problem. This is explored in this chapter.

In Chapter 3, the identification procedure of the bending stiffnesses in undamaged composite laminated plates is validated on simulated and experimental measurements. In the orthotropy basis, four bending stiffnesses are determined from a single bending test using the VFM. In the experimental part, specimen surface preparation required for deflectometry is introduced and the identification results depending on camera positions in deflectometry are presented.

Chapter 4 contains a review of the damage in composite structures in terms of damage resistance and tolerance. Damage resistance is defined as an ability to resist damage ‘onset’ and ‘growth’ from a specific cause such as impact and damage tolerance refers to the capability of the damaged structure to still fulfil its task (*i.e.*, sustain loading, for instance). Both aspects are reviewed in this chapter, with a view to impact and delamination damage.

In Chapter 5, several techniques for the efficient FE modeling of damage in composite laminates are introduced and the proposed methodology in Chapter 2 is validated on simulated FE measurements for the case of intralaminar and interlaminar damage. Several possibilities and the effects of several variables on the quality of the predictions are explored. In this chapter, the potential of the VFM to locate and quantify the local stiffness reduction in damaged composite plates is investigated.

Chapter 6 presents a wider validation of the proposed methodology against experimental data, both on artificial and real impact damage in composite laminated plates. Two types

of delamination dependent on the through-the-thickness position are examined. The first type is the delamination located near the surface, which generally induces local buckling under loading, and the second is the delamination at the mid-plane. Stiffness reduction associated to the two types of delamination is identified and extensive comments on the mechanism and the different behavior of these delaminations are given. The last verification performed in the present study concerns real impact damage. Several techniques developed in the previous chapters are validated on experimental measurements.

Chapter 1

Full-Field Measurement Technique

1.1 Introduction

The interest of full-field measurement techniques is increasing in experimental mechanics owing to their versatile non-contact features and the fact that they produce a wealth of data able to quantify heterogeneous kinematic fields [1, 2].

Full-field measurement techniques are particularly useful for the analysis of heterogeneous and anisotropic materials such as composite materials, since these techniques are able to provide full heterogeneous displacement or strain fields of specimens of interest, whereas conventional measurement techniques such as electric strain gages or extensometers only provide local and average information. The obtainability of full kinematic information allows investigating material properties and structural behavior even in complicated structures under complex loading conditions. This enables new approaches for data processing of experimental results by observing not just a single measurement but a series of measurement, so that the evolution of displacement or strain fields during loading can be traced. These advantages are a result of the advancement of digital cameras, optical component technology, and software for data processing algorithms [1, 2].

There is a variety of techniques which can be used for full-field measurement. The measurement fields could be in-plane (grid method, digital image correlation, speckle interferometry, moiré interferometry) or out-of-plane displacements (shadow and projection moiré, speckle interferometry, moiré interferometry) [1, 2]. Strain fields can be obtained from the measured displacements by numerical differentiation or directly (shearography).

Also, slopes can be measured (deflectometry). Generally, these methods are categorized into two groups by the nature of physical phenomena [1-3].

The first group is non-interferometric methods (also called geometric methods, or white light methods) such as the grid method, moiré, digital image correlation, fringe projection and deflectometry. The optics is generally restricted to image formation. Physical phenomena allowing the measurement are geometrical - *i.e.*, deformation of a surface pattern, triangulation *etc.* The second concerns the interferometric methods as in moiré interferometry, speckle interferometry, shearing interferometry and photoelasticity. Generally, the sensitivity of interferometric methods is higher by more than one order of magnitude than the white light methods. However, the interferometric methods are susceptible to environmental disturbances like vibrations because of their high sensitivity.

Basically, full-field methods are utilizing the hidden physical quantity information such as displacement or strain components which are encoded as fringes or speckle intensity fields. Thus, the methods can also be classified into two categories of periodical carrier encoding and random encoding depending on the nature of information encoding [3, 4].

In the case of periodical carrier encoding, the kinematic fields are derived from fringe intensity fields. The intensity fields are obtained from the surface encoding by structured light or attached grid pattern to the surface in geometrical methods or by a diffraction grating in interferometric techniques. A signal having a natural spatial frequency is used as the spatial carrier. In this method, the displacement and strain information are related to the phase modulation. The common techniques for periodical carrier encoding are the grid method, moiré, fringe projection, deflectometry and grating shearography.

In contrast, random encoding utilizes the natural texture of materials directly. In some cases, the surface can be marked with a random pattern such as a speckle intensity field or paint spray. Any point in the random pattern is correlated between the initial and final stages for the analysis. The position change of each point is calculated through specific algorithms. Digital image correlation, ESPI and shearography are included in random encoding. Generally, the performance, characterization and resolution of the periodic encoding are better than those of random encoding; also, the phase detection can be performed more efficiently in the periodic encoding since the carriers can be more easily characterized in terms of frequency, amplitude and signal-to-noise ratio (SNR) than random patterns. However, carrier-based methods require non-trivial specimen preparation. Also, phase unwrapping may be necessary due to periodic information [3].

The optimal choice among the various methods is not easily determinable since the scattered literature over numerous journals makes it difficult to have a general view of the methods [1]. The selection of the most relevant technique may be based on the two re-

quirements [4]: the first is the characteristics of the mechanical test and the analysis method (mechanics). The other is the performance of an optical technique (optics, data treatment). All the techniques have merits and drawbacks in terms of accuracy, expense, robustness and level of instrumentation required. Therefore, the type of measurand (small or large in-plane displacement, out-of-plane deflection, strains, and slopes), the range of the measurement, the sensitivity, resolution, spatial resolution, the cost and the complexity of a technique are the parameters which need to be considered in the selection process [4].

1.1.1 Out-of-plane measurement techniques

The present study aims at taking advantage of the availability of full-field out-of-plane measurements in order to detect damage in composite laminated plates. Simple bending tests will be performed for the measurements. In this section, common full-field methods which can be used for the out-of-plane measurements and their characteristics will be reviewed.

1.1.1.1 Electronic Speckle Pattern Interferometry (ESPI)

Electronic Speckle Pattern Interferometry (ESPI) is an interferometric technique which uses coherent light for out-of-plane or in-plane deformation measurement [5, 6]. It is also known as Digital Speckle-Pattern-Interferometry (DSPI) or TV-Holography. This optical technique allows detecting deformation to a sensitivity smaller than the wavelength of the light.

When coherent light such as a laser is illuminated on a rough surface, speckle patterns are obtained due to the interference of the back-scattered light. These speckles are inherent to the target surface like a fingerprint. For the measurement of out-of-plane displacement, a second reference laser beam is required. The object beam scattered from the target surface (speckles) and the reference beam, originating from the same laser light source, are superimposed via a beam splitter on a CCD camera. This results in the so-called interferogram. Interferogram is a fringe pattern with sinusoidal modulation and its intensity is formed by interference process of two coherent beams. As the surface is deformed, the wave front emanating from the object is slightly deformed, whereas the wave front of the reference beam remains constant, so the speckle interferogram also changes. Thus, a subtraction of the interferograms of the surface before and after loading will result in a typical fringe pattern, which reveals the displacement of the surface during loading as contour lines of deflection. The change of the optical phase between the two beams due to

displacements enables out-of-plane measurement. A procedure called phase shifting treats a series of speckle images for each surface state and calculates a quantitative phase map. In contrast to the fringe images, this phase map contains quantitative and directional information that can be directly transformed into a displacement field. The displacement fields are numerically differentiated in order to obtain strain maps. The resolution of the displacement is determined by the wavelength of the laser employed and the geometrical arrangement. Typical values are as small as 50 nm.

This method requires surfaces which scatter light, meaning that neither grating nor a smooth surface is necessary. However, these qualitative fringe images using the diffused light are of low contrast and noisy due to the presence of the speckles. Therefore, the image or the phase map degraded by the spatial noise requires a filtering or fitting inducing a degradation of its spatial resolution. Additionally, ESPI is very sensitive to environmental disturbances, particularly vibration, which limits the industrial application of the method.

1.1.1.2 Shearography

Shearography is also an interferometric technique. While in ESPI, the interference is generated between a reference and an object beams, shearography utilizes the interference effect between the waves coming from the two object points separated by image shearing [7, 8]. Consequently, shearography measures the first derivative of out-of-plane and in-plane deformation directly by an optical differentiation. With this technique, slope or strain fields can be obtained without the procedure of the numerical differentiation.

An expanded laser light illuminates the target surface. The light reflected from the surface is transmitted into a shearing device - a Michelson interferometer. The Michelson interferometer splits the beam of light into two paths, so that one beam bounces off a fixed mirror and the other off a movable mirror. So a pair of laterally sheared images of the surface is generated by adjusting the movable mirror through a very small angle from normal position. When the reflected beams are recombined, a speckle pattern is generated due to an interference of the two sheared images. This intensity distribution of the speckle pattern is recorded by an image-shearing CCD camera. When the surface is deformed, the intensity distribution is changed. It is captured by the CCD camera again. By subtracting the two images before and after deformation, a fringe pattern (digital shearogram) can be obtained. This digital shearogram is the first-order derivative of surface displacements (surface gradient). In this way, strain fields or slope fields can be directly obtained from the measurements.

The shear distance, which is the optical path length difference between the two sheared

images, can be used to adjust the performances of shearography as with SNR, sensitivity, spatial resolution and resolution. Shearography is insensitive to vibration disturbance because rigid body motions do not produce strain. Shearography does not require surface preparation, although a filtering or fitting needs to be performed due to the speckle noise as with ESPI.

1.1.1.3 Shadow moiré

Shadow moiré is a white light method which can be used for the measurement of out-of-plane displacements [9]. The shadow moiré method utilizes the moiré effect as a result of the geometric interference of a reference grating and its own shadow on an object surface.

A reference grating of pitch p is positioned in front of the surface of an object. When the white light illuminates the grating with an incident angle α , the light creates a shadow of the grating on the surface. The shadow of the grating is elongated on the surface due to the contour of the object and the shadow shifts depending on the incidence angle and the distance between the grating and the object. The geometric interference of the shadow and the reference grating produces moiré fringes of light and dark areas. A CCD camera observes the fringes at an angle normal to the surface of the grating. Depending on the alignment of the shadows and grating, the light and dark areas are generated. If there are N fringes between two specific points, the out-of-plane displacement is:

$$w = \frac{Np}{\tan(\alpha)} \quad (1.1)$$

where α is the incident angle, p the grating pitch, N the moiré fringe order. If the incidence angle α is 45° , the displacement that each fringe represents is equal to the pitch p of the grating.

1.2 Deflectometry

Deflectometry [10, 11] is a white light noninterferometric method. Deflectometry has high sensitivity and resolution although it is a noninterferometric method.

When bending tests are performed on thin plates, the strains are related to the curvatures of the specimen in the framework of the Love-Kirchhoff thin plate theory. Therefore, if out-of-plane deflections are measured, double differentiation is required. This will amplify the effect of measurement noise dramatically. An alternative is to measure slopes that will give access to curvatures with only one differentiation. The deflectometry technique is able

to measure full-field heterogeneous slope fields (derivatives of the out-of-plane deflection fields) directly. The technique is inexpensive, quite insensitive to environmental vibration disturbance and far easier to implement than interferometry techniques.

In this study, deflectometry was chosen as the full-field measurement technique since curvature data are required and also the size of the investigation field is well suited to the approach adopted.

1.2.1 Principle

The principle of deflectometry is based on Snell's law of specular light reflection. The deflectometry setup is shown in Fig. 1.1.

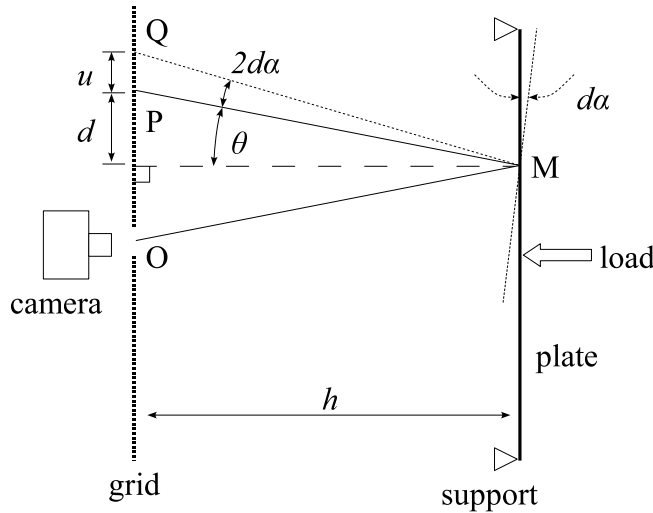


Figure 1.1: Principle of deflectometry.

It consists of observing the image of a grid (cross-line grating) at the surface of the tested specimen then to process the change of phase caused by a local rotation. Consequently, this technique requires the surface of the specimen to have a sufficient amount of specular reflection. The technique is briefly described as follows: at rest, the light from point P of the reference grid is reflected at point M on the plate before reaching the CCD camera. When the plate deforms in bending, the local slope at point M changes by $d\alpha$ and the CCD camera records the light coming from point Q of the reference grating, separated from P by u . Therefore, a change of slope on the tested plate leads to a local shift of the image of the reference grid viewed by the camera. This shift can be evaluated by spatial phase stepping [12]. A first image of the plate at rest is taken and the phase

field is computed using a specific phase stepping algorithm. Then, the plate is deformed and another phase field is computed. The difference of phase between the initial and deformed images directly relates to the local slope field. Since the phase modulation is 2π when u equals p , from geometrical considerations, the relation between the spatial phase difference $d\varphi$ and the slope variation $d\alpha$ is:

$$d\varphi = 2\pi \frac{u}{p} = 2\pi \frac{2hd\alpha}{p} = \frac{4\pi h}{p} d\alpha \quad (1.2)$$

where p is the pitch of the reference grid and h the distance between the plate and the grid. The equality $u = 2hd\alpha$ can be obtained as follows:

From Fig. 1.1, one has

$$\begin{aligned} \tan(\theta + 2d\alpha) &= \frac{d + u}{h} \\ \tan(\theta) &= \frac{d}{h} \end{aligned} \quad (1.3)$$

Subtracting two terms,

$$\tan(\theta + 2d\alpha) - \tan(\theta) = \frac{d + u}{h} - \frac{d}{h} = \frac{u}{h} \quad (1.4)$$

From trigonometric formulae, $\tan(\theta + 2d\alpha)$ can be expressed as:

$$\tan(\theta + 2d\alpha) = \frac{\tan(\theta) + \tan(2d\alpha)}{1 - \tan(\theta)\tan(2d\alpha)} \quad (1.5)$$

Thus,

$$\frac{u}{h} = \frac{\tan(\theta) + \tan(2d\alpha)}{1 - \tan(\theta)\tan(2d\alpha)} - \tan(\theta) \quad (1.6)$$

Multiplying both terms by $h(1 - \tan(\theta)\tan(2d\alpha))$,

$$u(1 - \tan(\theta)\tan(2d\alpha)) = h(\tan(\theta) + \tan(2d\alpha)) - h(1 - \tan(\theta)\tan(2d\alpha))\tan(\theta) \quad (1.7)$$

Rearranging the above terms,

$$u(1 - \tan(\theta)\tan(2d\alpha)) = h\tan(2d\alpha)(1 + \tan^2(\theta)) \quad (1.8)$$

Assuming that $d\alpha$ is small, one has $\tan(2d\alpha) \simeq 2d\alpha$, then:

$$u = 2hd\alpha \frac{1 + \tan^2(\theta)}{1 - 2d\alpha \tan(\theta)} \quad (1.9)$$

Since $2d\alpha$ is very small and $\tan(\theta)$ is small in this case, one can neglect $2d\alpha \tan(\theta)$ with respect to 1. Hence,

$$u = 2hd\alpha(1 + \tan^2(\theta)) \quad (1.10)$$

If h is reasonably larger than the tested plate size, then $\tan^2(\theta)$ can be also neglected with respect to 1. Therefore, one can extract u : $u=2hd\alpha$. This relation (Eq. 1.2) was also checked experimentally using a specific setup to apply a calibrated rotation [13]. The effect of out-of-plane movements was also investigated in the same study and was found to be negligible in the configuration of Fig. 1.1.

Since the cross-line grating (grid) is used in the deflectometry, the two-dimensional phase difference components $d\varphi_x$ and $d\varphi_y$ can be obtained simultaneously. Then it follows that the phase modulations are:

$$d\varphi_x = 2\pi \frac{u_x}{p} = \frac{4\pi h}{p} d\alpha_x \quad (1.11)$$

$$d\varphi_y = 2\pi \frac{u_y}{p} = \frac{4\pi h}{p} d\alpha_y \quad (1.12)$$

1.2.2 Sensitivity, resolution and spatial resolution

Before proceeding further, important terminologies for optical performance of deflectometry will be reviewed in this section. The sensitivity s is the ratio between the measured phase and the slope [11]. The sensitivity can be directly obtained from the Eq. 1.2 and written as:

$$s = \frac{d\varphi}{d\alpha} = \frac{4\pi h}{p} \quad (1.13)$$

The resolution σ_α can be defined as the smallest slope value detectable above the noise. It is obtained from the amount of noise σ_φ in the phase measurement.

$$\sigma_\alpha = \frac{\sigma_\varphi}{s} \quad (1.14)$$

By taking two consecutive images of the plate at rest, it is possible to evaluate the standard deviation σ of the noise. Then, σ_φ is obtained from σ by $\sigma_\varphi = \frac{\sigma}{\sqrt{2}}$ as the standard deviation of the noise was calculated by subtracting two phase images. The noise level is only related to the optical conditions (for instance, wave length of light used, quality of reflection surface on the specimen) and the CCD camera. In the present configuration of Fig. 1.1, the resolution has been evaluated to be 1.11×10^{-4} radians (0.00635 deg) for a pitch size of 2.9 mm, with a grain (number of pixels sampling each period) of 9, an observation distance h of 0.915 m and a 1360×1024 pixels PCO PixelFly CCD camera. This level will be used for the noise level in the numerical simulations.

The spatial resolution is the smallest distance over which two measurements are independent [4]. In deflectometry, it is half the reference grid pitch since the pitch size for the spatial resolution corresponds to the size of the pitch of the image reflected onto the plate. It is worth noting that the spatial resolution is in inverse proportion to the resolution. As the pitch size of the grid increases, the spatial resolution deteriorates, whereas the resolution improves. This is due to the fact that the noise level decreases when the number of pixels sampling one period of the pitch increases. Thus, we must accept some compromise between the resolution and spatial resolution.

1.2.3 Fringe Analysis

Most of the optical measurement techniques produce fringe (intensity) patterns as an output, meaning the fringe patterns should be analyzed in order to acquire the required physical quantities such as deformation, slope or strain fields.

Fringe analysis is the data processing method for extracting the encoded physical quantity from fringes [12]. Phase detection and phase unwrapping are the two main processes. In the phase detection, the corresponding phase field is extracted from the recorded intensity patterns. Generally, an arc-tangent function is used to calculate the phase distributions. The obtained phase field is wrapped onto the range $[-\pi, +\pi]$. Phase unwrapping is a step which removes the 2π -jumps in the field to make it continuous. This unwrapped phase map is directly proportional to the physical quantity of interest. The image processing procedures for the fringe analysis and unwrapping are presented in Figs. 1.2 and 1.3.

An example of a fringe pattern obtained from deflectometry is shown in Fig. 1.2 (a). From the fringe patterns of undeformed and deformed states, phase fields are obtained (Fig. 1.2 (b)). The subtraction of phases between the initial and deformed images is directly proportional to the slope field. The wrapped phase field (Fig. 1.2 (c)) which is within the range $[-\pi, +\pi]$ has to be unwrapped as in Fig. 1.2 (d). The loading and

boundary configuration for the phase field is shown in Fig. 1.2 (e). In the same fashion, the unwrapped phase y can be measured (Fig. 1.3).

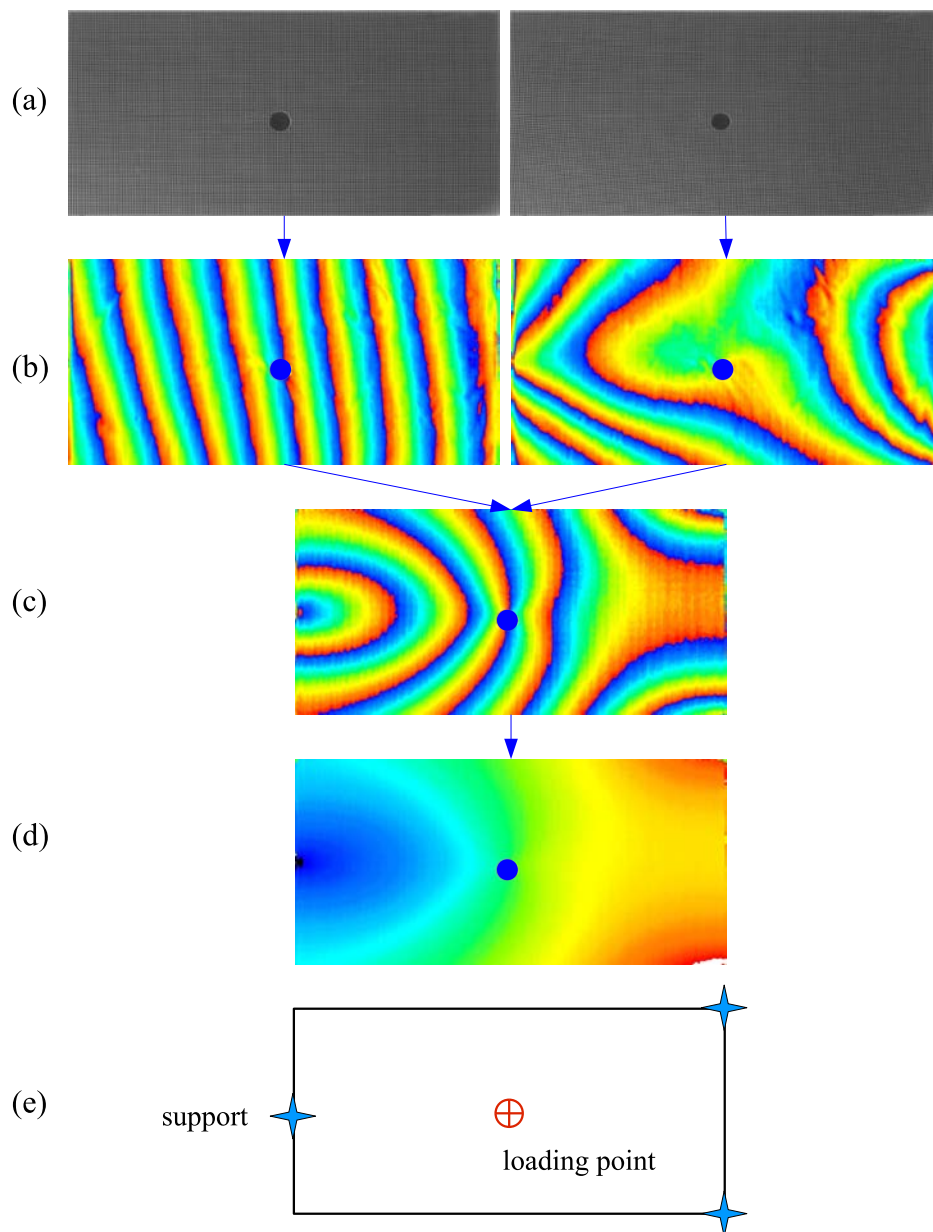


Figure 1.2: Fringe analysis in phase x (a) Intensity pattern (b) Phase field x (c) Corresponding wrapped phase (d) Unwrapped phase (e) Loading and boundary conditions.

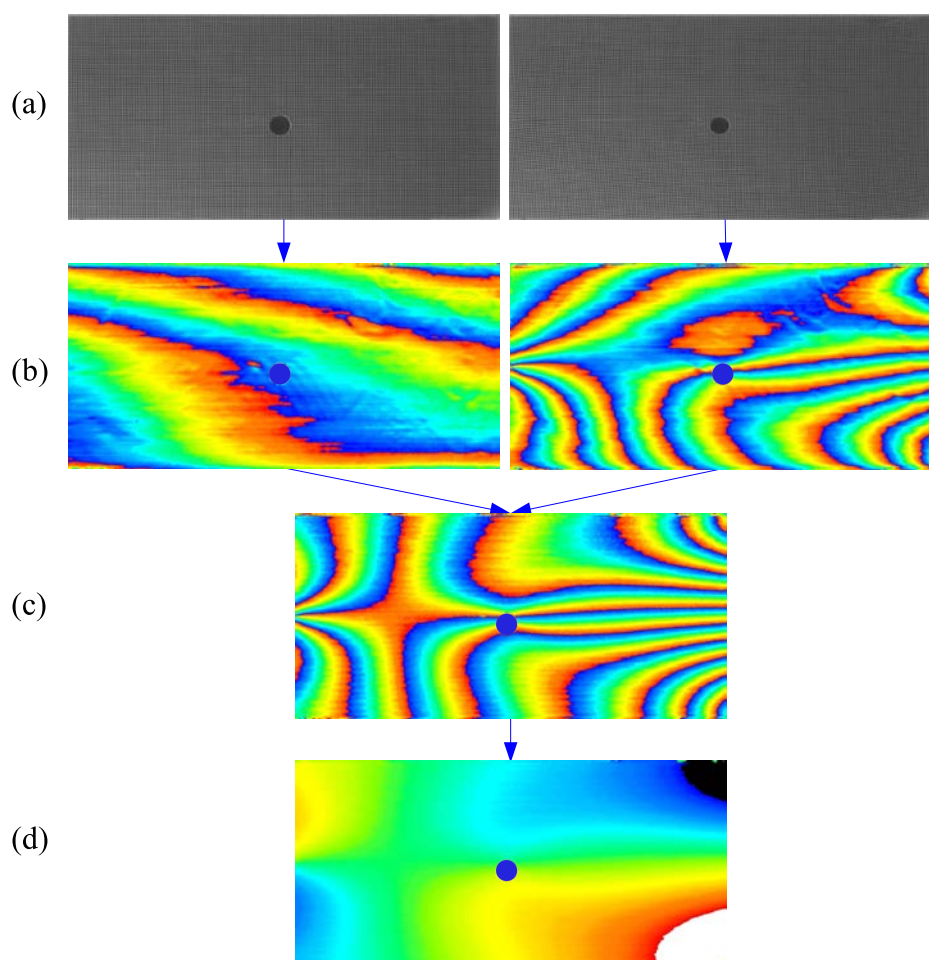


Figure 1.3: Fringe analysis in phase y (a) Intensity pattern (b) Phase field y (c) Corresponding wrapped phase (d) Unwrapped phase.

1.2.3.1 Phase detection

There exist two main methods for phase detection, which are known as ‘global’ and ‘local’ approaches [12]. The global approach which is also known as the Fourier transform technique processes the whole intensity field at the same time. The output phase data depend on the whole set of data in the intensity field. This method is used widely, however the phase accuracy and spatial resolution is poor compared to local approach [14].

The local approach which is called phase-stepping or phase-shifting treats only local intensity fields and processes uniformly the entire measurement field. The meaning of terms ‘phase-stepping’ and ‘phase-shifting’ is slightly different. The shifter stops during image capture in the former and not in the latter. The phase-shifting method decreases the con-

trast at the expense of some amount of time averaging and introduces a low-pass filtering effect which removes the unwanted high frequency phase noise [12]. Further, the local method is divided into temporal and spatial phase-stepping. In temporal phase-stepping, a sequence of images is recorded with a controlled phase shift introduced between successive images. The calculated phase at a given pixel is only dependent on the intensities grabbed at this same pixel. In spatial phase-stepping, a given integer number of adjacent pixels of the CCD camera grabs the periodic intensity signal. The values recorded by adjacent pixels are treated as the phase-stepped intensities and all the data needed to calculate a phase map are acquired from one single frame. It is well suited for optical methods which have a carrier such as the grid method. In this instance, however, it requires a specific tuning which means that an integer number of pixels should correspond to one period of the grid [15]. Additionally, the unwrapping process can generate large phase errors since noise and low modulated pixels can produce breaks in the phase steps [14].

1.2.3.2 Spatial phase stepping

Deflectometry is based on the phase detection from the carrier grid deformation. Phase detection can be performed by spatial phase-stepping [11]. Since the grid is bi-directional (cross-line grating), two components of the slope field can be obtained simultaneously. This requires an initial image processing which separates x and y direction information [11, 15]. By using image averaging, unwanted frequencies can then be filtered out. For the x component information, the image averaging is used for the recorded image intensity over one set of adjacent vertical pixels that captures one period of the grid. Thus, the vertical periodic intensity variation is filtered out. This leaves only the vertical lines on the image, so that the x component phase modulation can be observed. In a similar manner, the y component is obtained. This process is illustrated in Fig. 1.4.

Spatial phase-stepping is the process which captures the phase-stepped intensities by the adjacent pixels of the CCD camera [12]. Specific tuning is required so that an integer number of pixels correspond to one period of grid. The grid line intensity profile usually contains high order harmonics (sharp transitions between black and white). However, depending on the amount of defocus of the CCD camera, sharp transitions will be smoothed and the intensity profile may be observed as sinusoidal [11]. The ideal intensity profile generated from artificial grid deformation is illustrated in Fig. 1.5.

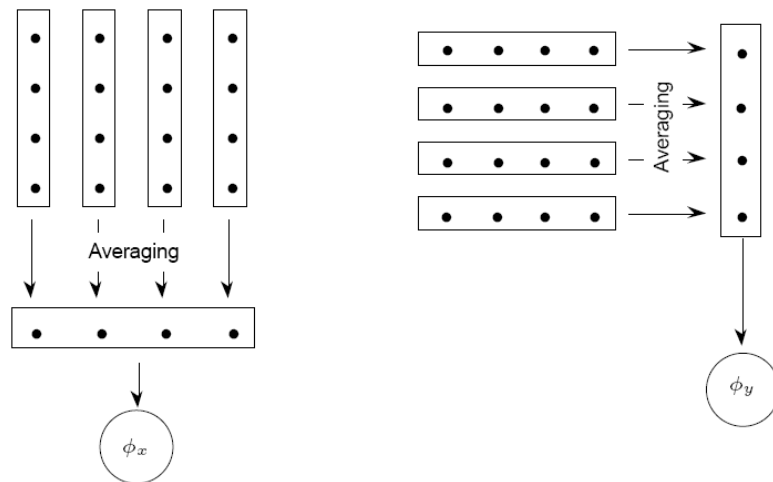


Figure 1.4: Removing of the periodic horizontal or vertical information by period-wise averaging [11].

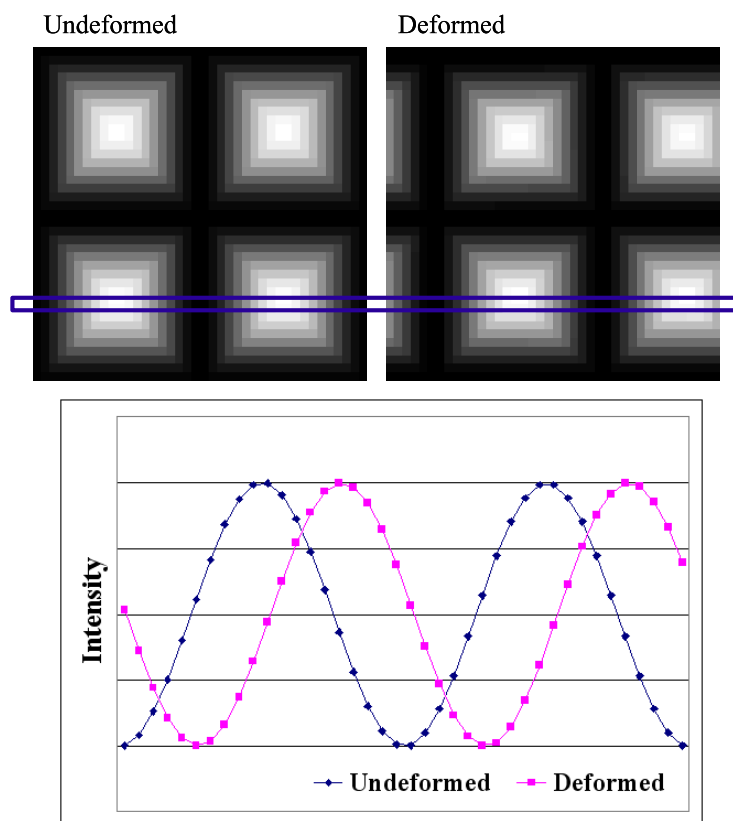


Figure 1.5: Ideal intensity profile.

Now, the sinusoidal reflected light intensity, which is recorded by a CCD camera can be described by the following equation [12, 16, 17]. In the undeformed state:

$$I(x, y) = I_0(x, y)[1 + \gamma(x, y)\cos(\varphi(x, y))] \quad (1.15)$$

where I_0 and γ are the average intensity and the visibility (contrast) that are slowly varying functions and φ is phase of the considered point. After the grid is deformed, the intensity distribution is changed slightly to I' :

$$I'(x, y) = I_0(x, y)[1 + \gamma(x, y)\cos(\varphi(x, y) + \Delta\varphi(x, y))] \quad (1.16)$$

where $\Delta\varphi$ is the phase variation. Hereafter, the phase field can be extracted from the intensity field. The phase $\varphi(x, y)$ indicates the position on the reflected intensity signal and varies with a rate of 2π per pitch p . So, $\varphi(x, y)$ can be written as:

$$\varphi(x, y) = \frac{2\pi d}{p} \quad (1.17)$$

The phase variation $\Delta\varphi(x, y)$ is equivalent to the displacement u of the given point and represented as:

$$\Delta\varphi(x, y) = \frac{2\pi u}{p} \quad (1.18)$$

The geometrical configuration of the setup (see Fig. 1.1) and the phase shifting will extract the phase variation $\Delta\varphi$, which is the variable to be determined for each point of the deformed reflection [16].

For the sake of simplicity, if four pixels of the CCD camera correspond to one period of the grid (*i.e.*, phase stepping increment is $\pi/2$), then the intensity profile of each pixel can be formulated as [17]:

$$\begin{aligned} I_1(x, y) &= I_0[1 + \gamma\cos(\varphi + 0)] = I_0[1 + \gamma\cos(\varphi)] \\ I_2(x, y) &= I_0[1 + \gamma\cos(\varphi + \frac{\pi}{2})] = I_0[1 - \gamma\sin(\varphi)] \\ I_3(x, y) &= I_0[1 + \gamma\cos(\varphi + \pi)] = I_0[1 - \gamma\cos(\varphi)] \\ I_4(x, y) &= I_0[1 + \gamma\cos(\varphi + \frac{3\pi}{2})] = I_0[1 + \gamma\sin(\varphi)] \end{aligned} \quad (1.19)$$

By solving the above equations, the phase $\varphi(x, y)$ at coordinates (x, y) can be calculated as:

$$\varphi = \tan^{-1} \left[\frac{I_4 - I_2}{I_1 - I_3} \right] \quad (1.20)$$

Similarly, the process is repeated for the deformed grid, then:

$$\varphi + \Delta\varphi = \tan^{-1} \left[\frac{I'_4 - I'_2}{I'_1 - I'_3} \right] \quad (1.21)$$

Thus, the phase variation $\Delta\varphi(x, y)$ due to grid deformation can be obtained by subtracting Eq. 1.20 from Eq. 1.21. The local slope variation is calculated from the phase variation by multiplying by the sensitivity. However, it must be noted that this simple example is based on the assumption that the random phase $\varphi(x, y)$ is not changed during deformation [17].

1.2.3.2.1 Windowed-DFT Algorithm The term ‘algorithm’ means a formula which calculates the phase field from the intensity profile [12]. It must be noted that the simple algorithm above cannot be used in practice because the phase stepping method is confronted with two specific problems [15]. The first problem is that the intensity signal is no longer an ideal sinusoidal profile as shown in Eq. 1.15. The experimental intensity profile captured by a CCD is shown in Fig. 1.6. It is worth mentioning that the profile would be closer to the ideal sinusoidal profile if more pixels were used to describe one period of intensity.

Secondly, it is impossible to sample one period with exactly an integer number N of pixels, especially in the case of the deformed grid. Since the grid pitch changes after deformation, the tuning requirement can not be achieved. Thus, there is a mismatch between the nominal and actual phase-steps (it is called miscalibration). So, the phase detection algorithm should be insensitive to miscalibration. These two practical problems can be solved if a proper phase-stepping algorithm is used.

In this study, the windowed discrete Fourier transform (WDFT) algorithm [12] is chosen. The WDFT is a so-called self-calibrating algorithm and calculates the discrete Fourier transform of a set of intensity samples with a triangular windowed kernel. For a given set of $2N$ pixels, the phase is described in Eq. 1.22.

$$\varphi = \tan^{-1} \left[- \frac{\sum_{k=1}^{N-1} k(I_{k-1} - I_{2N-k-1}) \sin(2k\pi/N)}{NI_{N-1} + \sum_{k=1}^{N-1} k(I_{k-1} + I_{2N-k-1}) \cos(2k\pi/N)} \right] \quad (1.22)$$

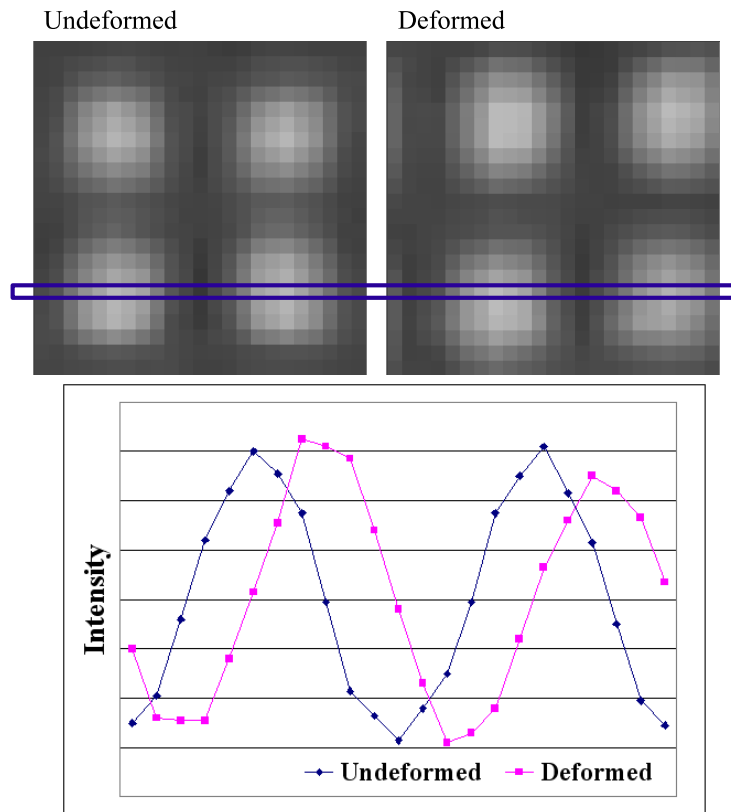


Figure 1.6: Experimental intensity profile.

where I_k is the light intensity of the k th pixel ($k = 0 \dots 2N-1$), N the number of pixels sampling one grid period. This algorithm has proved to be insensitive to a linear phase-step miscalibration and harmonics up to $N - 1$ [12].

1.2.3.3 Unwrapping

In the current study, an undeformed image of the plate is taken and the phase field is computed using the WDFT algorithm. Then, the plate is deformed and another phase field is computed with the same algorithm. By subtracting the initial phase from the final phase, the wrapped phase field directly related to the local slope field is obtained. However, this phase pattern has discontinuities due to the wrapping of the phase modulo 2π . Thus, an unwrapping process which removes the 2π -jumps by adding the adequate multiple of 2π is required [12].

This unwrapping is not always easily performed in the two dimensional sample, since the experimental data always contain high frequency noise. This noise may induce false jumps or missed jumps. If the wrapped phase includes a high level of noise, local spatial

smoothing is required before unwrapping [12]. If the surface includes real discontinuities, *e.g.* cracks, spatial unwrapping can cause a large phase error due to unwrapping across a crack boundary [18]. Finally, when the unwrapped phase field is correctly scaled by multiplication by the sensitivity, the slope field can be obtained.

1.2.3.4 Numerical differentiation to obtain curvatures from the slope fields

1.2.3.4.1 Spatial smoothing The three curvature components are then obtained from the two measured slope components by numerical differentiation. This is a critical step, because differentiation is very sensitive to the spatial noise. Numerical differentiation amplifies the effect of noise. It is therefore necessary to apply some spatial smoothing. Several approaches are possible for this purpose. Here, the slope maps have been fitted by polynomials [19, 20] before the differentiation. This procedure is very efficient when the spatial frequencies of the signal (slope maps, low frequency) and the noise (high frequency) are well separated, which is the case here. Another advantage of the polynomial curve fitting is that a reconstruction of missing data is possible through polynomial interpolation. Due to the geometrical setup configuration (see Fig. 1.1) of deflectometry, the data of the hole (through which the camera observes the specimen) reflection area can not be obtained.

The fitting is performed using a linear least-square method and the method is briefly reviewed below [20]. The experimental slope fields are approximated by a 2D polynomial function, P_x and P_y as defined below:

$$P_x(x, y) = \sum_{i=0}^N \sum_{j=0}^N a_{ij} x^i y^j \quad (1.23)$$

$$P_y(x, y) = \sum_{i=0}^N \sum_{j=0}^N b_{ij} x^i y^j \quad (1.24)$$

where N is the degree of the polynomials. The coefficients a_{ij} and b_{ij} of the polynomial functions are determined by minimization of the quadratic deviation:

$$R_x^2 = \frac{1}{pq} \left[\sum_q \sum_p w(x_p, y_q) [P_x(x_p, y_q) - u_x(x_p, y_q)]^2 - \left(\sum_q \sum_p w(x_p, y_q) [P_x(x_p, y_q) - u_x(x_p, y_q)] \right)^2 \right] \quad (1.25)$$

$$R_y^2 = \frac{1}{pq} \left[\sum_q \sum_p w(x_p, y_q) [P_y(x_p, y_q) - u_y(x_p, y_q)]^2 - \left(\sum_q \sum_p w(x_p, y_q) [P_y(x_p, y_q) - u_y(x_p, y_q)] \right)^2 \right] \quad (1.26)$$

where (x_p, y_q) are the pixel coordinates.

The weighting function $w(x, y)$ is used here to check the validity of each pixel. The approximation process is performed twice. In the first run, the weighting function is set to zero for the missing pixel location and one for the rest. The residual difference between approximated and measured slope fields is computed at each pixel location. In the second run, the weight is set to zero for all the pixels whose value is greater than $2R_x$ and $2R_y$ respectively in the first calculation. Then, a new set of coefficients is determined by the minimization process: in this way, erroneous pixels are removed efficiently.

The determination of the optimal polynomial degree will be performed by comparing the residual difference, the difference between curvature data directly obtained from finite element strain field, and fitted curvature data from FE slope field. If the degree is too low, the slope fields are smoothed too much and will not be described accurately. On the contrary, if the degree is too high, the effect of noise will be exaggerated. The details of this procedure will be addressed in section 3.2.2.

1.2.3.4.2 Numerical differentiation after spatial smoothing From the fitted slope fields, the curvature fields are obtained by numerical differentiation. The curvature fields obtained from experimental slope data are shown in Fig. 1.7 (a). In this case, 9th order polynomial curve fitting is used. The numerical differentiation is performed through the *gradient* command in Matlab.

1.2.3.4.3 Numerical differentiation without spatial smoothing Despite the advantage of polynomial curve fitting, this process inevitably causes loss of spatial resolution. Therefore, the obtained curvature fields are less accurate, and local effects such as stress concentrations due to local damage or concentrated loads may not be observed after polynomial smoothing. In the identification of global bending stiffness, the loss of local spatial resolution does not deviate the identified results much because only average values of curvatures are required. However, if the target is to identify local stiffness of restricted area, this smoothing effect may lead to big deviation in the identified results. Since local damage induces local stress and strain redistribution, the accurate representation of local

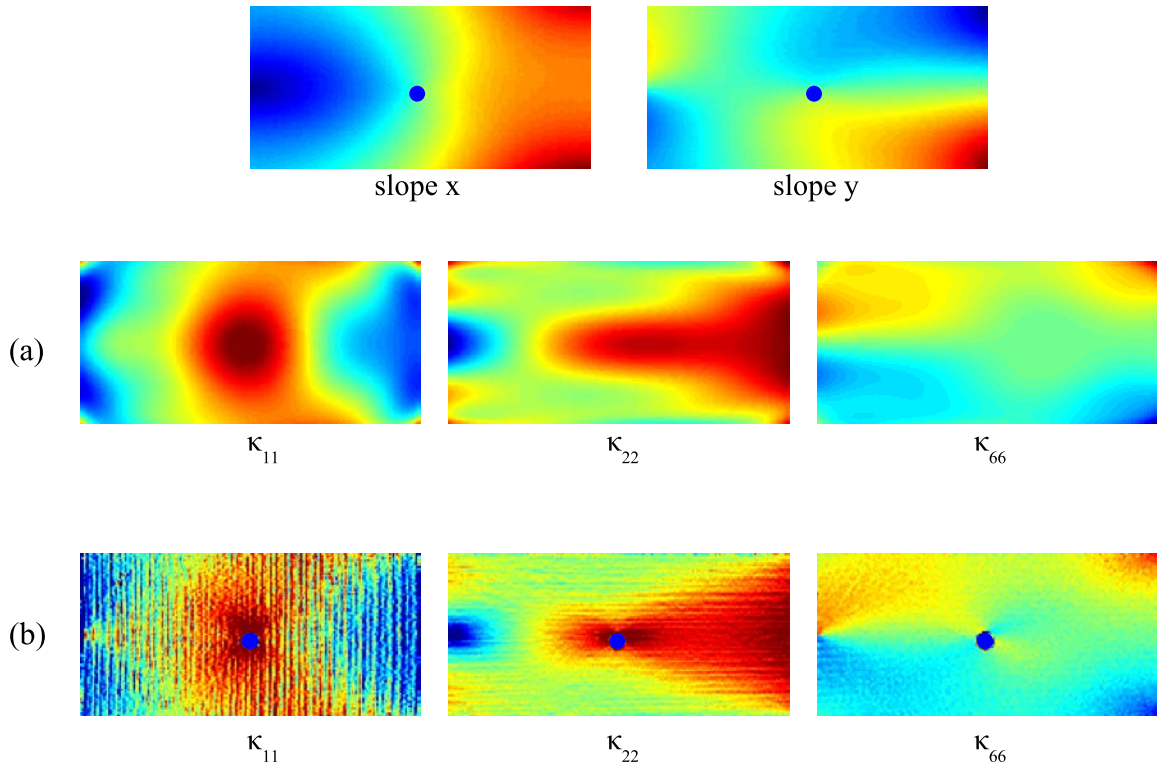


Figure 1.7: Curvatures fields obtained from slope fields (a) with polynomial spatial smoothing (b) without spatial smoothing

information is very important. In addition, the reconstruction of the missing data with polynomial curve fitting may disorder the surrounding local fields. The best solution to avoid the above difficulties is utilizing direct differentiation without smoothing.

However, as discussed above, numerical differentiation is very sensitive to noise. Due to the high frequency noise effects and very small displacement fields, direct point-to-point differentiation of experimental data is extremely difficult to perform in most of the current full-field measurement techniques.

Nonetheless, thanks to the high sensitivity and resolution of the deflectometry technique, the curvature fields can be obtained without spatial smoothing as shown in Fig. 1.7 (b). When Fig. 1.7 (b) is compared with Fig. 1.7 (a), a significant difference can be seen in terms of spatial resolution. For instance, local curvature variations due to the concentrated load applied at the center of the plate can be observed clearly. In this case, some orange peel effects due to noise also can be seen. The influence of the curvature field irregularity on the identification will be discussed in Chapter 3.

It is worth noting that higher order polynomial curve fitting may increase the spatial

resolution, however, important local field information might be changed due to the exaggeration of noise effect.

1.2.3.5 Effects of camera position

1.2.3.5.1 Calibration for camera position One of the reasons for utilizing the spatial smoothing is because of the missing data from the reflected hole image, in a given deflectometry set-up, as mentioned in section 1.2.3.4. In the case of direct differentiation without smoothing, this geometrical set-up cannot be used due to the missing data (see Fig. 1.7 (b)). Thus, a new geometrical set-up configuration is required, which can avoid the hole image. For this purpose, the camera is located beside the grid (Fig. 1.8 (b)) instead of behind the grid (Fig. 1.8 (a)).

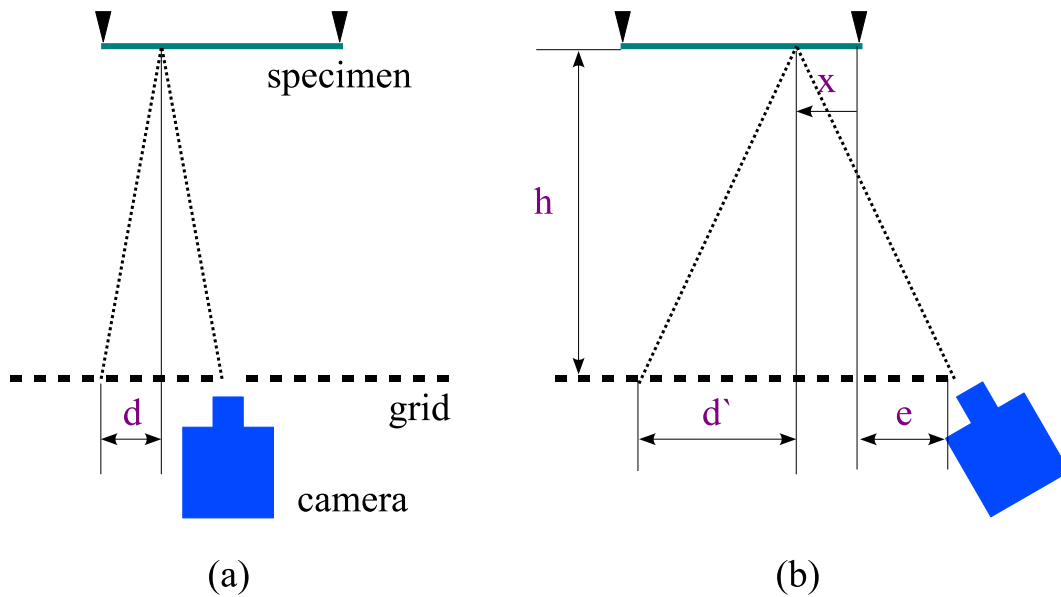


Figure 1.8: Camera position (a) behind the grid (b) beside the grid

However, this configuration requires specific calibration of the camera position, as the observation is not made with normal incidence. The relation between the displacement u and the slope variation $d\alpha$ in the original deflectometry setup is derived in Eq. 1.10. In the set-up represented in Fig. 1.1, the value of $\tan^2(\theta)$ is negligible with respect to 1, but in the new configuration, the value should be included in the calculation of sensitivity as the value of $\tan^2(\theta)$ increases. In the Fig. 1.8 (b), $\tan^2(\theta)$ can be expressed as:

$$\tan^2(\theta) = \left(\frac{d'}{h}\right)^2 = \left(\frac{x+e}{h}\right)^2 \quad (1.27)$$

Considering the two-dimensional observation on the plate specimen, $\tan^2(\theta)$ can be written as:

$$\tan^2(\theta) = \left(\frac{d'_x}{h}\right)^2 + \left(\frac{d'_y}{h}\right)^2 \quad (1.28)$$

So it follows that,

$$d\varphi = 2\pi\frac{u}{p} = 4\pi\frac{h}{p}\left[1 + \left(\frac{d'_x}{h}\right)^2 + \left(\frac{d'_y}{h}\right)^2\right]d\alpha \quad (1.29)$$

This means that a 2D distribution of sensitivity should be considered in this case. Strictly speaking, the sensitivity value is not a constant number even in Fig. 1.1. However, the variation is negligible, so constant sensitivity value can be used without deviation. The identified results, dependent on the camera position and calibration will be discussed in Chapter 3. It should be mentioned here that too large a camera incidence angle is not allowed because the investigated object should not be distorted much.

1.3 Conclusion

In this study, deflectometry was chosen as the full-field measurement technique since curvature data are required, and also the size of the investigation field is well suited to the approach adopted. Full-field heterogeneous slope fields are measured through the deflectometry technique and the three curvature components are then obtained from the two measured slope components by numerical differentiation. Since differentiation is very sensitive to the spatial noise, the slope maps are fitted by polynomials before the differentiation. However, the polynomial curve fitting process inevitably causes loss of spatial resolution. Therefore, the obtained curvature fields are less accurate, and local effects such as stress concentrations due to local damage or concentrated loads cannot be observed after polynomial smoothing. The best solution to avoid the above difficulties is utilizing direct differentiation without smoothing. Thanks to the high sensitivity and resolution of the deflectometry technique, the curvature fields were obtained without spatial smoothing. Nonetheless, in the case of direct differentiation without smoothing, the original geometrical set-up of deflectometry cannot be used due to the missing data (reflected hole image). Thus, a new deflectometry configuration was developed and the required

calibration for new camera position was derived. The identified results, dependent on the camera position and calibration will be presented in Chapter 3.

Chapter 2

The Virtual Fields Method

2.1 The Virtual Fields Method

The objective of the present study is to identify the spatial stiffness distribution in damaged composite plates. To retrieve the stiffness reduction in the local damaged region, a method which can quantify the loss of stiffness is required. The virtual fields method (VFM) first developed by Grédiac [21] is used as an inverse procedure for the identification. The stiffness components can be determined directly from the VFM when the material is homogeneous, however, the VFM must be adapted to the case of a plate with stiffnesses varying with the space variables. This chapter will introduce the principles of the VFM and its application to the present problem.

The virtual fields method (VFM) is based on the principle of virtual work, which describes the global equilibrium of the solid. A relevant use of the equilibrium equation leads to the identification of the constitutive parameters. The identification procedure with the VFM consists of three steps. First, the equilibrium equation (in a weak form) for static loading, and in absence of volume forces, is written as follows:

$$\underbrace{- \int_V \sigma_{ij} \epsilon_{ij}^* dV}_{W_i^* \text{ (Internal Virtual Work)}} + \underbrace{\int_{\partial V} T_i u_i^* dS}_{W_e^* \text{ (External Virtual Work)}} = 0 \quad (2.1)$$

where index repetition indicates summation and:

- V : the volume of the specimen
- dV : the elementary volume element
- dS : the elementary outer surface element
- ∂V : the entire surface area of the specimen
- σ : the stress field
- ϵ^* : the virtual strain field
- T : the surface tractions acting on ∂V
- u^* : the virtual displacement field associated with ϵ^*

The equilibrium equation means that the external virtual work done by the external forces is equal to the internal virtual work (stress field statically admissible). This equation is valid for any kinematically admissible virtual displacement/strain fields. Secondly, the constitutive equation for linear elasticity is written as:

$$\sigma_{ij} = C_{ijkl}\epsilon_{kl} \quad (2.2)$$

Replacing the stress field in Eq. 2.1 with Eq. 2.2,

$$-\int_V C_{ijkl}\epsilon_{kl}\epsilon_{ij}^* dV + \int_{\partial V} T_i u_i^* dS = 0 \quad (2.3)$$

The proper choice of any kinematically admissible virtual field leads to an identification of the constitutive parameters provided that actual strain fields and load distribution are measured through experiment. The selection of as many independent virtual fields as the unknown parameters results in a set of linear equations from which the unknown constitutive parameters are extracted. Thus, the choice of the virtual fields is very critical for the identification. Finally, the kinematic equation (small strains/displacements) is written as:

$$\epsilon_{ij} = \frac{1}{2}(u_{i,j} + u_{j,i}) \quad (2.4)$$

The actual strain fields can be obtained from the measured displacement fields by numerical differentiation.

The VFM shows several outstanding advantages. It is independent from stress distribution and geometry, thus very attractive when dealing with many different shapes of specimen having heterogeneous stress fields, and is also very efficient in processing the experimental data, since it is less sensitive to parasitic effect such as boundary condition effect. The major advantage is the direct identification without any iterative calculation as in finite element model updating. A limitation of the VFM is that the volume integral in Eq. 2.3 needs to be calculated from the measurement of surface strain since strain fields cannot be obtained from inside the specimen. However, this may be overcome with the development of bulk full-field measurement techniques. The first extension of the VFM to three-dimensional full-field displacement data from MRI technique has been presented recently [22].

2.1.1 Application of the VFM to thin plate bending

In the case of plate bending, the VFM utilizes the kinematic assumptions of plate theories. In this section, Kirchhoff and Mindlin plate theories will be reviewed and the application of the classical lamination theory (CLT) to the VFM will be discussed.

2.1.1.1 Kirchhoff thin plate theory and Mindlin plate theory

Plate-like structures are widely used as primary structural components in many engineering applications. Plate theories such as the classical Kirchhoff and shear deformable theories are utilized for the analysis of plate deformation. These plate theories have an advantage of reduced complexity of plate elements over 3D elasticity theory by adopting kinematic assumptions. These assumptions are related to the through-the-thickness displacement and strain fields. Therefore, the plate theories can emphasize the important deformation modes such as bending and transverse shear by filtering out trivial deformation modes [23].

The Kirchhoff plate theory neglects the implications of transverse shear deformation effects. It is a two-dimensional extension of the one-dimensional Euler-Bernoulli beam theory [24]. The simplest shear deformable plate theory is the first-order shear deformable theory (FSDT), also known as the Mindlin plate theory. Mindlin theory includes the kinematic assumption of transverse shear deformation. The one-dimensional counterpart of the Mindlin plate theory is the Timoshenko beam theory. In both of the plate theories, the plane stress assumption is used. Therefore, the transverse normal stress σ_{zz} is zero, and plate behavior can be described by displacements and rotations at and relative to the midplane.

The Kirchhoff plate theory assumes that straight lines perpendicular to the mid-plane remain straight and perpendicular after deformation. On the other hand, in Mindlin theory, these straight lines remain straight but not perpendicular to the mid-plane any more after deformation. These kinematic assumptions are illustrated in Figs. 2.1 and 2.2.

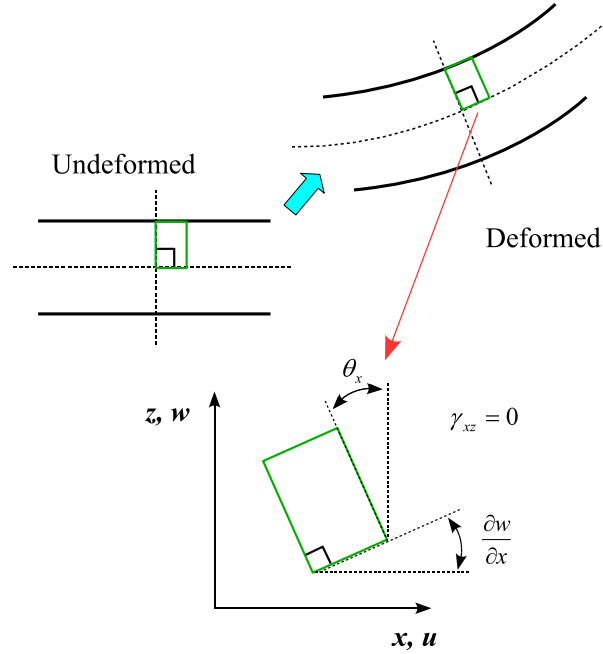


Figure 2.1: Displacement field through-the-thickness in Kirchhoff plate theory.

2.1.1.1.1 Mindlin plate theory In Mindlin theory, the displacement fields are given as [25, 26]:

$$\begin{aligned}
 u(x, y, z) &= u_0(x, y) + z\theta_x = u_0(x, y) + z \left[\gamma_{xz} - \frac{\partial w_0}{\partial x}(x, y) \right] \\
 v(x, y, z) &= v_0(x, y) + z\theta_y = v_0(x, y) + z \left[\gamma_{yz} - \frac{\partial w_0}{\partial y}(x, y) \right] \\
 w(x, y, z) &= w_0(x, y)
 \end{aligned} \tag{2.5}$$

where, u , v and w are the displacement components in x , y and z coordinate directions respectively, and u_0 , v_0 , and w_0 are the midplane displacements which are independent of z . The terms $\frac{\partial w_0}{\partial x}$ and $\frac{\partial w_0}{\partial y}$ mean physical slopes of the mid-plane in the $x - z$ and $y - z$ planes, while θ_x and θ_y are rotations resultant from bending alone in those respective

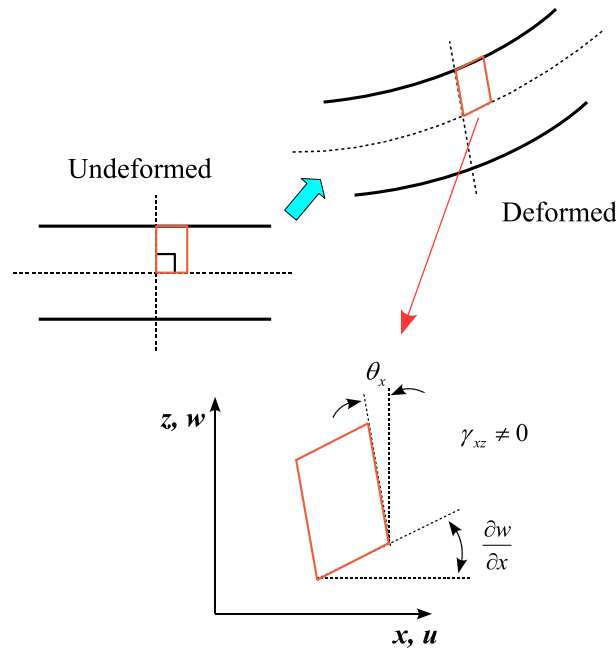


Figure 2.2: Displacement field through-the-thickness in Mindlin plate theory.

planes. Transverse shear strains can be described by the algebraic sum of the slopes and rotations. Translational displacements can be calculated at any location in the through-the-thickness direction relative to the mid-plane by multiplying rotation with the distance from the mid plane as in Eq. 2.5.

The displacement in the z direction is assumed to occur only because of the bending motion, and no variation of w through the thickness occurs. Since the FSDT includes a transverse shear deformation in its kinematic assumptions, transverse shear strains γ_{xz} and γ_{yz} are not zero. However, the transverse shear strains are assumed to be constant through the thickness. This assumption violates the shear stress free surface conditions. So, a shear correction factor is required to satisfy the discrepancies between the actual transverse shear stress and strain distributions and those calculated approximately from the FSDT.

The distributions of actual transverse shear strains γ_{xz} and γ_{yz} are parabolic through the thickness. This satisfies the boundary condition of zero transverse shear on the top and bottom surfaces of the plate. To describe the transverse shear strain distributions more accurately, higher order plate theories which use higher order polynomial functions of z were developed. For instance, the third order shear deformation plate theory (TSDT) can describe quadratic variation of transverse shear strains and satisfy the stress bound-

ary conditions. The shear correction factor is therefore no longer required. However, computational cost increases significantly using the third order theory, with only a slight improvement in accuracy compared with the FSDT solution [27].

2.1.1.1.2 Kirchhoff plate theory In Kirchhoff theory, in distinction to Mindlin theory, the interlaminar shear strains γ_{xz} and γ_{yz} are zero due to its assumption that straight lines perpendicular to the mid-plane remain straight and perpendicular to the deformed mid-plane after deformation. Therefore, the displacement fields are written as:

$$\begin{aligned} u(x, y, z) &= u_0(x, y) + z\theta_x = u_0(x, y) - z\frac{\partial w_0}{\partial x}(x, y) \\ v(x, y, z) &= v_0(x, y) + z\theta_y = v_0(x, y) - z\frac{\partial w_0}{\partial y}(x, y) \\ w(x, y, z) &= w_0(x, y) \end{aligned} \quad (2.6)$$

It is important to note that the deformation results entirely from bending and in-plane stretching in the Kirchhoff theory, since both transverse shear and transverse normal effects are neglected. The following strain field components can be obtained from strain-displacement relationship:

$$\begin{Bmatrix} \epsilon_x \\ \epsilon_y \\ \gamma_{xy} \end{Bmatrix} = \begin{Bmatrix} \frac{\partial u}{\partial x} \\ \frac{\partial v}{\partial y} \\ \frac{\partial u}{\partial y} + \frac{\partial v}{\partial x} \end{Bmatrix} = \begin{Bmatrix} \frac{\partial u_0}{\partial x} \\ \frac{\partial v_0}{\partial y} \\ \frac{\partial u_0}{\partial y} + \frac{\partial v_0}{\partial x} \end{Bmatrix} + z \begin{Bmatrix} -\frac{\partial^2 w}{\partial x^2} \\ -\frac{\partial^2 w}{\partial y^2} \\ -2\frac{\partial^2 w}{\partial x \partial y} \end{Bmatrix} \quad (2.7)$$

Thus, strain fields can be expressed as:

$$\begin{Bmatrix} \epsilon_x \\ \epsilon_y \\ \gamma_{xy} \end{Bmatrix} = \begin{Bmatrix} \epsilon_x^0 \\ \epsilon_y^0 \\ \gamma_{xy}^0 \end{Bmatrix} + z \begin{Bmatrix} \kappa_x \\ \kappa_y \\ \kappa_{xy} \end{Bmatrix} \quad (2.8)$$

where ϵ_x^0 , ϵ_y^0 , γ_{xy}^0 are mid-plane strains and κ_x , κ_y , κ_{xy} are curvatures of the mid-plane of a plate. Stress fields are derived from the strain fields using the constitutive equation:

$$\{\sigma\} = [Q]\{\epsilon\} = [Q](\{\epsilon^0(x, y)\} + z\{\kappa(x, y)\}) \quad (2.9)$$

where $[Q]$ is the stiffness matrix. The force and moment resultants are derived by integrating the stresses over the thickness of the plate:

$$\begin{aligned}\{N\} &= \int_{-\frac{h}{2}}^{\frac{h}{2}} \{\sigma\} dz = \int_{-\frac{h}{2}}^{\frac{h}{2}} [Q] \{\epsilon\} dz = \int_{-\frac{h}{2}}^{\frac{h}{2}} [Q] (\{\epsilon^0(x, y)\} + z \{\kappa(x, y)\}) dz \\ \{M\} &= \int_{-\frac{h}{2}}^{\frac{h}{2}} \{\sigma\} z dz = \int_{-\frac{h}{2}}^{\frac{h}{2}} [Q] \{\epsilon\} z dz = \int_{-\frac{h}{2}}^{\frac{h}{2}} [Q] (\{\epsilon^0(x, y)\} + z \{\kappa(x, y)\}) z dz\end{aligned}\tag{2.10}$$

where M and N are moments and forces per unit width respectively. Since the Kirchhoff theory assumes that the material is homogeneous through the thickness, the stiffness components can be moved outside of the integration sign, thus,

$$\begin{aligned}\{N\} &= [Q] \{\epsilon^0\} \int_{-\frac{h}{2}}^{\frac{h}{2}} dz + [Q] \{\kappa\} \int_{-\frac{h}{2}}^{\frac{h}{2}} z dz = h [Q] \{\epsilon^0\} \\ \{M\} &= [Q] \{\epsilon^0\} \int_{-\frac{h}{2}}^{\frac{h}{2}} z dz + [Q] \{\kappa\} \int_{-\frac{h}{2}}^{\frac{h}{2}} z^2 dz = \frac{h^3}{12} [Q] \{\kappa\}\end{aligned}\tag{2.11}$$

Substituting Eq. 2.11 into Eq. 2.9 gives:

$$\{\sigma\} = \frac{1}{h} \{N\} + \frac{12z}{h^3} \{M\}\tag{2.12}$$

2.1.1.1.3 Classical lamination theory The classical lamination theory (CLT) is an extension of the Kirchhoff thin plate theory to composite laminated plates. In the analysis of composite materials, their particular anisotropic behavior must be taken into account to predict the directional properties. The CLT requires C^1 -continuity (Hermite interpolation) of the transverse deflection and C^0 -continuity (Lagrange interpolation) of the in-plane displacements [28]. In CLT, good predictions can be made for in-plane stresses σ_x , σ_y , and τ_{xy} and strains, however, interlaminar stresses σ_z , τ_{xz} , and τ_{yz} are not obtainable because of the Kirchhoff assumption.

As the CLT is an application of Kirchhoff theory to laminated plates, most of the equations are identical. However, composite laminated plates are no longer isotropic since the rigidity Q of each ply may be different depending on the fibre orientation of the ply. Thus, for the calculation of the force and moment resultants, the stiffness components cannot be moved outside of the integration sign as in Eq. 2.10:

$$\begin{aligned}
\{N\} &= \{\epsilon^0\} \sum_{k=1}^N \int_{h_{k-1}}^{h_k} [\bar{Q}] dz + \{\kappa\} \sum_{k=1}^N \int_{h_{k-1}}^{h_k} [\bar{Q}] z dz \\
\{M\} &= \{\epsilon^0\} \sum_{k=1}^N \int_{h_{k-1}}^{h_k} [\bar{Q}] z dz + \{\kappa\} \sum_{k=1}^N \int_{h_{k-1}}^{h_k} [\bar{Q}] z^2 dz
\end{aligned} \tag{2.13}$$

where $[\bar{Q}]$ is the stiffness matrix in the x, y coordinate system of each ply.

The force and moment resultants can be related to the strains and curvatures in the laminates through the integration of material property for each ply group. These relations can be expressed in terms of matrices that are conventionally labeled A , B , and D by custom.

$$\begin{Bmatrix} N_x \\ N_y \\ N_{xy} \end{Bmatrix} = \begin{bmatrix} A_{11} & A_{12} & A_{16} \\ & A_{22} & A_{26} \\ sym & & A_{66} \end{bmatrix} \begin{Bmatrix} \epsilon_x^0 \\ \epsilon_y^0 \\ \gamma_{xy}^0 \end{Bmatrix} + \begin{bmatrix} B_{11} & B_{12} & B_{16} \\ & B_{22} & B_{26} \\ sym & & B_{66} \end{bmatrix} \begin{Bmatrix} \kappa_x \\ \kappa_y \\ \kappa_{xy} \end{Bmatrix} \tag{2.14}$$

$$\begin{Bmatrix} M_x \\ M_y \\ M_{xy} \end{Bmatrix} = \begin{bmatrix} B_{11} & B_{12} & B_{16} \\ & B_{22} & B_{26} \\ sym & & B_{66} \end{bmatrix} \begin{Bmatrix} \epsilon_x^0 \\ \epsilon_y^0 \\ \gamma_{xy}^0 \end{Bmatrix} + \begin{bmatrix} D_{11} & D_{12} & D_{16} \\ & D_{22} & D_{26} \\ sym & & D_{66} \end{bmatrix} \begin{Bmatrix} \kappa_x \\ \kappa_y \\ \kappa_{xy} \end{Bmatrix}$$

where A is the in-plane stiffness matrix, B the bending-extension coupling stiffness matrix and D the bending stiffness matrix. The in-plane and bending stiffness can be calculated from the A and D matrices, respectively. Unlike homogeneous isotropic materials, however, heterogeneous anisotropic composite plates show very unique behavior characterized by couplings between the extension, bending, and shearing modes. The B matrix is a bending-extension coupling stiffness and vanishes for symmetric laminates. There exist two other types of coupling effect: in-plane extension-shear coupling due to the presence of A_{16} and A_{26} , and bending-twisting coupling dependent on the presence of D_{16} and D_{26} . The A_{16} and A_{26} terms vanish for balanced laminates which have an equal number of laminae of $+\theta$ and $-\theta$ angles regardless of the location. Though the D_{16} and D_{26} terms do not vanish for symmetric and balanced laminates, these coupling terms are negligible when compared with other D terms, if the number of layers are over 16 [29].

It is worth mentioning that the force and moment resultants are derived by integrating (averaging) through the plate thickness. This procedure is referred to as a ‘homogenization’ which leads to new constitutive relations at the structural level [23]. Through the

homogenization procedure in the CLT, the stress resultants can be related to strains at the structural level in terms of the material elastic properties and the geometry of a plate. This means that the heterogeneous composite laminated plate is replaced implicitly by a single homogeneous plate, with the stiffness and inertia properties of the new single homogeneous plate becoming equivalent to those of a heterogeneous laminated plate in the integral sense [28]. Also in the CLT, linear displacement field (kinematic continuity between layers) and plane stress state are assumed owing to the small thickness compared to other dimensions. For the above reasons, the CLT can be applied efficiently to describe the global structural response of composite laminated plates. However, for the same reasons, the CLT may have the limitation of characterizing local response coming from localized damage. This will be discussed further in Chapter 6.

2.1.1.2 The Virtual Fields Method in the case of plate bending

In the case of thin anisotropic plates in pure bending, if body forces are neglected, the principle of virtual work can be derived from the stress and resultants relationship (Eq. 2.12). In pure bending ($N = 0$), Eq. 2.12 becomes:

$$\{\sigma\} = \frac{12z}{h^3}\{M\} \quad (2.15)$$

Now the internal virtual work in Eq. 2.1 can be written as:

$$-\int_V \sigma_{ij} \epsilon_{ij}^* dV = -\frac{12}{h^3} \int_V M_i \epsilon_i^* z dV \quad (i = 1, 2, 6) \quad (2.16)$$

The virtual strain fields ϵ^* can be written in bending case,

$$\{\epsilon^*\} = z\{\kappa^*\} \quad (2.17)$$

Then the internal virtual work is written as:

$$\begin{aligned}
-\frac{12}{h^3} \int_V M_i \epsilon_i^* z dV &= -\frac{12}{h^3} \int_V M_i \kappa_i^* z^2 dV \\
&= -\frac{12}{h^3} \int_S M_i \kappa_i^* dS \int_{-\frac{h}{2}}^{\frac{h}{2}} z^2 dz \\
&= - \int_S M_i \kappa_i^* dS
\end{aligned} \tag{2.18}$$

Thus, finally one has:

$$- \int_S M_i \kappa_i^* dS + \sum_{j=1}^n F_j w_j^* = W_i^* + W_e^* = 0 \tag{2.19}$$

where index repetition indicates summation for $i = 1, 2$ and 6 and:

- W_i^* : internal virtual work
- W_e^* : external virtual work
- S : surface of the plate
- w^* : virtual deflection field
- F : normal forces applied to the plate at n points
- κ^* : virtual curvature fields derived from w^* by $\kappa_1^* = -\frac{\partial^2 w^*}{\partial x^2}$, $\kappa_2^* = -\frac{\partial^2 w^*}{\partial y^2}$, $\kappa_6^* = -2\frac{\partial^2 w^*}{\partial x \partial y}$
- M : generalized bending moments

The principle of the VFM is to substitute the stress information in the above equation (here, the generalized moments) from the constitutive equation. In linear elasticity, this is straightforward. For classical lamination theory in the orthotropy basis and in absence of B coupling (symmetric laminate), one has:

$$\begin{pmatrix} M_1 \\ M_2 \\ M_6 \end{pmatrix} = \begin{bmatrix} D_{11} & D_{12} & 0 \\ D_{12} & D_{22} & 0 \\ 0 & 0 & D_{66} \end{bmatrix} \begin{pmatrix} \kappa_1 \\ \kappa_2 \\ \kappa_6 \end{pmatrix} \tag{2.20}$$

where the D matrix is the bending stiffness matrix of the laminate. Eq. 2.19 then becomes:

$$-\int_S D_{11}\kappa_1\kappa_1^*dS - \int_S D_{22}\kappa_2\kappa_2^*dS - \int_S D_{12}(\kappa_1\kappa_2^* + \kappa_2\kappa_1^*)dS - \int_S D_{66}\kappa_6\kappa_6^*dS + \sum_{j=1}^n F_j w_j^* = 0 \quad (2.21)$$

When the material is homogeneous, the stiffness components can be moved outside of the integration sign and the choice of a particular set of virtual fields will provide a linear system relating the unknown stiffnesses to the external forces (measured by the load cell), geometrical parameters and weighted integrals of the true curvatures that can be computed provided that full-field measurements are available.

Several studies have already been published on this problem [19, 21, 30]. It was even applied in dynamics, initially for stiffness [31, 32] and then also for damping identification [13, 33], with very successful results. It is also worth noting that some authors managed the same identification using finite element model updating on static [34] or dynamic [35] tests.

2.1.1.3 Special virtual fields method

The key issue of the VFM is the choice of appropriate virtual fields among the infinite possibilities. Indeed, the stability of the method is very much affected by this choice. Several papers have been published using virtual fields defined empirically. However, as the number of unknowns increases, this is not easily performed. Recently, the so-called special virtual fields method [36, 37] has been developed. This method has established an automatic procedure for virtual fields selection. Eq. 2.21 can be written as:

$$D_{11}I_{11} + D_{22}I_{22} + D_{12}I_{12} + D_{66}I_{66} = \sum_{j=1}^n F_j \cdot w_j^* \quad (2.22)$$

where,

$$I_{11} = \int_S \kappa_1\kappa_1^*dS, \quad I_{22} = \int_S \kappa_2\kappa_2^*dS, \quad I_{12} = \int_S (\kappa_1\kappa_2^* + \kappa_2\kappa_1^*)dS, \quad I_{66} = \int_S \kappa_6\kappa_6^*dS \quad (2.23)$$

Now, the idea is to find the special virtual fields which can make one of the four I terms equal to unity and three others equal to zero. In the same way, by finding three other special virtual fields, direct identification of all the rigidities can be done independently

as in Eq. 2.24. Thus, the identification problem leads to the determination of four special virtual fields $w^{*\alpha}$, where $\alpha = a, b, c, d$.

$$\begin{bmatrix} I_{11}^a & I_{22}^a & I_{12}^a & I_{66}^a \\ I_{11}^b & I_{22}^b & I_{12}^b & I_{66}^b \\ I_{11}^c & I_{22}^c & I_{12}^c & I_{66}^c \\ I_{11}^d & I_{22}^d & I_{12}^d & I_{66}^d \end{bmatrix} \begin{bmatrix} D_{11} \\ D_{22} \\ D_{12} \\ D_{66} \end{bmatrix} = \begin{bmatrix} 1 & 0 & 0 & 0 \\ 0 & 1 & 0 & 0 \\ 0 & 0 & 1 & 0 \\ 0 & 0 & 0 & 1 \end{bmatrix} \begin{bmatrix} D_{11} \\ D_{22} \\ D_{12} \\ D_{66} \end{bmatrix} = \sum_{j=1}^n \begin{bmatrix} F_j w_j^{*a} \\ F_j w_j^{*b} \\ F_j w_j^{*c} \\ F_j w_j^{*d} \end{bmatrix} \quad (2.24)$$

Finally,

$$\begin{bmatrix} D_{11} \\ D_{22} \\ D_{12} \\ D_{66} \end{bmatrix} = \sum_{j=1}^n \begin{bmatrix} F_j w_j^{*a} \\ F_j w_j^{*b} \\ F_j w_j^{*c} \\ F_j w_j^{*d} \end{bmatrix} \quad (2.25)$$

As can be seen in Eq. 2.25, the unknown rigidity is directly equal to the external virtual work of the applied loads.

2.1.1.4 Construction of the special virtual fields

For the construction of special virtual displacement fields, any set of C^1 functions can be used. Either polynomial [36, 37] or piecewise virtual fields [38, 39] have been used in the literature. In the polynomial virtual fields method, polynomial functions are used to define the special virtual displacement fields as in Eq. 2.26:

$$w^* = \sum_{i=0}^m \sum_{j=0}^n a_{ij} x^i y^j \quad (2.26)$$

where a_{ij} 's are unknown coefficients which define the special virtual displacement fields. The polynomial special virtual displacement fields also can be written if the coefficients of the polynomial are arranged in a column vector $| Y \rangle$ and the monomial of x and y as a line vector $\langle f(x, y) |$ [40]:

$$w^*(x, y) = \langle f(x, y) \parallel Y \rangle \quad (2.27)$$

where,

$$\langle f(x, y) \parallel = (1 \ x \ y \ x^2 \ xy \ y^2 \ \dots \ x^{m-1}y^n \ x^m y^n) \quad (2.28)$$

$$\parallel Y \rangle = \begin{pmatrix} a_{00} \\ a_{10} \\ a_{20} \\ \vdots \\ a_{mn} \end{pmatrix} \quad (2.29)$$

In the piecewise virtual fields method, the special virtual displacement fields are defined as shape functions as used in the finite element method. Either one or many piecewise virtual fields can be constructed over the whole specimen geometry. Such piecewise virtual fields are constructed over virtual elements. Since separate virtual elements can be used in one specimen, piecewise virtual fields can be adapted more flexibly to a complicated geometry. The piecewise special virtual displacement fields can be written as [38]:

$$w^*(x, y) = \langle N(x, y) \parallel u^* \rangle \quad (2.30)$$

where $N(x, y)$ is the vector containing the shape function and u^* the nodal virtual displacements. The principle of virtual work is only valid for C^0 virtual displacement fields over a given specimen. In the case of plate bending, the deflection must be C^1 over the specimen so that the virtual slopes, related to the in-plane displacements, are C^0 [39]. Thus, four degrees of freedom ($w, \theta_x (= \frac{\partial w}{\partial x}), \theta_y (= \frac{\partial w}{\partial y}), \theta_{xy} (= \frac{\partial^2 w}{\partial x \partial y})$) should be used for each node of rectangular virtual elements [39]. Therefore, $N(x, y)$ and u^* can be expressed as:

$$\langle N(x, y) \parallel = (\phi_{11} \ \phi_{12} \ \phi_{13} \ \phi_{14} \ \dots \ \phi_{M4}) \quad (2.31)$$

$$| u^* \rangle = \begin{pmatrix} w_1 \\ \frac{\partial w_1}{\partial x} \\ \frac{\partial w_1}{\partial y} \\ \frac{\partial^2 w_1}{\partial x \partial y} \\ \vdots \\ \frac{\partial^2 w_M}{\partial x \partial y} \end{pmatrix} \quad (2.32)$$

where M is the number of virtual nodes.

The virtual curvature fields are derived from Eq. 2.27 by differentiation with respect to x and y :

$$\begin{aligned} \kappa_x^*(x, y) &= -\frac{\langle \partial^2 f(x, y) |}{\partial x^2} | Y \rangle \\ \kappa_y^*(x, y) &= -\frac{\langle \partial^2 f(x, y) |}{\partial y^2} | Y \rangle \\ \kappa_s^*(x, y) &= -2\frac{\langle \partial^2 f(x, y) |}{\partial x \partial y} | Y \rangle \end{aligned} \quad (2.33)$$

Now the identification problem is formulated as finding the unknown vector $| Y \rangle$, the coefficients for polynomial virtual fields, or nodal degrees of freedom for piecewise virtual fields.

2.1.1.5 Optimization of special virtual fields

But still the question is to find optimized special virtual fields among the infinite number of special virtual fields. This problem has been solved efficiently by the optimization of these special fields with respect to noise sensitivity [40]. This method provides unique optimized virtual field for the identification of each stiffness. In reality, the identified stiffnesses are greatly influenced by the noise of a given experiment. In Ref. [40], the noise was assumed to be standard Gaussian white noise. It was shown that the standard deviation of the identified rigidities is proportional to the standard deviation of the noise γ .

$$Std(D_{ij}) = (\eta^\alpha)\gamma \quad (2.34)$$

where η^α is the sensitivity of the VFM to a random noise with $\alpha = a, b, c, d$ respectively for $D_{11}, D_{22}, D_{12}, D_{66}$. Now, the optimization procedure of the special virtual fields is to find the special fields which can minimize η^α . The sensitivity η^α was derived from noise minimization theory in [40]:

$$\begin{aligned} (\eta^\alpha)^2 = & [D_{11}^2 + D_{12}^2] \int_S (\kappa_1^{*\alpha})^2 dS + [D_{22}^2 + D_{12}^2] \int_S (\kappa_2^{*\alpha})^2 dS \\ & + [D_{66}^2] \int_S (\kappa_6^{*\alpha})^2 dS + [D_{12}(D_{11} + D_{22})] \int_S (\kappa_1^{*\alpha} \kappa_2^{*\alpha}) dS \end{aligned} \quad (2.35)$$

The above equation can be written as a shorter expression including the unknown vector $|Y\rangle$ [40]:

$$(\eta^\alpha)^2 = \frac{1}{2} \langle Y^{*\alpha} | H | Y^{*\alpha} \rangle \quad (2.36)$$

where H is a semi-definite positive matrix derived from the unknown rigidities. The sensitivity η^α indicates that the lower the value of η^α , the more accurate the identification result. However, the η^α value should be normalized by the identified rigidity D_{ij} , since a lower value of η^b compared to η^a does not guarantee that D_{22} is more accurate than D_{11} if D_{11} is much greater than D_{22} . Therefore, the criteria which should be compared are $\frac{\eta^a}{D_{11}}, \frac{\eta^b}{D_{22}}, \frac{\eta^c}{D_{12}}$ and $\frac{\eta^d}{D_{66}}$.

2.2 The Adapted Virtual Fields Method

So far, identification procedure with the VFM for a specimen whose stiffnesses do not change inside the solid has been reviewed. However, in the case of a plate with stiffnesses varying within the material, the VFM should be adapted. When the plate has stiffnesses that vary with the in-plane space variables x and y , the D stiffness components cannot be moved outside the integrals in Eq. 2.21. It is then necessary to find some ‘parameterization’ to solve the problem. This is explored in this study, and is the first development of the VFM for this case, providing the originality of the current study, although its principle has already been announced previously [36].

In this section, only the identification procedure will be described and its validation on simulated and experimental measurements will be given in Chapters 5 and 6 respectively.

2.2.1 Continuous parameterization

In the present study, since the damage is already present in the plate when the test is performed, a specific parameterization for the stiffness reduction has to be devised. Two main routes can be followed for the parameterization of the stiffness variation with the space variables.

The first one is to use a continuous approach. The use of polynomials is considered in this approach, which will have the performance of high sensitivity to the stiffness reduction but poor spatial resolution owing to the nature of polynomials.

2.2.1.1 Isotropic damage

As a first step to demonstrate the feasibility of the method, the number of unknowns are kept relatively low by using the following parameterization:

$$\tilde{D} = D^0 \{1 - p(x/L, y/W)\} \quad (2.37)$$

where \tilde{D} is the bending stiffness tensor of the damaged area of the plate, D^0 is that of the virgin material and p is a polynomial function of the normalized in-plane coordinates x/L and y/W , where L is the length and W the width of the panel. This polynomial can be interpreted as a stiffness reduction coefficient. Its values should be positive where the damage is located, so that $1 - p$ is less than 1. It is worth noting however that the procedure does not force p to be positive. The virtual fields method can be adapted to identify the coefficients of the polynomial, provided that the undamaged stiffnesses are known. Indeed, the polynomial can be written as:

$$p(x/L, y/W) = \sum_{i=1}^n \sum_{j=1}^n a_{ij} \left(\frac{x}{L}\right)^i \left(\frac{y}{W}\right)^j \quad (2.38)$$

By inputting this formulation into Eq. 2.21 and regrouping the terms of each polynomial coefficient, a new linear equation is obtained:

$$\begin{aligned}
\sum_{i=0}^n \sum_{j=0}^n a_{ij} \left\{ \int_S D_{11}^0 \left(\frac{x}{L}\right)^i \left(\frac{y}{W}\right)^j \kappa_1 \kappa_1^* dS + \int_S D_{12}^0 \left(\frac{x}{L}\right)^i \left(\frac{y}{W}\right)^j (\kappa_1 \kappa_2^* + \kappa_2 \kappa_1^*) dS \right. \\
\left. + \int_S D_{22}^0 \left(\frac{x}{L}\right)^i \left(\frac{y}{W}\right)^j \kappa_2 \kappa_2^* dS + \int_S D_{66}^0 \left(\frac{x}{L}\right)^i \left(\frac{y}{W}\right)^j \kappa_6 \kappa_6^* dS \right\} = \sum_{j=1}^n F_j w_j^*
\end{aligned} \tag{2.39}$$

Supposing that the D^0 stiffnesses are known, the above system where the a_{ij} coefficients are unknown is linear and the classical VFM approach can be used. Here, the choice of the degree of the polynomial is critical, and this will be discussed in detail in Chapter 5.

It must be noted that the damage here is supposed isotropic, *i.e.*, all the stiffness components are reduced by the same quantity. Again, this enables the number of parameters to remain low. If the same reduction polynomial is applied to each stiffness component, then the number of unknowns will be multiplied fourfold. Since in practice, there is little chance that the damage will be isotropic, the justification here is that this first approach will be good enough to roughly locate the damage. Then, the discrete approach which will be discussed in section 2.2.2.2 can be used with no assumption on the damage. It should be noted however that real impact damage might result in a rather continuous stiffness reduction distribution and that in this case, the continuous approach might be more appropriate than the discrete one.

At this stage, it is worth considering how the VFM recognizes the stiffness reduction, more exactly stiffness variation. When there is a localized damage in a composite laminated plate, the damage induces a reduction of local stiffness. The reduced local stiffness will redistribute the stress fields, and thereby the strain fields around the damaged area. Since the VFM utilizes the global equilibrium of a given specimen having specific force and boundary conditions, it can examine the stress and strain fields all over the specimen. Therefore, it can recognize any abnormal state of strain due to the damage using the given geometry, loading, and boundary conditions. However, the identification process in the VFM is performed implicitly. It was observed that the three in-plane strain components do not change by the same quantity even with isotropic damage. Therefore, it is not straightforward to understand the detection mechanism of the VFM. The attempts to identify the local stiffness loss merely by comparing the strain fields of undamaged and damaged plates without using the VFM will not be successful.

2.2.1.2 Anisotropic damage

In the case of anisotropic damage, the polynomial parameterization can be adapted to the description of each stiffness variation. But the identification of four stiffness variations

simultaneously induces too many unknown parameters, leading to instability of the system. Consequently, the assumption made here is that only one stiffness changes whereas the other terms remain unchanged. In this case, the VFM equation is written as:

$$\begin{aligned} \sum_{i=0}^n \sum_{j=0}^n a_{ij} \left\{ \int_S D_{11}^0 \left(\frac{x}{L}\right)^i \left(\frac{y}{W}\right)^j \kappa_1 \kappa_1^* dS \right\} \\ = \sum_{j=1}^n F_j w_j^* - \int_S D_{12}^0 (\kappa_1 \kappa_2^* + \kappa_2 \kappa_1^*) dS - \int_S D_{22}^0 \kappa_2 \kappa_2^* dS - \int_S D_{66}^0 \kappa_6 \kappa_6^* dS \end{aligned} \quad (2.40)$$

From the above equation, the variation of D_{11} can be obtained. From the point of view of the virtual work, the three integral terms on the right hand side of Eq. 2.40 are treated as external virtual work. In the same fashion, the variation of the other stiffness components can be traced.

2.2.2 Discrete parameterization

The second possibility for parameterization is to use a discrete one. In this case, the stiffness components are assumed to be piecewise-constant over a virtual mesh. A scalar damage parameter driving the stiffness reduction over each element of the mesh needs to be identified. The main advantage of this approach is its good spatial resolution to pick up localized damage. However, as the number of virtual material elements increases, the number of unknowns also increases. The great number of unknowns in this case gives a degraded resolution on the damage indicator as a result of measurement noise. When the area of interest is divided into $N_k \times N_l$ virtual meshes, the discrete parameterization can be described as:

$$\begin{aligned} \sum_{k=1}^{N_k} \sum_{l=1}^{N_l} a_{kl} \left\{ \int_{S_{kl}} D_{11}^0 H^{kl} \kappa_1 \kappa_1^* dS + \int_{S_{kl}} D_{22}^0 H^{kl} \kappa_2 \kappa_2^* dS \right. \\ \left. + \int_{S_{kl}} D_{12}^0 H^{kl} (\kappa_1 \kappa_2^* + \kappa_2 \kappa_1^*) dS + \int_{S_{kl}} D_{66}^0 H^{kl} \kappa_6 \kappa_6^* dS \right\} = \sum_{j=1}^n F_j w_j^* \end{aligned} \quad (2.41)$$

where H^{kl} is a Heaviside function which is defined as:

$$\begin{aligned} H^{kl} &= 1, & \text{if } (x, y) \in S_{kl} \\ H^{kl} &= 0, & \text{otherwise} \end{aligned} \quad (2.42)$$

The damage parameter a_{kl} in each element is identified in Eq. 2.41 provided that the undamaged stiffnesses are known. However, this method is very sensitive to measurement noise owing to the great number of unknowns. This will be shown in Chapter 5.

The alternative strategy of the above discrete parameterization is that the damage location and extent are determined by using the polynomial parameterization in a first stage since the location of damage is unknown *a priori* in practice. In a second step, a discrete approach (independent identification of each stiffness component) could be applied in the areas detected by the polynomial, which would greatly reduce the number of parameters, therefore lessening one of the major drawbacks of the discrete parameterization. In this way, the bending stiffnesses of the damaged region can be identified directly.

2.2.2.1 Isotropic damage

In the case of isotropic damage, the VFM equation for a description with only two areas (one undamaged and one damaged) can be expressed as:

$$\begin{aligned} p \left\{ D_{11}^0 \int_{S_d} \kappa_1 \kappa_1^* dS + D_{22}^0 \int_{S_d} \kappa_2 \kappa_2^* dS + D_{12}^0 \int_{S_d} (\kappa_1 \kappa_2^* + \kappa_2 \kappa_1^*) dS + D_{66}^0 \int_{S_d} \kappa_6 \kappa_6^* dS \right\} = \\ \sum_{j=1}^n F_j w_j^* - \left\{ D_{11}^0 \int_{S_u} \kappa_1 \kappa_1^* dS + D_{22}^0 \int_{S_u} \kappa_2 \kappa_2^* dS + D_{12}^0 \int_{S_u} (\kappa_1 \kappa_2^* + \kappa_2 \kappa_1^*) dS + D_{66}^0 \int_{S_u} \kappa_6 \kappa_6^* dS \right\} \end{aligned} \quad (2.43)$$

where S_u is the undamaged area of the damaged plate and S_d the damaged area. In this case, only one element for the whole damaged area is used, resulting in one unknown p provided that the undamaged stiffnesses are known. Therefore, the value p will be the magnitude of stiffness loss due to the given damage. This method can be extended to identify the stiffness reduction of several separate pieces in the damaged area. For instance, the stiffness reduction of four separate pieces for the whole damaged area can be identified simultaneously. In this case, the equation writes the same but with four separate damaged surfaces, with four unknowns (p_1 to p_4). However, increasing the number of elements will induce instability in the identified results.

2.2.2.2 Anisotropic damage

The greater challenge of the VFM in the discrete approach is to identify eight rigidities (four for the undamaged zone and four for the damaged zone) simultaneously for the identification of anisotropic damage. In this case, the VFM equation can be written as [41]:

$$\begin{aligned}
& D_{11}^u \int_{S_u} \kappa_1 \kappa_1^* dS + D_{22}^u \int_{S_u} \kappa_2 \kappa_2^* dS + D_{12}^u \int_{S_u} (\kappa_1 \kappa_2^* + \kappa_2 \kappa_1^*) dS + D_{66}^u \int_{S_u} \kappa_6 \kappa_6^* dS \\
& + D_{11}^d \int_{S_d} \kappa_1 \kappa_1^* dS + D_{22}^d \int_{S_d} \kappa_2 \kappa_2^* dS + D_{12}^d \int_{S_d} (\kappa_1 \kappa_2^* + \kappa_2 \kappa_1^*) dS + D_{66}^d \int_{S_d} \kappa_6 \kappa_6^* dS = \sum_{j=1}^n F_j w_j^*
\end{aligned} \tag{2.44}$$

where D^u is the bending stiffness tensor of the undamaged area, and D^d that of the damaged area. As was developed in section 2.1.1.5, the sensitivity η^α is used as an objective function for the optimization of special virtual fields. However, in this approach, this objective function must be calculated separately in the two zones because these zones have different stiffness values.

Three important issues will be discussed in the following Chapters 5 and 6. The first one is that the identification of all the four stiffnesses in the damaged area simultaneously may not be feasible if the local area of interest does not have enough spatial information. The second is that the accuracy of identified rigidity in an undamaged region strongly influences that of identified damaged rigidity since both rigidities are correlated to each other in the same equation (as in Eq. 2.44). Therefore, inaccurate identification of D^u may significantly deteriorate the accuracy of identified D^d . Finally, the assumption used in this case is that the location of the damaged zone is known. However, in practice, the selection of the damaged area from the polynomial parameterization will influence the identification results, therefore, a criterion is required for the selection of the area.

2.3 Conclusion

The virtual fields method (VFM) was chosen as an inverse procedure to process curvatures for the identification of the local loss of stiffness. In the case of a plate with stiffnesses varying within the material, the VFM should be adapted. Two parameterization methods for the stiffness reduction were devised. The first one is to use a continuous approach.

The use of polynomials is considered in this approach, which has the performance of high sensitivity to the stiffness reduction but poor spatial resolution owing to the nature of polynomials. The second is to use a discrete one. The main advantage of this approach is its good spatial resolution to pick up localized damage. However, the great number of unknowns in this case gives a degraded resolution on the damage indicator as a result of measurement noise. The alternative strategy of the above discrete parameterization is that the damage location and extent are determined by using the polynomial parameterization in a first stage and in a second step, a discrete approach (independent identification of each stiffness component) is applied in the areas detected by the polynomial, which greatly reduces the number of parameters. The proposed methodology in this chapter will be validated on simulated and experimental measurements in Chapters 5 and 6 respectively.

Chapter 3

Identification of undamaged plate bending stiffnesses

3.1 Introduction

Composite materials offer many advantages over conventional metallic counterparts such as high specific stiffness, strength and excellent fatigue and corrosion resistance. Laminated composite plates fabricated by stacking unidirectional plies exhibit directional properties which can be adopted very efficiently under various structural loading conditions. The increasing applications of composite materials make it necessary to determine accurately their elastic properties. Laminated composite plates are the primary structural components, having many engineering applications. Therefore, the determination of the governing parameters which satisfy the constitutive equations of the composite plates is considered to be very important.

To identify the elastic properties of given specimens, mechanical tests such as static tensile tests have been performed utilizing strain gages or extensometers. These tests are based on homogeneous stress/strain fields in the specimens and only a few parameters can be obtained for each test from the relationship between the applied load and the measured strains. However, in the case of anisotropic materials such as composites, the number of parameters increases, so several tests need to be performed. This makes the identification procedure time consuming. Moreover, during the mechanical tests, such homogeneous fields are not easily obtained in composite materials due to their high anisotropy and heterogeneity [1].

These difficulties may be avoided by using full-field measurement techniques which can extract full-field heterogeneous strain fields, provided that proper analytical tools are available. In this case, all the constitutive parameters can be determined in only one static or dynamic test. Another advantage of full-field measurement is that more complicated specimen geometry, loading and boundary conditions can be applied. This allows one to carry out more representative tests (closer to the actual states) [1]. However, generally, direct identification is not feasible in this approach, due to the fact that direct relationship between the parameters and the measured heterogeneous strain fields does not exist. Therefore, a new method which can extract constitutive parameters from heterogeneous strain fields is required. Such a problem is termed an inverse problem [1, 36]. While the direct solution calculates displacement, strain and stress fields from given constitutive parameters, geometry, loading and boundary conditions, the inverse problem is aimed at identifying the constitutive parameters from other given conditions [1, 36].

The most popular strategy to solve the inverse problem is to perform finite element (FE) model updating. Numerical methods are utilized to solve the direct problem. Guessed elastic parameters are input into the FE program and the result is compared with the measured data, displacement fields in static tests or natural frequencies in dynamic tests [15]. A cost function is used to minimize the difference between the simulated and measured data. The FE model updating method requires an intensive iteration procedure, which is computationally expensive. The identified parameters can be obtained by terminating the iteration if the cost function reaches the convergence threshold. The initial guessed values should be chosen carefully to guarantee the convergence [15]. In addition, unexpected bias may occur if the experimental boundary conditions are not accurately simulated in the FE model.

An alternative strategy to FE model updating is the virtual fields method (VFM) [21]. The VFM can identify the constitutive parameters directly without any iterative calculation. From an experimental point of view, the VFM is very adaptable since it is less sensitive to experimental parasitic effects such as boundary conditions. The theoretical aspects of the VFM have been described in Chapter 2. In this chapter, the identification procedure of the bending stiffnesses in composite laminated plate will be validated on simulated and experimental measurements.

3.1.1 Bending stiffness identification using the VFM

In this study, the VFM is used as an inverse procedure for the identification of the bending stiffness of thin composite plates. Heterogeneous curvature fields obtained with the

deflectometry technique are used as input data. In the orthotropy basis, four bending stiffnesses will be determined from a single bending test. This is possible since the whole set of unknown parameters is involved in the heterogeneous strain fields on the top surface of the bent plate.

Bending tests with full-field measurements offer a low-cost and efficient strategy for the characterization of constitutive parameters. Owing to their simple implementation, bending tests are widely used, as boundary and loading conditions are generally well controlled in bending tests whereas some parasitic effects may occur in tensile tests due to the clamped boundary conditions [11]. Bending tests are also well suited to full-field measurement techniques to obtain heterogeneous strain fields. In the application of the full-field measurement, the strain gradients are more difficult to detect accurately from plate in-plane loading than from bending [15]. Consequently, identifying in-plane rigidities by inverse solution is more difficult than determining bending ones.

3.2 Results and discussion

3.2.1 Validation on FE simulated data without noise

3.2.1.1 FE modeling

In order to validate the proposed approach, simulated measurements were produced using the *ANSYS* 8.0 package. A static linear elastic analysis was carried out with a ‘shell99’ four-noded element which has 6 degrees of freedom at each node: translations in the x , y , and z directions and rotations about the same directions.

A 16-ply unidirectional (UD) carbon-epoxy plate was considered for the identification. The size of the plate is $190 \times 140 \text{ mm}^2$, the ply thickness is 0.16 mm, with a total laminate thickness of 2.56 mm. The material properties used as inputs in the finite element calculations are: $E_{11} = 129 \text{ GPa}$, $E_{22} = 9.5 \text{ GPa}$, $G_{12} = 4.7 \text{ GPa}$, $\nu_{12} = 0.34$. The stiffness values used in the FE model are the reference values taken from Ref. [42]. In this study, the plate is tested in bending according to the load configuration as in Fig. 3.1. The applied force is 5 N.

This test configuration yields a heterogeneous strain field at the top surface of the plate, therefore, the four rigidities can be retrieved from this single bending test.

The size of the FE mesh was selected after a convergence study on the plate. Several mesh sizes were tested with 4th order optimized polynomial virtual fields. The choice of the number of degrees of freedom (DOFs) of the virtual fields will be discussed in the

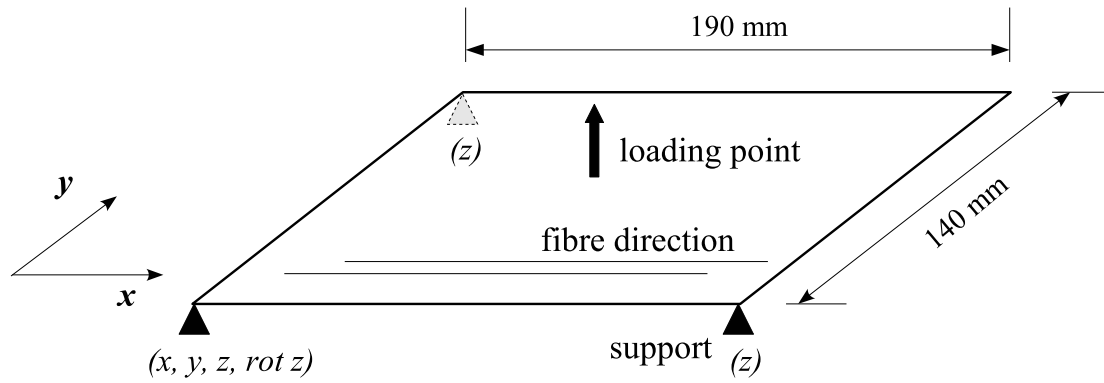


Figure 3.1: Geometry and test configuration of the plate.

next section. The mesh was refined and the stiffnesses were retrieved from the curvature data using the VFM. A mesh with 76×56 elements was finally chosen, corresponding to values of the stiffnesses less than 1% from the reference.

3.2.1.2 Validation from FE curvature data

The initial step was to use curvature data from the FE analysis without considering noise. Before proceeding further, it is worth reviewing briefly the bending stresses and curvatures in a thin bent plate. In plate bending, the in-plane stress components can be divided into two normal stresses σ_{xx} and σ_{yy} and one shear stress σ_{xy} . The distribution of these stress components is illustrated in Fig. 3.2.

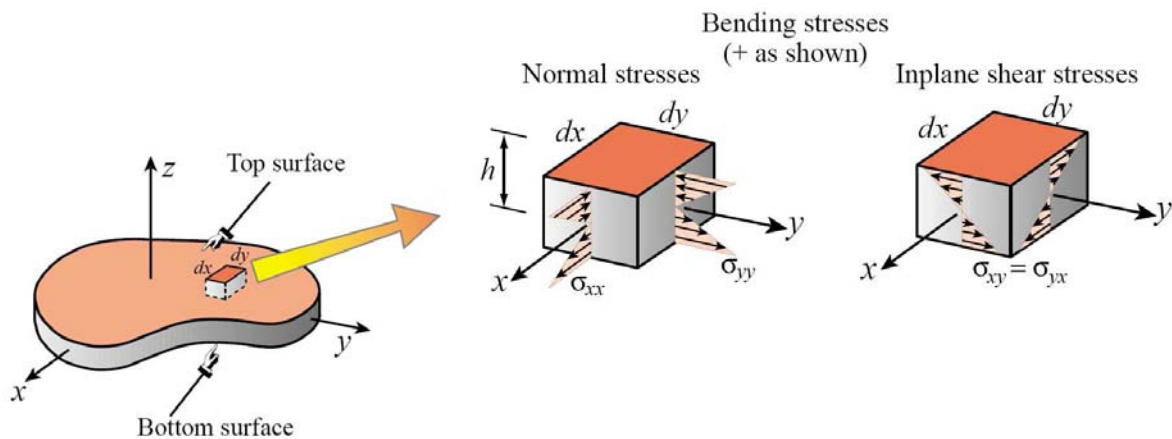


Figure 3.2: Bending stresses in a thin plate [43].

As reviewed in section 2.1.1.1.2, when bending tests are performed on thin plates, the strains are related to the curvatures of the specimen within the Kirchhoff theory of thin plates. Therefore, curvature fields can be derived from FE strain fields by using the relationship:

$$\{\kappa\} = \frac{2}{h}\{\epsilon^t\} \quad (3.1)$$

where $\{\epsilon^t\}$ is the strain fields on the top surface, and h the thickness of the plate. Three curvature components κ_{11} , κ_{22} and κ_{66} can be obtained from three in-plane strain fields. The κ_{11} , κ_{22} are direct (or normal) curvatures along x and y directions respectively and designate the rate of change in slope along the direction [44]. The κ_{66} is twist (or shear) curvature and represents the rate of change in the slope perpendicular to the direction. These curvatures were input into the virtual fields method programme. Next, the number of DOFs for the polynomial virtual fields was investigated. In order to choose the degree of the polynomial virtual fields, identification results with 3rd to 7th degree polynomials were examined.

	D_{11} (Nm ²)	D_{22} (Nm ²)	D_{12} (Nm ²)	D_{66} (Nm ²)
Reference	181.9	13.4	4.55	6.57
Identified (3 rd)	-104000	-1390	12100	6.57
R.D. (%)	57400	10400	-266000	-0.01
Identified (4 th)	182.1	13.4	4.54	6.57
R.D. (%)	-0.11	0.02	0.28	-0.01
Identified (5 th)	182.1	13.4	4.54	6.57
R.D. (%)	-0.11	0.02	0.28	-0.01
Identified (6 th)	182.2	13.4	4.52	6.57
R.D. (%)	-0.14	0.01	0.58	-0.01
Identified (7 th)	182.2	13.4	4.52	6.57
R.D. (%)	-0.14	0.02	0.58	-0.01

Table 3.1: Identification results depending on the polynomial degrees (R.D.: Relative Difference).

As can be seen in Tab. 3.1, the identification results with all degrees except degree $n = 3$ are satisfactory. Therefore, in terms of computational efficiency, 4th order polynomial virtual fields was chosen for the global stiffness identification, giving a total number of DOFs of 15. Also, it was observed that the lower degrees showed better stability when the identification was performed with noisy data.

As discussed in Chapter 2, either piecewise or polynomial virtual fields can be used for the identification. In Tab. 3.2, the identification results are compared between the two virtual fields types. For the fair comparison, almost same number of DOFs was used for piecewise virtual fields, which is 16 (one virtual element). As can be seen in Tab. 3.2, there is not much difference between the two. In both cases, the difference between the identified value and the reference value is less than 1%. However, from the programming point of view, the polynomial virtual fields method is more simple, therefore, polynomial method has been selected for the present study.

3.2.2 Validation on FE simulated data with noise

The next step is to assess the effect of measurement noise in the identification. To realistically evaluate this effect, the noise levels derived from experimental evaluation (see section 1.2.2) are used and applied to the FE slope maps. Then, the differentiation process that will be used experimentally is applied. Here, the spatial smoothing process using a polynomial curve fitting discussed in section 1.2.3.4 is used. The curvatures are then obtained by analytical differentiation of these polynomials.

	D_{11} (Nm ²)	D_{22} (Nm ²)	D_{12} (Nm ²)	D_{66} (Nm ²)
Reference	181.9	13.4	4.55	6.57
Identified (Polynomial)	182.1	13.4	4.54	6.57
R.D. (%)	-0.11	0.02	0.28	-0.01
Identified (Piecewise)	182.5	13.4	4.49	6.57
R.D. (%)	-0.31	-0.03	1.26	-0.01

Table 3.2: Comparison between polynomial and piecewise methods.

There can be two ways to choose the degree of the polynomial to fit the slope field. The first one is to compare the residuals obtained from the difference between the approximated curvature fields and the curvature fields directly derived from FE strain fields. The second

is to evaluate directly the identification results depending on the polynomial degree. In this section, the first approach will be introduced. The residuals were compared for 3rd to 21th degree polynomials. Four different randomized noise sets were used for the residual test. The formula used for the quadratic difference is as follows:

$$\text{Quadratic difference} = \sqrt{res_x^2 + res_y^2 + res_s^2} \quad (3.2)$$

where

$$res_x = \sum_{pixels} abs(\kappa_{11} - \bar{\kappa}_{11}), \quad res_y = \sum_{pixels} abs(\kappa_{22} - \bar{\kappa}_{22}), \quad res_s = \sum_{pixels} abs(\kappa_{66} - \bar{\kappa}_{66}). \quad (3.3)$$

κ_{11} , κ_{22} and κ_{66} are the curvature fields directly derived from the FE strain fields and $\bar{\kappa}_{11}$, $\bar{\kappa}_{22}$ and $\bar{\kappa}_{66}$ are the approximated curvature fields from the noisy slope fields. The residual results are shown in Fig. 3.3. It was observed that if the degree is too low, the polynomial curve fitting does not describe the curvature fields well and if the degree is too high, the polynomial fitting amplifies the effect of noise. Therefore, as a compromise, 9th order polynomials were chosen here to represent the curvature fields. However, it should be noted that since the measurement noise level could be different depending on the measurement technique in a real case, the corresponding identification results should be analyzed depending on the range of values for the polynomial curve fitting degree.

Following the selection of the polynomial degree, the identification results with fitted data using the VFM are shown in Tab 3.3. The identified values are close to the reference values, but it was observed that D_{11} and D_{12} were more affected by the noise. Since UD material is used in this bending test, D_{11} is much higher than D_{22} and D_{66} (much stiffer in the x direction). Thus, the x curvature values are much lower than the other two components and more affected by the noise. One way of improving the identification is to increase the magnitude of the applied load to the plate. In the elastic range, the level of strain fields is proportional to the level of load. Since the noise is only related to the optical conditions and the CCD camera, its level is independent from the applied load. As a consequence, if the amount of the applied load is increased, the signal to noise ratio will be increased. This is considered a good strategy which can be used in the experiment. Therefore, in experiment, the maximum force magnitude compatible with deflectometry technique will be applied, while ensuring a maximum deflection less than the thickness of the plate (small displacements assumption).

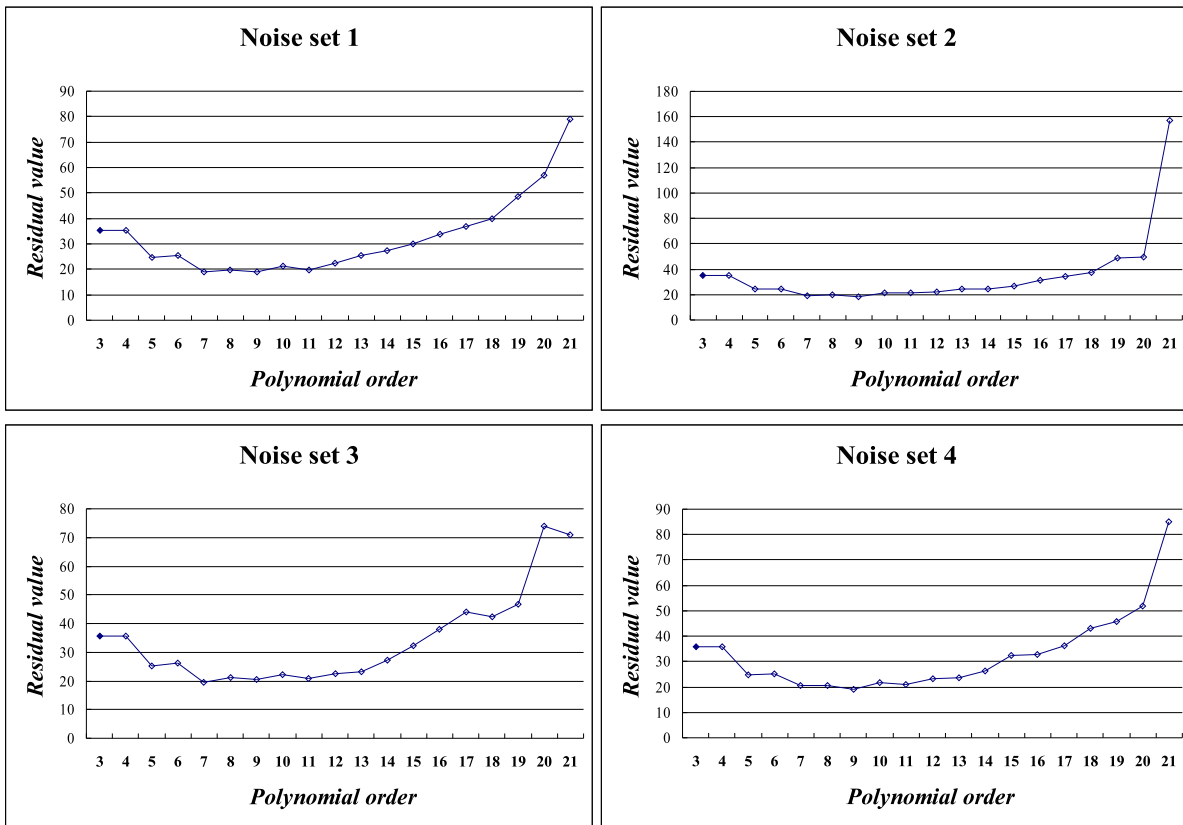


Figure 3.3: Residual values depending on the polynomial degree.

3.2.3 Experimental identification results

In order to assess the suitability of the identification procedure, a validation experiment was undertaken on a carbon-epoxy plate. A unidirectional T300/914 carbon-epoxy laminated plate was fabricated using a hot press machine. The material properties are the same as the ones used for the FE work. The plate size is $190 \times 140 \text{ mm}^2$ and its thickness is 2.56 mm with 16 layers of prepreg.

It is worth mentioning that in the manufacturing of thin laminated plates, the autoclave is more preferable than a hydraulic press machine. When the laminated plate is cured in using a hot press, adjustable stops on the tool are utilized to set the final thickness. The applied pressure will be undertaken by the prepreg until the laminate is consolidated down to the set thickness. Once the set thickness is reached, almost all the applied pressure will be undertaken by the four stops in the tool. Therefore, the final thickness of the laminates is determined by the set thickness, not by the pressure. In addition, in the case of autoclave, the pressure is more evenly distributed over the top surface of the laminates during the curing process, so the thickness variation after curing is less than in

	D_{11} (Nm ²)	D_{22} (Nm ²)	D_{12} (Nm ²)	D_{66} (Nm ²)
Reference	181.9	13.4	4.55	6.57
Identified (Noise 1)	180.7	13.5	3.24	6.50
R.D. (%)	0.65	-0.60	28.8	1.09
Identified (Noise 2)	187.6	13.5	1.62	6.50
R.D. (%)	-3.15	-1.06	64.5	1.05
Identified (Noise 3)	185.9	13.4	3.05	6.46
R.D. (%)	-2.24	-0.18	32.9	1.61
Identified (Noise 4)	181.7	13.5	3.64	6.52
R.D. (%)	0.13	-0.63	19.9	0.80

Table 3.3: Identification results with noisy data.

the case of manufacture with a hydraulic press. The thickness setting for the press must be acquired from the calculation of fibre volume fraction, whereas this is not necessary with the autoclave.

3.2.3.1 Specimen preparation with resin coating

Usually, as the surface of a composite plate is not naturally reflective enough to be used for deflectometry, surface preparation is necessary. A special thin resin coating (gel coat) is applied to the surface to make it specular (mirror-like). This surface preparation technique was initially developed by Grédiac and Vautrin [45], but no details of the procedure for producing the coating were provided. The equipment required for the specimen preparation is as follows: Surf Clear gel coat (epoxy resin) and SD Surf Clear (hardener) manufactured by SICOMIN (www.sicomin.com), clean glass panel, bees' wax (release agent), alcohol, soft cloth, plastic cup, and a wooden stick. The detailed procedure is described in Figs. 3.4 and 3.5.

In Fig. 3.6, the specimen surface with the resin coating is compared with the same material without coating. It is clear that the coating dramatically improves the reflectivity of the composite with a sharp image of the ceiling light that appears blurred on the untreated surface (left). Microscopic observation of the coated plate has revealed a final thickness of the resin coating of about $30 \sim 40 \mu\text{m}$, obtained by differential measurement

1. Preparation

Clean the surface of the glass panel and composite specimen with a cleaning agent, here, alcohol.

2. Applying a release agent

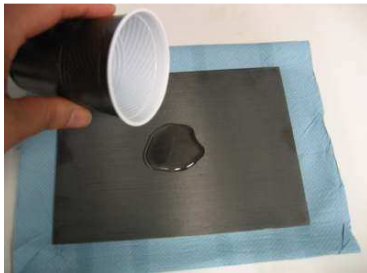
Here, bees' wax is used as a release agent to detach the resin coated specimen from the glass panel after curing of the gel coat. Apply a small amount of bee wax to the glass panel with a soft cloth. Wipe the wax over the glass panel surface with a soft cloth back and forth or in a circle until all stains are cleaned out. It is important to note that if some wax stains remain on the surface of the glass, after curing, the stains will transfer to the resin coating surface, spoiling its reflectivity.

3. Mixing epoxy resin and hardener

SICOMIN Surf Clear is applied to make a thin reflective resin coating on the specimen. Mix epoxy resin and hardener with the weight ratio of 100:38 in a clean plastic cup and wait for 5 to 10 minutes to eliminate air bubbles trapped in the mixture. Important recommended working conditions for the Surf Clear gel coat [8] are as follows:

- working temperature: 20°C minimum and 35-40°C maximum
- maintain a constant temperature during curing.
- avoid high ambient humidity, must be lower than 70%.

4. Applying the resin mixture



Pour the resin and hardener mixture carefully on the surface of the specimen.



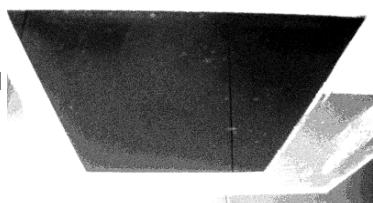
Spread the resin all over the plate.

Figure 3.4: A procedure for producing reflective coatings.

5. Applying the specimen onto the glass panel



Apply the specimen face with the resin onto the glass panel and press the top surface of the specimen gently to spread the resin out in all direction.



Check the other side of glass panel and identify the locations of the remaining air bubbles.



Squeeze the air bubbles out by pressing the top surface of specimen from the centre to the edge in all directions.

6. Curing

The curing profile on the Surf Clear resin [8] is as follows:

- time before curing: 24 hours at room temperature;
- minimum cure: 12 hours 40 °C;
- optimum cure: 8 hours 60 °C.

However, it is observed that sometimes the thin composite plate bends slightly after curing at 60°C due to the thermal coefficient mismatch between the resin and the composite. So, room temperature curing is preferable to avoid this problem. Curing at room temperature takes 3 to 4 days depending on room temperature and ambient humidity. It must be emphasized that no pressure is applied onto the composite plate during curing, the weight of the composite plate is enough.

7. Finishing touches

After curing, release the specimen carefully from the glass panel with a knife blade and trim the edge of the specimen with a grinding wheel. Remove dust with an air spray.

Figure 3.5: A procedure for producing reflective coatings (Cont'd).

of the thickness before and after coating. Therefore, the effect of coating on the global composite stiffness can be neglected. It could be argued that the application of resin coating on real structures may be inconvenient, then other slope measurement techniques, for example shearography, could be used at the expense of higher cost. The other possibility would be to measure deflection (with ESPI, for instance) but then, the resolution of the identification will be limited by the double differentiation necessary to obtain curvatures.

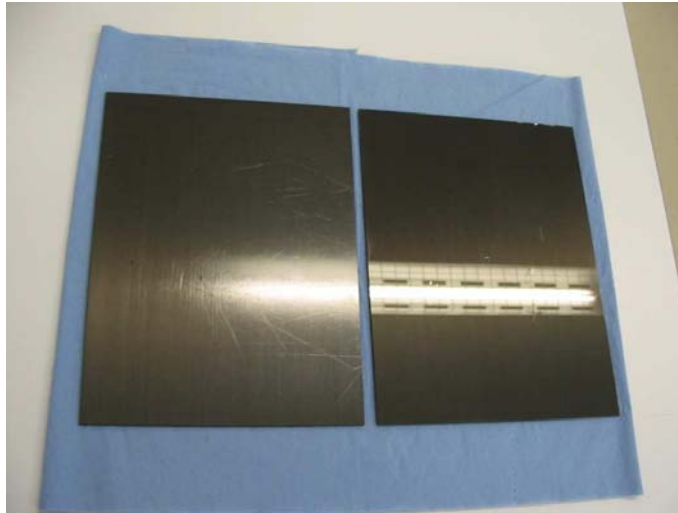


Figure 3.6: Comparison of surfaces with and without coating (image of a ceiling light)

3.2.3.2 Experimental Set-up

The experimental implementation was performed using the deflectometry set-up shown in Fig. 3.7. A 2272×1704 pixels CCD camera observes the specimen surface through a hole on the grid panel. A light illuminates the reference grid. The ambient light should be stable during the measurements. The reference grid of pitch 2 mm was printed with a HP plotter from a PostScript file. The composite plate is supported by specially designed point grips to give simple support conditions and the load is applied by a load sensor developed in-house. The zoom lens in front of the CCD camera was set up so that the image of the plate fills the maximum of the CCD array. The pixel size of the recorded image was 2077×1537 , with 11 pixels per grid period (one pitch). The distance h between the plate surface and the grid was measured with a metallic tape measure, giving $h = 1350 \pm 1$ mm. From the geometrical configuration of Fig. 1.1, the sensitivity s was calculated as 8482.

The focus of the lens was adjusted to get a sharp image on the measurement area and the aperture was controlled to yield sufficient contrast. Decreasing the aperture size increases

the contrast (the range of difference between the dark and bright areas in an image) of the image (decreasing the noise of the signal); this also increases the depth-of-field (the range of distance in a scene that appears to be in focus) [46]. As in Eq. 1.15, increasing contrast γ increases phase modulation and therefore sensitivity. On the other hand, using the zoom function with a longer focal length reduces the depth-of-field, as well as resulting in optical distortion of the image. It should be noted here that the depth-of-field is important for the case of large deflections. As discussed in section 3.2.2, to improve signal-to-noise ratio, maximum force magnitude is to be applied. The deflection of the bent plate will increase as the amount of force increases. In this case, sufficient depth-of-field is required to obtain good focus over the whole measurement area.



Figure 3.7: Deflectometry set-up.

To study the maximum load magnitude which can be applied to the specimen, several force amounts were tested. It was observed that too high loads induce too many fringes on the phase map. This makes the phase subtraction and unwrapping difficult. The maximum possible load magnitude with the given UD composite specimen and the given boundary condition was found to be approximately 10 N. Consequently, the applied load was chosen as 10 N.

3.2.3.3 Data processing

As discussed in Chapter 1, a first image of the plate at rest was taken. A phase map was computed from the obtained grid intensity field with the WDFT algorithm. An algorithm implemented in the *Frangyne*[®] software (phase processing engine of the Ondulo package, see www.techlab.fr) enables to separate the information in the two directions of the grid by averaging the signal in the other direction. Then, the plate was deformed and another phase field was computed. Phase subtraction of the deformed phase map from the undeformed one produced a wrapped phase map. The wrapped phase map was unwrapped (demodulation) using an unwrapping algorithm in the same software. These unwrapped phase maps were then converted to slope data by means of the sensitivity, as given in Eq. 1.13.

3.2.3.4 Comparison between FE data and experimental data (slopes, strains)

In order to assess the quality of the measurements, a comparison of the x and y slope maps with finite element simulations is presented visually in Fig. 3.8. The patterns of the slope maps are very close between the FE model and the experimental measurements, however the values are different (see the scales in Fig. 3.8). This is caused by some solid rotation adding up when the plate is loaded, because of the specimen settling in on the support. It should be noted however that the ranges of the amplitude of the slopes are the same, about 18×10^{-3} for the x component and 30×10^{-3} for the y component, suggesting that the strains will be similar. The three strain components ϵ_{11} , ϵ_{22} and ϵ_{66} were then obtained from the slopes by numerical differentiation after spatial smoothing. Here, 9th order polynomials were used as recommended from section 3.2.2. It can be seen from Fig. 3.9 that the simulated strains are in good agreement with the experimental ones (the same scale is used to represent both results). As shown in Fig. 3.9, ϵ_{11} is of the order of 10^{-5} as ϵ_{22} and ϵ_{66} are of the order of 10^{-4} . This is caused by the high anisotropy of the carbon unidirectional plate and means that the present situation is probably the most difficult one. Any plate with a lower anisotropy will be much easier to deal with. The good agreement between the experimental and simulated strain maps indicates not only good measurements but also good boundary conditions and stiffness values. This suggests that the following identification procedure will be successful.

It is important to note that the finite element simulation here is only performed to assess the quality of the measurements but is not needed for the identification. Indeed, even if the above comparison had not been successful, the identification could still have been successful since the virtual field method does not require stringent assumptions on the

boundary conditions.

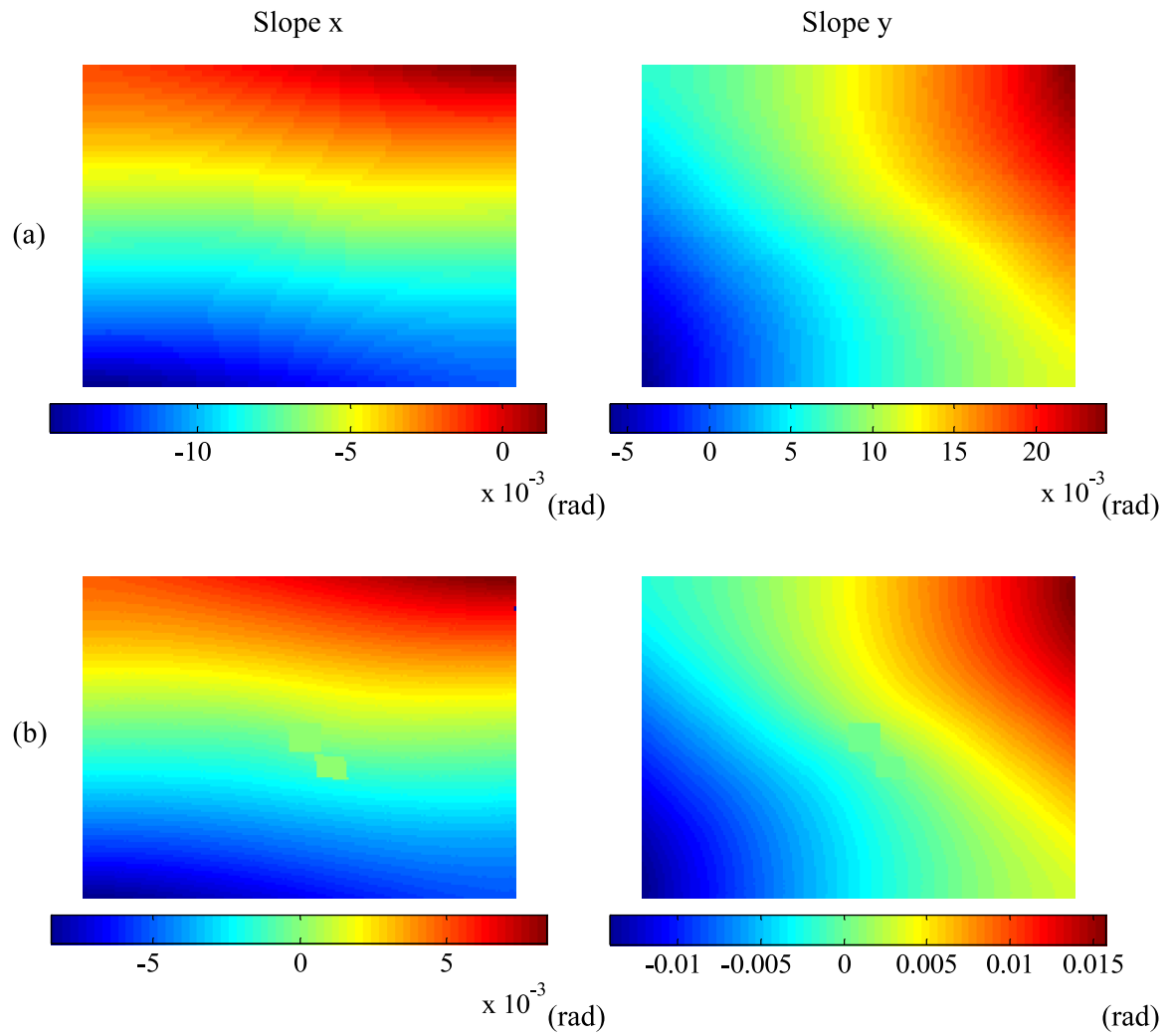


Figure 3.8: Comparison of slope fields between (a) FEA and (b) experiment.

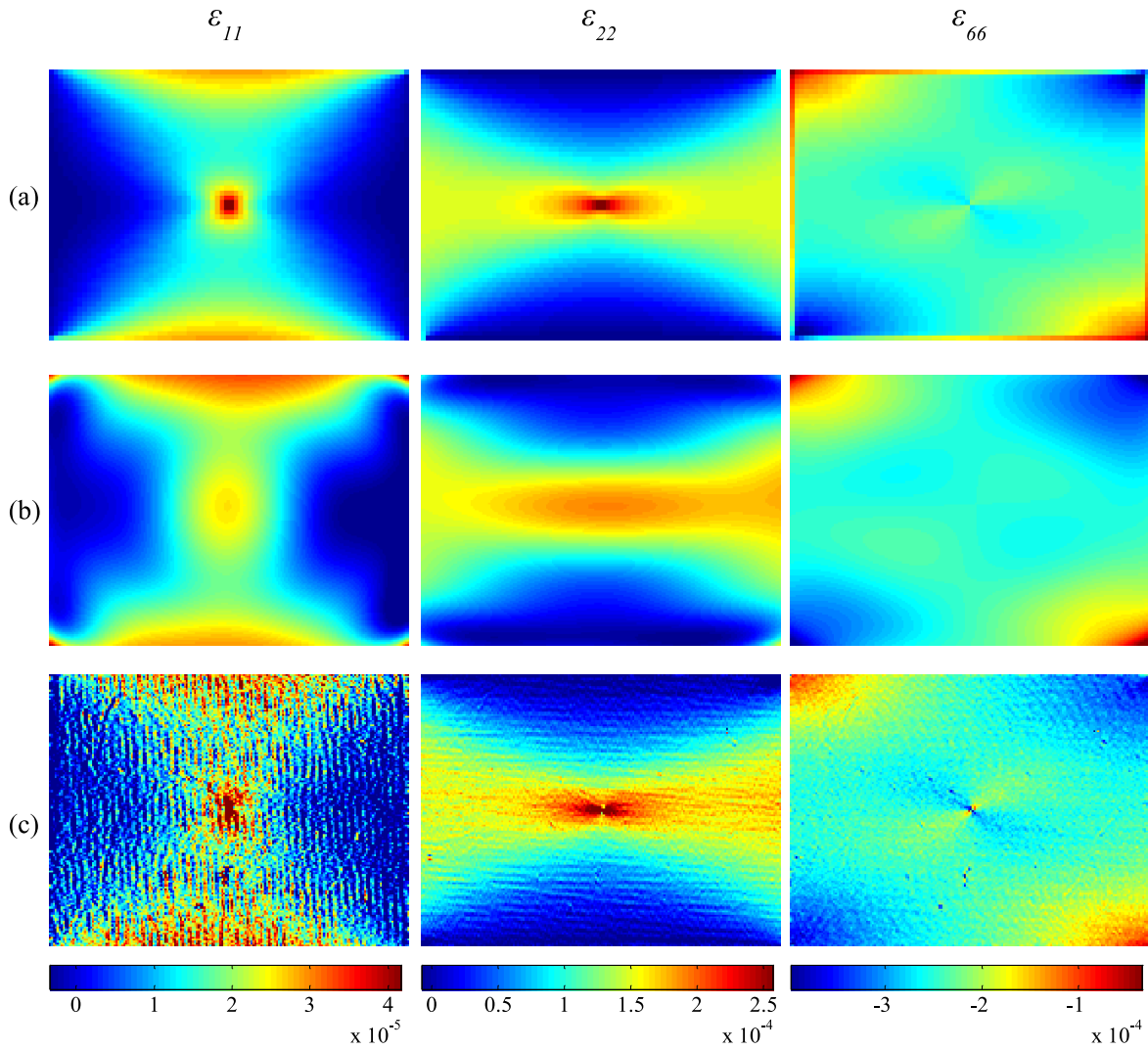


Figure 3.9: Comparison of strain fields between (a) FEA and (b) experiment, with original camera position (spatial smoothing, 9th order) and (c) experiment, with offset camera position (without spatial smoothing).

3.2.3.5 Identification results with original camera position (with spatial smoothing)

The identification results of global bending stiffnesses on the bent plate are reported in Tab. 3.4 (a). The identified values are close to the reference ones but it must be stated that when the order of the slope fitting polynomial is changed, D_{11} and D_{12} vary significantly (between 15% and -15% of the reference for D_{11} , more for D_{12}), while D_{22} and D_{66} remain very stable. This is caused by the high anisotropy of this unidirectional material and the

fact that the bending test performed here leads to x strain values that are much lower than the other two components, as can be seen in Fig. 3.9. Therefore, the present results are consistent with this remark.

	D_{11} (Nm ²)	D_{22} (Nm ²)	D_{12} (Nm ²)	D_{66} (Nm ²)
Reference	181.9	13.4	4.55	6.57
Identified (a)	159.8	12.5	3.88	6.29
R.D. (%)	12.2	7.00	14.8	4.10
Identified (b)	162.7	12.8	5.27	6.41
R.D. (%)	10.5	4.80	-15.8	2.50
Identified (c)	165.4	12.9	5.45	6.52
R.D. (%)	9.10	3.50	-19.7	0.80

Table 3.4: Identified stiffness components for the carbon epoxy plate (a) with original camera position (spatial smoothing, 9th order) (b) with offset camera position (without spatial smoothing, before calibration) (c) with offset camera position (without spatial smoothing, after calibration).

3.2.3.6 Identification results with offset camera position (without spatial smoothing)

As discussed in section 1.2.3.5, the new deflectometry configuration (see Fig. 1.8 (b)) requires a calibration for the camera position. In this section, the proposed calibration will be validated with the identification of global bending stiffnesses.

Same experimental conditions were used except the camera position. The distance e in Fig. 1.8 (b) was measured as 5 cm. The two dimensional distribution of sensitivity for the new setup calculated from Eq. 1.29 is shown in Fig. 3.10. New slope fields were obtained by multiplication of the 2D sensitivity values and then strain fields were retrieved from the slope fields through direct differentiation. The strain fields are shown in Fig. 3.9 (c). Compared with the fitted strain fields (Fig. 3.9 (b)), the new strain fields describe the details accurately and are very close to the FE simulated strain fields. First, the identification result without calibration is reported in Tab. 3.4 (b). Secondly, the identification result after calibration is shown in Tab. 3.4 (c). It can be seen that the new identified values are closer to the reference values than the fitted values. This result is very promising.

It is clear that this approach will be very useful for the identification of the local stiffness variation. It is worth noting that the influence of the strain field irregularity (see Fig. 3.9 (c)) on the identified stiffnesses is negligible.

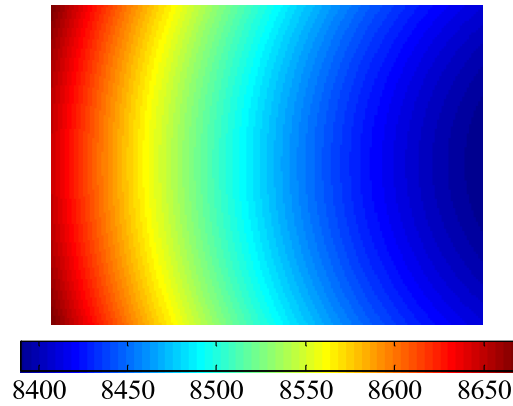


Figure 3.10: The 2D distribution of sensitivity.

3.3 Conclusion

In this chapter, the identification procedure of the bending stiffnesses in non damaged composite laminated plates was validated on simulated and experimental measurements. In the orthotropy basis, four bending stiffnesses were determined from a single bending test using the VFM. In the experimental part, the identification results depending on camera positions in deflectometry were presented. The thin resin coating applied to the surface was well suited for providing sufficient reflectivity for the deflectometry technique. In order to increase the signal to noise ratio, maximum force magnitude compatible with the deflectometry technique was applied. It was observed that the experimental strains are in good agreement with the simulated ones. The identified values from the new deflectometry configuration were closer to the reference values than those from the original deflectometry configuration. The identified D_{11} and D_{12} values showed some deviation while D_{22} and D_{66} were close to the reference values. This is caused by the high anisotropy of the unidirectional material and the fact that the bending test performed here leads to x strain values that are much lower than the other two components.

Chapter 4

Review of damage process and detection techniques for composite plates

4.1 Introduction

The advantages of fiber reinforced plastic (FRP) laminated composites have long attracted the attention of many engineers and researchers interested in the design of more efficient structures. However, the inherent anisotropy and the brittle characteristics of fibres and resin of composite laminated plates result in failure mechanisms that are very different from those of homogeneous metallic ones [47, 48]. While ductile metallic components can yield and absorb kinetic energy via plasticity, on the contrary, brittle composites can only dissipate energy by a variety of damage modes. Particularly, the lack of through-the-thickness reinforcement of composite laminates develops a unique type of damage as a form of discontinuity between layers. Accordingly, the damage modes in composite laminates involve not only intralaminar damage (matrix cracking, fiber breakage) but also interlaminar damage (delamination) [49]. Moreover, the high anisotropy of composite laminates makes more complicated an already complex failure mechanism.

The strength and stiffness of composite laminates are significantly impaired in the presence of damage, therefore evaluation of the residual properties and prognosis of the remaining service life of the structure have been of great interest. Insufficient understanding of the failure mechanisms and the absence of efficient tools which can reliably assess the safety

in composite structures prohibited composite materials from being used in load-bearing primary structural components [50].

In this chapter, the damage in composite structures will be reviewed and diagnosed in terms of damage resistance and tolerance [51]. Damage resistance is defined as an ability to resist damage ‘onset’ and ‘growth’ from a specific cause such as impact and damage tolerance refers an ability to perform with the given damage state of a structure. Thus, the damage tolerance is associated with residual properties (strength and stiffness) and life of the structure. In the following sections, the damage resistance of delamination and impact damage, and the damage tolerance regarding strength and stiffness reduction as a result of damage in composite laminates will be reviewed.

4.2 Damage in composites

An end user survey concerning the most important damage types in aircraft structures has been performed by the research project called MONITOR (Staszewski 2000) [52]. A summary of this survey is shown in Tab. 4.1. It can be seen that fatigue crack is considered to be the most important damage mechanism in conventional metallic components, on the other hand, impact damage and delamination are the major concerns in composite materials.

Metallic structure	
- Fatigue crack development	100
- Corrosion	82
- Bonding/debonding of joints	70
- Stress corrosion cracking	47
- Impact damage	24
Composite structure	
- Impact damage (including battle damage)	65
- Delamination (including growth)	65
- Bonding/debonding	59

Table 4.1: Damage statistics in metallic and composite structures taken from the MONITOR end-user surveys [52].

4.2.1 Delamination

Delamination is an interlaminar failure in the resin rich interface between the layers. Laminated composites consist of several orthotropic layers which are laminated in the through-the-thickness direction. Each layer is made up of fibre reinforcement embedded in a polymer matrix. The interface area is especially susceptible to failure since usually there is no reinforcement through that direction. Consequently, the delamination is considered as a unique damage mode of the composite laminates.

One of the advantages of composites is that, unlike metallic counterparts, a specific design requirement can be met by controlling the stacking sequence lay-up. Therefore, in general, the laminated composites are comprised of layers having different fibre orientations. Delaminations are usually generated between the layers with different fibre orientations, not between the layers in the same lay-up angle [53]. In addition, the magnitude of delamination depends on the relative difference of fibre orientations of the neighboring layers.

Delamination damage is caused by large interlaminar stresses resulting from low-velocity impact (maintenance tool, bird strike, *etc.*) [54], the structure's free edge effect [55], or faulty manufacturing processes. It has been reported that delaminations due to low-velocity impact are induced by the bending stiffness mismatch of adjacent plies [56]. This is owing to the fact that bending stress is the major stress which generates delamination damage when low-velocity impact occurs on the surface of a structure. On the other hand, delaminations due to the free edge effect are caused by the Poisson's ratio mismatch between adjacent laminae [26].

Before proceeding to the analysis of delaminations, it is required to distinguish two types of delaminations depending on their through-the-thickness position. The first type is delamination which is located within laminates and the second is delamination located near the surface of laminates [57]. Two types of delaminations are shown in Fig. 4.1. The first type of delaminations can be considered as cracks which have been treated in conventional fracture mechanics. In the analysis of the second type of delamination, local instability should be taken into account, as the near-the-surface delamination generally induces local buckling under loading. The local instability may be extended to global instability of structural members such as columns, and plates under compressive loads, which could finally lead to a catastrophic failure [57].

In composite laminates, the major axial and bending loads are supported by the fibres and the shear loads by the matrix [58]. Basically, once a structural component is delaminated, the component loses interlaminar shear carrying capability [59]. If the location

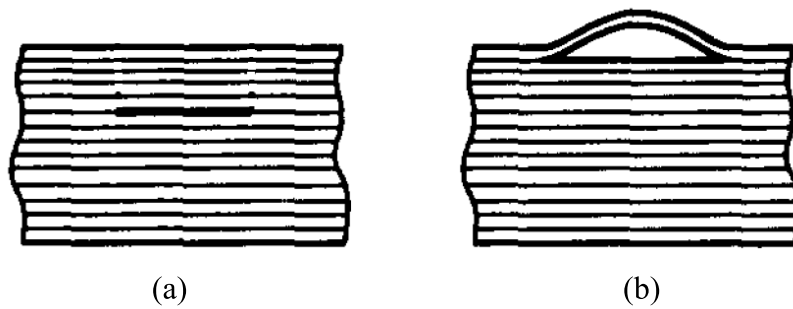


Figure 4.1: Types of delaminations: (a) internal (b) near-surface [57].

of delamination is closer to the mid-plane of the member, the loss of interlaminar shear carrying ability increases. Nevertheless, the presence of delaminations causes stress redistribution within the structure regardless of the position. Due to delamination, one part of a structure may lose the load carrying capability. This means that another part will sustain increased stresses and these increased stress states may initiate the propagation of the existing delaminations [60]. Additionally, the delamination can propagate in a stable or unstable way depending on the stress redistributions. When the delamination grows under constant applied load, the growth is called ‘unstable growth’ and if the delamination propagates only when the load is increased, it is called ‘stable growth’ [61].

When delamination grows under compressive loads and reaches a critical size, buckling, the main failure mechanism owing to delamination, can occur. Even for originally symmetric laminates, delamination and initial buckling cause a material imbalance. The unsymmetrical lay-up may lower the buckling load and expedite the propagation of delamination, leading to a final structural failure at loads lower than the design level. Therefore, it is necessary to understand the onset and growth mechanisms of delamination for the prediction of failure and safe use of composite structures. A significant body of research has focused on the initiation and propagation of delamination in laminated composites.

4.2.1.1 Initiation and propagation

Interlaminar normal and shear stresses are responsible for the mechanism of delamination initiation and propagation. Generally, initiation and propagation are investigated separately [62]. In the prediction of initiation of delamination, strength analysis approach is usually used, and for the analysis of propagation, fracture mechanics approach is mainly employed, provided that initial delamination exists [26]. Strength analysis is associated with stress-based consideration and fracture mechanics with energy-based consideration [58]. Both approaches are complementary for the purposes of this study.

4.2.1.1.1 Strength analysis This approach consists in comparing the calculated interlaminar stress from a finite element analysis with interlaminar stress allowable [26]. Usually, the interlaminar stress allowable is determined from experimental tests. The high stress gradient in the neighborhood of the delamination front necessitates the use of very fine finite element meshes to avoid the stress singularity at the crack tip [62]. Nonetheless, the use of fine meshes does not guarantee to avoid the singularity. That is why fracture mechanics is used if there is a crack.

4.2.1.1.2 Fracture mechanics approach Fracture mechanics is based on the assumption that an initial crack-like flaw exists. Delamination is treated as a crack in fracture mechanics. Especially, the delaminations which are located within the bulk of the material are involved in this case. However, *a priori* assumptions regarding the size and distribution of delaminations may limit the application of this approach, since this data is unknown *a priori* in real situations [63].

In the case of linear elasticity, there are two fracture mechanics approaches [64]. The first one is the stress intensity factor approach. In this approach, the stress intensity factor (SIF) K is used to perform stress analysis of the crack tip. However, in the analysis of anisotropic materials, the stress function becomes very complicated mathematically. The second is the strain energy approach. The strain energy release rate (SERR) G is used to characterize the fracture. This approach is simpler than the stress intensity factor approach, and can be easily applied to the analysis of anisotropic materials. SERR can be used as a criterion for determining delamination growth in composite laminates, and is defined as:

$$G = \frac{dW}{dA} - \frac{dU}{dA} \quad (4.1)$$

where dW is the change in external work done, dU the change in total strain energy, and dA the change in crack area. It is assumed that delamination propagates when the SERR exceeds a certain critical value, G_C , which is called material toughness. The material toughness is the energy required to fracture the material per unit volume, so it follows that the material will fracture if the dissipation of the strain energy released by the crack is greater than the cohesive force of the atoms. Several methods have been used to calculate the SERR, for instance, the J -integral [65], the virtual crack extension (VCE) approach [66], and the virtual crack closure technique (VCCT) [67]. The most common approach is the VCCT. It calculates the SERR using the nodal forces and displacements near the crack tip in the finite element analysis. The VCCT can predict accurately the SERR with

relatively coarse finite element meshes and can be applied easily to FE programs [58]. Currently, the SERR has been accepted as the standard fracture parameter. Once the SERR is determined, it is compared to the material toughness which is experimentally measured. Thus, it is possible to assess the propagation of the crack front under a given loading condition.

Depending on the fracture modes, the total energy release rate G can be decomposed into mode I component G_I due to interlaminar tension, mode II component G_{II} due to interlaminar sliding shear, and mode III component G_{III} due to interlaminar tearing shear, and also, the corresponding critical magnitude G_C into G_{IC} , G_{IIC} , and G_{IIIC} [57]. Generally, the patterns of interlaminar fracture are complicated since the three fracture modes are mixed in most of the practical cases. The three types of modes are illustrated in Fig. 4.2.

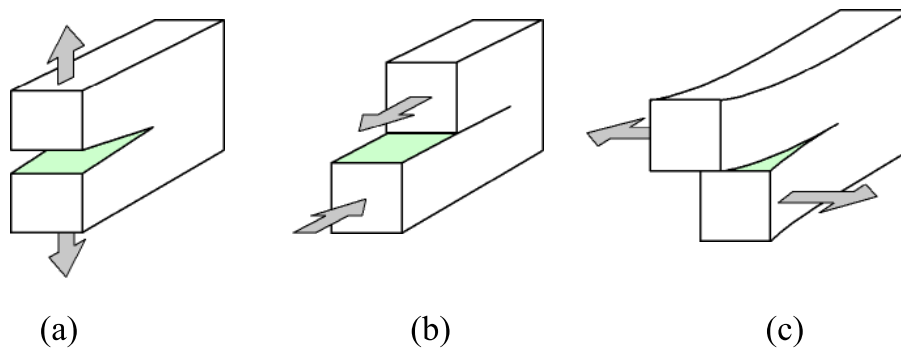


Figure 4.2: Three basic modes of crack tip deformation: (a) Mode I (tension, opening) (b) Mode II (in-plane shear, sliding) (c) Mode III (out-of-plane shear, tearing) [68].

For better understanding of delamination and improving interlaminar fracture toughness, experimental tests which can perform single mode of interlaminar crack propagation are required. The most widely used interlaminar fracture tests are the double-cantilever beam (DCB) test for mode I and the end-notched flexure (ENF) test for mode II. Those test configurations are illustrated in Fig. 4.3.

To determine the SERR in progressive crack propagation using FE analysis, the crack front of a FE model should be moved to represent the crack propagation by adjusting the finite element mesh or by disconnecting nodes between elements [70].

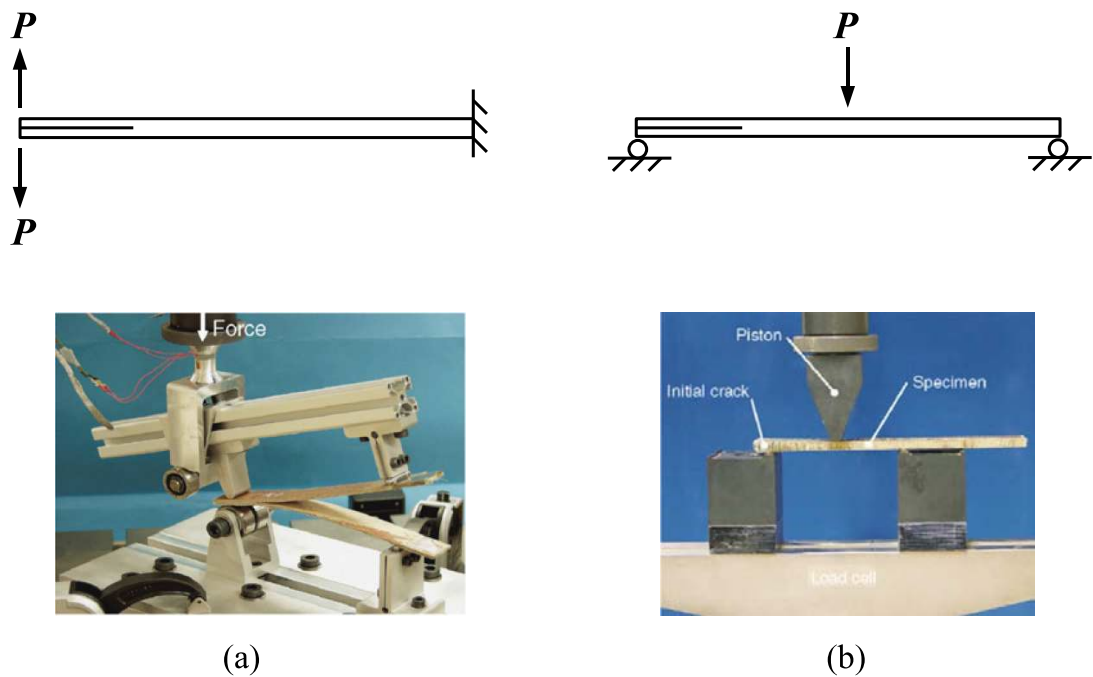


Figure 4.3: Basic fracture mechanics tests: (a) DCB test (b) ENF test [69]

4.2.1.2 Buckling

Under compressive load, further delamination propagation is greatly influenced by buckling. Buckling increases the unexpected interlaminar stresses at the delamination front and accelerates the propagation of delamination [71].

When an orthotropic laminate with a through-the-width delamination is subjected to in-plane compressive loading, three different buckling modes can occur depending on the location and size of the delamination [72]. These buckling modes are shown in Fig. 4.4. If the delamination is located near the surface and the size of the delamination is relatively large, the local buckling mode is dominant. On the other hand, if a relatively small delamination is located deeper inside, the global buckling mode is prevalent. A combination of local and global buckling modes creates a mixed buckling mode. The buckling loads decrease significantly as the location of the delamination is closer to the surface of the laminates [73]. Each buckling mode determines the dominant crack opening mode, but in practice, the buckling mode may be very complicated since there are many parameters (location, size, number of the delamination, stacking sequence and boundary condition, *etc.*) which can affect the buckling mode.

The progressive failure mechanism of laminated plates with delamination starts with ini-

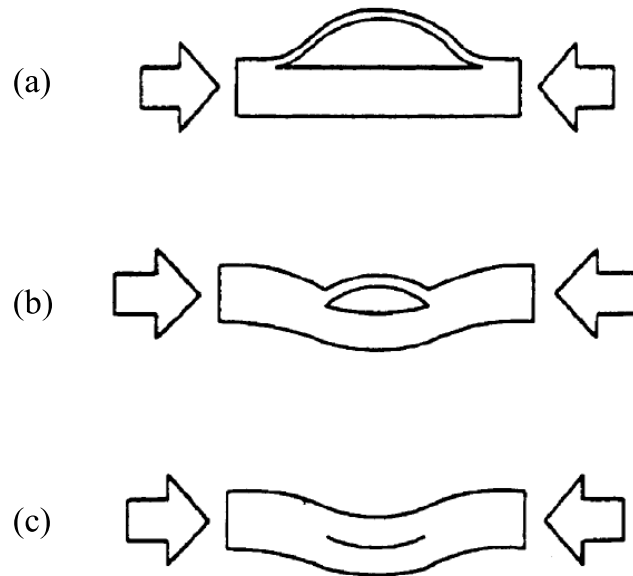


Figure 4.4: Three types of buckling mode shapes: (a) Local buckling mode (b) Mixed buckling mode (c) Global buckling mode [74].

tial buckling and involves delamination propagation and post-buckling, ending with final failure [75]. In the case of the local buckling mode, the sublaminates above delamination may buckle locally at a very low compressive load. Generally, delamination occurs unsymmetrically with respect to the mid-plane of a plate. Out-of-plane buckling of plies above or below the delamination makes the remaining unbuckled sublaminates unsymmetrical even if the original laminates are symmetric [76]. This induces bending-extension coupling for remaining plies and asymmetric loading. So, in-plane compressive load results in out-of-plane bending. Since there is no strain compatibility of the delaminated plate cross-section, the effective moment of inertia in the delaminated region decreases [77]. Consequently, the loss of local bending stiffness may extend the local buckling area, increasing the stresses in the remaining plies, finally leading to global buckling of the plate. Once global buckling occurs, bending-twisting coupling is induced, resulting in post-buckling and final failure. Therefore, the presence of delamination may decrease the critical buckling load of the plate and reduce the compressive strength [76].

It has been shown that there is a linear correlation between bending stiffness reduction and critical buckling load [78, 79]. In addition, it has been reported that in the case of near-the-surface delamination, small changes in bending stiffness cause large changes of strain energy release rates for mode I and mode II [80], which will induce local instability and promote propagation of delamination and buckling.

In practice however, multiple delaminations are likely to occur instead of a single delamination, complicating the buckling behavior of composite laminated plates which may lead to a higher degradation in compressive strength [81].

4.2.2 Impact damage

Composites are mostly used in laminated form and inherently weak in through-the-thickness direction since there are no fiber reinforcements in this direction. Therefore, composites are vulnerable to transverse impact loading. Impact damage can be induced from tool drops, bird strikes, runway debris, and hailstorms and may create serious damage to the composite structures [82, 83].

The nature of impact damage modes in composite laminates is very different from that of conventional metallic counterparts. Impact damage can be easily detected in metals since damage occurs at the impacted surface and it is not considered to be a big threat because metallic components can yield and most of the impact energy is absorbed as plastic deformation. On the contrary, composites absorb the kinetic energy only in elastic deformation and dissipate energy by a variety of damage fracture mechanisms, not via plastic deformation [48]. Low velocity impact can be particularly dangerous since the majority of the impact damage is produced towards the rear surface and the damage may be only barely visible [84]. Nevertheless, the barely visible impact damage (BVID) can seriously reduce the structural integrity such as strength and stiffness.

The impact damage modes in composites are complicated, consisting of varying amounts of matrix cracking, delamination, and fiber breakage [84]. Those modes are governed by several parameters, for instance, impactor shape, impactor speed, laminates properties, *etc.* The combination of different types of damage complicates the impact damage behavior.

4.2.2.1 Low / High velocity impact

Generally, impact events are classified into low or high velocity impact. However, the definition of each impact is different depending on the authors [48]. In Ref. [85], low-velocity impact is defined when the impactor speed is from one to tens m/s depending on the target stiffness and the impactor's mass and stiffness. In this case, the global structural response is important because the contact time between the impactor and the target surface is long enough. On the other hand, in high-velocity impact, the contact time is very short and the global structure does not have time to respond, so that only very localized

damage occurs. Other authors defined that high velocity impact is characterized by fibre breakage due to penetration of the impactor, and low velocity impact by delamination and matrix cracking [86].

4.2.2.2 Damage mechanisms in low velocity impact

The fracture process as a result of impact involves interlaminar damage (delamination) and intralaminar damage (matrix cracking, fibre fracture). It is crucial to characterize the damage modes as they can offer important information regarding the residual strength and stiffness of a given structure [48].

4.2.2.2.1 Matrix damage Matrix cracking and debonding (between fibre and matrix) are the initial failure mechanisms of low velocity impact. There are two types of matrix cracking [87]. The first is shear cracks which initiate from the contact area with the impactor. These shear cracks are caused by high shear stresses. The second is bending cracks which start from the obverse side of impact. These are generated by tensile stresses due to bending. The crack types are also dependent on the structure geometry [88]. Bending cracks are dominant in long and thin specimens and shear cracks in short and thick specimens. Matrix cracking promotes delaminations owing to high interlaminar stress concentrations at the crack tip. The debonding is produced by the mismatch between fibre and matrix properties and usually occurs parallel to the fibre direction [48].

4.2.2.2.2 Delamination Delamination is an interlaminar crack in the resin rich region between each lamina. In low-velocity impact, delamination is generated by the bending stiffness mismatch between adjacent layers with different fibre orientations [56]. Delamination shape is peanut-like and the major axis is parallel to the fibre orientation of the layer below the delamination. If the bending stiffness mismatch is higher, the delamination area will be larger. Therefore, cross-ply laminates which have $[0^\circ/90^\circ]$ lay-up combination are the worst case in terms of delamination occurrence. It has been shown that the majority of the impact damage (delamination, matrix crack, and fibre breakage) take place towards the opposite side owing to high tensile bending stress [84]. Other research has observed that delamination only occurs with matrix cracking [87]. The delaminations induced by shear cracks are located on the impact side and the size is usually small [89]. The major delaminations are generated by bending cracks on the other side with large size. The resin rich interface between two layers and the delamination propagation induced by matrix cracking are shown in Fig. 4.5.

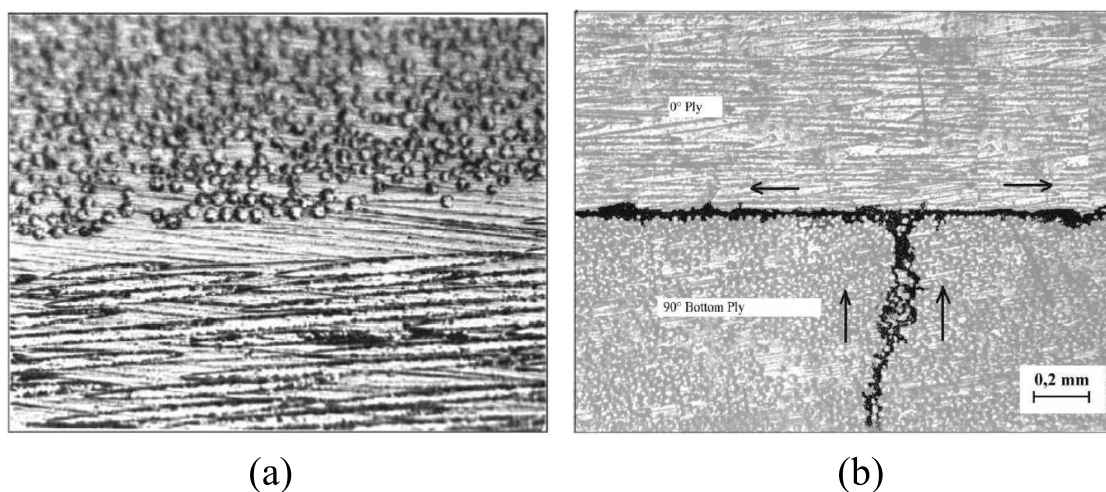


Figure 4.5: Optical micrograph of virgin and failed sample: (a) Rich resin interface between two layers (b) Delamination propagation for a $[90_2/0_2]_s$ specimen [90].

4.2.2.2.3 Fibre failure Fibre breakage occurs by locally concentrated shear and compression stress (indentation effect) on the impact side and by high bending stress on the obverse side of impact [48]. While fibre breakage can be a fatal damage, however, it is usually generated in the later part of fracture process, so it is less important in a low-velocity impact event.

4.3 Effects of damage on mechanical performance

The damage modes reviewed in section 4.2 can cause significant reduction in residual load carrying capabilities such as strength and stiffness. Therefore, the residual performances of damaged composite structures have attracted considerable attention among structural engineers and researchers.

Composite structures are subjected to various loading conditions during their service life. The reduction in strength and stiffness will arise in varying degrees, depending on the loading conditions and dominant damage mode [48]. The common loading types are in-plane tension, compression, and bending. Among the three damage modes, matrix cracking affects the residual performance the least. Matrix cracking does not significantly deteriorate the material properties of laminates in itself. However, delamination can be induced at the crack tip when the matrix cracks reach the interface between layers [77]. Delamination is the most dangerous failure mechanism in composite laminates. If a lam-

inated plate with delamination is under tensile loading, delamination does not affect load carrying capability much. On the contrary, under compressive or bending load, delamination can be critical. Under compressive load, each sublaminates of delaminated region should resist its own buckling load. Owing to the reduced thickness of each sublaminates, flexural stiffness decreases [91]. Consequently, the critical buckling load is much lower than that of the virgin laminate. The critical buckling load is dependent on the size and location of the delamination. Once the plate buckles, either in local or global mode, the delamination propagates and the instability increases [77]. In bending case, the presence of delamination can reduce the bending rigidity drastically as the second moment of area decreases with the third power of thickness. In addition, load carrying capability from undamaged part to damaged part is seriously impaired because the delaminated part loses its ability to transfer interlaminar shear stress. If the delamination is located in the compression side, the sublaminates above the delamination can buckle. Fibre breakage can be fatal to the load carrying capability since fibres represent the major load carrying path, seriously deteriorating structural performance under tensile loading [77].

4.3.1 Residual strength

In order to assess the residual properties of a composite structure in the presence of specific damage modes, the applied loading type the structure sustains should be distinguished. It has been reported that tensile, compressive, and flexural strengths can be reduced significantly in the presence of impact damage [92, 93]. In order to design damage tolerant structures, considerable amount of research has been aimed at the study of the residual strengths under in-plane loads, however, those under bending loads have not received much attention [94]. In this section, the residual strengths under tension, compression, and bending will be reviewed.

4.3.1.1 Residual tensile strength

The residual tensile strength of impacted plates depends on the impact energy [48]. As shown in Fig. 4.6, there is no strength reduction in region I, owing to the fact that the damage is produced when the impact energy reaches a threshold value. In region II, as the damage magnitude increases, the strength reduces rapidly. The strength reduction is constant in region III because of clean penetration caused by high velocity impact. It can be seen that the strength reduction in region II may be higher than that of region III. This is because of the damage propagation over a larger area. Residual tensile strength is mainly affected by the amount of fibre damage as the fibres sustain the major part

of the tensile load. In tensile loads, delamination does not play an important role. An estimation of the tensile strength after impact can be obtained from the net-section of unbroken plies [84].

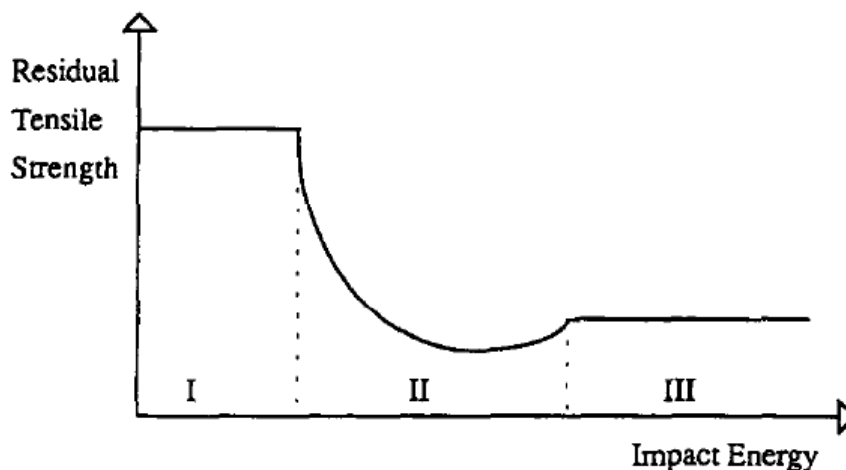


Figure 4.6: Characteristic residual strength versus impact energy curve [48].

4.3.1.2 Residual compressive strength

The compressive strength of composite laminates is generally much lower than the tensile strength. Furthermore, the compressive strength reduction in damaged laminates is much higher than the reduction of tensile and other strengths [95]. Even BVID can induce up to 50% strength reduction under compressive loads [48].

Low velocity impact can generate delaminations. Local instability resulting from delaminations is the main mechanism in compressive strength reduction [96]. As discussed in section 4.2.1.2, local loss of bending stiffness in the plate where the delamination has occurred may cause initial buckling and post-buckling, leading to final failure at loads below the design level. Another cause of local instability can be the change of local fibre curvature in the impacted area [95]. Such a local curvature change may create asymmetric loading under compression.

Compression after impact (CAI) tests are commonly used to examine the residual compressive strength of composite laminates which have been subjected to impact. CAI test needs to prevent global buckling while allowing local buckling. Therefore, it requires complex antibuckling guide having a big window for local buckling, resulting in a new problem of increasing global flexural stiffness of a specimen [48].

4.3.1.3 Residual flexural strength

Not much work has been done on the characterization of residual flexural strength [48]. Generally, bending test creates more complicated stress field than in-plane one, so the analysis of residual strength is more difficult.

Residual flexural modulus and strength of impacted glass/epoxy specimens were investigated in [97]. Three point bending tests were carried out to measure flexural modulus and strength. The flexural properties reduced in varying degrees with increasing impact energy. As the impact energy increased, the flexural strength reduced by up to 30%, whereas the flexural modulus reduced less than flexural strength. The residual properties as a function of the impact energy are shown in Fig. 4.7. The residual flexural strength was more sensitive to the localized impact damage than residual flexural modulus, since the flexural strength was obtained from the ultimate force that the specimen could resist, whereas the flexural modulus was measured in a linear elastic region of force/deflection curves.

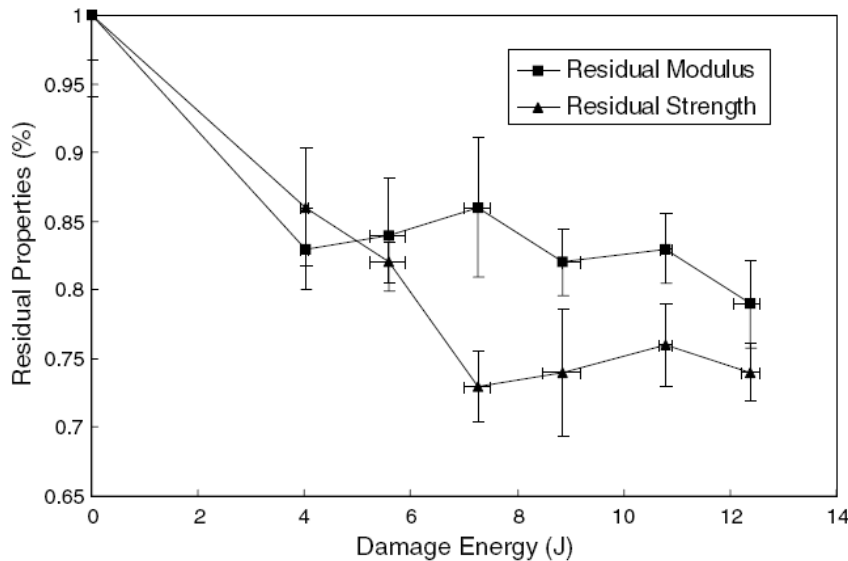


Figure 4.7: Residual flexural properties as a function of absorbed impact energy [97].

A similar experimental result was observed in [53]. In ductile glass/epoxy specimens, both flexural modulus and strength decreased as low-velocity impact energy increased. However, in brittle graphite/epoxy specimens, no reductions were observed until complete failure.

4.3.2 Residual stiffness

In this section, residual in-plane and flexural stiffnesses will be reviewed. In the literature, few investigations have been performed on the stiffness reduction resulting from delamination and fibre breakage, although there has been a considerable amount of research on the stiffness reduction due to matrix cracking.

4.3.2.1 Residual in-plane stiffness

4.3.2.1.1 Stiffness reduction due to matrix cracking A significant amount of research has been carried out for the prediction of the degradation of elastic properties in laminates due to matrix cracking [98]. Cross-ply laminates comprised of two different fibre orientations (0° and 90°) have been commonly analyzed in many studies on elastic properties reduction. Matrix cracking is the first damage mode occurring in cross-ply laminates under uni-axial loading. Transverse matrix cracks are intralaminar cracks which develop parallel to the fibres. As the applied strain increases, more transverse matrix cracks occur. The severity of matrix damage can be characterized by crack density (the number of cracks per unit length in the loading direction). The degradation of elastic properties such as longitudinal Young's modulus and major Poisson's ratio is related to the crack density.

Several approaches have been proposed for the modeling of modulus degradation resulting from matrix cracking. Those have adopted several stress analysis methods to calculate the stress distributions in the cracked laminates. Among them, two approaches are mainly used [98]. The first one is the shear-lag approach and the other is the variational approach. Both approaches can predict the reduction of elastic properties with reasonable accuracy. However, the major limitation of these approaches is that they can be applied to only limited lay-ups of laminates.

4.3.2.1.1.1 Shear-lag approach Shear-lag analysis utilizes stress-transfer model. In the case of cross-ply laminates, the axial stress in the 90° layer including matrix cracks is transferred to adjacent undamaged 0° layer by shear stress in a thin interface layer [26]. The shear-lag equation is based on the force equilibrium of a material element in the layer including the transverse cracks. Accordingly, the normal stress change in the cracked layer is related to the shear stress, and the stress distribution can be derived from the equation. Displacement field is obtained from the stress distribution, and the stiffness reduction derived from the displacement field. Different modifications of the shear-lag model are currently used, but the basic assumptions used in the model are same [98]. The

assumptions are that the shear layer is an isotropic resin-rich layer which separates the outside layer and 90° layer of the laminate, and the elastic properties of this layer are matrix properties, but the thickness of the layer needs to be assumed. By using shear-lag analysis, a correlation has been established between stiffness reduction and transverse crack density in the 90° ply [99]. Shear-lag model is simple and produces reasonably good predictions of stiffness reduction with closed form solutions, however, accurate results cannot be obtained [100].

4.3.2.1.1.2 Variational approach The variational approach is based on the principle of minimum complementary energy. It was first employed by Hashin [101] for the analysis of stiffness reduction of cross-ply laminates containing matrix cracks. Normal stress distribution through-the-thickness of the cracked layer was assumed constant and complementary energy was defined through the stress fields in the layer. An approximation of stress fields was found through a minimization procedure of the defined complementary energy. The variational approach was improved by including a non-uniform stress distribution through-the-thickness in the layer [102]. The variational approach is mainly limited to the analysis of symmetric cross-ply laminates owing to complicated calculation of the stress fields in a cracked laminate [100].

4.3.2.1.2 Stiffness reduction due to delamination induced by matrix cracking Compared with the extensive efforts regarding stiffness reduction due to transverse matrix cracking, the stiffness reduction owing to delamination has not yet been thoroughly investigated [103].

Several authors have extended the shear-lag analysis to evaluate axial stiffness degradation due to delamination induced by transverse cracking. Ref. [50] investigated the effects of transverse cracks and delamination on Young's modulus reduction of $[0/90_n/0]$ ($n = 4, 8, 12$) cross-ply laminates by using the shear-lag approach. It showed that the normalized Young's modulus was affected by not only transverse crack density but also delamination ratio. The shear-lag prediction showed better agreement with the experimental results when the laminates had thicker 90° plies including extensive delamination, and the interaction between transverse cracks and delamination was considered. Similar results were reported in [104]. A modified shear-lag approach was used to predict Young's modulus reduction due to transverse cracking and local delaminations in balanced $[\pm\theta_m/90_n]_s$ laminates. They derived a closed-form solution for the reduced properties of the damaged 90° layer and showed that the modulus reduction was dependent on cracking density and relative delamination area. In another study [103], numerical shear-lag analysis showed

that transverse crack tip delaminations in $[\pm\theta/90_4]_s$ laminates caused reduction of not only axial modulus but also shear modulus and Poisson's ratio. Depending on the value of θ , each modulus reduced in varying degrees. The axial modulus showed the smallest reduction when θ equals 0° (cross-ply) and the reduction increased as θ increased. On the other hand, the degradation of shear modulus and Poisson's ratio was the largest in cross-ply laminates and the smallest when θ was 45° .

Some authors have shown that the laminate stiffness reduction is related to matrix crack tip delamination area using plate theories such as classical lamination plate theory [105] and first-order shear deformation theory [106].

4.3.2.1.3 Stiffness reduction due to impact damage Some experimental results concerning elastic modulus degradation due to impact damage were shown in [107]. Quasi-isotropic carbon/epoxy laminates with 2.2 and 6.4 mm thickness were used for the impact tests. The applied impact energy was 8J for 2.2 mm laminates and 30J for 6.4 mm laminates. Mechanical testing was performed to measure strains. Measurement of strains was obtained by extensometers and strain gauges in the strain range of $\pm 0.15\%$. Due to the low strains, local delamination buckling did not occur, so the stress was directly proportional to the strain. From the slopes of the stress-strain curves, the elastic moduli were obtained. In the compression tests, global buckling was prevented by using anti-buckling guides. It showed that the elastic modulus reduction due to impact damage was mainly affected by the amount of fibre breakage in both tension and compression. Higher elastic modulus was observed in compression than in tension because the layers with broken fibres could support some compressive load. It concluded that the effect of delaminations on the elastic modulus was negligible in both tension and compression.

In other research [108], the reduction of residual mechanical properties depending on impact energy amount was investigated. In this case, cross-ply glass/epoxy laminates with 2.24 and 6.69 mm thickness were used. Compression after impact (CAI) test was performed to determine residual compressive stiffness (the slope of a force-displacement curve from CAI test) and residual compressive maximum force (the force to cause buckling, *i.e.* the peak force of the force/displacement relation) of impacted specimens. Experimental results showed that the reduction of residual compressive stiffness was not significant as impact energy increased, whereas residual compressive maximum force decreased rapidly. The given reason was that there was no local buckling due to delamination during the measurement of compressive stiffness, while the residual compressive maximum force was greatly affected by the presence of local buckling. They concluded that local buckling induced by delamination plays a very important role in residual properties degradation

under compressive loads.

4.3.2.2 Residual flexural stiffness

Although the bending stiffness is closely associated with critical buckling load, the main concern in compressive failure mechanism, very few attempts have been devoted to investigating the bending stiffness reduction of damaged composite laminates.

Post-impact residual flexural properties of GRP materials were evaluated using three point bending tests [97]. As shown in Fig. 4.7, the residual flexural stiffness was less affected with increasing impact energy than residual flexural strength. The maximum reduction of flexural modulus was approximately 20%. The lower sensitivity of flexural modulus to localized impact damage was explained by the fact that global properties such as modulus are less affected by localized damage. The modulus was calculated in the initial linear part of force/deflection curve. Other research [53] reported that flexural modulus decreased as low-velocity impact energy increased in ductile glass/epoxy specimens, however there was no reduction until the point of complete failure in brittle graphite/epoxy specimens.

4.4 Damage detection methods

As reviewed above, various damage modes in composite laminates can significantly deteriorate their load bearing capabilities. Generally, damage is produced in a structure during in-service operation. This means that the damage location and the characteristics of damage modes are unknown *a priori* [60]. In the case of low-velocity impact especially, damage is embedded in the substrate, and barely visible on the surface. Estimation of residual properties may be possible when the geometry (size and location) and type of the damage are known. In order to assess the integrity and reliability of composite structures, efficient techniques which can detect damage and characterize adverse ‘changes’ due to the damage are required [109].

On the average, 27 % of aircraft operation costs are spent on inspection and repair [109]. Accordingly, the development of cost effective techniques for early detection of damage has become essential for manufacturers and operators. Damage detection in composites is more complicated than that of metals owing to the anisotropy of the material and complexity of damage modes [109]. Furthermore, acoustically, thermally, and electrically the heterogenous nature of composite materials complicates the application of conventional damage detection techniques.

Various non-destructive testing (NDT) methods have been developed to detect damage in composite laminates [52, 59, 110]. All the techniques have their own advantages and disadvantages. In the choice of a damage detection technique, the factors one should consider are sensitivity, resolution, and its range of applications [111]. In the following, conventional NDT techniques will be reviewed briefly.

4.4.1 Visual inspection

Visual inspection is the most common NDT technique because it is simple, quick, and cost-effective [52, 110]. This method is useful for the detection of surface and near-surface damage. However, visual inspection does not reveal hidden internal damage like BVID, since usually there is no indication of damage on the surface. Recently, several illumination techniques have been developed to improve visual inspection capability.

4.4.2 Ultrasonic inspection

Ultrasonic inspection utilizes various properties of ultrasonic waves for damage detection [52]. This technique is often called A-, B-, and C-scans. A-scan measures a single point, B-scan a line, and C-scan is a collection of B-scans for surface measurement. C-scan is widely used in the inspection of composite materials. Either pulse-echo mode or pitch-catch mode can be used for the test. The pulse-echo mode uses one probe as an actuator and sensor, whereas the pitch-catch mode needs two probes, one as an actuator, and the other as a sensor. The actuator sends ultrasonic waves through the material and the sensor receives the transmitted waves. Conventional ultrasonic inspection technique requires gel couplants between probes and specimens due to the acoustic impedance mismatch between air and solids. Usually, water is used as a couplant in the inspection of composite plates, so the specimens need to be immersed in water. Recently, laser induced ultrasonic inspection technique which can use air as a couplant was developed. However, the sensitivity is relatively poor owing to acoustic impedance mismatch between air and the specimen, and owing to ultrasonic wave attenuation in air. Ultrasonic inspection technique is very sensitive to small damage and able to detect deep delamination. The difficulties of the technique are coupling and sensitivity to geometry. Also, the detection time is a significant factor since the inspection requires time-consuming scanning.

4.4.3 Eddy current

The eddy current technique performs inspection by identifying electromagnetic impedance changes resulting from strain in the specimen [52]. When alternating current is applied to the eddy current probe (coil), magnetic fields are created in and around the probe. The eddy currents are closed loops of current in the target material induced by the magnetic fields from the probe. This process is called electromagnetic induction. If there is damage in the material, the eddy currents are distorted. The eddy current technique is easily implemented and relatively inexpensive. Nonetheless, it requires a large amount of power and the data acquired is not easy to interpret. In addition, this technique is more appropriate for metallic components than for composite ones.

4.4.4 Acoustic emission

Acoustic emission (AE) is released elastic energy caused by fractures in the material [52]. The sources of AE may be matrix cracking, fibre breakage, fibre debonding, and delamination in composite materials. The emitted energy due to damage is recorded by sensors such as accelerometers, piezoelectrics or microphones. The multiple arrays of sensors can locate the damage by triangulation. AE can be applied to large structures because it is not sensitive to geometry. However, it is a passive technique which requires load, and its sensitivity to small damage is poor. In addition, AE only detects progressive damage owing to its nature of detection.

4.4.5 Radiography

Radiography utilizes gamma rays or X-rays [52]. When the rays penetrate a specimen, some energy is absorbed by the specimen. The amount of absorption of the rays is recorded on X-ray film. Radiography is easy to interpret and fast inspection is possible. However, it is not sensitive to small damage and requires radiation shielding for safety issues.

4.4.6 Thermography

Thermography utilizes thermal conductivity and emissivity of a specimen [52, 59]. The specimen emits infrared radiation depending on its temperature and this radiated energy is recorded into thermal images. It can detect defects which are located near the surface of composite laminates effectively. Thermography can cover large areas and fast monitoring is possible, however, it is relatively expensive and not sensitive to small damage. In

addition, it has difficulty in detecting deep-lying defects in thick laminates because of heat diffusion.

4.4.7 Lamb waves

Lamb waves are guided ultrasonic waves which propagate in plates with parallel free boundaries [112]. Lamb waves can propagate over a long distance and examine a broad area quickly. Propagation of Lamb waves is dependent on vibration modes of the waves as well as density and elastic material properties of the plates. When propagating Lamb waves meet an obstacle, mode conversion may happen. By interpreting the mode conversion, location and size of damage can be detected [113]. In addition, with various Lamb modes, not only surface damage but also internal damage can be identified. The propagation of Lamb waves in anisotropic material is very complicated, so the interpretation may not be easily performed [112].

4.4.8 Optical methods

The principles of optical methods such as shearography and ESPI were described in section 1.1.1. Strain fields on the surface of a specimen can be measured from the difference between undeformed and deformed states. Damage may induce reduction in local stiffness. The reduced stiffness will redistribute the strain fields where the damage has occurred. Identification of the abnormalities in the strain profiles leads to the detection of damage. Shearography and ESPI have high sensitivity and are able to inspect relatively large surface in real time. Nevertheless, these methods are expensive and require loads in detection (passive methods).

An example of shearography image for delamination is shown in Fig. 4.8 [114]. In this case, heat loading was used for the shearography test. Since shearography presents gradients of deformation, a typical detection image of delamination is a ‘butterfly pattern’. Though the in-plane damage location was detected accurately, the exact depth of delamination was not determined. Some researchers identified not only the planar location but also the depth of delamination using ESPI and finite element model updating [115].

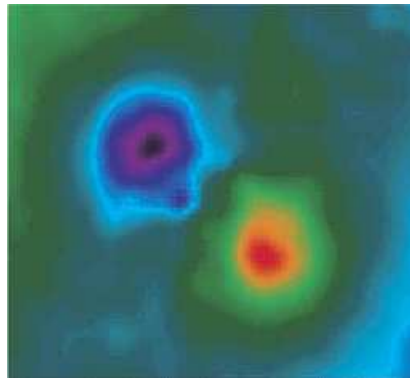


Figure 4.8: Shearography image of delamination [114].

4.4.9 Vibration-based analysis using eigenfrequency and mode shapes

Extensive studies have been undertaken on vibration-based damage detection techniques [116]. The vibration-based methods utilize modal parameters, for instance, eigenfrequencies, mode shapes, and damping properties. These parameters are dependent on the physical properties of a structure such as stiffness. Therefore, the changes of the physical properties owing to damage will affect the modal parameters. For instance, the presence of delaminations decreases natural frequencies and increases vibratory damping.

Most of the NDT techniques require accessibility to the structural components to be inspected. However, vibration-based technique can assess global structural integrity without direct access to the components since it examines the changes of global indicators. Thus, this technique can be applied to very large and complicated structure. Conversely, the vibration-based techniques are not very sensitive to local defects. Some authors proposed methods which are more sensitive to local damage. These methods utilized curvature fields obtained from mode shapes by differentiation [117]. The selection of the most changed mode shape due to damage led to the best localization of the damage.

4.5 Conclusion

Although various damage detection techniques have been developed, most of them provide limited and mostly qualitative information regarding damage modes and distributions. Therefore, it is of primary importance to develop analytical tools which can assess whether the detected damage is critical or not for the life of the component. In order to

effectively diagnose the reliability of the damaged structure, both qualitative and quantitative information concerning the damage should be addressed. Consequently, the tools should have the ability to quantify the adverse ‘changes’ due to damage. In this case, the key question is which ‘changes’ we need to look for.

As reviewed in sections 4.3.1 and 4.3.2, various damage modes in composite laminates can seriously deteriorate the residual strength and stiffness. Thus, the evaluation of residual strength and stiffness in a quantitative sense would be a good choice for the assessment of reliability in composite structures. Nevertheless, measurement of residual strength during damage development is not practical because the destruction of the test specimens is involved [118]. Measurement is not repeatable for one specimen. Furthermore, comparison of damage states between two specimens may be difficult since the scatter on the strength is large compared to that on the stiffness. On the other hand, measurement of residual stiffness can be done repeatedly and continuously during damage development without destruction of the specimen. Damage state in laminates may evolve from matrix cracking to delamination under service loading. Gradual stiffness reduction due to damage evolution can be also measured since the measurement does not disturb the damage development. Accordingly, residual stiffness can be a very promising parameter which can be used for the evaluation of structural reliability non-destructively.

However, as discussed in section 4.3.2, the global stiffness is not sensitive to local damage. The more important parameter which needs to be considered is the local stiffness reduction. The local instability induced by local stiffness reduction plays an important role in failure mechanism of composite laminates through stress redistribution. Therefore, accurate evaluation of actual state and prediction of final failure require the identification of local stiffness reduction of the damaged zone rather than the global stiffness reduction.

Different techniques have been developed to locate damage, but the evaluation of the local loss of stiffness remains an open problem. Classical measurement techniques such as strain gages may be applied to the measurement of local stiffness reduction. However, the contact procedure inevitably induces deviation in measurement and it is very difficult to measure large area with limited number of sensors, if not impossible. The present study aims at taking advantage of the availability of non-contact full-field measurements and adapted inverse identification procedures in order to not only locate the damage but also to identify the local stiffness reduction of the panel. In Chapter 5, the procedure will be validated on simulated measurements and experimental results will be given in Chapter 6.

Also, because the geometry will be very simple, this work is also aimed at providing an experimental tool to validate impact damage models, avoiding the tiresome procedure of

cutting a multitude of tensile coupons for impacted plates.

Chapter 5

Identification of the local stiffness reduction Part I: simulation

5.1 Introduction

As discussed in Chapter 4, the damage mechanisms in composite laminates are very complicated and the various damage modes can cause significant degradation of the residual strength and stiffness of composite structures. Many experimental investigations have been performed to understand these mechanisms and predict the residual properties. However, experimental testing has limited applications with specific geometries of specimens and loading types. In addition, it is not practicable in terms of time and expense to consider the effects of a wide range of variables [119]. Therefore, it is required to predict the effects of damage on the performance of composite structures analytically or numerically. These methods can provide valuable insight for the efficient design of damage-tolerant structures.

Generally, solutions based on exact analytical methods which satisfy all governing equations of the linear elasticity theory are not feasible when the shapes of specimens, the applied loading, and boundary conditions are complicated [60]. Only limited closed-form analytical solutions have been developed for specific geometries, lay-ups, loading, and boundary conditions [119]. This leads to the employment of approximate models. Efficient techniques using approximate models can reduce the number of expensive experiments. The approximate models which have been developed for the modeling of damage in composite laminates generally fall into one of two categories. The first one is the finite

element (FE) approach and the second is the plate theory approach. However, both are complementary since many numerical FE models are based on plate theory [120].

In this chapter, several techniques for the efficient FE modeling of damage in composite laminates will be reviewed and the proposed methodology in Chapter 2 will be validated on simulated FE measurements for the case of the intralaminar and interlaminar damage.

5.1.1 Modeling scale levels

For the modeling of damage suitable for a particular purpose in composite laminates, levels of length scale should be considered. Generally, three length scales can be used for the analysis of heterogeneous materials [121, 122]. Each length scale is interacting with each other. The first length scale is the micro scale. The micro scale approach considers all the heterogeneities in the constituents of the composite material; the constituents are fibres, matrix, and the fibre-matrix interface. The second scale is the macro scale which treats the whole structure as a completely homogeneous continuum. This scale is the global length scale and associated with the entire laminate thickness. The global behavior is described by an anisotropic constitutive law. Global buckling or behavior of the whole plate can be modeled with this scale. In both length scales, the ply itself or lay-up of the plies is not considered as the basic entity. Consequently, an intermediate scale between micro and macro scale is required. It is called meso scale. The meso scale treats the ply as the basic object for the description of composite laminates. Thus, this length scale is related to the lamina thickness and very useful for the modeling of damage in composite laminates, as the damage modes are either intralaminar (fibre breakage, matrix cracking), or interlaminar (delamination). At this scale, the ply is considered as homogeneous, and the properties of the ply as orthotropic or transversely isotropic in its principal axes.

In order to model the damage with the meso scale, parameters which can characterize each damage mechanism are required. These parameters should have the capability to describe the local effects due to the damage in each ply or in the interface between the plies. Then, the equivalent homogeneous behavior of the damaged ply or cracked interface can be described by a homogenization method. By analyzing the stress fields in each ply of the laminates subjected to an external loading, the evolution of damage in the ply or in the interface can be predicted. Although the meso scale is important in the damage modeling, its effect on macro scale should be analyzed, so that the global behavior can be determined by using finite element simulation or appropriate plate theories.

5.1.2 Finite element (FE) approach

The finite element (FE) approach has many advantages over experimental testing [119]. It can be applied to simulate models having various shapes, sizes, material properties, loading, and support conditions without the expense required by experimental testing, meaning that the FE approach is very powerful and efficient. Nonetheless, the accuracy and reliability of the results from the FE simulation depend on many parameters such as governing theories, the level of structural detail, mesh refinement, material parameters, and correct use of boundary and loading conditions.

5.1.2.1 3D/2D

In reality, any failure mode (fiber breakage, matrix cracking, and delamination) induces three-dimensional (3D) stress states [119]. The FE model representing realistic damage in composite laminates should have the capability of describing the 3D stress state. Consequently, a 3D FE model is a natural choice for the FE analysts owing to its ability of 3D simulation. In spite of this advantage, usually, many layers of brick elements through the thickness are required for the 3D models [123]. If the interest lies in the lamina microstructure, the relative dimension of the lamina thickness is very small compared to the structural dimension. This requires very fine finite element mesh size for the analysis of the structure due to aspect ratio considerations [60]. Thus, the size of finite element models required for accurate analysis makes the FE approach to be prohibitively expensive. An example of a 3D model for the analysis of delamination effect is shown in Fig. 5.1.

To reduce the computational expense of the 3D models, alternative numerical models have been developed using two-dimensional (2D) plane strain FE models [87, 125]. This approach is very efficient for the analysis of beam-like structures owing to its simplicity. Nonetheless, this kind of simple plane strain FE model may not be sufficient to accurately model the delamination damage in the laminated plates. In order to overcome the complexity of 3D models and improve detailed stress analysis of 2D models, some researchers have employed quasi-3D models utilizing plate or shell elements [126, 127]. In most of the FE softwares, plate or shell elements are offered as built-up structures, yet these elements do not precisely describe the individual plies, and transverse shear stress components are not analyzed well with these elements. Accordingly, modeling with conventional shell elements may cause difficulty in representing delamination [47]. This issue will be discussed further in the next section. Other FE analysts developed a shell/3D modeling technique which utilizes solid elements in the vicinity of the delamination crack tip and plate or shell elements in the remainder of the structure [128].

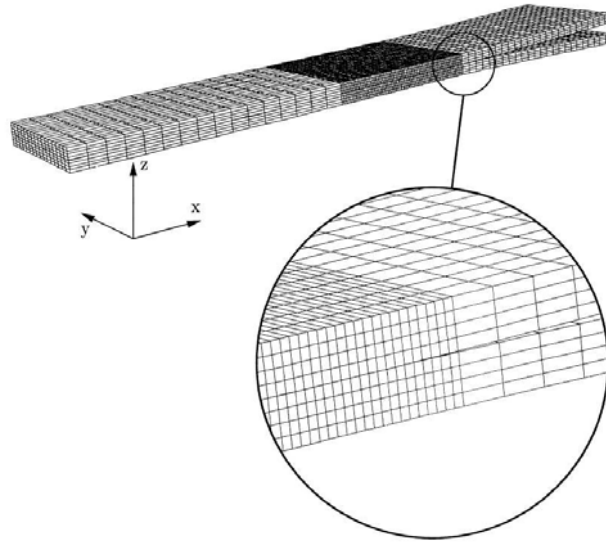


Figure 5.1: FE model of DCB experiment [124].

5.1.2.2 Damage modeling

5.1.2.2.1 Intralaminar damage In the modeling of intralaminar damage, such as matrix cracking and fiber breakage, the most common approach is to substitute the damaged material with an equivalent material of reduced elastic properties [94, 129]. This approach considers the effect of damage modes in an average sense with meso or macro scale modeling, so it does not describe specific damage modes accurately. Initially, the problem is to determine the degraded properties of the damaged material. Most property degradation models can be organized into three groups [130]. The first is the total discount approach, which assumes the stiffness of the damaged material as zero. However, the actual damage size can be very small compared to the element size used in FE analysis. Assigning zero stiffness for the whole element may underestimate the actual stiffness of the damaged material [94]. The equivalent material properties of damaged element may be somewhere between the undamaged element properties and zero. Consequently, this approach has some limitation in applications. The second approach is the limited discount method, which considers the stiffness reduction depending on the specific damage mode. For instance, the longitudinal stiffness is reduced due to fibre breakage and the transverse stiffness owing to matrix cracking. In Ref. [131], transverse modulus E_{yy} and Poisson's ratio ν_{xy} were set to zero for matrix cracking, whereas longitudinal modulus E_{xx} and shear modulus G_{xy} remain unchanged. In this case, the fact that the FE analysis should not violate the thermodynamic constraints on the elastic property values must be taken into account, since the constitutive parameters are required to satisfy the

law of conservation of energy [94]. The last approach is the residual property method. In this method, stiffness reduction can be estimated by using continuum damage models. The calculation of the stiffness reduction may be very complicated using this approach, because damage accumulation during loading should be considered by damage evolution laws.

5.1.2.2.2 Interlaminar damage Delamination is a structural failure, so generally its effect on load-carrying capability of a structure is not described well with the property degradation models as used in the intralaminar damage [123]. For instance, the behavior of a double cantilever beam (DCB) or an end notched flexure (ENF) specimen cannot be predicted with these models. In order to model delamination, some researchers have developed a sublaminar model utilizing plate or shell finite elements. In this model, a laminated plate consists of several separate shell elements in the through-the-thickness direction such that each sublaminar is connected by interface elements having large stiffness but no thickness. With this modeling method, the delamination damage can be simulated by removing the interface elements [123].

Inter-penetration or overlapping of adjacent elements is an important issue which needs to be taken into account in the FE modeling of delamination [132]. The overlapping of neighboring sublaminates (thin delaminated layers) should be avoided since it is physically inadmissible (only possible as a numerical solution). In 3D analysis, special techniques such as contact analysis, double coincident nodes, and artificial springs can be used to prevent inter-penetration. When the shell elements are used to describe delamination damage, contact node pairs connected by a virtual beam element or artificial elements such as rigid or gap elements can be utilized to avoid the overlapping of shell elements. The rigid elements can sustain both tensile and compressive loads, but the gap elements only compressive load.

As mentioned in section 4.2.1.1, strength analysis and fracture mechanics have been used to model delamination onset and propagation. Generally, strength analysis is applied to predict the initiation of delamination and fracture mechanics to evaluate the propagation of the existing delamination. For the FE analysis of the delamination onset and propagation, one of the most common techniques is cohesive zone modeling combining the advantages of strength analysis and fracture mechanics [123, 133]. In this technique, the interface element is treated as a softening material which has a traction/displacement curve. Initially, the interface element is undamaged. The initiation of delamination is related to the maximum traction on the curve. For example in mode I, once the traction over the interface is equal to the interlaminar tensile strength, loss of cohesion occurs,

and the cohesion gradually decreases until a stress-free surface is generated. If the area under the softening curve reaches the critical fracture energy (strain energy release rate), the traction is reduced to zero and the delamination propagates. The advantage of this method is that it does not need initial delamination, however, it requires a very fine element mesh for convergence. On the other hand, some researchers have employed horizontal and vertical non-linear spring elements between the plies to model the initiation and propagation of delaminations [134]. When the threshold force reaches the interlaminar strength, the stiffness of spring decreases and the spring opens fully to physically represent delamination initiation and growth.

5.1.3 Plate theory approach

Laminated composite plates are widely used for many basic structural applications. Naturally, many researchers have used equivalent 2D plate theories such as classical lamination theory (CLT) and first order shear deformation theory (FSDT) to analyze the behaviour of such structures [135]. Basically, the CLT and FSDT were derived from integration of the virtual work statement through the laminate thickness, so the heterogeneous laminate is treated as a single homogeneous layer [28]. Due to the homogenization characteristics resulting from equivalent stiffness and inertia properties in the integral sense, the CLT and FSDT are not able to describe the kinematics of delamination with their original formulation. Some authors modified these plate theories to represent delamination. For instance, delamination effect was included by using modified classical Kirchhoff displacement fields [136]. A jump discontinuity using Heavyside step function was added to the original displacement fields. In Ref. [137], the first-order shear deformation theory was used for the analysis of a local delamination. A delaminated plate with $[+25/-25/90_n]_s$ lay-up was modeled with a sublaminar approach using the delamination interfacial surface. In the case of simple geometry, the plate theory approach can be used as an alternative to the FE analysis. However, in complicated geometry, detailed stress analysis, such as stress concentration or transverse stress distribution owing to delamination cannot be obtained with this approach [47, 138].

5.2 Results and discussion (Intralaminar damage)

In this study, the meso scale will be employed to simulate behaviour using FE models representing the intralaminar and interlaminar damage. Quasi-3D models utilizing thin shell elements will be used for the efficient FE modeling of damage.

Before moving on to the topic of damage modeling and detection, it is worth discussing the basic mechanisms of intralaminar damage and interlaminar damage that induce the loss of bending stiffness from the meso scale modeling point of view. The bending stiffness is defined as EI in the case of a homogeneous and isotropic material where E is the elastic modulus (Young's modulus) and I the second moment of area. The loss of bending stiffness can be caused by either reduction of E or reduction of I . In terms of meso scale, the intralaminar damage contributes to the reduction of E , while the interlaminar damage to the reduction of I since the interlaminar damage is a structural failure (a failure form of the laminate, not of the lamina in composite laminates). Strictly speaking, the intralaminar damage is also the structural failure at the micro scale level. In addition, even in meso scale, stiffness reduction due to the intralaminar damage is related to I as the through-the-thickness location of the damaged layer affects the bending stiffness. Nevertheless, the above discussion is useful to understand the damage mechanism.

In this section, the proposed methodology in Chapter 2 will be validated on simulated measurements for the case of the intralaminar damage. The intralaminar damage modes include matrix cracking and fibre breakage as reviewed in Chapter 4. On the other hand, the near-the-surface delamination having a bulge zone (the sublaminates above delamination buckles locally) can also be considered as intralaminar damage, if the delamination is located at the compression side of the specimen in bending. As discussed in Chapter 4, the local buckling plays a very important role in properties degradation under compressive loads, thus, proper FE modeling and detection of this damage mode are quite important.

5.2.1 Polynomial parameterization

5.2.1.1 Validation on FE simulated data for isotropic damage

5.2.1.1.1 FE model Simulated measurements were produced using a finite element model of a sixteen-ply unidirectional (UD) carbon-epoxy plate with a rectangular shaped damage characterized by a constant stiffness reduction coefficient. The *ANSYS* 8.0 software was used for the FE modeling. The size of the plate is 190×140 mm², with a nominal damaged area of 50×50 mm². The ply thickness is 0.16 mm, so that the total laminate thickness is 2.56 mm. For the simulation of the damaged plate, two different materials are considered. Type A, the virgin material, has the material properties of a typical carbon-epoxy UD, *i.e.*, $E_{11} = 129$ GPa, $E_{22} = 9.5$ GPa, $G_{12} = 4.7$ GPa, $\nu_{12} = 0.34$. Type B is a dummy material with negligible properties (reduced by 1000). Then, the damaged plies are replaced with the material type B having degraded elastic properties. By controlling the stacking sequence of plies having material types A & B, a particular stiffness

reduction can be obtained. The reduced stiffness will be affected to the square damaged area. As a first validation, symmetric damage is considered to avoid the B matrix effect. Here in this study, the plate is tested in bending according to the load configuration in Fig. 5.2. The size of the FE mesh was selected after a convergence study on the undamaged plate. The mesh was successively refined and the stiffnesses were retrieved from the curvature data using the classical VFM. A mesh with 76×56 elements was finally chosen, corresponding to values of the stiffnesses less than 1% from the reference.

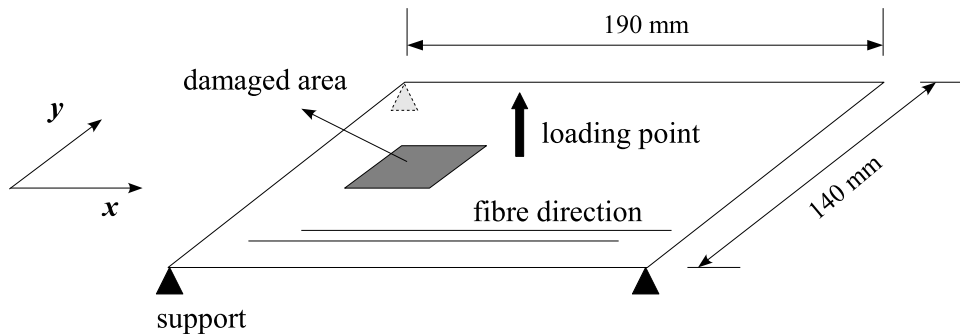


Figure 5.2: Geometry and test configuration of the damaged plate.

5.2.1.1.2 Validation from FE curvature data The initial step was to use curvature data from the FE analysis without considering noise. This data was input in the virtual fields method programme.

Here, the choice of the degree of the polynomial parameterization is important. Indeed, the degree n must be chosen carefully, since if n is too low, the damaged area will not be located properly (or might even be missed altogether if its size is small), and if n is too high, the number of unknowns increases and the whole process becomes unstable. The second important choice is the number of degrees of freedom (DOFs) of the virtual fields. Either piecewise or polynomial virtual fields have been used in the past and in the present case, there is not much difference between the two. From the programming point of view, the polynomial virtual fields method is more simple, therefore, polynomial virtual fields have been selected for the present study. In the choice of the degree, one must ensure that the DOFs are significantly higher than the number of unknowns to have good stability. However, too many DOFs result in unnecessarily large computation time and onset of instability. In order to choose the degree of the polynomial parameterization, detection results with 4^{th} to 12^{th} degree polynomials were examined. As a rule of thumb, one has to keep the number of virtual DOFs about double that of unknowns (*i.e.*, the number of

unknowns for degree 6 is 27, thus 9th order polynomial virtual fields which have 54 DOFs were used). The detection results and the lay-up used in this study are shown in Fig. 5.3. The stiffness reduction for this lay-up is 30%.

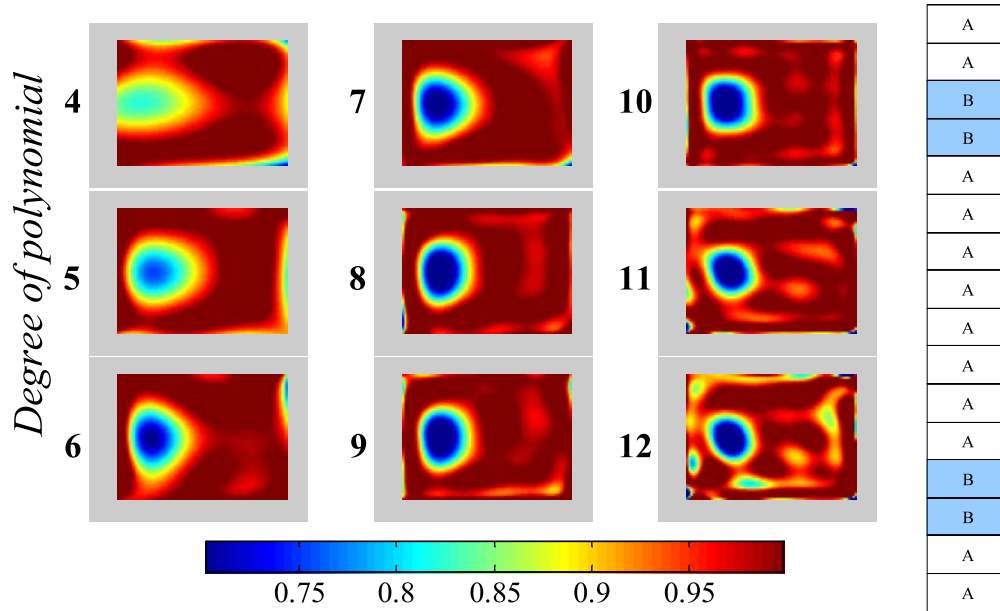


Figure 5.3: Detection results as a function of the degree of the polynomial parameterization.

As can be seen in Fig. 5.3, the 4th degree polynomial is not locating the damaged area accurately and the detection result becomes unstable for the 12th degree. It was found that degrees ranging from 6 to 10 locate the damage satisfactorily. However, it was observed that the effects of inaccuracy for lower degrees and instability for higher degrees were significantly increased when the identification was performed with noisy data. Therefore, degree $n = 8$ was chosen as a suitable compromise, giving a total number of unknowns of 44. In practice, since the location and severity of the damage are unknown *a priori*, a range of values for n should be tested and the corresponding results analyzed. Next, the number of DOFs for the virtual fields was investigated. Degree 12 (91 DOFs) was found to be a good compromise in the present case (44 unknowns). A validation is presented for two different modulus contrasts with the chosen polynomial degree and DOFs. Fig. 5.4 shows plots of the stiffness reduction map.

On the plots, the red color indicates no stiffness reduction (*i.e.*, no damage) and the blue, a reduction of stiffness (damage), with the magnitude of the stiffness reduction on the color bar. It is clear that the method not only picks up the location of the damage (see Fig. 5.2) but also provides a fairly good estimate of the stiffness reduction. It is to be

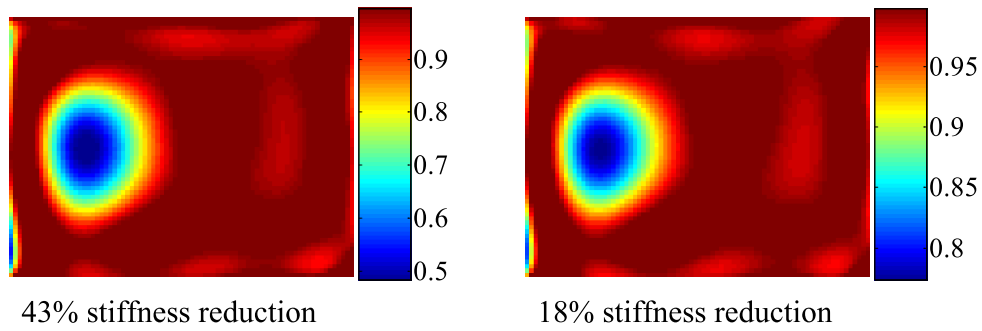


Figure 5.4: Example of identification of the stiffness reduction for different modulus contrast (simulated curvatures).

mentioned here that because a polynomial function is used to locate the damaged area, the damage figure is rather smooth though the actual damaged area is square and the maximum stiffness reduction is overestimated. This effect is well illustrated in Fig. 5.5.

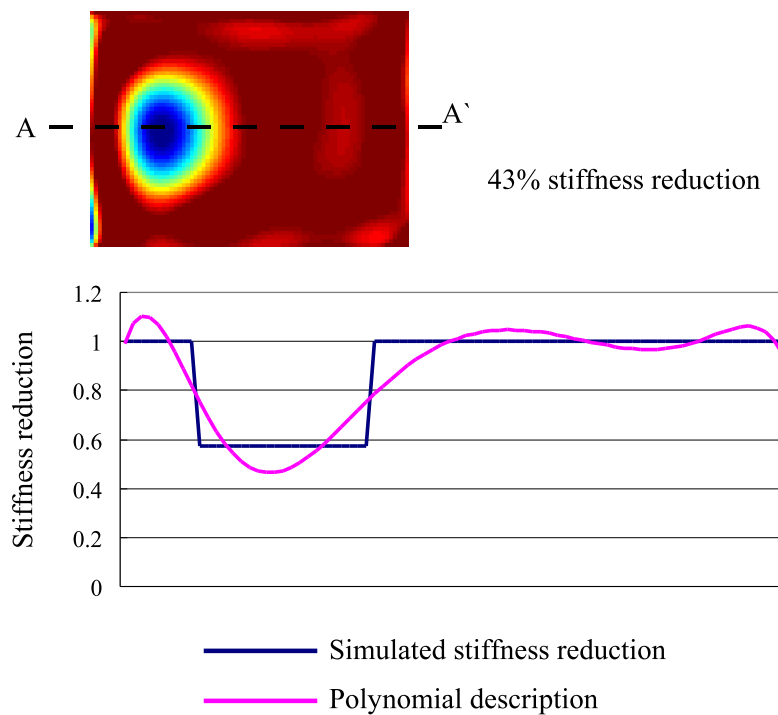


Figure 5.5: Damage description by a polynomial function.

In practice, the evolution of real impact damage will probably be smoother than the one simulated here. This will have to be studied on real impacted plates.

5.2.1.2 Sensitivity study for isotropic damage

5.2.1.2.1 Effect of the smoothing of the slope field The next step is to evaluate the effect of measurement noise in this approach. The same procedure of polynomial fitting and differentiation of these polynomials to the noisy FE slope maps was employed in order to simulate realistically this effect as depicted in Chapter 3.

To choose the degree of the polynomial, an identification with 4 different randomized noise sets was performed using 8th to 18th degree polynomials. These results are shown in Fig. 5.6.

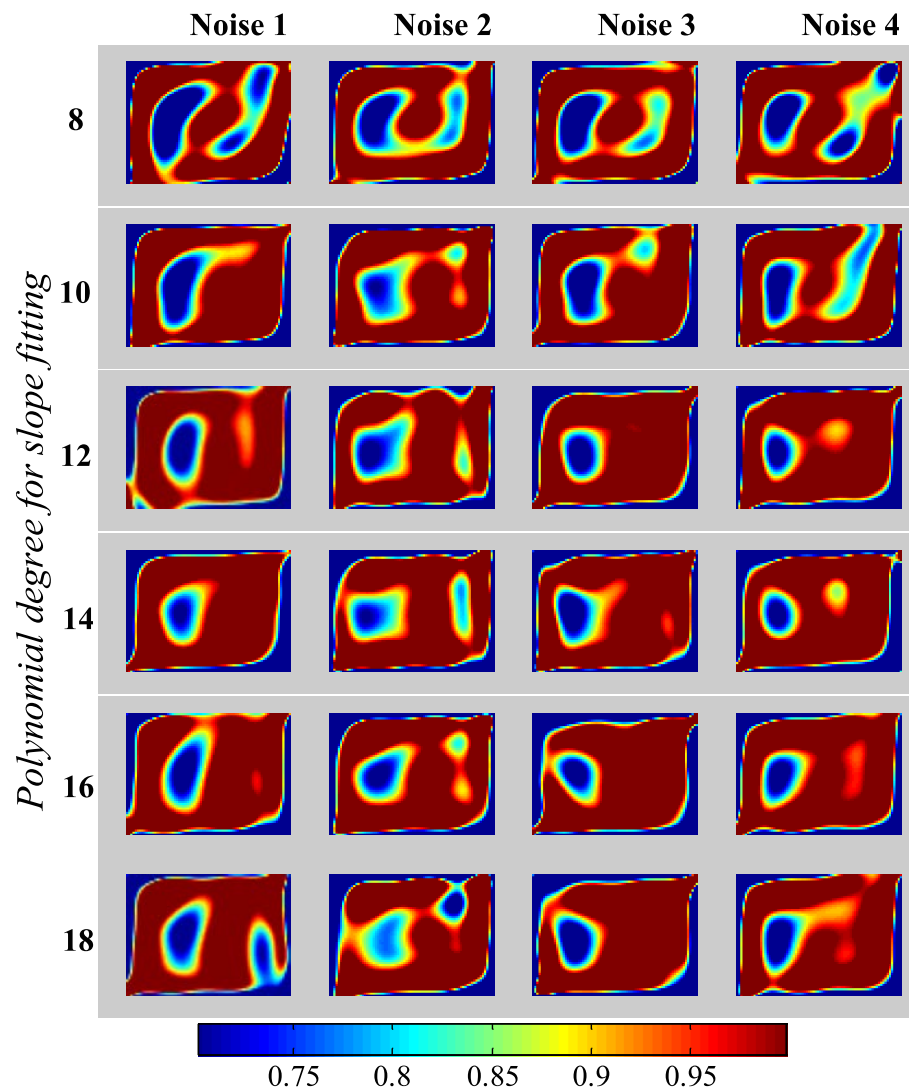


Figure 5.6: Detection results as a function of the degree of the slope curve fitting polynomials.

The stiffness reduction used in this study is 30 %. It has been observed that if the degree is too low, the polynomial curve fitting does not describe the curvature fields well and if the degree is too high, the polynomial fitting amplifies the effect of noise. Thus, 14th order polynomials were chosen here as a compromise to represent the curvature fields. It is also worth noting that the blue areas around the edges are not related to real damage. These effects are caused by the polynomial parameterization of the stiffness reduction (instability at the edges). In addition, there is some ‘reflection’ damage (false damage) in some figures. These are typical for the identification with noise. It is thought that these are artefacts related to the polynomial parameterization of the damage. These effects are enhanced by the magnitude of the measurement noise. Finally, it should be noted once again that since the location and severity of the damage are unknown *a priori* and measurement noise level could be different depending on the measurement technique in a real case, the corresponding detection results should be analyzed depending on the range of values for the polynomial curve fitting degree.

5.2.1.2.2 Effect of boundary conditions The effect of experimental noise is evaluated on four configurations with 2 different types of support location and damage position (left-hand side & right-hand side). These configurations are shown in Fig. 5.7.

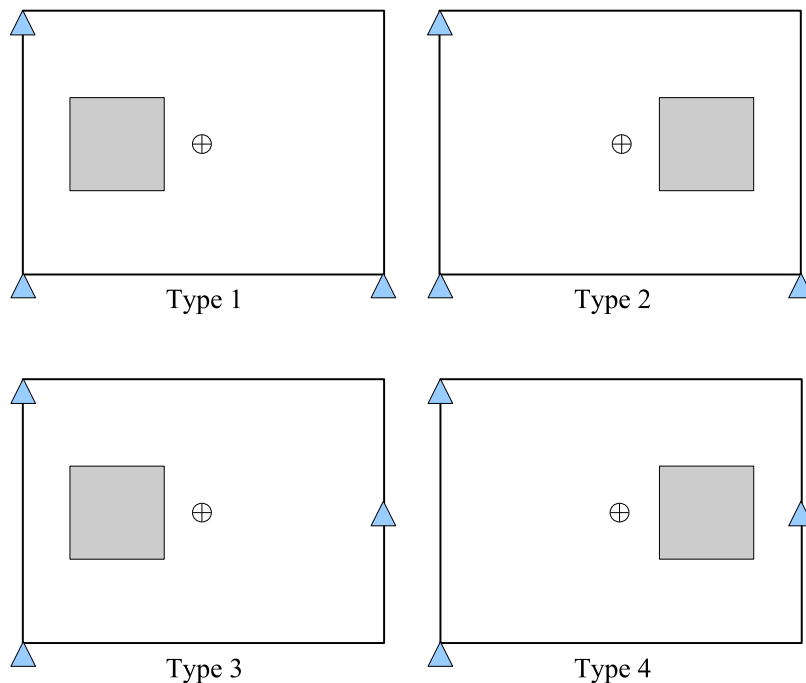


Figure 5.7: Four test configurations for the noise sensitivity test.

The identification was performed independently with three randomized copies of the noise. The results are given in Fig. 5.8. It can be seen that though all the configurations detect the damage, the best is clearly the third configuration. It was shown in [41] that for a homogeneous plate, the load configuration of cases 3 and 4 is better than that of 1 and 2, this seems to hold also for the damaged plate. To analyze this further, a comparison of the relative difference of curvatures between the undamaged and damaged cases was conducted. Fig. 5.9 shows that for the first load case (1 and 2), only κ_{11} is significantly affected by the presence of the damage while for the second load case (3 and 4), all three curvature components are affected, with case 3 more favorable than case 4. In addition, the present laminate, unidirectional carbon/epoxy, represents a very unfavorable situation because of the large anisotropy. Therefore, the strain components are unbalanced, with much smaller κ_{11} than κ_{22} and κ_{66} because of the large E_{11} stiffness. This may also play a role in the results of Fig. 5.9.

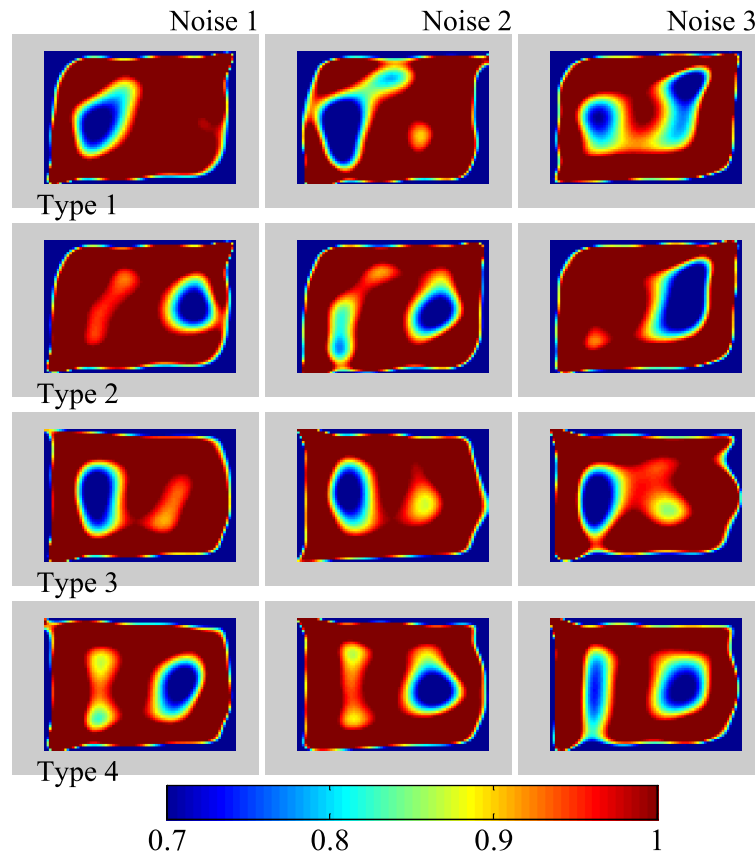


Figure 5.8: Damage identification figures in noise sensitivity test.

Before moving on to the next topic, it should be noted here that the optimization of boundary conditions has limitation as the location and extent of the damage are unknown

a priori in a real case. Furthermore, the boundary conditions cannot be easily changed in most of the practical cases. Consequently, the choice of an optimal load position with a given boundary condition would be a better strategy for damage detection. This issue will be discussed more in section 5.2.2.2.1. For the rest of the study, both type 1 and 3 will be used and compared to further analyze the effects of the configurations on detection.

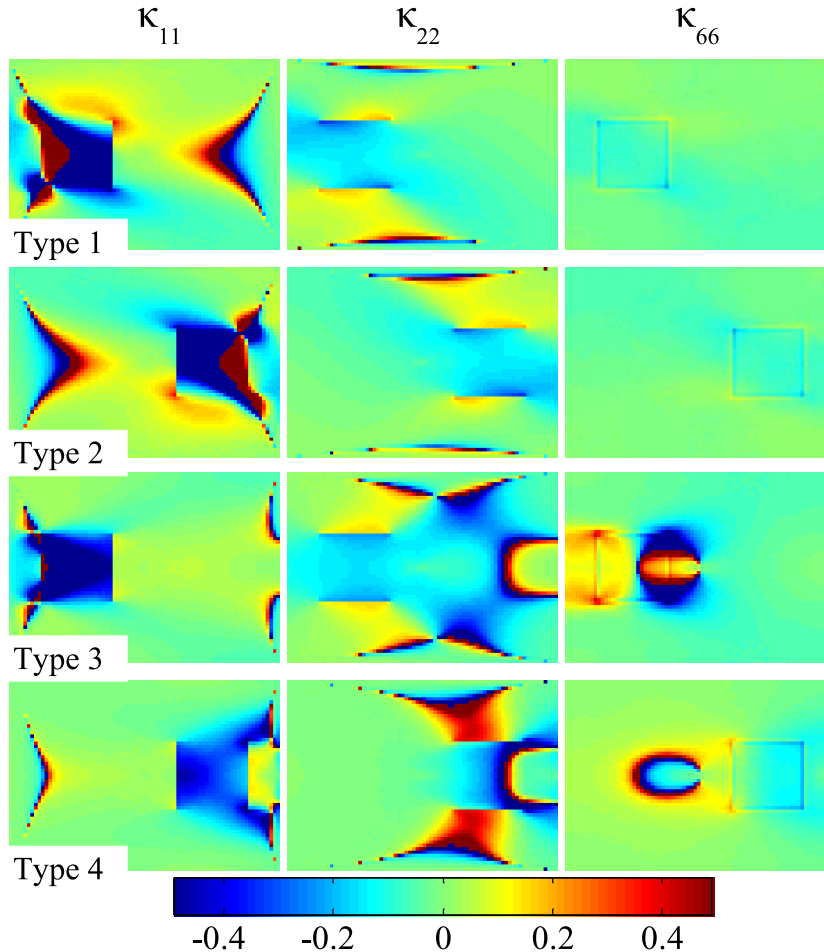


Figure 5.9: Relative difference of curvatures between undamaged and damaged plate in each configuration.

5.2.1.2.3 Effect of load magnitude Another interesting point concerns the magnitude of the load applied to the plate. Indeed, as the noise is only related to the optical conditions and the CCD camera, its level is independent from the applied load. As a consequence, the higher the applied load, the better the signal to noise ratio. This is illustrated in Fig. 5.10 where the identified damage map was plotted as a function of the load level. It can be seen that the higher the force, the better the damage detection,

although the effect is not overwhelming. It will be seen in the next section, however, that for lower stiffness contrasts and/or damage size, the effect of use of a larger force is much more important.

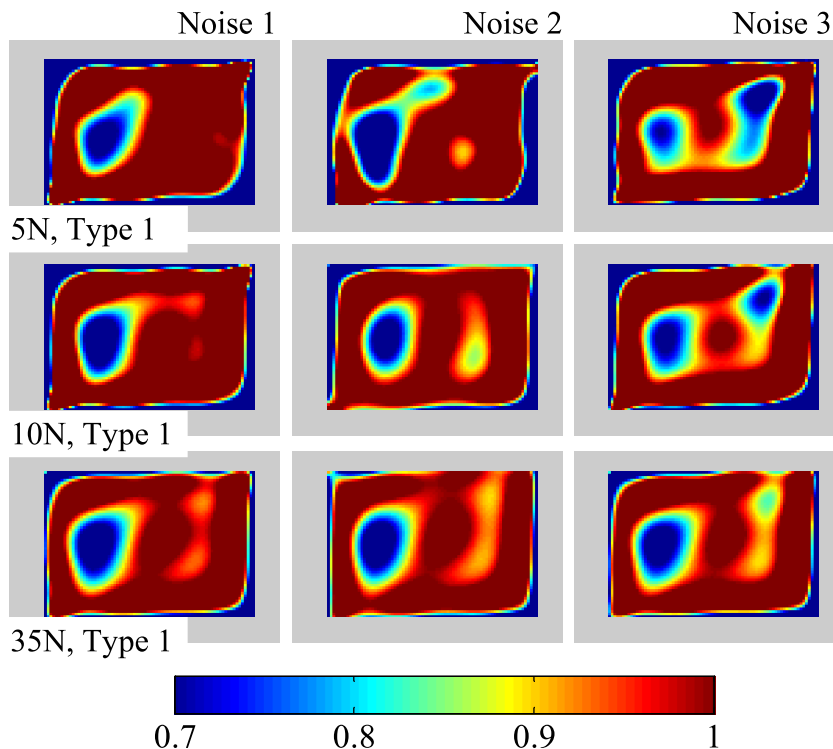


Figure 5.10: Effect of the magnitude of the applied force on damage detection.

5.2.1.2.4 Threshold of damage detection One of the important questions to be addressed concerns the threshold of damage detection of the method. For a given experimental set up (*i.e.*, given spatial resolution and noise level), this will be mainly affected by two parameters: the size of the damage and the stiffness reduction (or stiffness contrast). In the following, a sensitivity study was performed. The stiffness contrast between the damaged and undamaged material was changed as well as the size of the damage. The detection results are shown in Figs. 5.11 and 5.12, the first one corresponding to a 5 N load, and the second to a 10 N load. The first row of each figure shows the exact size of the damage. It is observed that the damage is clearly detected only in the worst cases when 5 N is applied. However, when the force is increased to 10 N, the detection results are improved and the damaged area is clearly visible even for the smallest values of stiffness contrast (7.2%) and surface damage (1.3%). This performance is very encouraging.

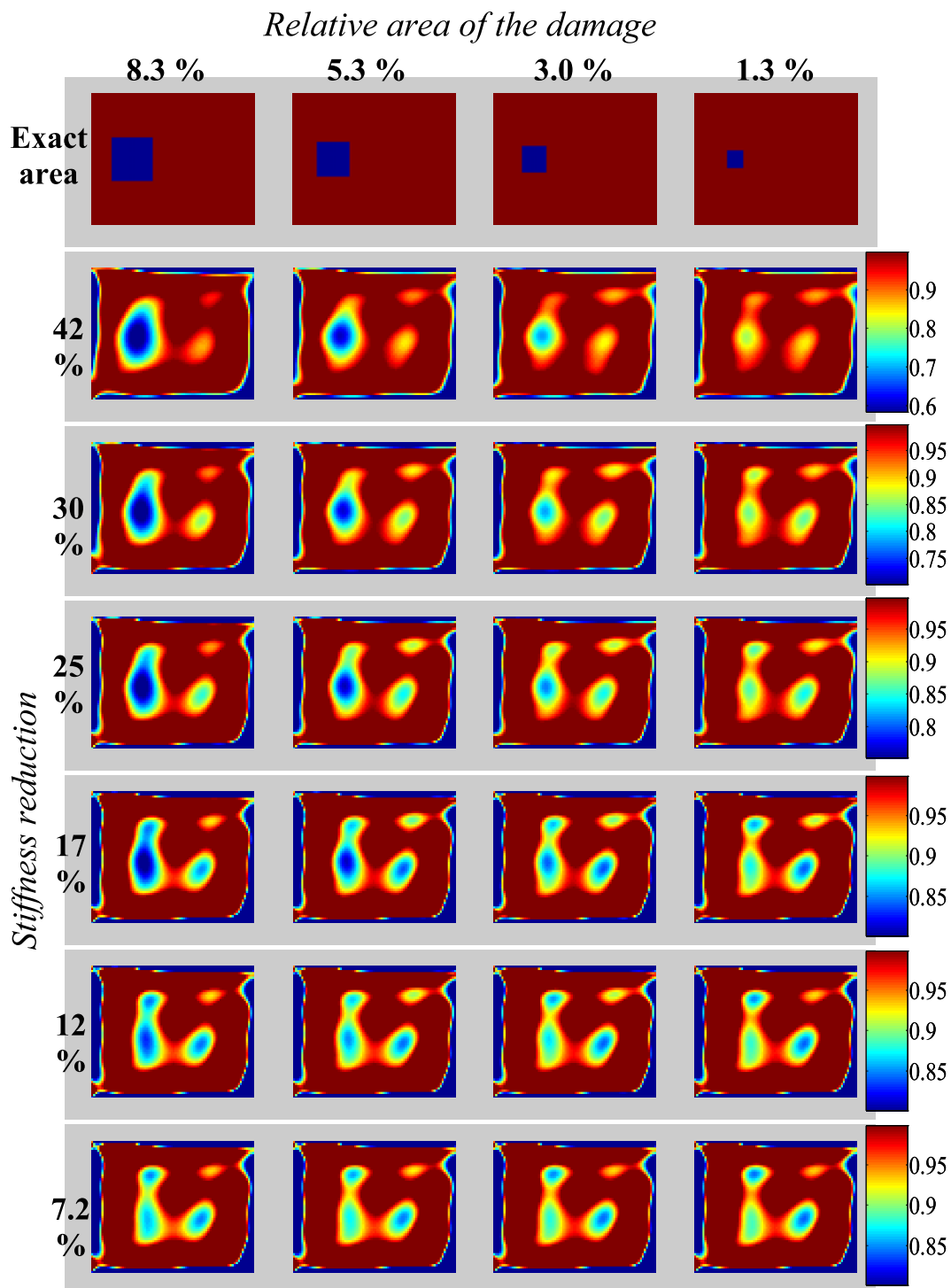


Figure 5.11: Detection results for different combinations of the size of the damaged area and the stiffness reduction (Applied force: 5 N).

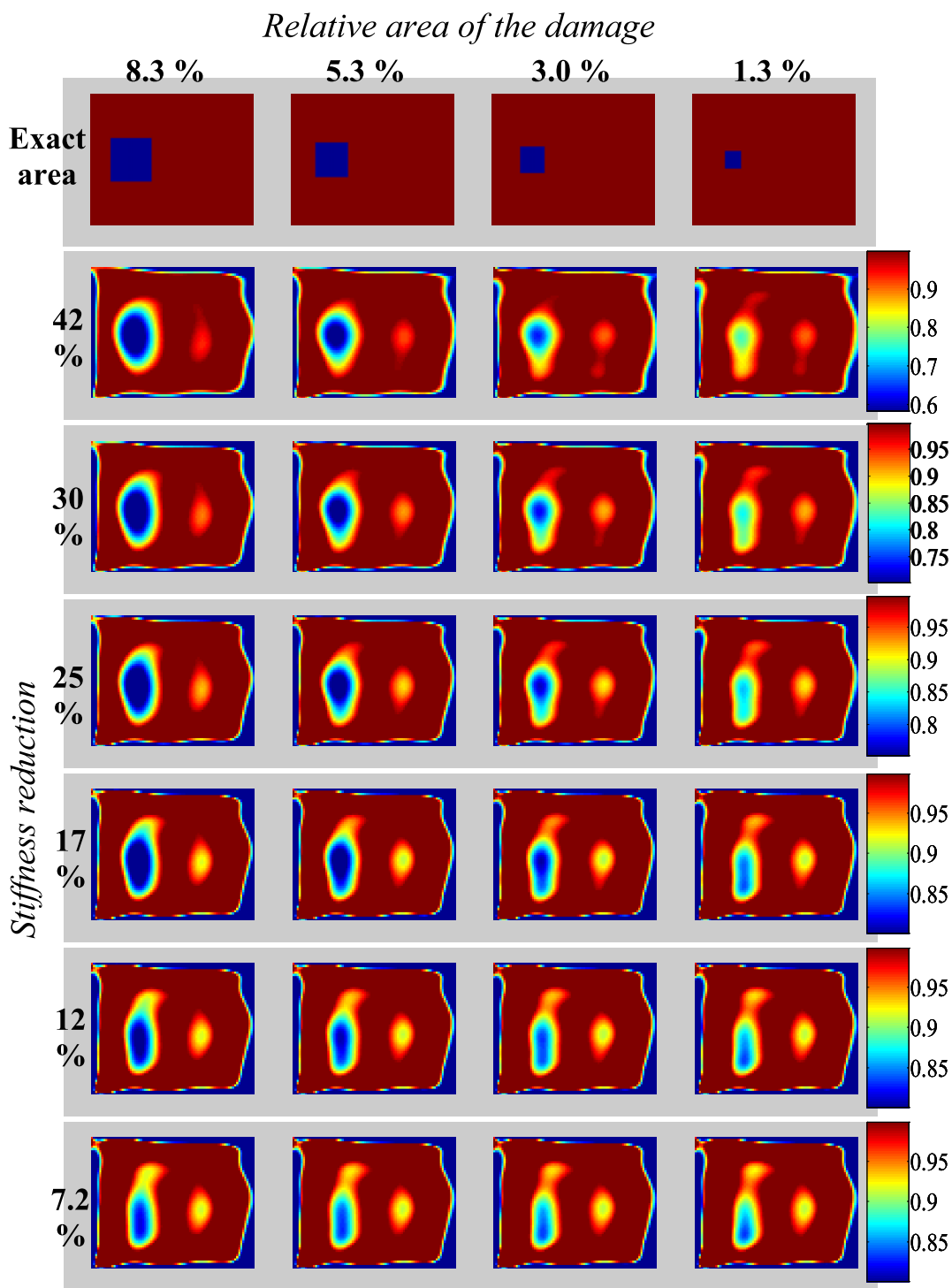


Figure 5.12: Detection results for different combinations of the size of the damaged area and the stiffness reduction (Applied force: 10 N).

5.2.1.2.5 Effect of spatial resolution The next verification performed in the present study concerns the effect of the spatial resolution of the measurement technique itself. In the case of deflectometry, this spatial resolution is equal to the pitch of the reflected grid (which is half that of the reference grid because of the laws of specular reflection). In order to investigate this point, a procedure for simulating the deformation of the grid by an FE simulated slope field was devised. The procedure is as follows:

- A numerical grid of points of coordinates (X_g, Y_g) was created. This grid simulates the CCD array of the camera.
- The recording of the undeformed grid by the CCD camera is simulated by calculating the value of intensity corresponding to a cross-line grid of pitch p at each of the (X_g, Y_g) points. The following formula was used:

$$I_{ini} = \text{floor}(I_0 - \frac{I_1}{2} [\cos(\frac{2\pi X_g}{p}) + \cos(\frac{2\pi Y_g}{p}) - \text{abs}(\cos(\frac{2\pi X_g}{p}) - \cos(\frac{2\pi Y_g}{p}))]) \quad (5.1)$$

where *floor* indicates the nearest lowest integer and *abs* the absolute value. I_0 is the mean intensity and I_1 the intensity variation linked to the contrast. In the present case, $I_0 = 135$ and $I_1 = 70$. These values are important when studying the effect of noise directly on the gray levels. However, here, the noise will be added directly on the phase maps so they are not important.

- The slope data from the finite element calculations are then used to ‘deform’ this reference grid. To do so, the first step is to find the values of the two slope components (θ_x^g, θ_y^g) at the (X_g, Y_g) locations. A linear interpolation is used through the *griddata* command in Matlab. However, because the FE displacements are given in the Lagrangian configuration, the (θ_x^g, θ_y^g) slopes must be expressed at the location $(X_g - 2l\theta_x^g, Y_g - 2l\theta_y^g)$. In this case, the process is implicit. It is solved by iterating the *griddata* function three times, first with (X_g, Y_g) (to find initial values for (θ_x^g, θ_y^g)) and then, twice with $(X_g - 2l\theta_x^g, Y_g - 2l\theta_y^g)$.
- The intensity I_{def} sampled by the CCD array after deformation of the grid is then calculated:

$$I_{def} = \text{floor}(I_0 - \frac{I_1}{2} [\cos(\frac{2\pi(X_g - 2l\theta_x^g)}{p}) + \cos(\frac{2\pi(Y_g - 2l\theta_y^g)}{p}) - \text{abs}(\cos(\frac{2\pi(X_g - 2l\theta_x^g)}{p}) - \cos(\frac{2\pi(Y_g - 2l\theta_y^g)}{p}))]) \quad (5.2)$$

- The two ‘images’ I_{ini} and I_{def} are then processed exactly as described in section 1.2. Images of the undeformed and deformed grids are shown in Fig. 5.13.

- Finally, the phase maps are converted into slope fields using the sensitivity defined in Eq. 1.2 and noise is added to produce the simulated slope fields. Again, the level of noise is that obtained in section 1.2.2. The curvatures are then obtained as stated in section 1.2.3.4 (polynomial fitting).

The objective here is to examine the effect of the pitch of the grid. Five grid pitch sizes (1, 2, 3, 4 and 5 mm) were tested (the pitch size corresponds to the size of the pitch of the image reflected onto the plate, half the size of the reference grid). The applied load was 5 N. It can be seen that the detection result is better with the smallest grid size as shown in Fig. 5.14. Therefore, a reference grid of 2 mm pitch (giving a 1 mm pitch for the grid image onto the plate) is recommended here.

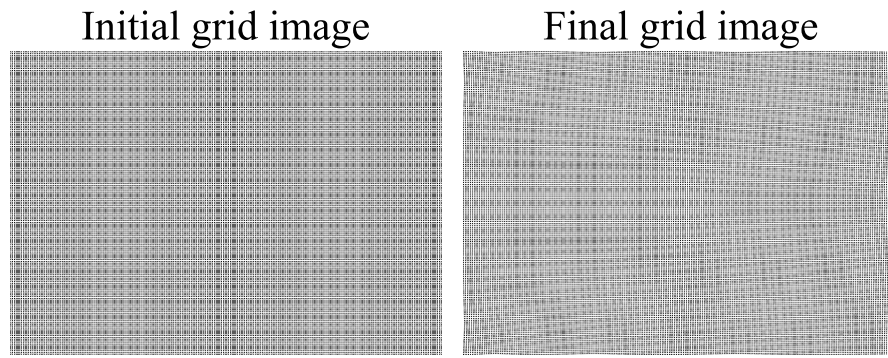


Figure 5.13: The undeformed and deformed grid images.

5.2.1.2.6 Effect of experimental conditions The next evaluation utilizes the above artificial grid deformation method in order to simulate experimental conditions. In the experiment, some data cannot be obtained owing to the nature of the deflectometry technique and the manufacturing process of resin coating. Therefore, masking is required for the area of missing data, then the data in this area is reconstructed using polynomial curve fitting.

There are three causes preventing data acquisition. The first is the reflected hole image. When the plate is deformed, this hole image moves from the initial position, so that normally two hole images can be observed on the slope field due to the differential process between the initial and final states. The second is point grips providing simple support condition for the bending test. The last is the edge area of resin coating. The quality of the coating in this area is spoiled when the specimen edges are trimmed with a grinding wheel after curing of the coating. Accordingly, several data elements around the edges of the slope field should be removed.

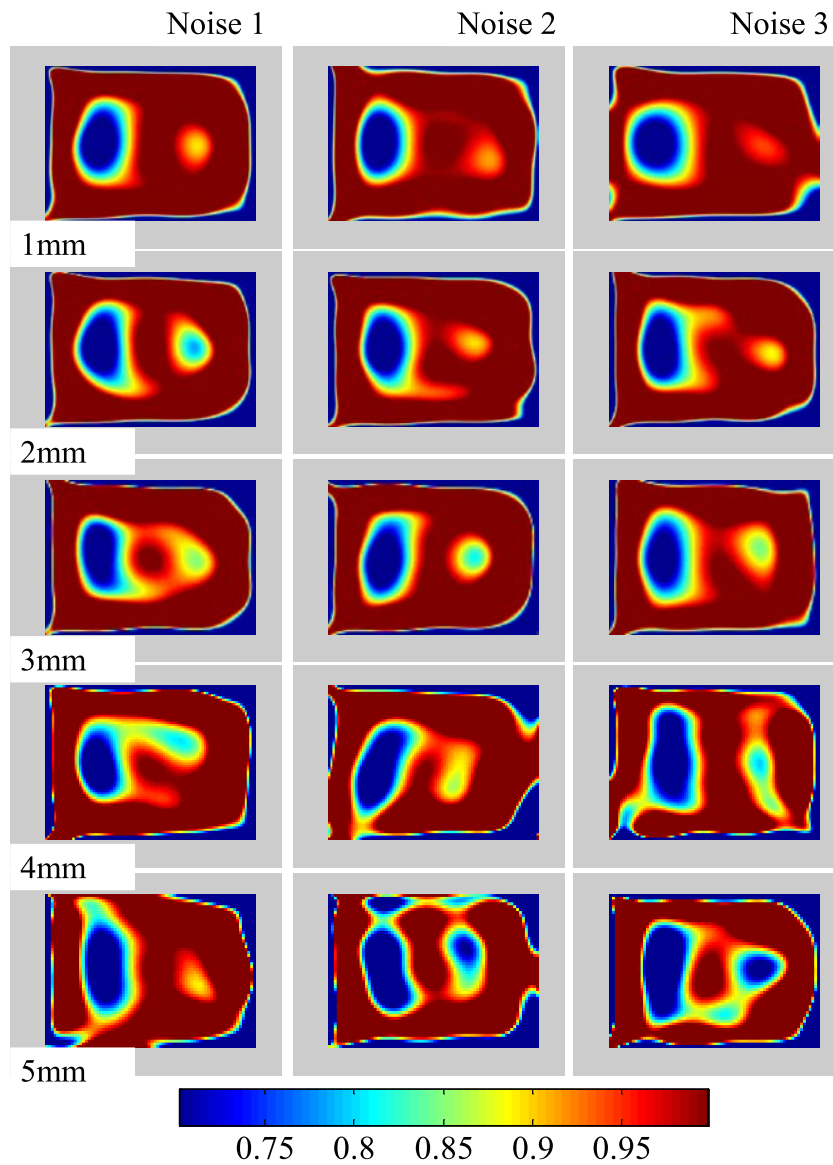


Figure 5.14: Damage detection results depending on various grid pitch sizes.

The objective of this simulation is to assess the effect of the above conditions on damage detection. The simulated slope field was obtained following the same procedure described in section 5.2.1.2.5 and the data was masked manually according to the given conditions. A parametric study was conducted as shown in Tab. 5.1.

The detection results depending on the conditions are shown in Fig. 5.15. The applied load was 5 N. Interestingly, it can be seen that the masking effects due to the hole images and the grips significantly deteriorate the damage detection. In order to enhance the detection, new methods which can avoid these effects were developed. First, new point

	Noise	Trimming away the edges (3 elements for each edge)	Hole image	Point grips
Case 0				
Case 1	✓			
Case 2	✓	✓		
Case 3	✓	✓	✓ (one image)	
Case 4	✓	✓	✓ (two images)	
Case 5	✓	✓	✓ (one image)	✓

Table 5.1: Conditions used in the parametric study.

grips were devised to minimize the effect of grips as shown in Fig. 5.16 (b). Secondly, a new camera position and required calibration were developed to avoid the hole images as discussed in section 1.2.3.5.

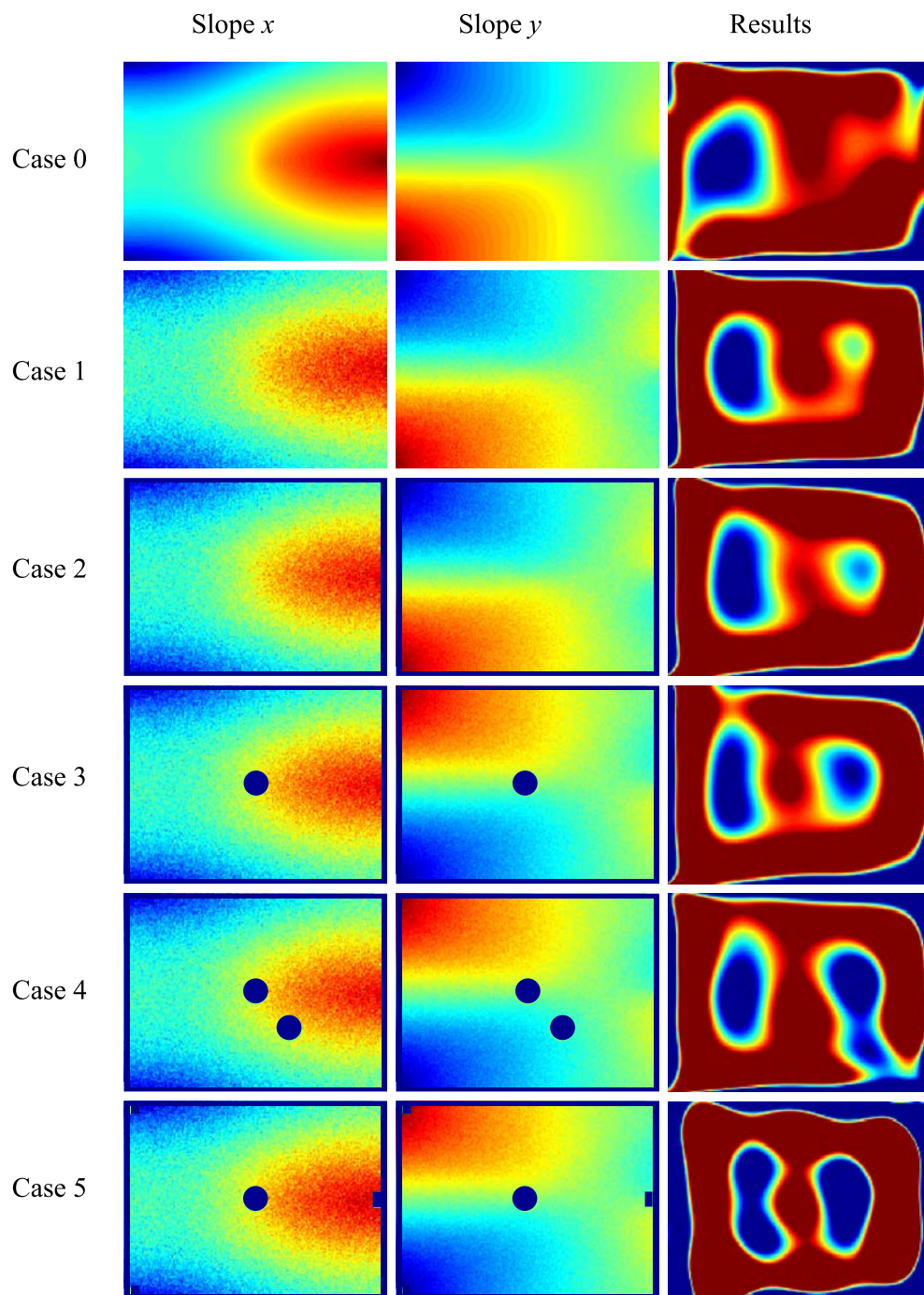


Figure 5.15: Damage detection results depending on the conditions in Tab. 5.1 .

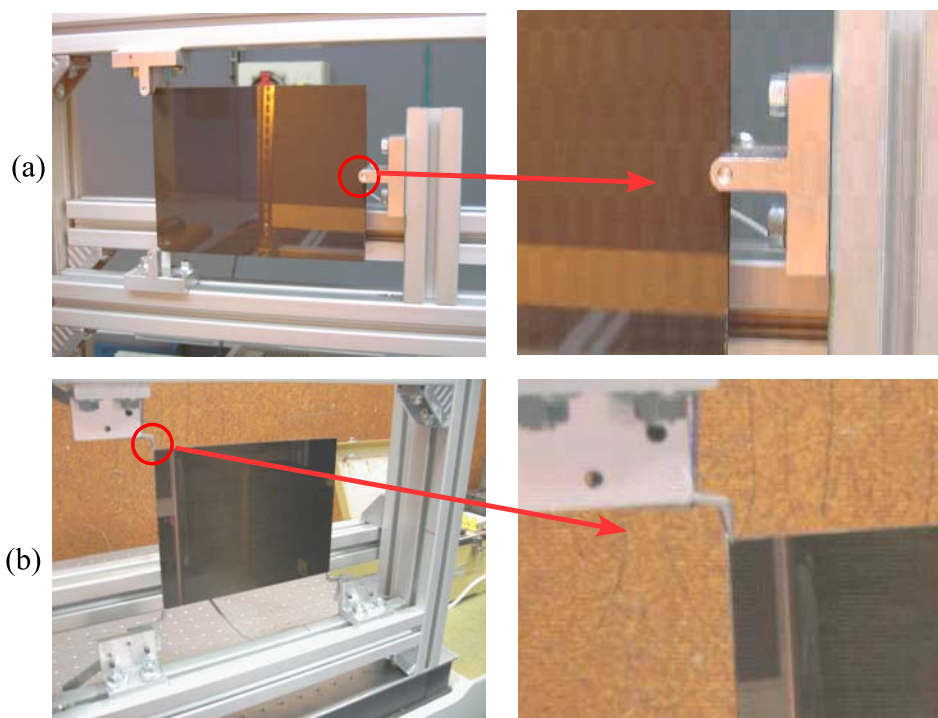


Figure 5.16: Point grips for bending test (a) previous grips (b) new grips.

5.2.1.2.7 Unsymmetrical damage So far, various aspects of identification of stiffness reduction have been investigated regarding isotropic and symmetric damage. In a real case, however, there is little chance that the damage will be symmetric. Consequently, the current methodology should be applicable to unsymmetrical damage. Otherwise, this approach will have significant limitations in the application to real damage.

As discussed in Chapter 2, Eq. 2.21 for the VFM in the case of plate bending was derived on the basis of a symmetric laminate, but, in the case of unsymmetrical laminate, the generalized moments are affected not only by the D matrix, but also by the B matrix. The influence of the B matrix should be taken into account in the case of unsymmetrical damage. In order to analyze the B matrix effect, two different lay-ups (one for symmetric and the other for unsymmetrical) were considered as shown below in Fig. 5.17. For fair comparison, almost the same stiffness reduction was compared between symmetric (30%) and unsymmetrical (27%) damage. As evident in Fig. 5.17, the detection results are very close to each other. These results are owing to the fact that the contribution of the B matrix to total resultant moment is less than 3% compared to that of the D matrix in this case. Though the B matrix is quite large, mid-plane strains are almost zero, with the result that B matrix effect is negligible. Therefore, the current methodology shows

possibility of detecting unsymmetrical damage.

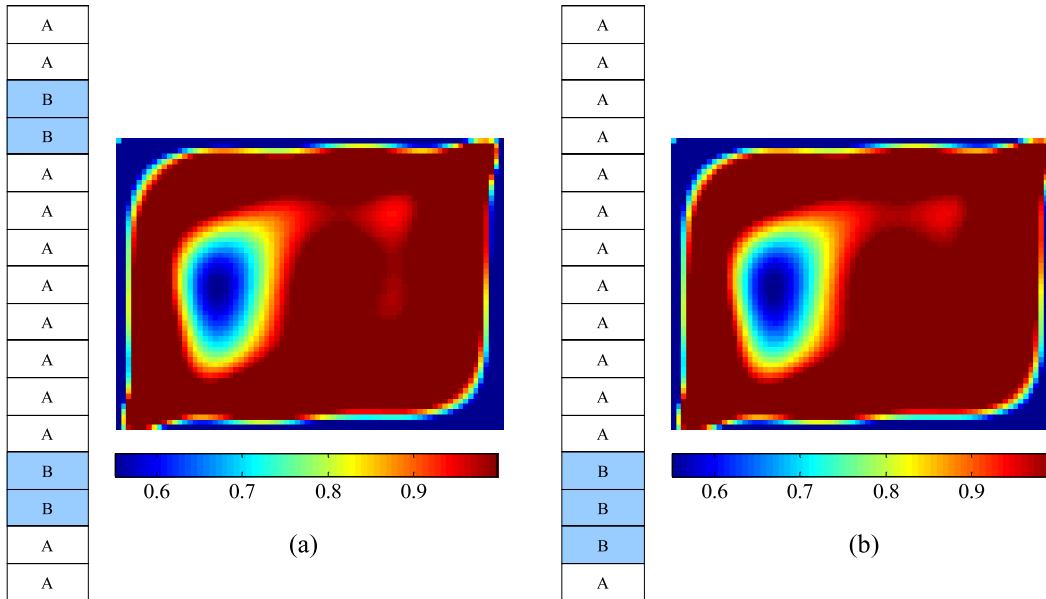


Figure 5.17: Comparison of detection results between (a) symmetric damage, and (b) unsymmetrical damage.

5.2.1.3 Validation on FE simulated data for anisotropic damage (without noise)

As described in section 5.2.1.1.1, in order to obtain specific stiffness reduction, damaged plies are replaced with equivalent plies having degraded material properties. In the case of UD, the damage generated by this method is always isotropic regardless of stacking sequence. On the other hand, other lay-ups such as cross-ply may produce anisotropic damage depending on the through-the-thickness location of the damaged layers. Furthermore, in practice, anisotropic damage is likely to occur instead of isotropic damage. Therefore, the performance of polynomial parameterization on anisotropic damage should be evaluated though this parameterization still assumes the damage to be isotropic.

Two different lay-ups of cross-ply (see Fig. 5.18) were considered. The blue color indicates damaged layers. As can be seen in Tab 5.2, the damage type B is indeed anisotropic. Nonetheless, even with this anisotropic damage, the damage location and the corresponding stiffness reduction are correctly identified as shown in Fig. 5.18. It is considered that the anisotropy used here is not significant. But if the damage is highly anisotropic, the current polynomial parameterization may not detect the damage properly, so, the polynomial parameterization was adapted to the description of each stiffness variation in the case

of anisotropic damage. As discussed in section 2.2.1.1, the identification of four stiffness variations simultaneously induces too many unknown parameters, leading to instability of the system. Consequently, the assumption made here is that only one stiffness changes whereas the other terms remain unchanged.

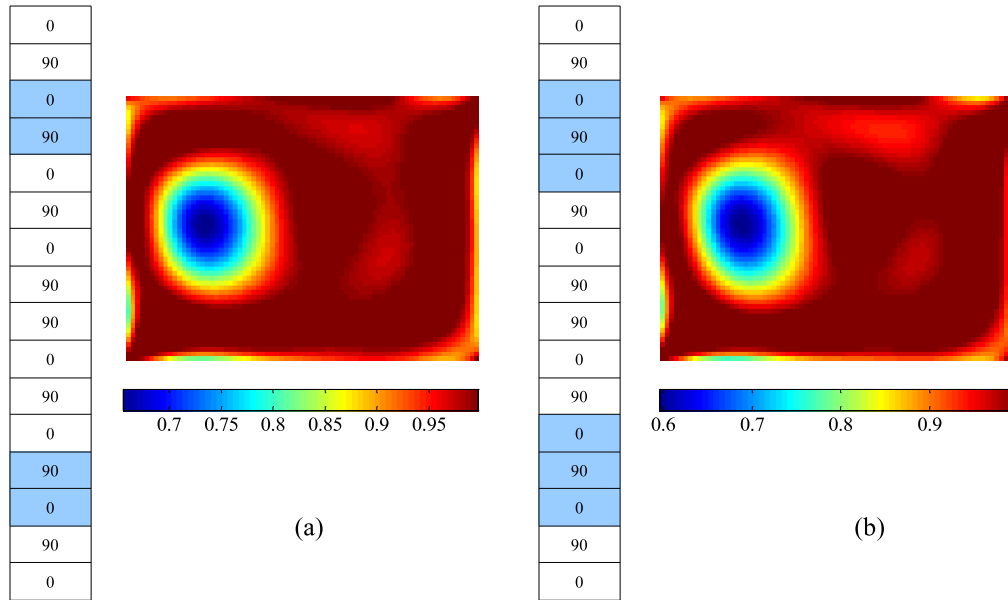


Figure 5.18: Comparison of detection results between (a) isotropic damage (type A) and (b) anisotropic damage (type B) in cross-ply laminates.

	Undamaged	Damaged (Type A)	R.D. (%)	Damaged (Type B)	R.D. (%)
D_{11} (Nm ²)	113.5	79.6	30	66.4	41
D_{22} (Nm ²)	81.9	57.8	30	56.8	31
D_{12} (Nm ²)	4.55	3.20	30	2.87	37
D_{66} (Nm ²)	6.57	4.62	30	4.15	37

Table 5.2: Stiffness reduction depending on the lay-up (R.D.: Relative Difference).

The investigation of variation of each stiffness (D_{11} , D_{22} , D_{12} , D_{66}) was conducted using Eq. 2.40. However, the damage was not detectable in any case when the force is applied to the center of the plate. In order to further examine this result, damage detection was analyzed as a function of the location of the applied force. With the given boundary conditions, the force location was changed according to the position in Fig. 5.19. Two important observations were obtained from this study. The first is that the detection was not successful in the cases of D_{11} , D_{22} , and D_{12} regardless of the force location. However, the stiffness reduction of D_{66} could be identified in some load cases as shown in Fig. 5.20. This result can be explained because D_{11} and D_{22} are coupled with D_{12} , so that the stiffness reduction of only D_{11} or D_{22} without affecting the coupled stiffness is not feasible. On the other hand, D_{66} is an independent term, resulting in successful identification depending on the force location. The second observation can be drawn from this point. As can be seen in Fig. 5.20, only when the force is applied to the upper right area of the given configuration, the stiffness reduction of D_{66} can be identified. The very important point of this observation is that the identification of each stiffness in a small local area is possible only when the area has sufficient spatial stress information. If the force is applied to the position of number 22 in Fig. 5.19, the plate is in an anticlastic state (pure twisting mode) offering maximum spatial shear information. Therefore, the present results are consistent with this remark. Additional study will be carried out in section 5.2.2.2.1 regarding the relationship between the force location and local spatial information.

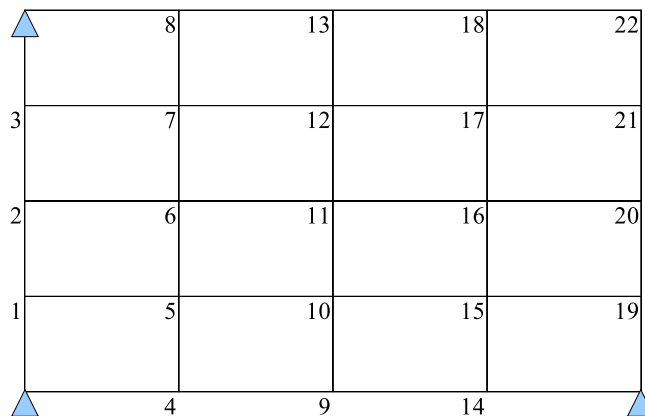


Figure 5.19: Force locations.

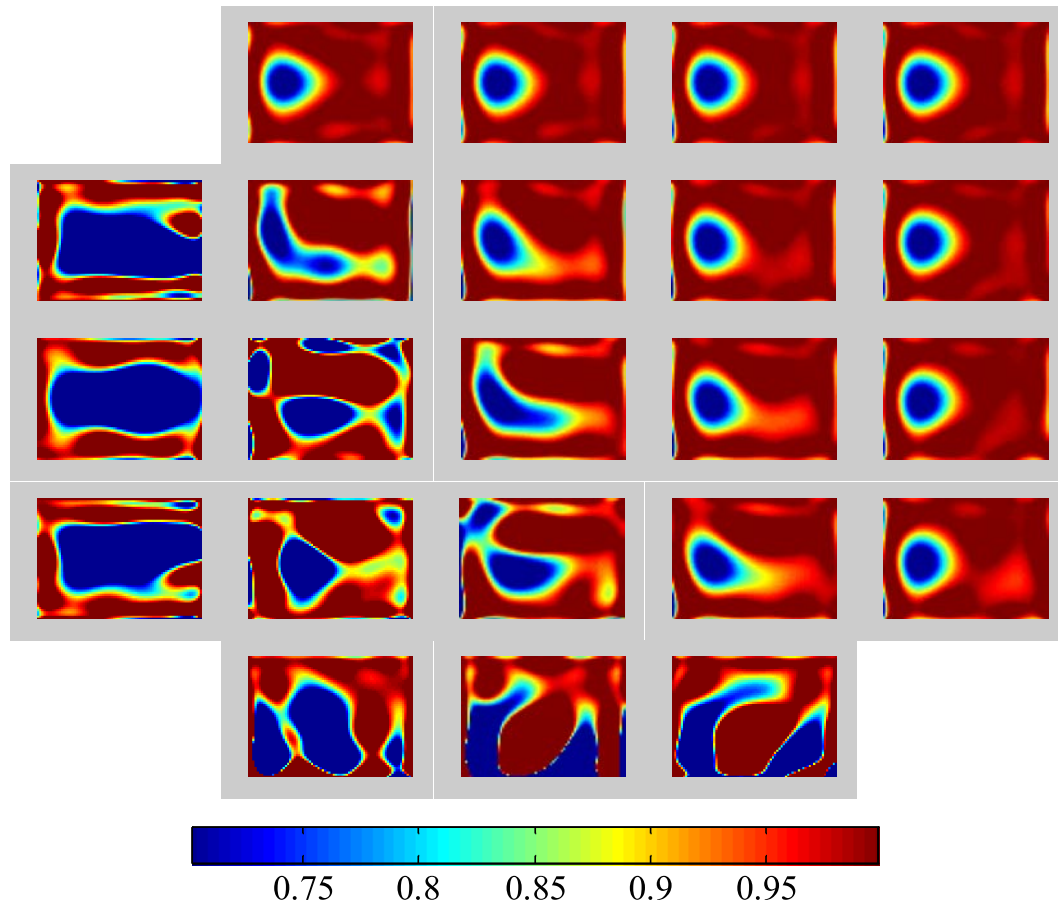


Figure 5.20: Corresponding stiffness reduction of D_{66} depending on force location.

5.2.2 Discrete parameterization

In this section, discrete parameterization will be validated on simulated measurements. The initial step was to identify the scalar damage parameters in Eq. 2.41 using curvature data from the FE analysis without considering noise. The detection results depending on three different mesh sizes are compared in Fig. 5.21. As the number of virtual elements increases, the description of damage becomes more accurate. In order to obtain good spatial resolution, a 19×14 mesh size is required in this configuration. Unlike the continuous parameterization, discrete one can identify the square damaged area more precisely. However, the number of unknowns is much greater (266) compared to that of polynomial parameterization (44). For this case, piecewise virtual fields were used to provide sufficient DOFs. The great number of unknowns makes the detection very sensitive to noisy data. Comparison of detection results between polynomial and discrete parameterization using noisy data is shown in Fig. 5.22. The instability of the discrete

parameterization to noisy data can be seen clearly. This is owing to the fact that stiffness contrast is the second derivative of slopes (strain gradient), thus identifying the stiffness contrast with the discrete parameterization is very difficult.

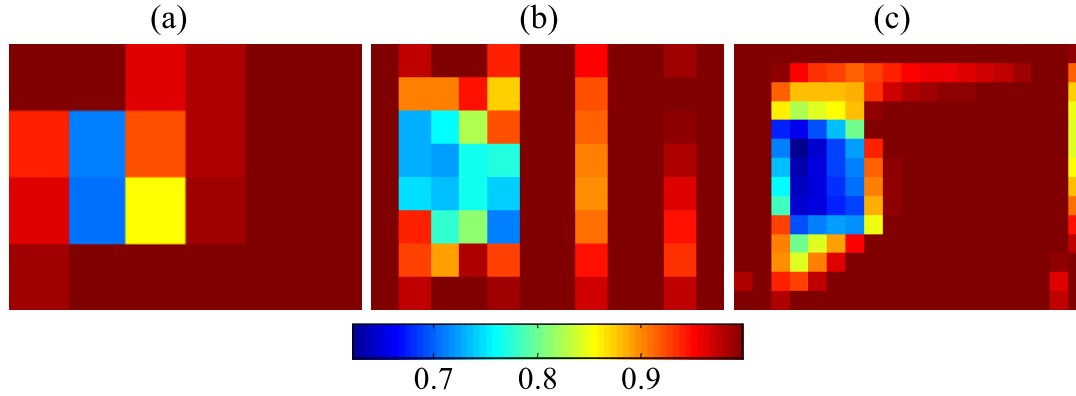


Figure 5.21: Detection results depending on the mesh size (a) 6×4 , (b) 12×8 , (c) 19×14 .

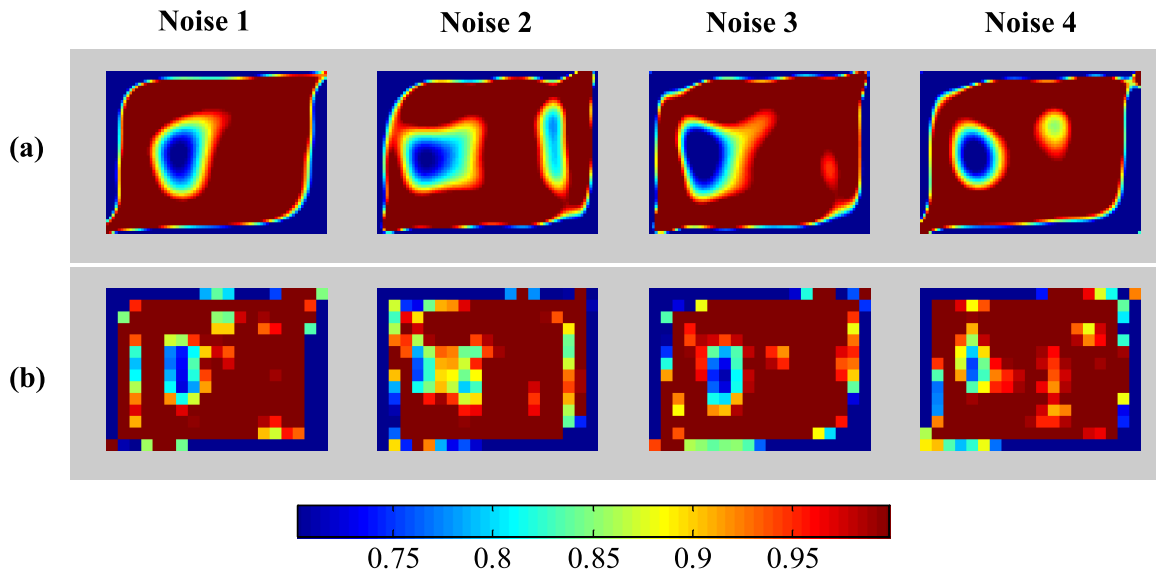


Figure 5.22: Comparison between (a) polynomial and (b) discrete parameterization.

5.2.2.1 Isotropic damage

The alternative strategy of the above discrete parameterization is that the damage location and extent are determined by using the polynomial parameterization in a first stage since the location of damage is unknown *a priori* in practice. In a second step, a discrete

approach (independent identification of each stiffness component) could be applied in the areas detected by the polynomial, which would greatly reduce the number of parameters, therefore lessening one of the major drawbacks of the discrete parameterization. In this way, the bending stiffnesses of the damaged region can be identified directly.

For the direct identification of stiffness reduction on isotropic damage, the scalar damage parameter p in Eq. 2.43 was determined for the cases of three different virtual element sizes. The first case used one element for the whole damaged area, the second four elements, and the third nine elements. As a first verification of this method, exact location and extent of the damage were used. The stiffness reduction used in this study is 30%, so that the p value will be 0.7, if the identification is conducted without any deviation. When the validation was performed on FE simulated data without noise, the identification was very successful in all cases. However, with noisy data, it was observed that the results became more unstable as the number of elements increased. The identification results for stiffness reduction are shown in Fig. 5.23. These results are mainly owing to the facts that the damaged area of interest is not large enough to have sufficient spatial information (the identification area for each piece is very small) and the stiffness contrast used in this case is rather low. Therefore, increasing the number of elements will only be reasonable for the cases having stronger spatial information and stiffness contrasts.

0.67 (4.3 %)	0.69 (1.4 %)	0.63 (10.0 %)	0.62 (11.4 %)	0.80 (-14.3 %)	0.57 (18.6 %)
	0.69 (1.4 %)	0.65 (7.1 %)	0.66 (5.7 %)	0.64 (8.6 %)	0.74 (-5.7 %)
			0.68 (2.9 %)	0.79 (-12.9 %)	0.54 (22.9 %)
(a)	(b)		(c)		

Figure 5.23: Identification results with noisy data depending on the mesh size (a) 1×1 , (b) 2×2 , (c) 3×3 (the number in parenthesis means relative difference from the reference).

5.2.2.2 Anisotropic damage

5.2.2.2.1 Validation on FE simulated data without noise The next verification was to identify eight rigidities (four for the undamaged zone, and four for the damaged

zone) simultaneously for the anisotropic damage. In this case, 4th order polynomial virtual fields used in the global stiffness identification do not perform well owing to the increased number of unknowns. After the systematic study of section 3.2.1.2, 12th order polynomial virtual fields were chosen. Identification was conducted on two boundary configurations (type 1 and type 3, see section 5.2.1.2.2). Again, exact location and extent of the damage were chosen. The stiffness reduction used in this study is 30%. The identified results and the corresponding sensitivity $\frac{\eta}{D}$ values are presented in Tabs. 5.3 and 5.4. In both cases, all the stiffness reductions are correctly identified. Nevertheless, it should be noted here that the sensitivity value $\frac{\eta^d}{D_{66}}$ of type 3 is much greater than that of type 1 in the damaged area. This indicates a poor identification of the D_{66}^d with type 3 when the identification is conducted with noisy data. In addition, the $\frac{\eta^a}{D_{11}}$ is larger by one order of magnitude than $\frac{\eta^b}{D_{22}}$ and $\frac{\eta^d}{D_{66}}$ in type 1 since a UD plate is used here. Generally, D_{12} is the most difficult term to identify because its influence on the strain field is lower than that of the other stiffness components.

	D_{11}^u	D_{22}^u	D_{12}^u	D_{66}^u	D_{11}^d	D_{22}^d	D_{12}^d	D_{66}^d
Reference	181.9	13.4	4.55	6.57	127.9	9.42	3.20	4.62
Identified (Type 1)	182.2	13.4	4.51	6.57	127.8	9.42	3.22	4.62
R.D. (%)	-0.14	-0.01	0.78	-0.02	0.09	-0.01	-0.55	0.04
Identified (Type 3)	182.1	13.4	4.50	6.57	127.9	9.43	3.21	4.41
R.D. (%)	-0.10	-0.09	1.08	0.00	0.04	-0.12	-0.23	4.59

Table 5.3: Comparison of results between type 1 and type 3 (D^u : stiffness for undamaged area, D^d : stiffness for damaged area, units for D : Nm^2).

	$(\frac{\eta^a}{D_{11}})^u$	$(\frac{\eta^b}{D_{22}})^u$	$(\frac{\eta^c}{D_{12}})^u$	$(\frac{\eta^d}{D_{66}})^u$	$(\frac{\eta^a}{D_{11}})^d$	$(\frac{\eta^b}{D_{22}})^d$	$(\frac{\eta^c}{D_{12}})^d$	$(\frac{\eta^d}{D_{66}})^d$
Type 1	1.02	0.20	3.31	0.12	12.8	0.82	25.3	1.37
Type 3	1.07	0.71	5.34	0.55	9.34	1.75	35.2	50.5

Table 5.4: Sensitivity values for each stiffness in type 1 and type 3.

5.2.2.2.2 Validation on FE simulated data with noise In order to analyze further the results obtained in the previous section, an identification with two different randomized noise sets was performed. These results are shown in Tab. 5.5. As expected, the identified D_{66} value (red color) in the damaged region has big deviation in type 3.

The identification of four bending stiffnesses in one test can be feasible owing to the fact that the area of interest has heterogeneous stress field, but if the area does not include sufficient heterogeneous information for each stiffness, the identification of all stiffnesses cannot be achieved in one test. The damaged region in type 3 is located in the mid area of symmetric configuration (see section 5.2.1.2.2), therefore, this region has very weak shear information. This is the reason why D_{66} shows poor identification in type 3. In addition, the identification of D_{11} is very sensitive to noise due to lower signal-to-noise ratio (the x curvature values are much lower than the other two components since UD material is used). From this observation, for the successful identification of stiffnesses in a local area, the local heterogeneous stress field should include sufficient spatial information.

	D_{11}^u	D_{22}^u	D_{12}^u	D_{66}^u	D_{11}^d	D_{22}^d	D_{12}^d	D_{66}^d
Reference	181.9	13.4	4.55	6.57	127.9	9.42	3.20	4.62
Type 1 (Noise 1)	172.2	13.3	4.70	6.49	90.1	9.58	4.00	4.87
R.D. (%)	5.3	0.7	-3.3	1.2	29.6	-1.70	-24.9	-5.40
Type 3 (Noise 1)	172.1	12.5	5.68	6.71	89.3	10.1	4.64	-2.68
R.D. (%)	5.4	6.7	-24	-2.1	30.2	-7.20	-44.9	158
Type 1 (Noise 2)	165.9	13.3	4.54	6.49	135.1	9.58	3.07	4.70
R.D. (%)	8.8	0.7	0.2	1.2	-5.60	-1.70	4.10	-1.70
Type 3 (Noise 2)	171.5	12.8	4.88	6.59	143.1	10.3	0.62	-2.43
R.D. (%)	5.7	4.5	-7.3	-0.3	-11.8	-9.40	80.6	152

Table 5.5: Comparison of results between type 1 and type 3 (Units for D : Nm^2).

5.2.2.2.2.1 Effect of force location As the local spatial information is very important in the identification of stiffness in a local area, the idea is to find optimal force location that maximizes spatial information for a local area of interest with the given boundary condition. This study is based on the fact that the local stress field changes depending on

the position of the applied load. In order to search the optimal force position, a criterion is required. This problem leads to use the noise sensitivity parameter $\frac{\eta}{D}$, indicating that a point which shows the lowest $\frac{\eta}{D}$ becomes the optimal position for each stiffness identification. However, the $\frac{\eta}{D}$ value is inversely proportional to strain level meaning that the η value is lower if the strain is higher. Thus, the sensitivity needs to be normalized for fair comparison; two normalization methods are employed:

- $\frac{\eta}{D} \times$ maximum deflection
- $\frac{\eta}{D} \times$ maximum von Mises strain

The first criterion has been used for the optimization of the force location in the case of global stiffness identification [41]. In this study, the normalized sensitivity values of each identified stiffness depending on various force locations (see Fig. 5.24 (a)) were compared. Before investigating the optimal force location for the given local area, the optimal position for the identification of global stiffness was traced in order to evaluate the validity of the above criteria. The distribution of the normalized sensitivity values are shown in Fig. 5.25 (a) and (b). Since D_{12} is the most difficult term to identify, the distributions for D_{11} , D_{22} , and D_{66} are presented here. As can be seen in Fig. 5.25, the optimal force position is not consistent with each other. Consequently, one more criterion was chosen. An identification with 30 different randomized noise sets was carried out for each force location shown in Fig. 5.24 (b). The standard deviation was examined for 30 sets of identified results on each point: the position which shows the lowest standard deviation can be considered as the optimal position. The results are shown in Fig. 5.25 (c). Unexpectedly, the optimum point does not match with the other results.

Though the optimal force locations are different depending on the criterion, some patterns of the optimum points can be seen. In the case of the criterion, $\frac{\eta}{D} \times$ maximum deflection, the optimum force locations are located on the lower left area. These results are very similar to previous ones [41]. In this criterion, the sensitivity parameter is normalized by maximum deflection. If the same magnitude of deflection is obtained using all the force locations, the strain level will be higher on the lower left area since this area is much stiffer (close to the bottom left boundary point). The sensitivity parameter η is inversely proportional to signal to noise ratio (SNR), thus indicating the lower left area as the optimum zone with this criterion. Consequently, this criterion somewhat misleads the optimization process by searching for the stiffer region. On the contrary, the criteria $\frac{\eta}{D} \times$ maximum von Mises strain and minimum standard deviation present similar patterns of optimal points. For the identification of D_{11} , these criteria show better identification in the middle of the plate in the x direction, since this area provide maximum bending

information. Similar pattern also can be found for D_{22} . For D_{66} , upper right area indicates better identification because this area provides maximum shear information. In view of the above observations, the latter two criteria are more suited to the aim of the optimization of the force location.

The objective of this study was to find an optimal force location, however, the process of choosing a proper criterion for the optimal force location was not straightforward. It should be mentioned here that even if the optimal force location can be found for a given local area, the optimal position will be valid only for this area. As the damage location moves, the optimal position will be changed. Since the location and extent of the damage are unknown *a priori* in practice, the optimization of force location inevitably has limitation. Because this study to search the optimum point of the force location was not successful, in the experiment, the maximum force magnitude compatible with deflectometry will be applied in order to increase the signal to noise ratio.

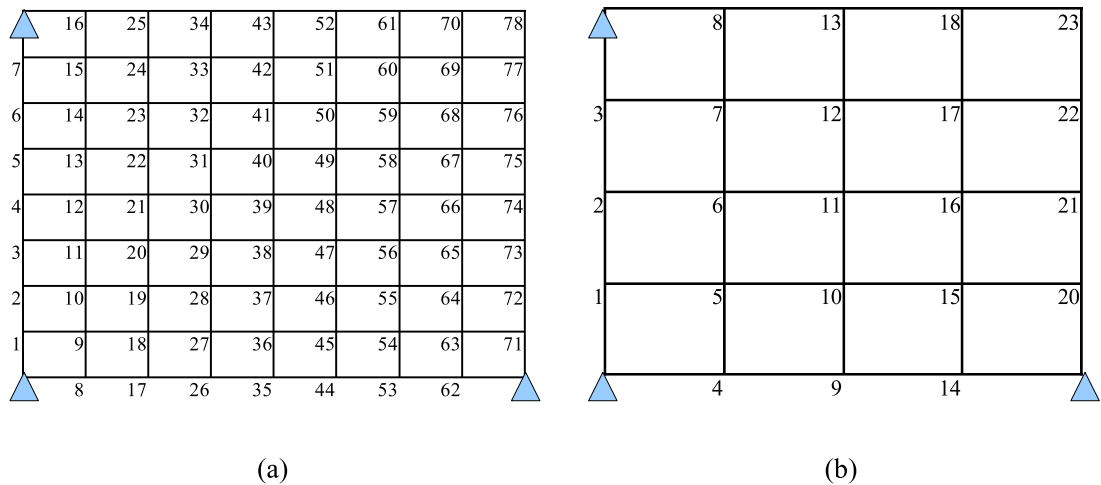


Figure 5.24: Force locations used for each criterion (a) $\frac{\eta}{D} \times$ maximum deflection and $\frac{\eta}{D} \times$ maximum von Mises strain; (b) minimum standard deviation.

5.3 Results and discussion (Interlaminar damage)

So far, most of the previous studies in the FE analysis of delamination have been focused on the topics of delamination onset and growth, buckling and postbuckling behavior, and residual strength analysis, but very few studies have been carried out on the detailed stress analysis of damaged laminates due to delamination and the corresponding stiffness reduction. In this study, an FE modeling technique for mid-plane delamination and

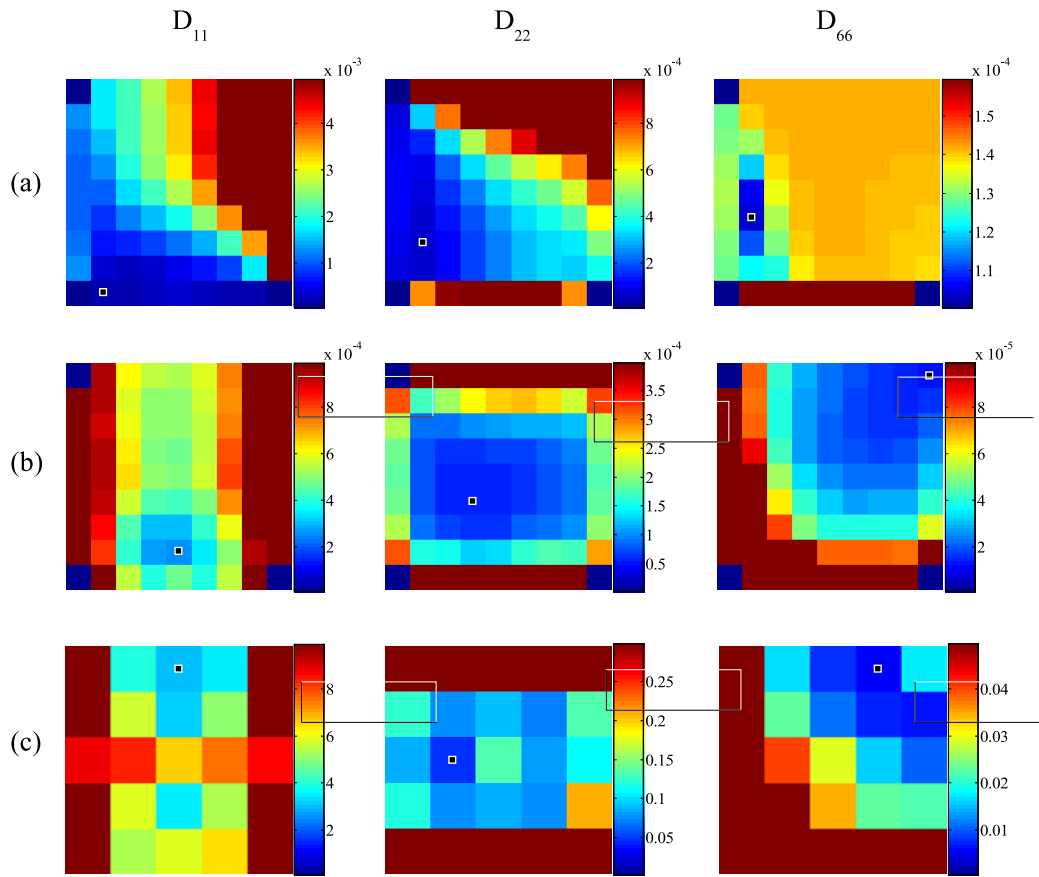


Figure 5.25: Optimal force location depending on each criterion: (a) $\frac{\eta}{D} \times$ maximum deflection; (b) $\frac{\eta}{D} \times$ maximum von Mises strain; (c) minimum standard deviation (the point in each figure indicates the optimal position).

the stiffness reduction owing to this delamination will be presented. For simplicity, a laminated plate with one embedded delamination will be investigated.

5.3.1 Polynomial parameterization

5.3.1.1 Validation on FE simulated data

5.3.1.1.1 FE model As discussed in section 5.1.2.2.2, mid-plane delamination is a structural failure, meaning its effect on structural integrity cannot be described with the FE model used in section 5.2.1.1.1. In this study, for efficient FE modeling, a sublaminated model utilizing two thin shell finite elements through-the-thickness direction was used to model the offsets (*i.e.* kinematic discontinuity due to delamination) between sublaminates.

Each sublaminates is connected by interface elements to represent undamaged laminate with the removal of interface elements simulating the delamination damage.

Finite element analysis was undertaken by using the *I-DEAS* 11 package. Several finite element approaches were investigated to properly model the mid-plane delamination. The reliability of the FE model however cannot be obtained without comparison with experimental results. Thanks to the availability of full-field measurement technique used in this study, full-field curvature field owing to the mid-plane delamination was acquired. Finally, a rigid bar element was chosen for the interface since the FE model utilizing this element has provided very similar curvature field with that of experiment. For the initial validation of this FE model, a UD plate was used. Its material properties and the configurations are the same as those used in section 5.2.1.1.1. In order to model undamaged laminate, each node of upper sublaminates (8 layers) was connected with the corresponding node of the lower sublaminates (8 layers). The distance between two sublaminates was set as 1.28 mm, half the full thickness to represent the thickness of the sublaminates above and below. The validity of a rigid bar element as interface element was checked first by comparing the undamaged stiffnesses from the current sublaminates model with those of the previous model used in section 3.2.1.1. The difference was less than 1%. Though it is not required to assign physical property to the rigid bar elements in *I-DEAS*, the property of resin was given to the elements. The material properties used as inputs are: $E = 9.5$ GPa, $\nu = 0.34$. No difference was observed between the two cases.

In order to represent the delaminated region, the rigid bars were disconnected. Indeed, two models can be used in this approach as shown in Fig. 5.26. It was observed that the performance of the two models is exactly same, however, the second model is more favorable since delamination damage can be made more easily just by removing the rigid bar elements of delaminated area. Therefore, the second model will be used in this study.

Next, contact analysis was performed to prevent physically inadmissible interpenetration of the two sublaminates (delaminated region) during loading. After trial and error, normal penalty factor for the contact analysis was chosen as 5000. The normal penalty factor specifies the normal penetration stiffness of the contact surfaces [139]. It was observed that too high penalty factor resulted in failure of the analysis. Regardless, there was no difference between the FE results with and without contact analysis. It is considered that no interpenetration occurs with the given configurations (a UD plate, the force is not applied on the delaminated area); if the force location is placed on the delaminated area, then the contact analysis is critical.

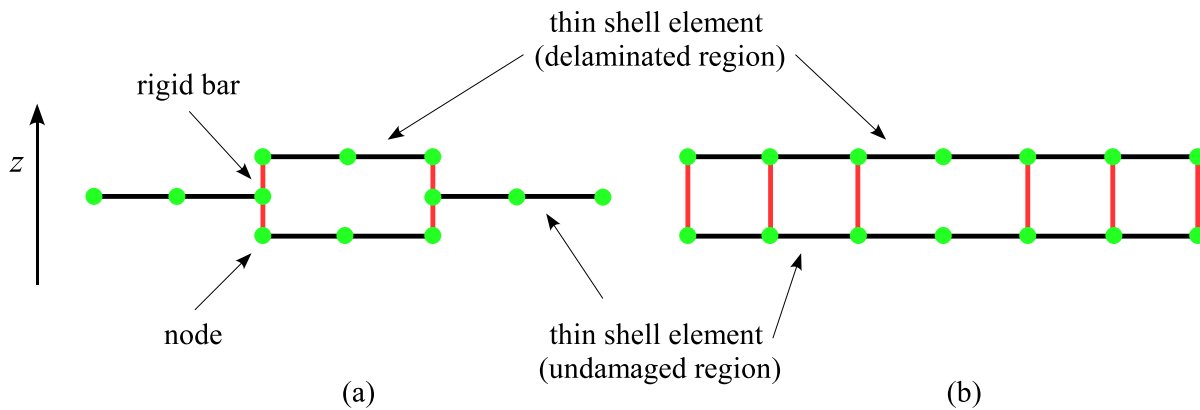


Figure 5.26: Two different delamination models.

5.3.1.1.2 Validation from FE curvature data The result of local stiffness reduction for the mid-plane delamination is shown in Fig. 5.27 (a). The plate is tested in bending according to the load configuration in Fig. 5.2. In this case, very unexpected results were observed both in location and stiffness reduction. The damage zone is not correctly located and the detected damage zone is elongated in the vertical direction. Furthermore, the stiffness reduction is less than that of the intralaminar damage having 30% stiffness reduction. In Fig. 5.27 (b), the exact location of delamination and the stiffness reduction with original scale are shown. Strange behavior showing stiffness reduction on the right hand side of delamination and stiffness increase on the left hand side can be seen. This comes from the nature of the mid-plane delamination and the current methodology. This is further discussed in Chapter 6 with the experimental results.

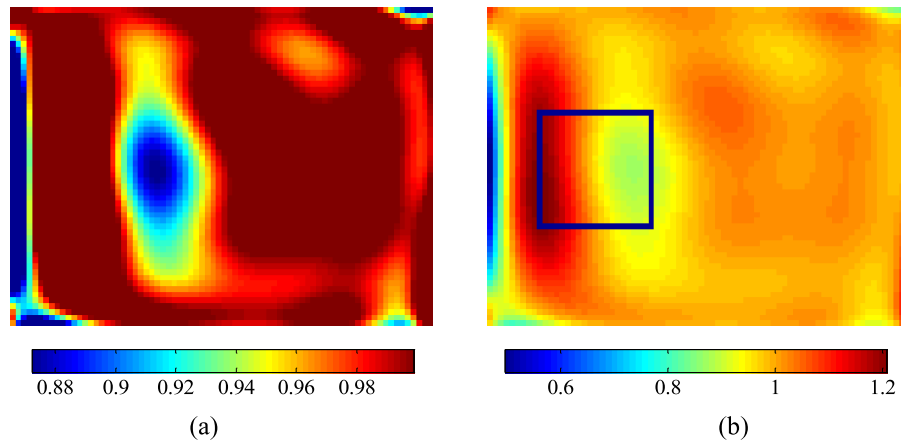


Figure 5.27: Stiffness reduction due to mid-plane delamination (a) with adjusted scale (b) with original scale (including exact location of delamination).

5.4 Conclusion

In this chapter, the proposed methodology in Chapter 2 was validated on simulated FE measurements. In the first part, finite element modeling technique for the case of the intralaminar damage was introduced. Various possibilities and the effects of several variables on the quality of the predictions were explored and the potential of the VFM to locate and quantify the local stiffness reduction in damaged composite plates was investigated for the intralaminar damage. Polynomial parameterization method not only picks up the location of the damage but also provides a fairly good estimate of the stiffness reduction in the damaged area. In order to assess the effect of experimental conditions on damage detection, the experimental conditions were simulated by utilizing the artificial grid deformation method. It was observed that the masking effects due to the hole images and the grips significantly deteriorated the damage detection. New methods which can avoid these effects were developed to enhance the detection. The identification of four bending stiffnesses directly in a local damaged area using discrete parameterization is feasible only when the area includes sufficient spatial information for each stiffness. In the second part, FE modeling technique for the interlaminar damage was presented, and the result of local stiffness reduction for the mid-plane delamination was shown. In this case, very unexpected results were observed both in location and stiffness reduction. In Chapter 6, the proposed FE model will be validated from the experimental measurements, and extensive comments on the mechanism and the behaviour of the mid-plane delamination will be given.

Chapter 6

Identification of the local stiffness reduction Part II: experiment

6.1 Introduction

This chapter will present a wider validation of the proposed methodology against experimental data, both on artificial and real impact damage in composite laminated plates.

As discussed in Chapter 4, the two most important damage types in composite laminates are delamination and impact damage. Two types of delamination dependent on the through-the-thickness position will be examined. The first type is the delamination located near the surface, which generally induces local buckling under loading, and the second is the delamination at the mid-plane. Stiffness reduction of two types of delamination will be identified and extensive comments on the mechanism and the different behavior of these delaminations will be given. The last verification performed in the present study concerns real impact damage. Several techniques developed in the previous chapters will be validated on experimental measurements.

6.2 Identification of stiffness reduction on artificial damage

6.2.1 Removal of plies

As a first proof of principle experiment in the identification of the local stiffness reduction, a unidirectional T300/914 carbon-epoxy laminated plate was fabricated. The material properties are the same as the ones used for the undamaged plate in Chapter 3. The plate size is $190 \times 140 \text{ mm}^2$ and its thickness is 2.56 mm with 16 layers of prepreg.

To create an artificial damage, a $50 \times 50 \text{ mm}^2$ size FEP release film was inserted into the interface between the 2nd and 3rd plies during the laying up of the laminate (9.4% relative area of damage). After curing, the 1st and 2nd plies over the film were taken off using a knife blade. It is considered that this artificial damage has a similar effect as a bulge zone due to delamination. The stiffness reduction in this case is about 30% and is indeed isotropic, corresponding to the model assumed in section 5.2.1.1.2.

The same experimental implementation as used in Chapter 3 was conducted. A special thin resin coating (gel coat) was applied to the surface of the specimen to make it specular (mirror-like). The original deflectometry set-up shown in Fig. 1.1 was used to perform the test. The plate is tested in bending according to the load configuration in Fig. 6.1. This configuration will be used for the rest of the experiments. The pitch of the reference grid is 2 mm, as recommended from section 5.2.1.2.5. The composite plate is supported by specially designed point grips to give simple support conditions and the load is applied by a load sensor developed in-house. The applied load was 6.5 N. The data acquired from the experiment was processed using the same procedure described in Chapter 3.

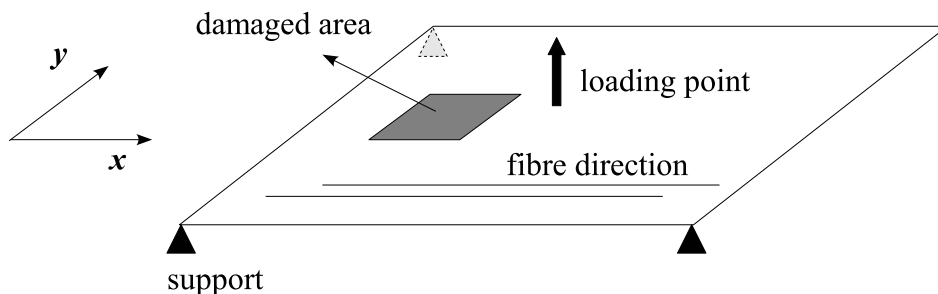


Figure 6.1: Geometry and test configuration of the damaged plate.

The slope and strain fields from the experiment are shown in Figs. 6.2 and 6.3. The strain fields were obtained from the slopes by numerical differentiation after spatial smoothing. Here, 14th order polynomials were used for the smoothing as determined in section 5.2.1.2.1. As shown in Fig. 6.3, ε_{11} is of the order of 10^{-5} as ε_{22} and ε_{66} are of the order of 10^{-4} . This is caused by the high anisotropy of the carbon unidirectional plate and means that the present situation is probably the most difficult one. Any plate with a lower anisotropy will be much easier to deal with.

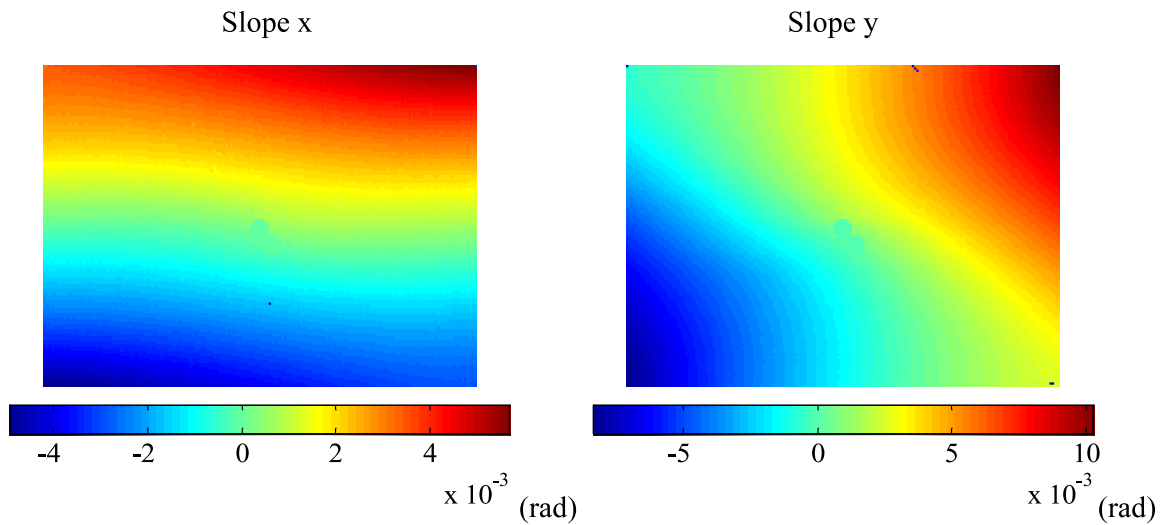


Figure 6.2: Experimental slope field data.

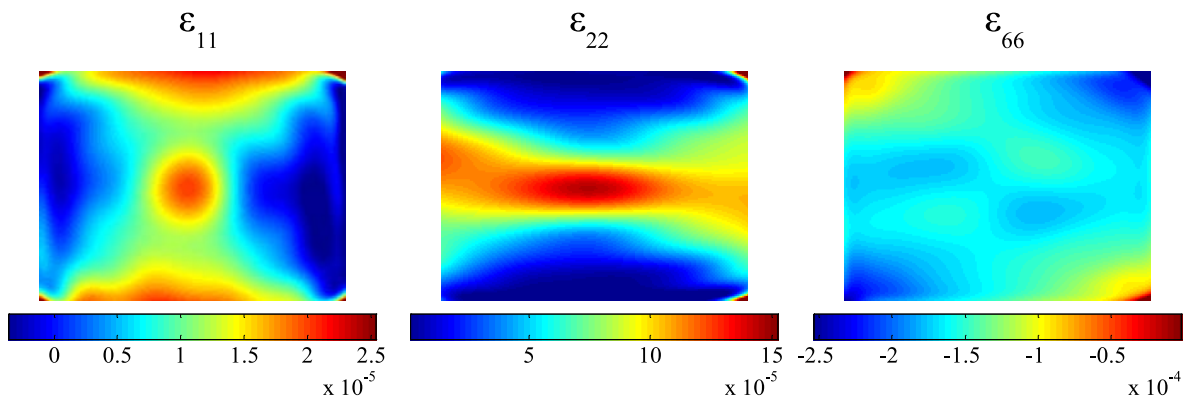


Figure 6.3: Experimental strain field data.

6.2.1.1 Polynomial parameterization

The first experimental result of identification of local stiffness reduction on the damaged plate using polynomial parameterization is shown in Fig. 6.4. It can be seen that the result from the experiment is similar to those from the previous numerical simulations in Chapter 5. Interestingly, the damage zone is indeed reasonably located and with a stiffness reduction corresponding to expectations. However, as can be seen in Figs. 6.4 and 6.5, the identified damage zone is slightly shifted to the right compared to the exact one. It is thought that this effect is mainly due to the low κ_{11} curvature (carbon UD is highly anisotropic) which induces poor sensitivity in the x direction. It must be emphasized that the present case, with high anisotropy and small stiffness contrast is a very demanding one. Nevertheless, this first result is very promising.

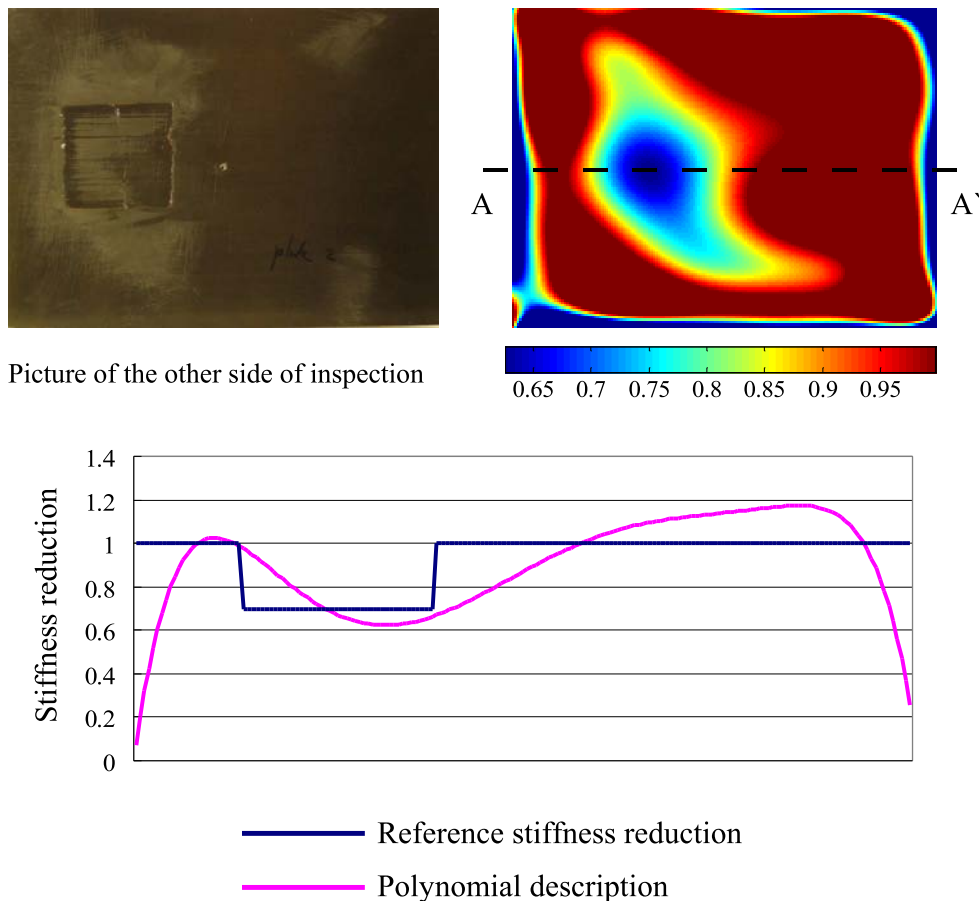


Figure 6.4: First experimental result for a damaged composite plate.

6.2.1.2 Discrete parameterization

The idea now is to check the output of a discrete parameterization. Two cases were studied: the first one corresponding to a situation where the exact location and extent of the damage was used (Fig. 6.5 (a)) and the second where the damage location and extent were determined from the polynomial approach (Fig. 6.5 (b)). For the second case, a criterion is required to designate the damage location from the polynomial. In order to choose a criterion, the polynomial description on a simulated stiffness reduction was examined in relation to damage threshold. When a square damage having 30% stiffness reduction is located at the center of the plate, the damage threshold of the polynomial description which is the closest to exact damage location was observed as half of the maximum stiffness reduction described by the polynomial function. Consequently, in this case the square is centered on the minimum of the polynomial and its size is adjusted manually to a 18% damage threshold (half of the maximum stiffness reduction, 36% in the damage map, see Fig. 6.4). It should be noted that since the type (smooth, abrupt) and severity of the damage are unknown *a priori* in a real case, this criterion should be tested and the corresponding results analyzed. An alternative method is to use other damage detection techniques, like C-scan, which can trace exact damage location.

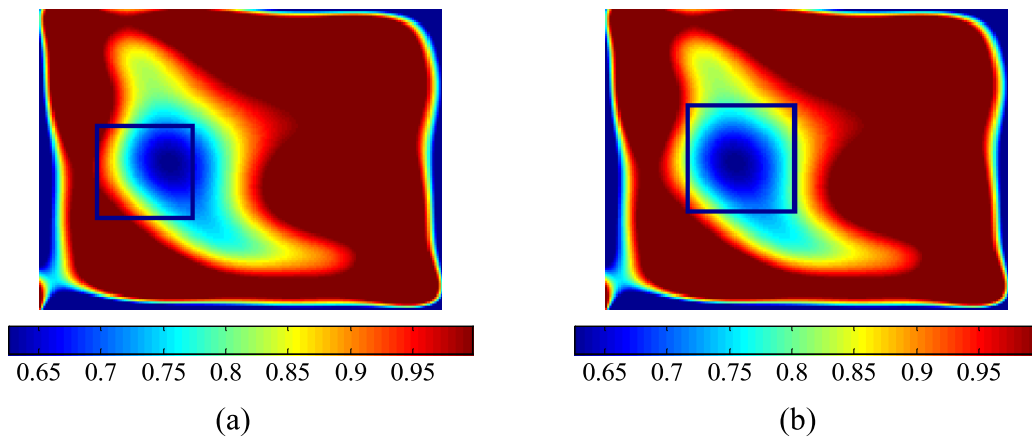


Figure 6.5: Damaged area (left: exact damaged area, right: chosen damaged area).

6.2.1.2.1 Isotropic damage Three spatial descriptions for the damaged zone were tested: the first one used one element for the whole damaged area, the second one, four elements, and the third one, nine elements. The identification results for stiffness reduction are shown in Figs. 6.6, 6.7 and 6.8. In the case of one element, it is observed that the stiffness reduction is 21% for the identified region, and 27% for exact region, while the

theoretical reduction is about 30%. This result is reasonable considering the rather low stiffness contrast and the small damaged area. As the number of elements increased, the results became more unstable. These results are mainly owing to the facts that the damaged area of interest is not large enough to have sufficient spatial information (the identification area for each piece is very small) and the stiffness contrast in this case is rather low. Increasing the number of elements will only be reasonable for the cases having stronger spatial information and stiffness contrasts.

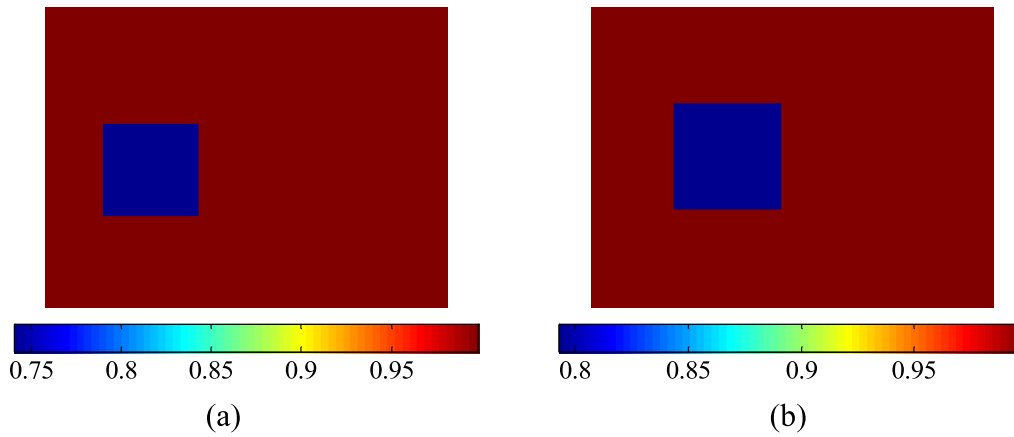


Figure 6.6: Stiffness identification results with 1 piece (left: exact damaged area (0.73), right: identified damaged area (0.79)).

6.2.1.2.2 Anisotropic damage The next verification was to identify eight rigidities (four for the undamaged zone and four for the damage zone) simultaneously. The identified results and the corresponding $\frac{\eta^\alpha}{D_{ij}}$ sensitivity values are presented in Tabs. 6.1 and 6.2. $\frac{\eta^\alpha}{D_{ij}}$ is the sensitivity of the VFM to a random noise with $\alpha = a, b, c, d$ respectively for D_{11} , D_{22} , D_{12} , D_{66} . This indicates that the lower the value of $\frac{\eta^\alpha}{D_{ij}}$, the more accurate the identification result (see section 2.1.1.5). It can be seen that the sensitivity values $(\frac{\eta^b}{D_{22}})^d$ and $(\frac{\eta^d}{D_{66}})^d$ are much lower than that of $(\frac{\eta^a}{D_{11}})^d$. This designates a poor identification of D_{11}^d and a good identification of D_{22}^d and D_{66}^d . As expected, the stiffness reduction is 26.9% (-4.4% relative difference from the reference of damaged rigidity, see Tab. 6.1) for the identified region and 31.7% (2.5%) for the exact region in the case of D_{22}^d , while the theoretical reduction is about 30%. However, in the case of D_{66}^d , the stiffness reduction is 56.9% (38.5%) for the identified region and 47.9% (25.6%) for the exact region. In spite of low sensitivity value, the identification results of D_{66}^d show large deviation.

	D_{11}^u	D_{22}^u	D_{12}^u	D_{66}^u	D_{11}^d	D_{22}^d	D_{12}^d	D_{66}^d
Reference	181.9	13.4	4.55	6.57	127.3	9.38	3.19	4.59
Exact	150.5	13.3	3.93	6.83	84.8	9.15	4.04	3.42
R.D. (%)	17.3	0.70	13.7	-4.0	33.4	2.5	-26.8	25.6
Identified	150.3	13.2	3.96	6.89	144.1	9.79	0.94	2.83
R.D. (%)	17.4	1.20	13.1	-4.9	-13.2	-4.4	70.6	38.5

Table 6.1: Comparison of results from exact damage location and identified damage location (D^u : stiffness for undamaged area, D^d : stiffness for damaged area, R.D.: Relative Difference, units for D : Nm^2).

	$(\frac{\eta^a}{D_{11}})^u$	$(\frac{\eta^b}{D_{22}})^u$	$(\frac{\eta^c}{D_{12}})^u$	$(\frac{\eta^d}{D_{66}})^u$	$(\frac{\eta^a}{D_{11}})^d$	$(\frac{\eta^b}{D_{22}})^d$	$(\frac{\eta^c}{D_{12}})^d$	$(\frac{\eta^d}{D_{66}})^d$
Exact	0.59	0.13	2.14	0.07	10.5	0.57	12.9	1.16
Identified	0.62	0.15	2.13	0.08	6.58	0.99	97.5	1.61

Table 6.2: Sensitivity values for each stiffness in exact and identified damage location ($(\frac{\eta}{D})^u$: for undamaged area, $(\frac{\eta}{D})^d$: for damaged area).

The first possible explanation for the deviation could be that the accuracy of the identified rigidities in the undamaged region strongly influences that in the damaged region since both rigidities are correlated to each other in the same equation. The deviation in the identification of D_{66}^u might have significantly deteriorated the accuracy of identified D_{66}^d . The second could be that the reconstruction of the missing data of the reflected hole image with polynomial curve fitting might have disordered the surrounding local field. This may have affected the shear information especially. This will be further discussed in the next section.

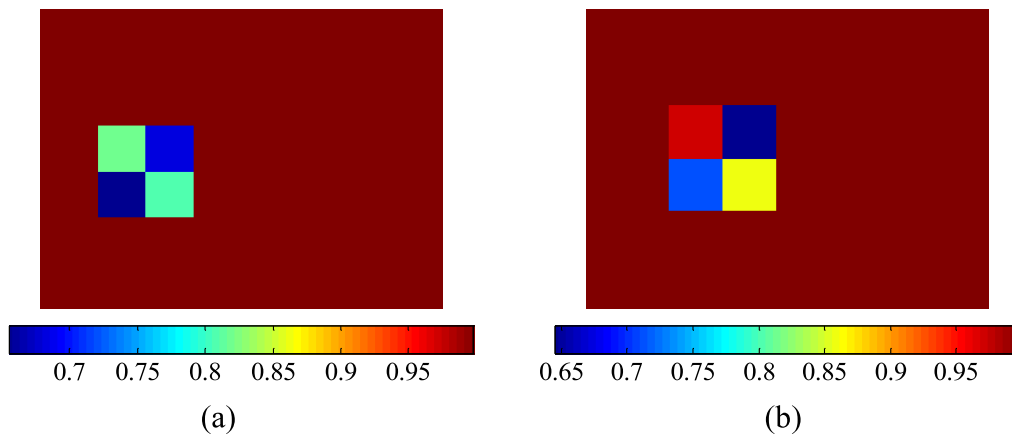


Figure 6.7: Stiffness identification results with 4 pieces (left: exact damaged area (0.65, 0.82, 0.68, 0.81, from lower left corner, clockwise direction), right: identified damaged area (0.71, 0.97, 0.64, 0.86)).

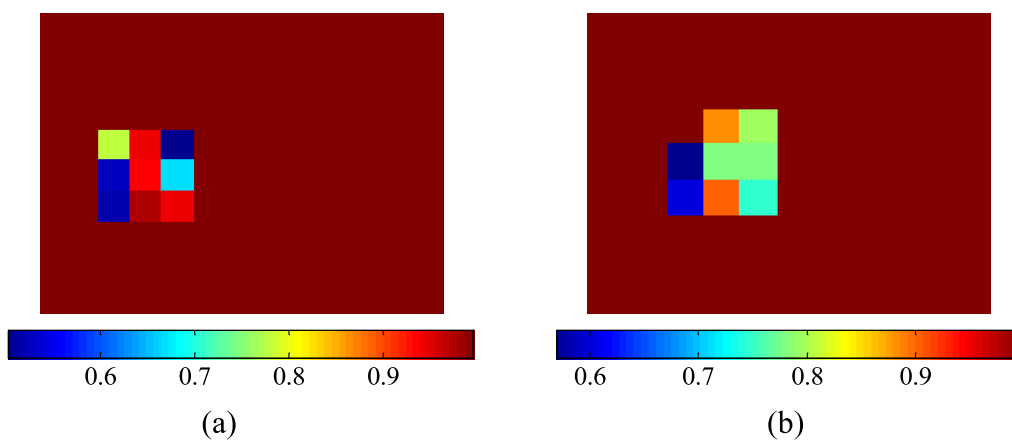


Figure 6.8: Stiffness identification results with 9 pieces.

6.2.2 Near-the-surface delamination

The next experimental validation was to identify the local stiffness reduction of a near-the-surface delamination having a bulge zone.

As discussed in Chapter 4, delaminations are usually generated between the layers with different fibre orientations, not between the layers in the same lay-up angle. In order to investigate realistically the effect of delamination, a cross-ply THR160/EH84 carbon epoxy laminated plate was fabricated. The plate size is $150 \times 120 \text{ mm}^2$ and its thickness is 2.5 mm with 16 layers of prepreg. A $40 \times 40 \text{ mm}^2$ size FEP release film was inserted into the two interfaces between the 1st - 2nd and 2nd - 3rd plies during fabrication of the laminate to create the near-the-surface delamination (8.9% relative area of damage). After curing the laminates, bulging (*i.e.* the surface was not flat) was observed on the area of the surface where the FEP release film was inserted.

The reference rigidity values of THR160/EH84 prepreg were not found in the literature. Thus, the undamaged stiffness values were identified from a unidirectional THR160/EH84 plate using the procedure described in Chapter 3. The identified results, depending on the camera position (behind the grid or beside the grid) are listed in Tab. 6.3. It was shown in section 3.2.3.6 that the identified results with offset camera position are closer to reference rigidities. Accordingly, the identified rigidities with the offset camera position (Tab. 6.3 (b)) will be used as a reference for the case of THR160/EH84 laminated plates. The reference rigidities of cross-ply plate were calculated from those of UD plate using classical lamination theory.

	D_{11} (Nm ²)	D_{22} (Nm ²)	D_{12} (Nm ²)	D_{66} (Nm ²)
Identified (a)	150.7	12.6	4.19	5.72
Identified (b)	138.2	12.5	3.96	5.7
R.D. (%)	8.25	0.12	5.61	0.33

Table 6.3: Identified stiffness components for a THR160/EH84 UD plate (a) with original camera position (spatial smoothing) (b) with offset camera position (without spatial smoothing, after calibration).

This time, two camera positions (*i.e.* central and offset) in deflectometry were used in order to further investigate the large deviation of identified D_{66}^d in section 6.2.1.2.2. The maximum possible load magnitude with the given cross-ply composite specimen was found

to be approximately 15 N. Consequently, the applied load was chosen as 15 N. The three strain components ε_{11} , ε_{22} and ε_{66} are compared between the cases with spatial smoothing and without spatial smoothing in Fig. 6.9 (the same scale is used to represent both results). A significant difference can be seen in terms of spatial resolution. In this case, all strain components are of the order of 10^{-4} , resulting in more balanced strain fields because of the cross-ply laminate.

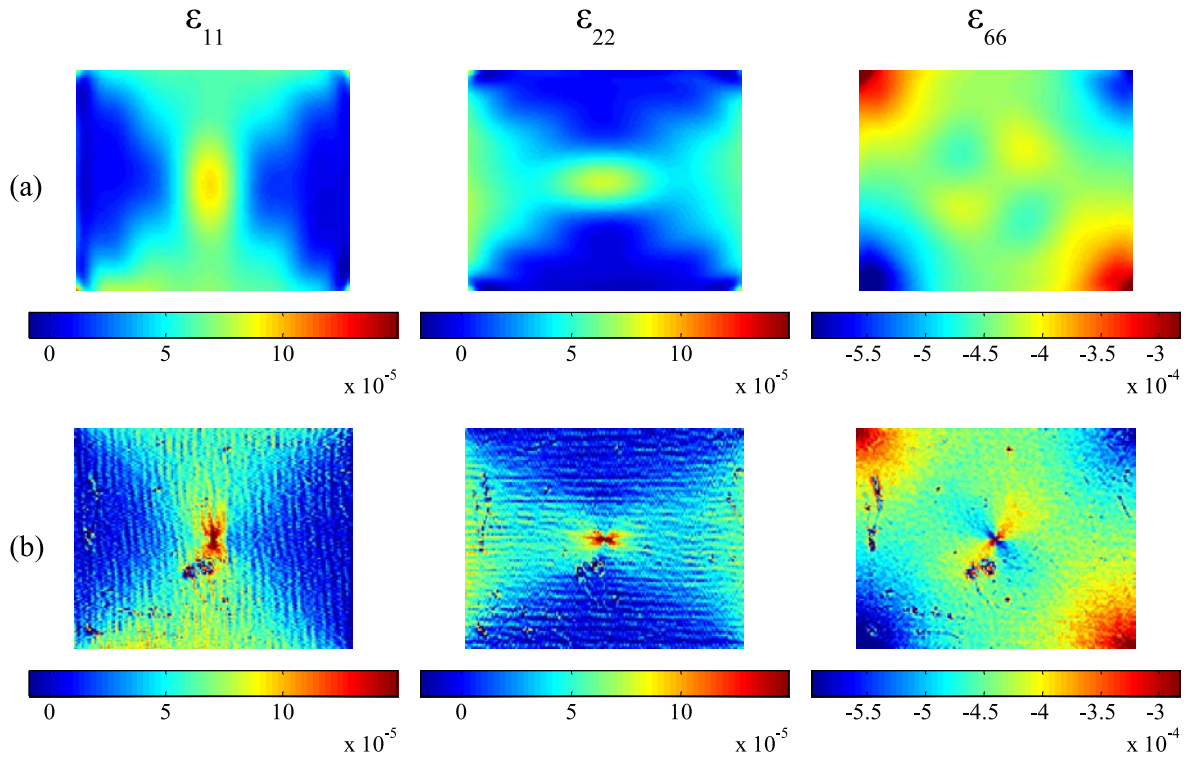


Figure 6.9: Comparison of strain fields between the cases (a) with original camera position (spatial smoothing, 14th order) (b) with offset camera position (without spatial smoothing).

6.2.2.1 Polynomial parameterization

The results of local stiffness reduction detection on the near-the-surface delamination are shown in Fig. 6.10. It can be seen that the damage zone is correctly located and with a stiffness reduction corresponding to expectations (about 30%, assumes zero stiffness in the delaminated plies due to the bulging) in both cases. Owing to the lower anisotropy of the cross-ply plate than that of UD one, the identified location is closer to the real one. In addition, the identified location from offset camera position is more accurate than

that of original camera position. It can therefore be said that the reconstruction of the missing data, which in this case is close to the damage zone, has a significant impact on the damage location and that camera offset is preferable.

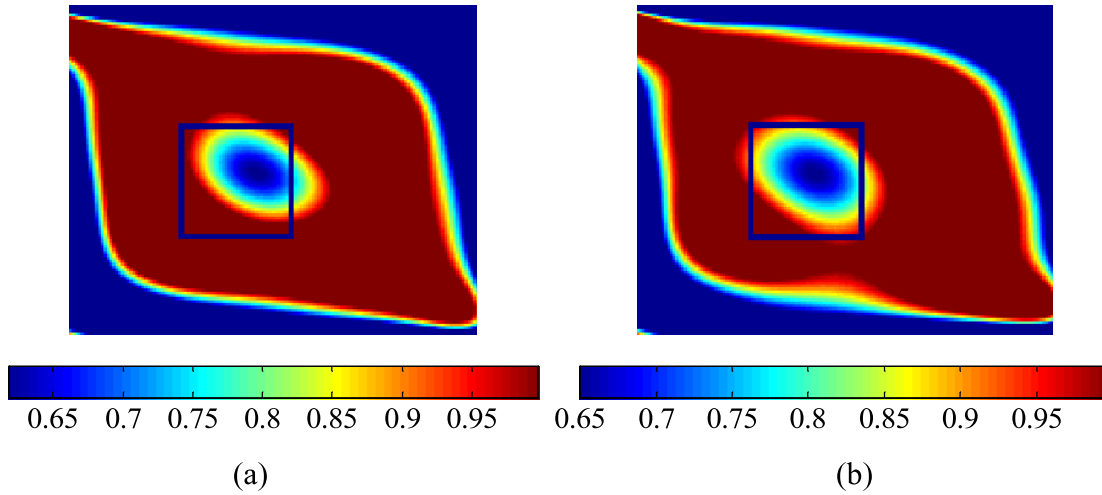


Figure 6.10: Identification of the stiffness reduction on the near-the-surface delamination with (a) original camera position (spatial smoothing) including exact damaged area (b) offset camera position (without spatial smoothing) including exact damaged area.

6.2.2.2 Discrete parameterization

The next step was to identify eight rigidities simultaneously for the near-the-surface delamination. The identified results and the corresponding sensitivity $\frac{\eta}{D}$ values are presented in Tabs. 6.4 and 6.5. It can be seen that the sensitivity values $((\frac{\eta^a}{D_{11}})^d)$, $(\frac{\eta^b}{D_{22}})^d$, and $(\frac{\eta^d}{D_{66}})^d$ are much more balanced in this case owing to the lower anisotropy.

In the case of the offset camera position, the identified D_{11}^d and D_{22}^d rigidities are closer to the reference values than those of the original camera position. However, D_{66}^d values obtained from both cases are still far from expectation in spite of lower sensitivity values. From the above observations, it is thought that the inaccurate identification of D_{66}^d in section 6.2.1.2.2 is mainly due to the insufficient spatial information. As discussed in section 5.2.1.3, only when the force is applied to the upper right area of the given configuration can the D_{66}^d stiffness reduction be identified. The identification of each stiffness in a small local area is possible only when the area has sufficient spatial stress information. Nonetheless, the lower sensitivity value of D_{66}^d is still a question, this will have to be investigated in more depth in the future.

	D_{11}^u	D_{22}^u	D_{12}^u	D_{66}^u	D_{11}^d	D_{22}^d	D_{12}^d	D_{66}^d
Reference	86.7	63.3	3.94	5.67	60.7	44.3	2.76	3.97
Identified (a)	80.6	73.5	0.62	5.17	71.8	40.6	2.83	6.20
R.D. (%)	7.1	-16	84	8.8	-18	8.3	-2.6	-56
Identified (b)	79.2	73.3	1.43	5.18	65.6	41.1	4.41	5.88
R.D. (%)	8.7	-15	63	8.6	-8.1	7.3	-60	-48

Table 6.4: Comparison of results from exact damage location (a) with original camera position (spatial smoothing) (b) with offset camera position (without spatial smoothing) (D^u : stiffness for undamaged area, D^d : stiffness for damaged area, units for D : Nm^2).

	$(\frac{\eta^a}{D_{11}})^u$	$(\frac{\eta^b}{D_{22}})^u$	$(\frac{\eta^c}{D_{12}})^u$	$(\frac{\eta^d}{D_{66}})^u$	$(\frac{\eta^a}{D_{11}})^d$	$(\frac{\eta^b}{D_{22}})^d$	$(\frac{\eta^c}{D_{12}})^d$	$(\frac{\eta^d}{D_{66}})^d$
(a)	0.29	0.36	19.6	0.13	1.20	2.95	34.2	0.68
(b)	0.27	0.34	7.96	0.12	1.08	2.58	18.5	0.66

Table 6.5: Sensitivity values for each stiffness in exact damage location (a) with original camera position (spatial smoothing) (b) with offset camera position (without spatial smoothing).

6.2.3 Mid-plane delamination

The next experimental verification performed in the present study concerns the stiffness reduction of mid-plane delamination. Before further discussion, it should be mentioned here that very peculiar behaviors were observed from the mid-plane delamination.

For the experiments, a UD THR160/EH84 carbon epoxy laminated plate with embedded mid-plane delamination was fabricated. The plate size is $150 \times 120 \text{ mm}^2$ and its thickness is 2.5 mm with 16 layers of prepreg. A double layer of FEP release film with size of $40 \times 40 \text{ mm}^2$ was inserted into the mid-interface during lay-up. After curing, a bending pre-load was applied to ensure the detaching of the film. The experimental implementation was performed using the offset camera position. The applied load was 15 N.

In order to validate the proposed FE model in section 5.3.1.1.1, the three curvature components κ_{11} , κ_{22} , and κ_{66} from the experimental measurements were compared with those from the FEA. The curvature fields are shown in Fig. 6.11. It is observed that the simulated curvatures (Fig. 6.11 (a)) are in good agreement with the experimental ones (Fig. 6.11 (b)) (the same scale is used to represent both results). It is considered that the current FE model describes accurately the characteristic of mid-plane delamination owing to the geometrical offset (kinematic discontinuity over the delaminated area) used in the FE model. From the experimental measurements (Fig. 6.11 (b)), the local curvature variations due to the stress concentration at the delamination crack tip can be observed clearly thanks to the high spatial resolution. Compared to the curvature fields from the plate containing near-the-surface delamination, the effect of delamination is more pronounced. On the other hand, the local high stress gradients cannot be observed on the curvature fields in the case of spatial smoothing (Fig. 6.11 (c)) due to loss of spatial resolution.

It is worth noting that though a number of studies have been performed on the effect of delamination including stress analysis with refined FE models, there has been limited research providing a direct comparison of FEA and experimental measurement as shown in Fig. 6.11, owing to the absence of proper measurement techniques. Thanks to the availability of the full-field measurement technique, the strain distribution in the presence of delamination can be investigated more thoroughly and the proposed FE model was validated efficiently.

6.2.3.1 Polynomial parameterization

The detection results of local stiffness reduction for the mid-plane delamination are shown in Fig. 6.12. Since the second moment of area (I) decreases with the third power of

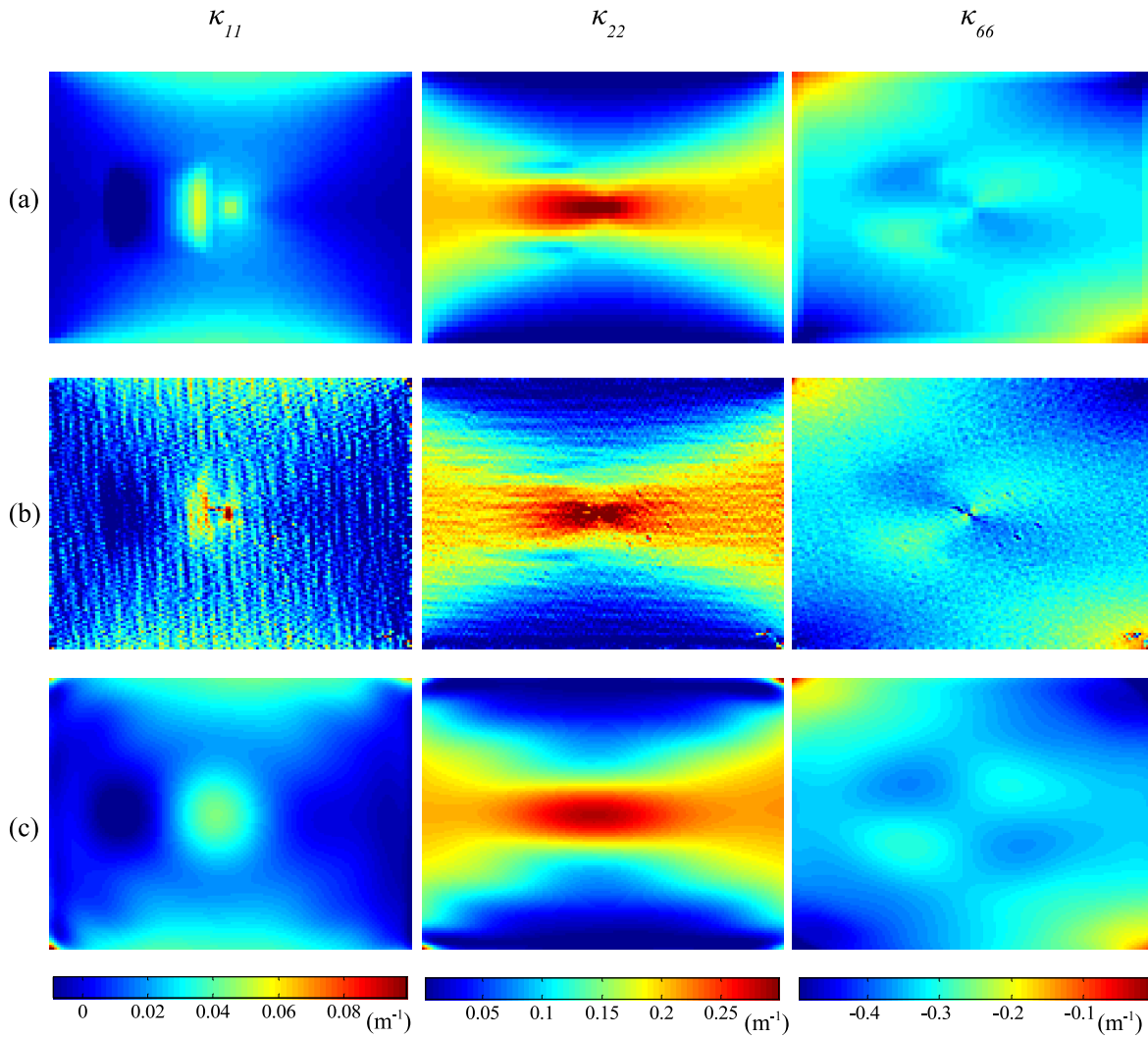


Figure 6.11: Comparison of curvature fields between (a) FEA and (b) the experiment, without spatial smoothing and (c) the experiment, with spatial smoothing (14th order).

thickness, much higher bending stiffness reduction was expected in the case of mid-plane delamination. Unexpected results were observed, however, both in location and stiffness reduction (see Fig. 6.12 (a)). The damage zone is not correctly located and the detected damage zone is elongated in the vertical direction. Despite the strong effect on the curvature field of the mid-plane delamination, the stiffness reduction is less than that of the near-the-surface delamination. In addition, though the curvature fields from the FE model are very close to those of the experimental measurements, the identified stiffness reduction with FE simulation (see Fig. 6.12 (b)) is less than that of experiment (see Fig. 6.12 (a)). As discussed in Chapter 3, there are two ways to obtain curvature fields from a FE software. The first is to use the relationship between the curvatures and top surface

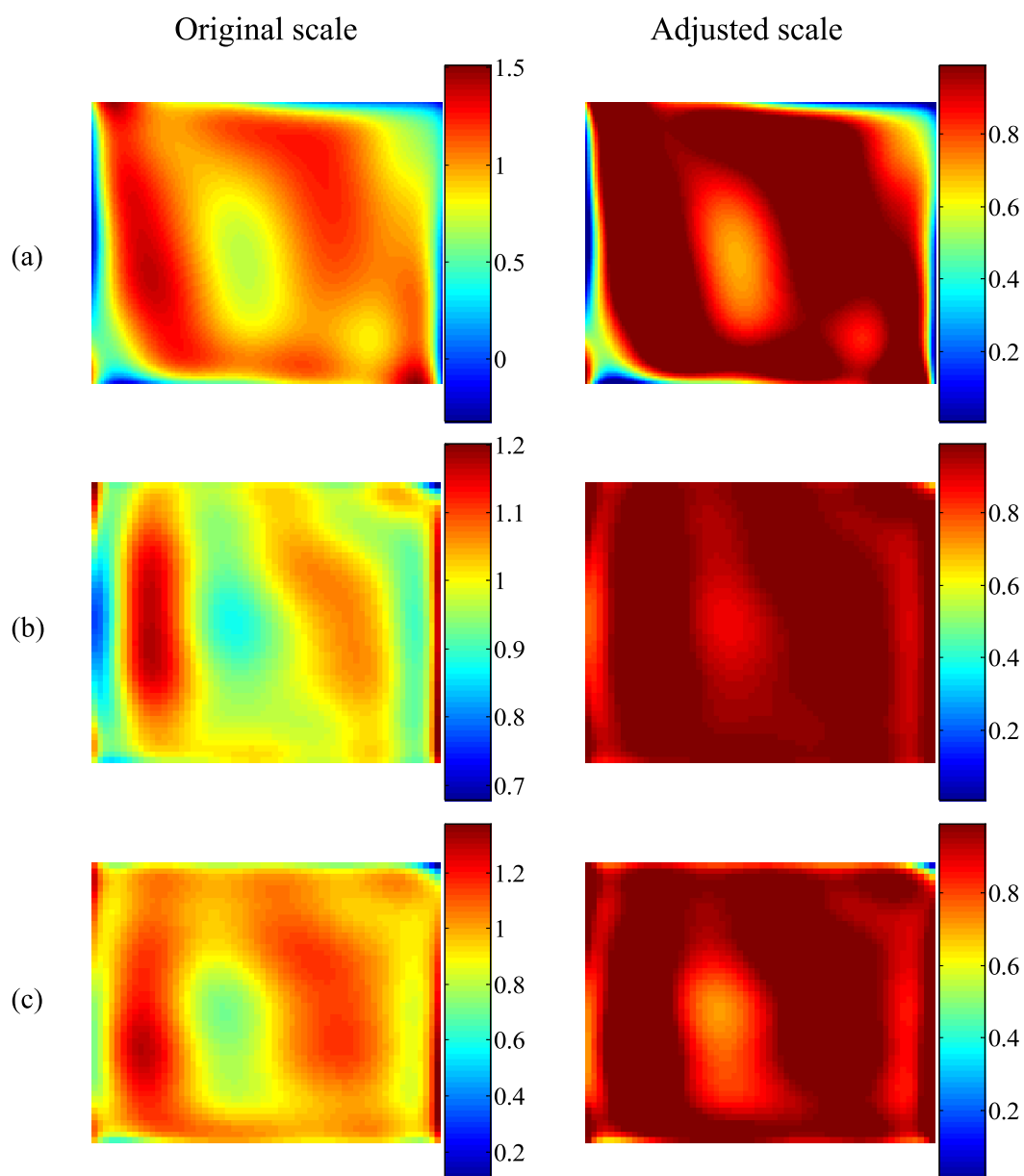


Figure 6.12: Comparison of stiffness reduction results between (a) experiment, and (b) FEA, using curvatures from strains, and (c) FEA, using curvatures from slopes.

strains (Eq. 3.1) from the Kirchhoff theory of thin plates. The second is to derive them from slope fields by analytical differentiation. The results in Fig. 6.12 (b) were obtained following the first procedure, and those in Fig. 6.12 (c) from the second. It can be seen that the identified result using the second method is much closer to that of the experiment. This will be further discussed in section 6.2.3.4.

6.2.3.2 Stress fields

In order to analyze the unexpected behaviour and the characteristics of the mid-plane delamination, the stress distribution in the x direction within each layer was examined using FE simulation. The sublaminate model utilizing two thin shell finite elements through-the-thickness direction (see section 5.3.1.1) was used for the stress analysis. The size of the plate is $190 \times 140 \text{ mm}^2$, with a nominal damaged area of $50 \times 50 \text{ mm}^2$. The material properties are the same as the ones used for the undamaged plate in Chapter 3. The applied load was 10 N. The stress distribution in the upper half (8 layers out of total 16 layers) is shown in Fig. 6.13.

A detailed stress analysis revealed that the stress field due to mid-plane delamination is significantly different from that due to other damage types. The comparison of the stress distribution on the top layer between the mid-plane delamination and other types of damage is illustrated in Fig. 6.14. For the mid-plane delamination and the half layers removal, the sublaminate model was used, and for other types of damage, the property degradation model (see section 5.2.1.1.1) was used. In the damage having bending stiffness reduction, the stress level over the damage zone is higher (stress increases) than that of the same area in the undamaged plate. If the reduction of bending stiffness increases, also the stress level increases. On the contrary, in the case of mid-plane delamination, a stress anomaly is observed on the left hand side of the delamination area. The stress reversal (negative stress) on the left hand side of mid-plane delamination is a very specific feature. Another interesting thing to note is that in the case of the damage with half layers removal (the lower sublaminate of mid-plane delamination removed), this stress anomaly disappears nearly completely. The behaviour of the damage with half layers removal will be discussed more in section 6.2.3.4 in conjunction with mid-plane delamination.

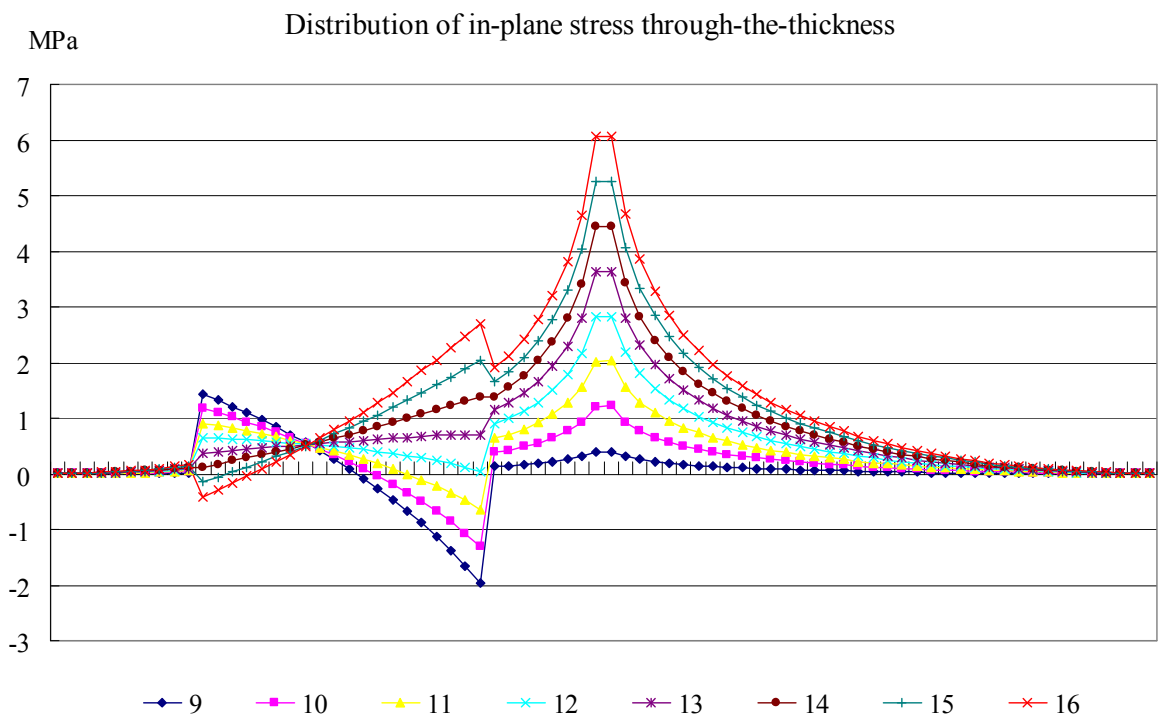
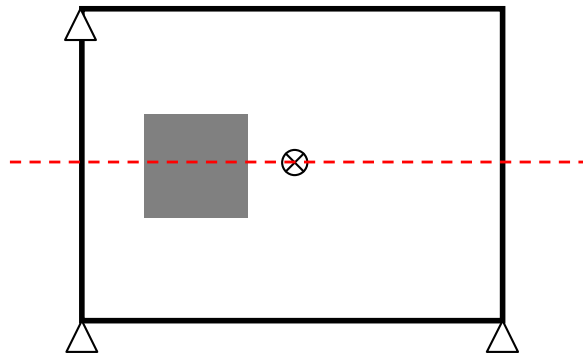


Figure 6.13: Stress distribution in the x direction within each layer (FEA).

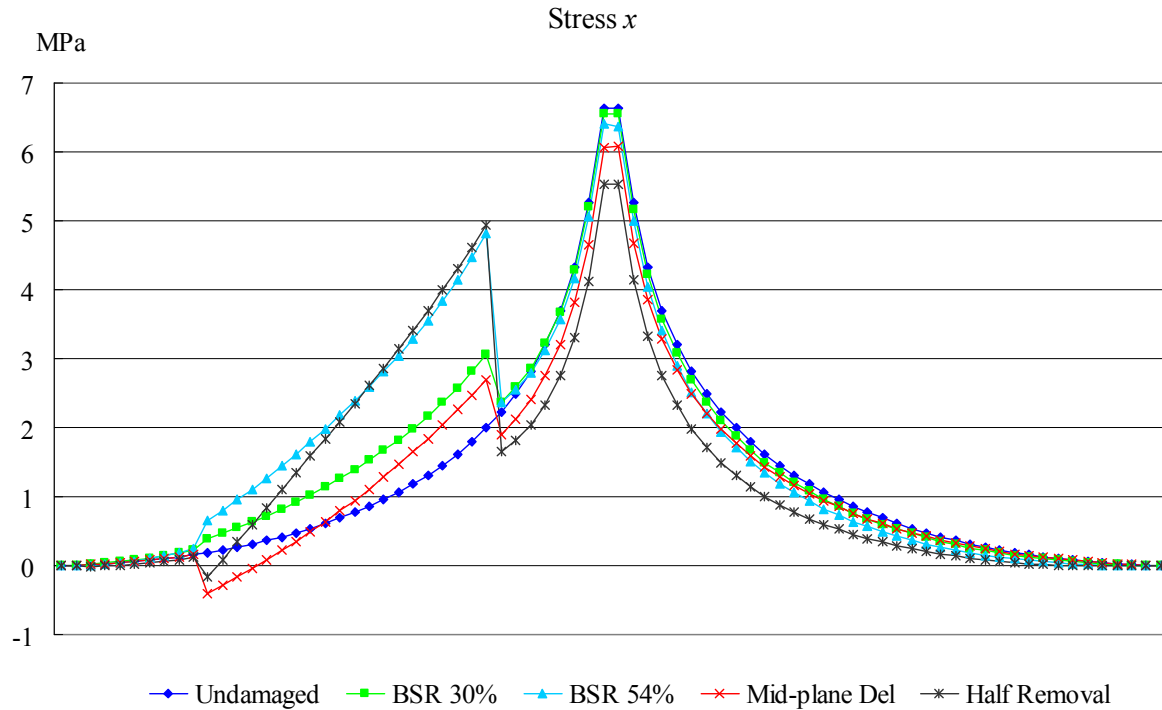


Figure 6.14: Comparison of stress fields in the x direction between several damage types (FEA, BSR: bending stiffness reduction).

As discussed in Chapter 2, when there is a localized damage in a composite laminated plate, the damage redistributes the stress fields around the damaged area. Since the VFM utilizes the global equilibrium of a given specimen having specific force and boundary conditions, it examines the stress fields all over the specimen. Consequently, it can recognize any abnormal state of stress due to the damage using the given geometry, loading, and boundary conditions. In the case of mid-plane delamination, the VFM recognizes the higher stress as stiffness reduction and the abnormal lower stress as stiffness increase. On the damage map (see Fig. 6.12), one can see stiffness reduction on the right hand side of the delamination, and stiffness increase on the left hand side due to the stress reversal.

6.2.3.3 Slope fields

To further investigate the stress anomaly (negative stress) on the left hand side of mid-plane delamination, the variation of slope field in the experimental measurement was examined. The slope field in the x direction is shown in Fig. 6.15. In this case, sharp transition of the slope field was observed.

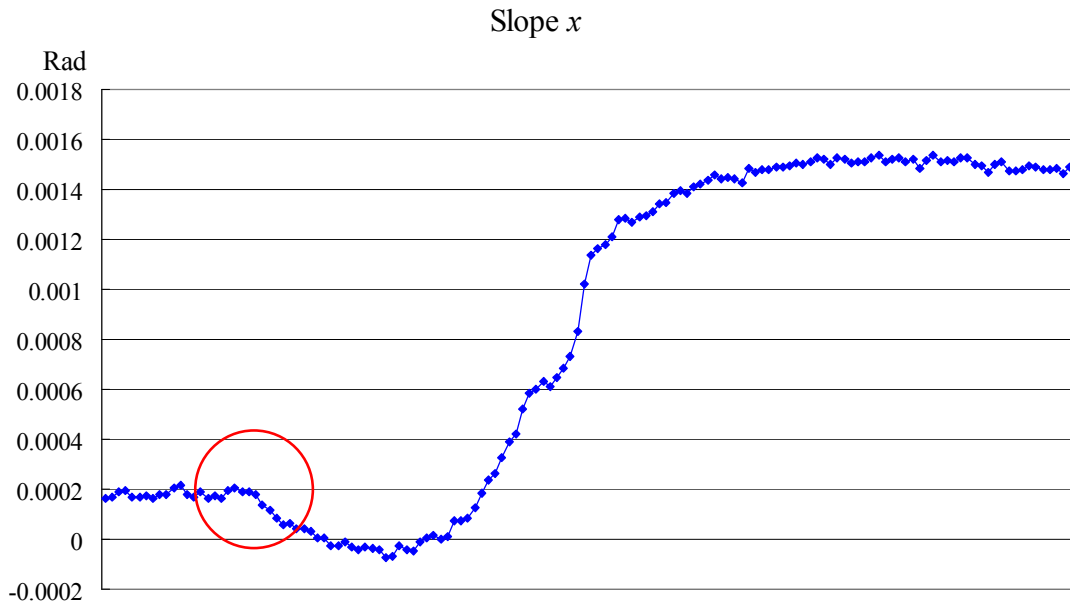


Figure 6.15: Experimental slope field in the x direction of mid-plane delamination.

In order to further discuss this behaviour, the slope fields in the x direction are compared between several types of damage using FE simulation in Fig. 6.16. The slope value is negative in FEA while positive in the experimental measurement. This is caused by some solid rotation adding up when the plate is loaded, because of the specimen settling in on the support. In the 30% and 54% bending stiffness reduction cases, no abrupt change of slope field is observed. The stress anomaly occurs only in the damage types including sharp transition of the slope field (mid-plane delamination and half layers removal). This peculiar behaviour may be associated with interlaminar shear and has to be studied in future.

6.2.3.4 Discussion on the current methodology

The current methodology with the adapted VFM utilizes the Kirchhoff plate kinematic assumption of linear through-the-thickness displacement distributions. In the case of mid-plane delamination (kinematic discontinuity), this kinematic assumption is no longer valid. This is illustrated in Fig. 6.17. Consequently, the current methodology has shown unsatisfactory identification for the case of mid-plane delamination.

The damage type which attracts considerable attention is the half layers removal case. Ideally, the bending stiffness reduction is 87.5% in this case. The identification result

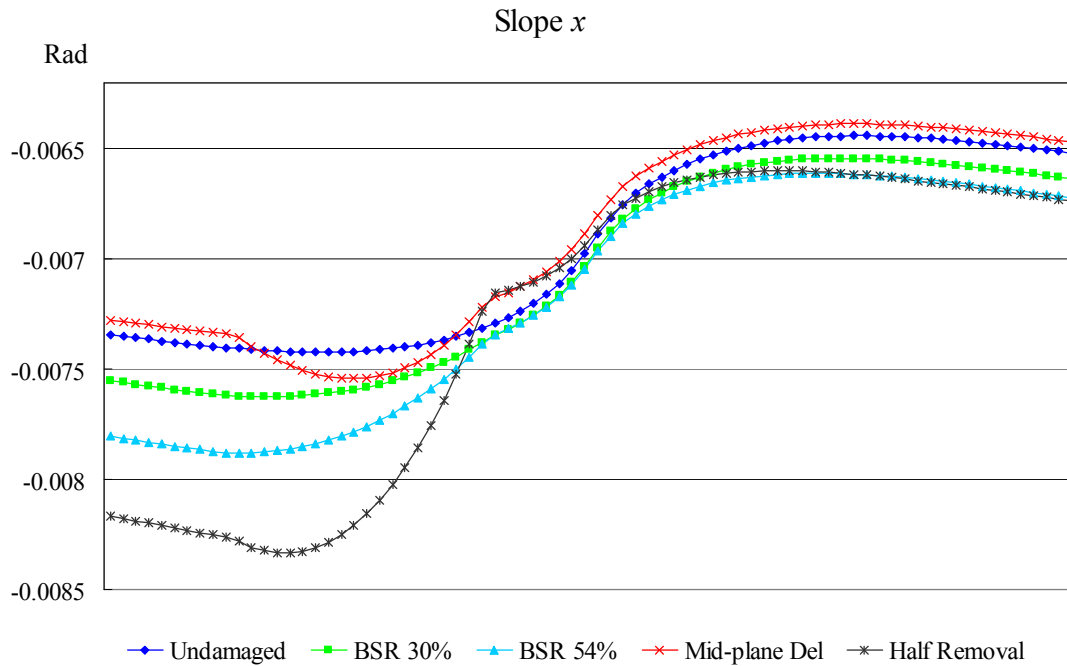


Figure 6.16: Comparison of slope fields in the x direction between several damage types (FEA, BSR: bending stiffness reduction).

of stiffness reduction of this damage is presented in Fig. 6.18. In this case, the damage zone is correctly located and with a stiffness reduction corresponding to expectation. Although this damage involves stress anomaly and significant mid-plane shift, the kinematic assumption of linear through-the-thickness displacement distributions is still valid (see Fig. 6.19), so that the current methodology is able to detect this type of damage.

In view of the above observation, it can be concluded that if a damage does not violate the kinematic assumption, it can be identified with the current methodology in a satisfactory manner. Conversely, if the through-the-thickness displacement distribution is significantly non-linear, then the current methodology cannot yield a correct identification. It is considered that however, in a real impact damage, the delaminations will be distributed through-the-thickness and the through-the-thickness displacement would be more linear.

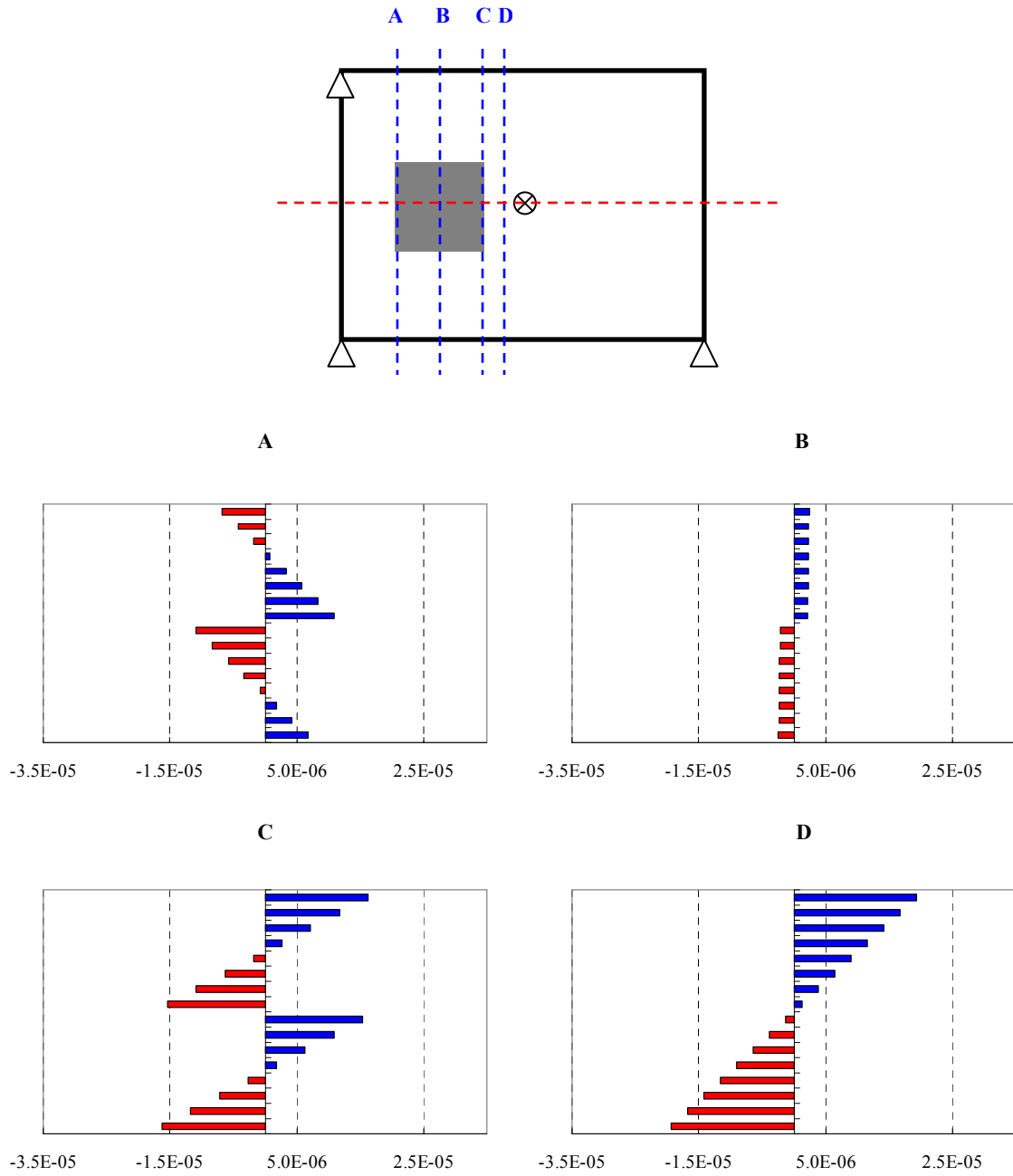


Figure 6.17: Through-the-thickness strain distributions in the mid-plane delamination.

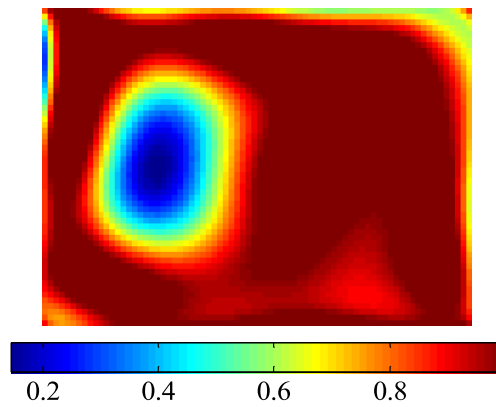


Figure 6.18: Identification of the stiffness reduction on the half layers removal (FE simulation).

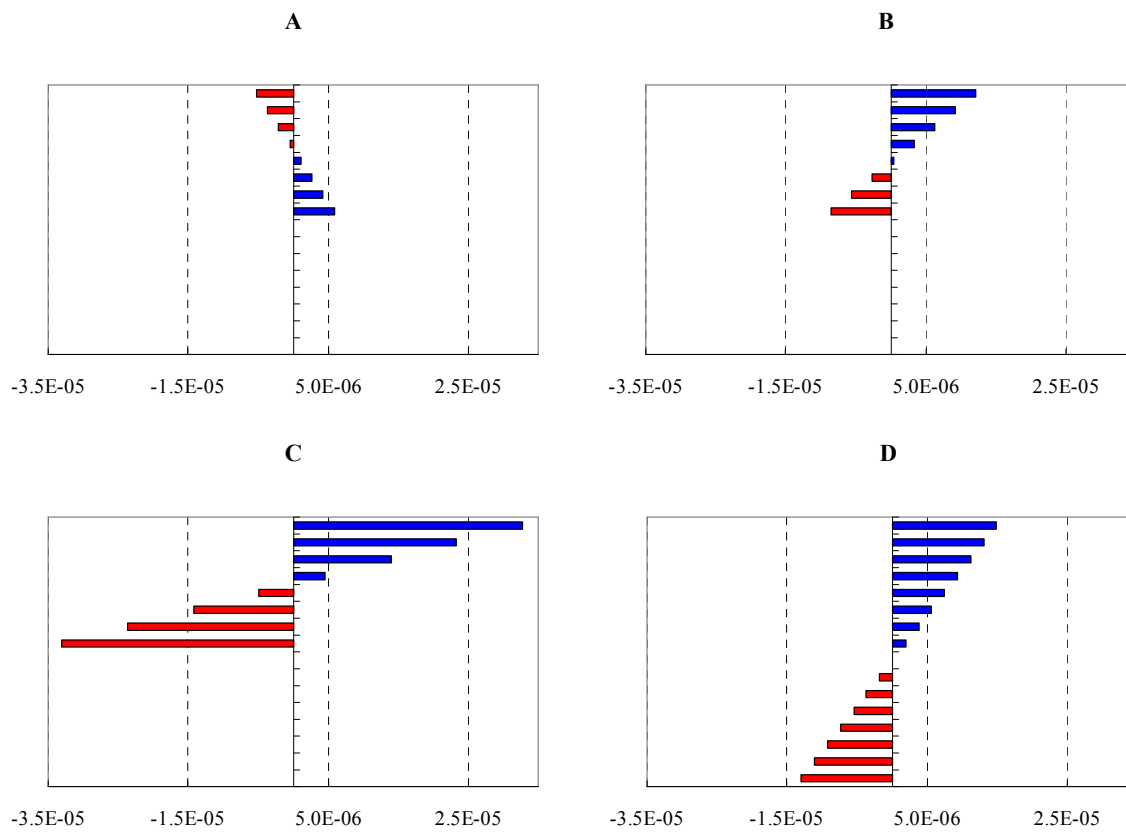


Figure 6.19: Through-the-thickness strain distributions in the half layers removal.

6.3 Identification of stiffness reduction on real impact damage

6.3.1 Impact test

The last experimental verification performed in the present study is real impact damage. A low velocity impact test was carried out on a cross-ply THR160/EH84 carbon epoxy laminated plate using a drop weight method. The plate size is $150 \times 120 \text{ mm}^2$ and its thickness is 2.5 mm with 16 layers of prepreg. A drop weight impactor with a spherical steelball of 28 mm diameter was used for the impact test. The plate was clamped on all four sides by a simple support fixture and the impact was applied directly to the plate. The impactor, with a total mass of 10 kg, was dropped from the distance of 20 cm above the specimen. The applied impact energy was about 20 J and the impact speed was 2 m/s, calculated from the potential energy. Reimpact due to rebounding of the impactor was prevented by holding the impactor after rebounding. The impactor and the test fixture are shown in Fig. 6.20.



Figure 6.20: Support fixture and impactor.

Barely visible impact damage (BVID) was observed on the surface of the specimen. Small indent was found on the impacted side and small bulging due to delamination on the obverse side of impact (see Fig. 6.21). The shape of the delamination was elliptical with the major axis extending parallel to the x direction of the specimen. The experimental implementation was performed according to the offset camera configuration. The applied load was 15 N.

When the thin resin coating was applied on the surface, image distortion due to the

indentation effect was observed on the impacted area as shown in Fig. 6.22. However, as can be seen in Fig. 6.23, this distorted image on the phase map was canceled out after subtraction between the undeformed and deformed images, owing to the differentiation process. It is interesting to note that the location of the indent perturbation remains the same after loading. This is because in this case, the light comes from the specimen's surface (and not the coating's surface). Therefore, it is caused by diffusive and not specular reflection, and is not sensitive to slope but deflection. It is different from the case of the image of the camera hole which was caused by the specular reflection on the coating and produced two separate holes in the initial and deformed images. This also confirms that some diffusively reflected light is present and may decrease the sensitivity of the measurements. It could be possible to use polarized light to improve this since polarization is kept by specular reflection but destroyed by diffusive reflection. Therefore, polarizing the lighting and using an analyzer in front of the camera to select the polarized light only would discard the light from the diffusive reflection and theoretically enhance the contrast. This will have to be investigated in more depth in the future.

With the given load of 15 N, there occurred many fringes on the deformed phase map, so that higher load will make the phase subtraction and unwrapping process difficult due to too many fringes.

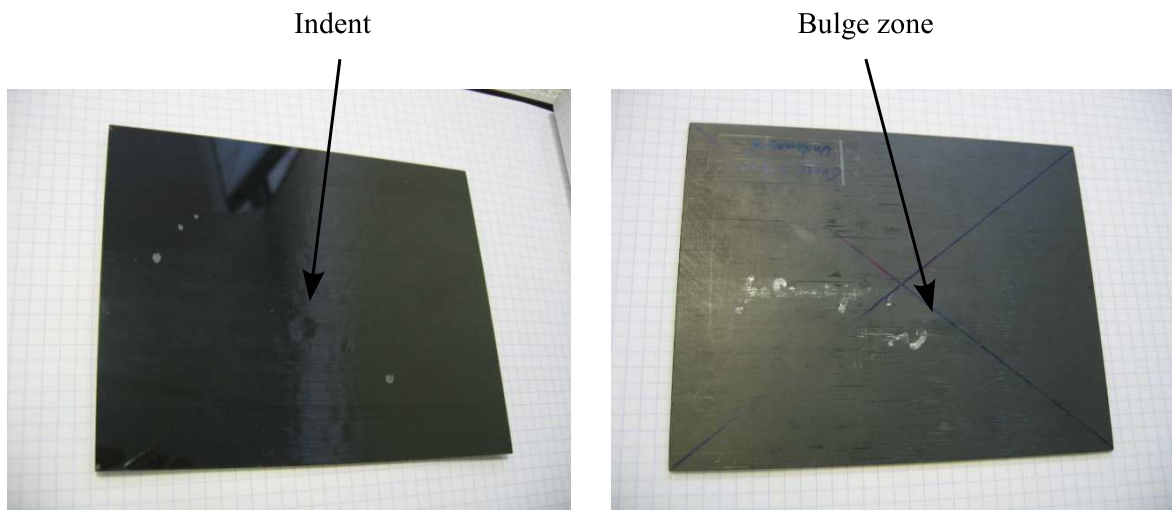


Figure 6.21: Small indent and bulge zone.

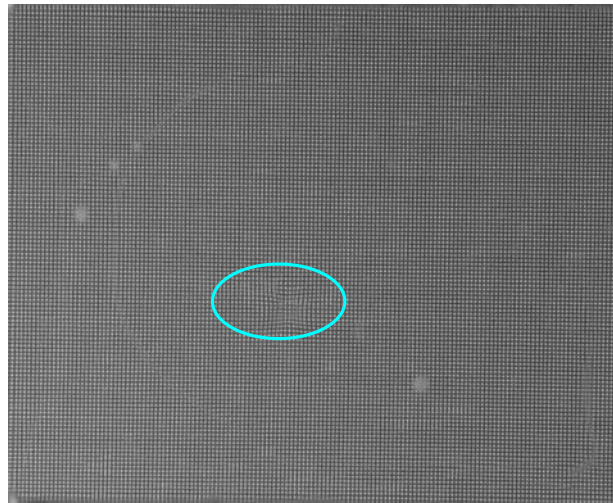


Figure 6.22: Image distortion on the impacted area.

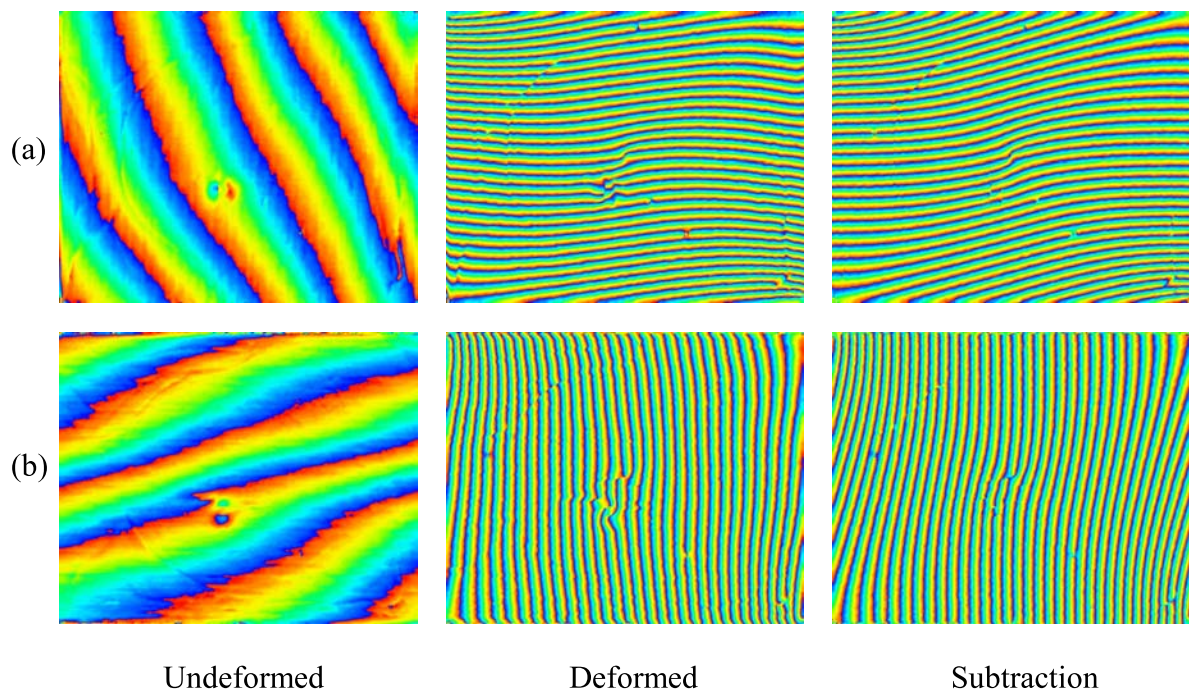


Figure 6.23: Phase field (a) x and (b) y.

6.3.2 Polynomial parameterization

The identification result of local stiffness reduction on the impacted plate is shown in Fig. 6.24. It is observed that stiffness reduction in this case is less than 10%. Despite the very small damage area and the low stiffness contrast, the damage zone is reasonably located and the elliptic form is retrieved. This also suggests that in a real impact damage, the delaminations will be distributed through-the-thickness and the problems encountered with mid-plane delaminations will be irrelevant. This will obviously have to be confirmed on a full study on real impacted plate with damage observation. It should be noted however that a stiffness contrast physically corresponds to local strain gradients. Indeed, a 10% stiffness variation corresponds to a local strain shift in the order of 10% of the local strain. This explains why such stiffness contrasts are so difficult to obtain and so sensitive to noise. The effect one has to detect here is one order of magnitude below the main effect (global bending of the plate). It is therefore very satisfactory that such a small effect can be detected here. This is due to both the quality of the measurements (deflectometry is very sensitive) and the polynomial parameterization of the damage distribution which provides the required amount of spatial smoothing.

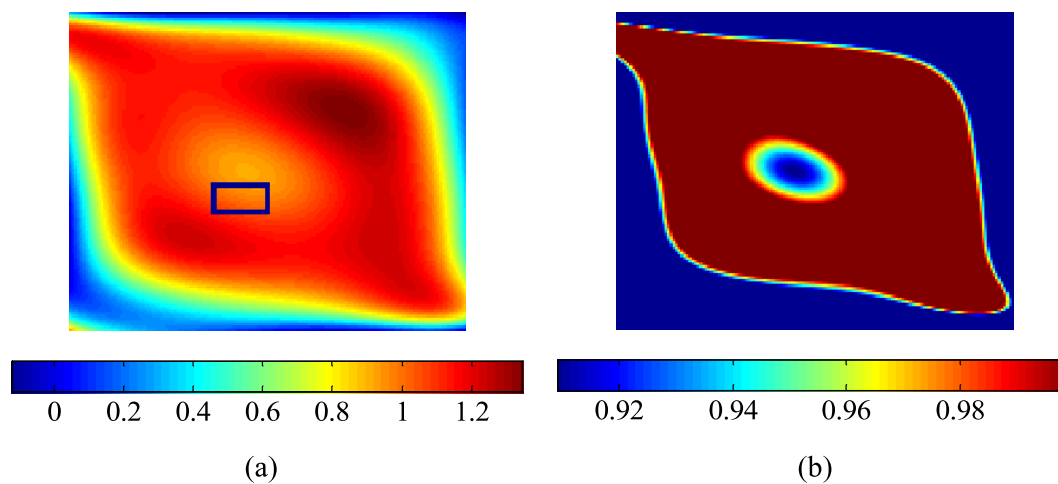


Figure 6.24: Identification of the stiffness reduction on the impact damage (a) with original scale (including exact location of impact damage, the location of the bulge zone was measured with a tape measure) and (b) with adjusted scale.

6.4 Conclusion

In this chapter, a wider validation of the proposed methodology against experimental data was presented, both on artificial and real impact damage in composite laminated plates. First, the results of local stiffness reduction detection on the near-the-surface delamination were presented. In this case, the damage zone is correctly located and with a stiffness reduction corresponding to expectations. The identified location and rigidities from offset camera position were more accurate than those of original camera position. Secondly, the proposed FE model for the mid-plane delamination in Chapter 5 was validated with experimental measurements. The simulated curvatures were in good agreement with the experimental ones. In the case of mid-plane delamination, unexpected results were observed, however, both in location and stiffness reduction. A detailed stress analysis revealed that the stress field due to mid-plane delamination is significantly different from that due to other damage types. It was realized that the Kirchhoff plate kinematic assumption of linear through-the-thickness displacement distributions used in the current methodology is no longer valid for mid-plane delamination. Finally, the identification result of local stiffness reduction on an impacted plate was presented. It was observed that stiffness reduction in this case is less than 10%. Despite the very small damage area and the low stiffness contrast, the damage zone was reasonably located and the elliptic form was retrieved.

General conclusions and perspectives

General conclusions

In this study, a new methodology has been applied to solve a damage detection problem in laminated composite plates. The identification of the local loss of stiffness was conducted by using the adapted Virtual Fields Method (VFM) as an inverse procedure to process curvatures obtained from full-field slope measurements. The main conclusions obtained in the present work are as follows.

- The deflectometry technique was used to measure full-field slope fields on the damaged plate. It was well suited for providing sufficient sensitivity of curvature variations for the purpose of the local damage detection. The original deflectometry configuration however requires polynomial curve fitting for the reconstruction of the missing data (reflected hole image), inevitably causing loss of spatial resolution. Because spatial resolution is very important in investigating the local fields, a new deflectometry configuration was developed and the required calibration for the new camera position was derived.
- The potential of the Virtual Field Method (VFM) to locate and quantify the local stiffness reduction in damaged composite plates was investigated. In the case of a plate with stiffnesses varying within the material, the VFM should be adapted. Two parameterization methods for the stiffness reduction were devised. The first one is to use a continuous approach. The use of polynomials was considered in this case. By using this approach, the 2D stiffness distribution map of a damaged carbon-epoxy plate was obtained. This map is very convenient to monitor the damage since the map not only locates the damage but also identifies the local stiffness reduction in the damaged area. The second is to use a discrete one. In

this case, the damage location and extent are determined by using the polynomial parameterization in a first stage and in a second step, a discrete approach is applied to identify each stiffness component directly in the areas detected by the polynomial. It was found that the identification of four bending stiffnesses directly in a local damaged area using discrete parameterization is feasible only when the area include sufficient spatial information for each stiffness.

- A wider validation of the proposed methodology against experimental data, both on artificial and real impact damage in composite laminated plates was presented. In the case of near-the-surface delamination, the damage zone was correctly located and with a stiffness reduction corresponding to expectations. The identified location from offset camera position was more accurate than that of original camera position. In addition, the identified D_{11}^d and D_{22}^d rigidities obtained from the offset camera position were closer to the reference values than those of the original camera position. It can therefore be said that the reconstruction of the missing data, which in this case is close to the damage zone, has a significant impact on the damage location and that camera offset is preferable. However, D_{66}^d values obtained from both cases were far from expectation in spite of lower sensitivity values.
- In the case of mid-plane delamination, a direct comparison of FEA and experimental measurement was presented. Thanks to the availability of the full-field measurement technique, the strain distribution in the presence of delamination can be investigated more thoroughly and the proposed FE model was validated efficiently. Unexpected results were observed, however, both in location and stiffness reduction. A detailed stress analysis revealed that the stress field due to mid-plane delamination is significantly different from that due to other damage types.
- It was realized that the Kirchhoff plate kinematic assumption of linear through-the-thickness displacement distributions used in the current methodology is no longer valid for mid-plane delamination. If a damage does not violate the kinematic assumption, it can be identified with the current methodology in a satisfactory manner. Conversely, if the through-the-thickness displacement distribution is significantly non-linear, then the current methodology cannot yield a correct identification.
- The identification result of local stiffness reduction on the real impacted plate was presented. It was observed that stiffness reduction in this case is less than 10%. Despite the very small damage area and the low stiffness contrast, the damage zone was reasonably located and the elliptic form was retrieved. This also suggests that in

a real impact damage, the delaminations will be distributed through-the-thickness and the problems encountered with mid-plane delaminations will be irrelevant.

Perspectives

- Deflectometry technique has shown very good performance in the present work. However, this technique has some limitation in the application to real structures owing to the surface preparation (resin coating). The other possibility would be to measure deflection (with ESPI, for instance) but then, the resolution of the identification will be limited by the double differentiation necessary to obtain curvatures. An interesting alternative would be to use quantitative shearography which can measure slope field directly.
- In the near-the-surface delamination, D_{11}^d and D_{22}^d rigidities were successively identified using discrete parameterization, however, D_{66}^d was far from expectation in spite of lower sensitivity value. It is thought that the inaccurate identification of D_{66}^d is mainly due to the insufficient spatial information. Nonetheless, the lower sensitivity value of D_{66}^d is still a question, this will have to be investigated in more depth in the future. In addition, in the case of real impact damage, the identification of each stiffness in the damaged region was not possible owing to the insufficient spatial information of the very small area. A new method which can increase local spatial information and the adapted VFM which can extract the information from the very local area are required. An interesting idea would be to combine several load cases to derive the stiffnesses.
- In the case of mid-plane delamination, a stress anomaly was observed on the left hand side of the delamination area. A detailed stress analysis revealed that the stress field due to mid-plane delamination is significantly different from that due to other damage types. In addition, sharp transition of the slope field was observed. The stress anomaly occurs only in the damage types including sharp transition of the slope field (mid-plane delamination and half layers removal). This peculiar behaviour may be associated with interlaminar shear and has to be studied in the future.
- Since the current methodology with the adapted VFM utilizes the Kirchhoff plate kinematic assumption of linear through-the-thickness displacement distributions, if the distribution is significantly non-linear, then the current methodology cannot yield a correct identification. This arises from the main limitation of the VFM

which is that the volume integrals need to be calculated from the measurement of surface strain since strain fields cannot be obtained inside the specimen. This may be overcome with the development of bulk full-field measurement techniques (OCT (optical coherence tomography) for glass fibre composites, for instance. A project is presently starting in collaboration with Loughborough University on this topic).

- When the thin resin coating was applied on the impacted area, image distortion due to the indentation effect was observed. This is because in this case, the light comes from the specimen's surface (and not the coating's surface). This also confirms that some diffusively reflected light is present and may decrease the sensitivity of the measurements. It could be possible to use polarized light to improve the measurements. Therefore, polarizing the lighting and using an analyzer in front of the camera to select the polarized light would discard the light from the diffusive reflection only and theoretically enhance the contrast. This will have to be investigated in more depth in the future.
- In the case of impact damage, the damage zone was reasonably located and the elliptic form was retrieved despite the very small damage area and the low stiffness contrast. This also suggests that in a real impact damage, the delaminations will be distributed through-the-thickness and the problems encountered with mid-plane delaminations will be irrelevant. This will obviously have to be confirmed on a full study on real impacted plate with damage observation. It would be very useful to have some better quantification of the damage, through ultrasonic C-scan imaging and by de-plying or cutting, and observing under a microscope. Then, a judgement could be made about whether the 10% reduction detected is reasonable.

References

- [1] M. GRÉDIAC. The use of full-field measurement methods in composite material characterization: interest and limitations. *Composites Part A: Applied Science and Manufacturing*, 35(7-8):751–761, 2004.
- [2] A. VAUTRIN, J. R. LEE, and J. MOLIMARD. Full-field optical techniques : Applications to strain measurement and mechanical identification. In *10th European Conference on Composite Materials (ECCM10)*, 2002. in Brugge, Belgium.
- [3] Y. SURREL. Full-field optical methods for mechanical engineering: essential concepts to find one' way. In *Composite Testing and Model Identification (CompTest2004)*, 2004. 21-23 September in Bristol, England.
- [4] A. VAUTRIN. The challenge of optical full-field measurement methods in experimental mechanics. In *OPTIMESS Workshop*, 2004. 12 October in Stuttgart, Germany.
- [5] Standardisation project for optical techniques of strain measurement (spots). <http://www.opticalstrain.org/>.
- [6] O. ERNE. Electronic speckle pattern interferometry: temporal vs. spatial phase-shifting. <http://physics.pdx.edu/>.
- [7] W. STEINCHEN, G. KUPFER, and P. MÄCKEL. Full field tensile strain shearography of welded specimens. *Strain*, 38:17–26, 2002.
- [8] J.-R. LEE, J. MOLIMARD, A. VAUTRIN, and Y. SURREL. Application of grating shearography and speckle shearography to mechanical analysis of composite material. *Composites Part A: Applied Science and Manufacturing*, 35:965–976, 2004.
- [9] M. A. SEIF, U. A. KHASHABA, and R. ROJAS-OVIEDO. Measuring delamination in carbon/epoxy composites using a shadow moiré laser based imaging technique. *Composite Structures*, 79:113–118, 2007.

- [10] Y. SURREL, N. FOURNIER, M. GRÉDIAC, and P.-A. PARIS. Phase-stepped deflectometry applied to shape measurement of bent plates. *Experimental Mechanics*, 39(1):66–70, 1999.
- [11] Y. SURREL. Deflectometry: a simple and efficient noninterferometric method for slope measurement. In *Xth SEM International Congress on Experimental Mechanics*, 2004.
- [12] Y. SURREL. Fringe analysis. in “Photomechanics”, pp. 57-104, P.K. Rastogi Ed., Springer, 1999.
- [13] A. GIRAUDEAU, B. GUO, and F. PIERRON. Stiffness and damping identification from full field measurements on vibrating plates. *Experimental Mechanics*, 46(6):777–787, 2006.
- [14] A. DAVILA, P. D. RUIZ, G. H. KAUFMANNB, and J. M. HUNTLEY. Measurement of sub-surface delaminations in carbon fibre composites using high-speed phase-shifted speckle interferometry and temporalphase unwrapping. *Optics and Lasers in Engineering*, 40:447–458, 2003.
- [15] M. GRÉDIAC, F. PIERRON, and Y. SURREL. Novel procedure for complete in-plane composite characterization using a single T-shaped specimen. *Experimental Mechanics*, 39(2):142–149, 1999.
- [16] R. HSAKOU. Curvature: the relevant criterion for class-a surface quality. Ondulo, Visuel technologies.
- [17] Y. Y. HUNGA and H. P. HO. Shearography: An optical measurement technique and applications. *Materials Science and Engineering*, 49:61–87, 2005.
- [18] C. R. COGGRIVE and J. M. HUNTLEY. Real-time visualisation of deformation fields using speckle interferometry and temporal phase unwrapping. *Optics and Lasers in Engineering*, 41:601–620, 2004.
- [19] S. AVRIL, M. GRÉDIAC, F. PIERRON, and Y. SURREL. Deflectometry and virtual fields for identification of static plate bending stiffnesses. In *Xth SEM International Congress on Experimental Mechanics*, 2004.
- [20] Y. PANNIER, S. AVRIL, R. ROTINAT, and F. PIERRON. Identification of elastoplastic constitutive parameters from statically undetermined tests using the virtual fields method. *Experimental Mechanics*, 46(6):735–755, 2006.

-
- [21] M. GRÉDIAC. Principe des travaux virtuels et identification/principle of virtual work and identification. *Comptes Rendus de l'Académie des Sciences*, II(309):1–5, 1989. In French with abridged English version.
- [22] S. AVRIL, J. M. HUNTLEY, F. PIERRON, and D. D. STEELE. 3D heterogeneous stiffness reconstruction using MRI and the Virtual Fields Method. *Experimental Mechanics*, 2008. In press.
- [23] D. C. SIMKINS JR and S. LI. Effective bending stiffness for plates with microcracks. *Archive of Applied Mechanics*, 73(3):282–309, 2003.
- [24] J. N. REDDY, C. M. WANG, G. T. LIM, and K. H. NG. Bending solutions of levinson beams and plates in terms of the classical theories. *International Journal of Solids and Structures*, 38(26):4701–4720, 2001.
- [25] S. W. TSAI. Theory of composites design. Think Composites, 1992.
- [26] S. R. SWANSON. Introduction to design and analysis with advanced composite materials. Prentice Hall, 1996.
- [27] J. N. REDDY and C. M. WANG. An overview of the relationships between solutions of the classical and shear deformation plate theories. *Composites Science and Technology*, 60(12):2327–2335, 2000.
- [28] D. H. ROBBINS, JR. and J. N. REDDY. Variable kinematic modelling of laminated composite plates. *International Journal for Numerical Methods in Eengineering*, 39(13):2283–2317, 1996.
- [29] R. D. HALE. Micromechanical behavior of a lamina.
<http://www.engr.ku.edu/rhale/ae510/mechcomp.pdf>.
- [30] M. GRÉDIAC. On the direct determination of invariant parameters governing anisotropic plate bending problems. *International Journal of Solids and Structures*, 33(27):3969–3982, 1996.
- [31] M. GRÉDIAC and P.-A. PARIS. Direct identification of elastic constants of anisotropic plates by modal analysis: theoretical and numerical aspects. *Journal of Sound and Vibration*, 195(3):401–415, 1996.
- [32] M. GRÉDIAC, N. FOURNIER, P.-A. PARIS, and Y. SURREL. Direct identification of elastic constants of anisotropic plates by modal analysis: experiments and results. *Journal of Sound and Vibration*, 210(5):645–659, 1998.

- [33] A. GIRAUDEAU and F. PIERRON. Identification of stiffness and damping properties of thin isotropic vibrating plates using the virtual fields method. Theory and simulations. *Journal of Sound and Vibration*, 284(3-5):757–781, 2005.
- [34] L. LEMAGOROU, F. BOS, and F. ROUGER. Identification of constitutive laws for wood-based panels by means of an inverse method. *Composite Science and Technology*, 62(4):591–596, 2002.
- [35] K.-E. FÄLLSTRÖM, K. OLOFSSON, H. O. SALDNER, and S. SCHEDIN. Dynamic material parameters in an anisotropic plate estimated by phase-stepped holographic interferometry. *Optics and Lasers in Engineering*, 24(5-6):429–454, 1996.
- [36] M. GRÉDIAC, E. TOUSSAINT, and F. PIERRON. Special virtual fields for the direct determination of material parameters with the virtual fields method. 1- Principle and definition. *International Journal of Solids and Structures*, 39(10):2691–2705, 2002.
- [37] M. GRÉDIAC, E. TOUSSAINT, and F. PIERRON. Special virtual fields for the direct determination of material parameters with the virtual fields method. 3- Application to the bending rigidities of anisotropic plates. *International Journal of Solids and Structures*, 40(10):2401–2419, 2003.
- [38] E. TOUSSAINT, M. GRÉDIAC, and F. PIERRON. The virtual fields method with piecewise virtual fields. *International Journal for Mechanical Sciences*, 48(3):256–264, 2006.
- [39] K. SYED-MUHAMMAD, E. TOUSSAINT, M. GRÉDIAC, S. AVRIL, and J.-H. KIM. Characterization of composite plates using the virtual fields method with optimized loading conditions. *Composite Structures*, 85(1):70–82, 2008.
- [40] S. AVRIL, M. GRÉDIAC, and F. PIERRON. Sensitivity of the virtual fields method to noisy data. *Computational Mechanics*, 34(6):439–452, 2004.
- [41] K. SYED-MUHAMMAD. Sur quelques aspects numériques de la Méthode des Champs Virtuels: optimisation de conditions d’essai et champs virtuels définis par sous-domaines. Ph.D. Thesis, Blaise Pascal University, Clermont-Ferrand, 2007.
- [42] P. P. CAMANHO and F. L. MATTHEWS. A progressive damage model for mechanically fastened joints in composite laminates. *Journal of Composite Materials*, 33:2248–2280, 1999.

-
- [43] C. A. Felippa. Kirchhoff plates: Field equations.
<http://www.colorado.edu/engineering/CAS/courses.d/AFEM.d>.
- [44] T.-S. PARK, S. SURESH, A. J. ROSAKIS, and J. RYU. Measurement of full-field curvature and geometrical instability of thin film-substrate systems through CGS interferometry. *Journal of the Mechanics and Physics of Solids*, 51(11-12):2191–2211, 2003.
- [45] M. GRÉDIAC and A. VAUTRIN. Mechanical characterization of anisotropic plates: experiments and results. *European Journal of Mechanics/A Solids*, 12(6):819–838, 1993.
- [46] Ondulo measurement protocol. Ondulo, Techlab.
- [47] P. H. GEUBELLE and J. S. BAYLOR. Impact-induced delamination of composites: a 2D simulation. *Composites Part B*, 29:589–602, 1998.
- [48] M. O. W. RICHARDSON and M. J. WISHEART. Review of low-velocity impact properties of composite materials. *Composites Part A*, 27:1123–1131, 1996.
- [49] M. MEO and E. THIEULOT. Delamination modelling in a double cantilever beam. *Composite Structures*, 71(3-4):429–434, 2005.
- [50] S. OGIHARA and N. TAKEDA. Interaction between transverse cracks and delamination during damage progress in CFRP cross-ply laminates. *Composites Science and Technology*, 54:395–404, 1995.
- [51] P. SJOÄBLOM. Simple design approach against low velocity impact damage. In *Proceedings of the 32nd SAMPE Symposium*, 1987. 6-9 April in Anaheim, USA.
- [52] W. STASZEWSKI, C. BOLLER, and G. R. TOMLINSON. Health monitoring of aerospace structures: smart sensor technologies and signal processing. Wiley, 2004.
- [53] S. ABRATE. Impact on laminated composite materials. *Applied Mechanics Reviews*, 44:155–190, 1991.
- [54] L. B. GRESZCZUK. Damage in composite materials due to low-velocity impact. In “Impact Dynamics”, pp. 55, L. A. Zukas ET AL Ed., Wiley, 1982.
- [55] R. L. SPILKER. Edge effects in symmetric composite laminates: importance of satisfying the traction-free-edge condition. *Journal of Composite Materials*, 14:2–20, 1980.

- [56] D. LIU. Impact-induced delamination a view of bending stiffness mismatching. *Journal of Composite Materials*, 22(7):674–692, 1988.
- [57] V. V. BOLOTIN. Delaminations in composite structures: its origin, buckling, growth and stability. *Composites Part B*, 27:129–145, 1996.
- [58] D. J. ELDER, R. S. THOMSON, M. Q. NGUYEN, and M. L. SCOTT. Review of delamination predictive methods for low speed impact of composite laminates. *Composite Structures*, 66:677–683, 2004.
- [59] A. RUOSI. Nondestructive detection of damage in carbon fibre composites by SQUID magnetometry. *Physica Status Solidi. C*, 2(5):1533–1555, 2005.
- [60] T. O. WILLIAMS and F. L. ADDESSIO. A general theory for laminated plates with delaminations. *International Journal of Solids and Structures*, 34(16):2003–2024, 1997.
- [61] E. J. BARBERO and J. N. REDDY . Modeling of delamination in composite laminates using a layer-wise plate theory. *International Journal of Solids and Structures*, 28:373–388, 1991.
- [62] C. FAN, P.-Y. B. JAR, and J. J. R. CHENG. Energy-based analyses of delamination development in fibre-reinforced polymers under 3-point bending. *Composites Science and Technology*, 66:2143–2155, 2006.
- [63] T. O. WILLIAMS. A generalized multilength scale nonlinear composite plate theory with delamination. *International Journal of Solids and Structures*, 36:3015–3050, 1999.
- [64] R. F. GIBSON. Principles of composite material mechanics. McGraw-Hill, 1994.
- [65] J. R. RICE. A path independent integral and the approximate analysis of strain concentrations by notches and cracks. *Journal of Applied Mechanics*, 35:379–386, 1968.
- [66] T. K. HELLEN. On the method of virtual crack extensions. *International Journal for Numerical Methods in Engineering*, 9:187–207, 1975.
- [67] E. F. RYBICKI and M. F. KANNINEN. A finite element calculation of stress intensity factors by a modified crack closure integral. *Engineering Fracture Mechanics*, 9:931–938, 1977.

-
- [68] Fracture mechanics.
<http://www.efunda.com/formulae/solid-mechanics/fracture-mechanics/fm-lefm-modes.cfm>.
- [69] R. A. CLEGG, D. M. WHITE, W. RIEDEL, and W. HARWICK. Hypervelocity impact damage prediction in composites: Part I - material model and characterisation. *International Journal of Impact Engineering*, 33:190–200, 2006.
- [70] J. J. MUNOZ, U. GALVANETTO, and P. ROBINSON. On the numerical simulation of fatigue driven delamination with interface elements. *International Journal of Fatigue*, 28:1136–1146, 2006.
- [71] M. ASLAN and W. M. BANKS. The effect of multiple delamination on postbuckling behavior of laminated composite plates. *Composite Structures*, 42:1–12, 1998.
- [72] H.-J. KIM. Postbuckling analysis of composite laminates with a delamination. *Computers & Structures*, 62(6):975–983, 1997.
- [73] N. HUA, H. FUKUNAGA, H. SEKINE, and K. M. ALI. Compressive buckling of laminates with an embedded delamination. *Composites Science and Technology*, 59:1247–1260, 1999.
- [74] J. W. H. YAP, R. S. THOMSON, M. L. SCOTT, and D. HACHENBERG. Influence of post-buckling behaviour of composite stiffened panels on the damage criticality. *Composite Structures*, 66:197–206, 2004.
- [75] H. CHEN and X. SUN. Residual compressive strength of laminated plates with delamination. *Composite Structures*, 47:711–717, 1999.
- [76] A. C. GARG. Delamination - a damage mode in composite structures. *Engineering Fracture Mechanics*, 29:557–584, 1988.
- [77] K. HENKHAUS. Overview of research on composite material impact behavior. In *The 16th ASCE Engineering Mechanics Conference*, 2003. 16-18 July in Seattle, USA.
- [78] H. KIM and K. T. KEDWARD. A nondestructive approach to evaluating impact damaged composite structures. In *Proceeding of the Eleventh International Conference on Composite Materials (ICCM-11)*, 1997. 14-18 July in Gold Coast, Australia.
- [79] P. MSRAO and D. SHU. Buckling analysis of two-layer beams with an asymmetric delaminations. *Engineering Structures*, 26(5):651–658, 2004.

- [80] J. D. WHITCOMB. Parametric analytical study of instability-related delamination growth. *Composites Science and Technology*, 25:19–48, 1986.
- [81] X. W. WANG, I. PONT-LEZICA, J. M. HARRIS, F. J. GUILD, and M. J. PAVIER. Compressive failure of composite laminates containing multiple delaminations. *Composites Science and Technology*, 65:191–200, 2005.
- [82] S. ABRATE. Impact on composite structures. Cambridge University Press, 1998.
- [83] W. CANTWELL and J. MORTON. The impact resistance of composite materials - A review. *Composites*, 22(5):347–362, 1991.
- [84] M. J. PAVIER and M. P. CLARKE. Experimental techniques for the investigation of the effects of impact damage on carbon-fibre composites. *Composites Science and Technology*, 55(2):157–169, 1995.
- [85] P. O. SJOBLUM, J. T. HARTNESS, and T. M. CORDELL. On low-velocity impact testing of composite materials. *Journal of Composite Materials*, 22:30–52, 1988.
- [86] D. LIU and L. E. MALVEM. Matrix cracking in impacted glass/epoxy plates. *Journal of Composite Materials*, 21:594–609, 1987.
- [87] H. Y. CHOI, H.-Y. T. WU, and F. K. CHANG. A new approach toward understanding damage mechanisms and mechanics of laminated composites due to low-velocity impact: Part II analysis. *Journal of Composite Materials*, 25:1012–1038, 1991.
- [88] W. J. CANTWELL and J. MORTON. Geometrical effects in the low velocity impact response of CFRP. *Composite Structures*, 12:39–59, 1989.
- [89] C. F. LIA, Y. J. YINA, H. SEKINEC, and H. FUKUNAGA. Low-velocity impact-induced damage of continuous fiber-reinforced composite laminates. Part I. An FEM numerical model. *Composites Part A*, 33:1055–1062, 2002.
- [90] D. COUTELLIER, J. C. WALRICK, and P. GEOFFROY. Presentation of a methodology for delamination detection within laminated structures. *Composites Science and Technology*, 66:837–845, 2006.
- [91] W. L. YIN, S. N. SALLAM, and G. J. SIMITSES. Ultimate axial load capacity of a delaminated beam-plate. *American Institute of Aeronautics and Astronautics Journal*, 24(1):123–128, 1986.

-
- [92] G. A. BIBO and P. J. HOGG. Role of reinforcement architecture on impact damage mechanisms and post impact compression behaviour. *Journal of Materials Science*, 31:1115–1137, 1996.
- [93] F. J. GUILD, P. J. HOGG, and J. C. RICHARD. A model for the reduction in compression strength of continuous fibre composites after impact damage. *Composites*, 24(4):333–339, 1993.
- [94] Y. S. N. REDDY, C. M. D. MOORTHY, and J. N. REDDY. Non-linear progressive failure analysis of laminated composite plates. *International Journal of Non-Linear Mechanics*, 30(5):629–649, 1995.
- [95] G. ZHOU. Compressive behaviour of large undamaged and damaged thick laminated panels. *Composite Structures*, 38(1-4):589–597, 1997.
- [96] G. DOREY. Impact damage tolerance and assessment in advanced composite materials. In *Seminar on Advanced Composites*, 1986. in Cranfield, UK.
- [97] Z. Y. ZHANG and M. O. W. RICHARDSON. Low velocity impact induced damage evaluation and its effect on the residual flexural properties of pultruded GRP composites. *Composite Structures*, 81:195–201, 2007.
- [98] R. JOFFE and J. VARNA. Analytical modeling of stiffness reduction in symmetric and balanced laminates due to cracks in 90° layers. *Composites Science and Technology*, 59:1641–1652, 1999.
- [99] A. L. HIGHSMITH and K. L. REIFSNIDER. Stiffness reduction mechanisms in composite laminates. In “Damage in composite materials”, pp. 103-117, K. L. Reifsnider Ed., ASTM STP 775, 1982.
- [100] D. ZHANG, J. YE, and D. LAM. Ply cracking and stiffness degradation in cross-ply laminates under biaxial extension, bending and thermal loading. *Composite Structures*, 75:121–131, 2006.
- [101] Z. HASHIN. Analysis of cracked laminates: a variational approach. *Mechanics of Materials*, 4(2):121–136, 1985.
- [102] J. VARNA and L. A. BERGLUND. Multiple transverse cracking and stiffness reduction in cross-ply laminates. *Journal of Composites Technology & Research*, 13:97–106, 1991.

- [103] M. KASHTALYAN and C. SOUTIS. The effect of delaminations induced by transverse cracks and splits on stiffness properties of composite laminates. *Composites Part A*, 31:107–119, 2000.
- [104] J. ZHANG, C. SOUTIS, and J. FAN. Strain energy release rate associated with local delamination in cracked composite laminates. *Composites*, 25(9):851–862, 1994.
- [105] T. K. O'BRIEN. Analysis of local delaminations and their influence on composite laminate behavior. *American Society for Testing and Materials STP*, 876:282–297, 1985.
- [106] J. ZHANG, J. FAN, and K. P. HERRMANN. Delaminations induced by constrained transverse cracking in symmetric composite laminates. *International Journal of Solids and Structures*, 36:813–846, 1999.
- [107] A. SJOÄGREN, A. KRASNIKOVS, and J. VARNA. Experimental determination of elastic properties of impact damage in carbon fibre/epoxy laminates. *Composites Part A: Applied Science and Manufacturing*, 32(9):1237–1242, 2001.
- [108] D. LIU, B. B. RAJUS, and X. DANG. Size effects on impact response of composite laminates. *International Journal of Impact Engineering*, 21(10):837–854, 1998.
- [109] S. S. KESSLER, S. M. SPEARING, M. J. ATALLA, C. E. S. CESNIK, and C. SOUTIS. Damage detection in composite materials using frequency response methods. *Composites Part B*, 33:87–95, 2002.
- [110] Z. Y. ZHANG and M. O. W. RICHARDSON. Visualisation of barely visible impact damage in polymer matrix composites using an optical deformation and strain measurement system (ODSMS). *Composites Part A*, 36:1073–1078, 2005.
- [111] N. ANGELIDIS and P. E. IRVING. Detection of impact damage in CFRP laminates by means of electrical potential techniques. *Composites Science and Technology*, 67:594–604, 2007.
- [112] Z. SU, L. YE, and Y. LU. Guided Lamb waves for identification of damage in composite structures: A review. *Journal of Sound and Vibration*, 295:753–780, 2006.
- [113] Y. L. KOH, W. K. CHIU, and N. RAJIC. Effects of local stiffness changes and delamination on Lamb wave transmission using surface-mounted piezoelectric transducers. *Composite Structures*, 57:437–443, 2002.

-
- [114] R. RÙŽEK, R. LOHONKA, and J. JIRONÈ. Ultrasonic C-Scan and shearography NDI techniques evaluation of impact defects identification. *NDT&E International*, 39(2):132–142, 2006.
- [115] A. MARANON, P. D. RUIZ, A. D. NURSE, J. M. HUNTLEY, L. RIVERA, and G. ZHOU. Identification of subsurface delaminations in composite laminates. *Composites Science and Technology*, 67:2817–2826, 2007.
- [116] Y. ZOU, L. TONG, and G. P. STEVEN. Vibration-based model-dependent damage (delamination) identification and health monitoring for composite structures. A review. *Journal of Sound and vibration*, 230(2):357–378, 2000.
- [117] J. V. ARAÚJO DOS SANTOS, H. M. R. LOPES, M. VAZ, C. M. MOTA SOARES, C. A. MOTA SOARES, and M. J. M. DE FREITAS. Damage localization in laminated composite plates using mode shapes measured by pulsed TV holography. *Composite Structures Volume*, 76(3):272–281, 2006.
- [118] W. VAN PAEPEGEM and J. DEGRIECK. Experimental setup for and numerical modelling of bending fatigue experiments on plain woven glass/epoxy composites. *Composite Structures*, 51(1):1–8, 2001.
- [119] A. N. PALAZOTTO, E. J. HERUP, and L. N. B. GUMMADI. Finite element analysis of low-velocity impact on composite sandwich plates. *Composite Structures*, 49:209–227, 2000.
- [120] S. ZHENG and C. T. SUN. Delamination interaction in laminated structures. *Engineering Fracture Mechanics*, 59(2):225–240, 1998.
- [121] J. RENARD and A. THIONNET. Damage in composites: From physical mechanisms to modelling. *Composites Science and Technology*, 66:642–646, 2006.
- [122] T. O. WILLIAMS. A generalized, multilength scale framework for thermo-diffusional-mechanically coupled, nonlinear, laminated plate theories with delaminations. *International journal of solids and structures*, 42(5-6):1465–1490, 2005.
- [123] Z. ZOU, S. R. REID, S. LI, and P. D. SODEN. Application of a delamination model to laminated composite structures. *Composite Structures*, 56:375–389, 2002.
- [124] R. BORG, L. NILSSON, and K. SIMONSSON. Modeling of delamination using a discretized cohesive zone and damage formulation. *Composites Science and Technology*, 62:1299–1314, 2002.

- [125] C. T. SUN and J. E. GRADY. Dynamic delamination fracture toughness of a graphite/epoxy laminate under impact. *Composites Science and Technology*, 31:55–72, 1988.
- [126] K. F. NILSSON, L. E. ASP, and J. E. ALPMAN. Delamination buckling and growth at global buckling. In “First international conference on damage and failure of interfaces”, pp. 193-202, H.-P. Rossmanith Ed., 1997.
- [127] F. LACHAUD, B. LORRAIN, L. MICHEL, and R. BARRIOL. Experimental and numerical study of delamination caused by local buckling of thermoplastic and thermoset composites. *Composites Science and Technology*, 58:727–733, 1998.
- [128] R. KRUEGER and T. K. O’BRIEN. A shell/3D modeling technique for the analysis of delaminated composite laminates. *Composites: Part A*, 32:25–44, 2001.
- [129] C. H. ROCHE and M. L. ACCORSI. A new finite element for global modeling of delaminations in laminated beams. *Finite Elements in Analysis and Design*, 31(2):165–177, 1998.
- [130] G. S. PADHI, R. A. SHENOI, S. S. J. MOY, and G. L. HAWKINS. Progressive failure and ultimate collapse of laminated composite plates in bending. *Composite Structures*, 40(3-4):277–291, 1998.
- [131] F. K. CHANG and K. Y. CHANG. A progressive damage model for laminated composites containing stress concentrations. *Journal of Composite Materials*, 21:834–855, 1987.
- [132] M. L. LIU and J. YU. Finite element modeling of delamination by layerwise shell element allowing for interlaminar displacements. *Composites Science and Technology*, 63:517–529, 2003.
- [133] R. T. TENCHEV and B. G. FALZON. A pseudo-transient solution strategy for the analysis of delamination by means of interface elements. *Finite Elements in Analysis and Design*, 42(8):698–708, 2006.
- [134] W. CUI and M. R. WISNOM. A combined stress-based and fracture-mechanics-based model for predicting delamination in composites. *Composites*, 24(6):467–474, 1993.
- [135] T. O. WILLIAMS. A new multilength scale plate theory with delamination. In *AIAA/ASME/ASCE/ASH/ASC structures conference*, 1997. 20-23 April in Long Beach, USA.

- [136] D. H. ALLEN, S. E. GROVES, and C. E. HARRIS. A cumulative damage model for continuous fiber composite laminates with matrix cracking and interply delaminations. In *Composite Materials: Testing and Design. Eighth Conference*, 1986. 29 April-1 May in Charleston, USA.
- [137] E. A. ARMANIOS, P. SRIRAM, and A. BADIR. Fracture analysis of transverse crack-tip and free-edge delamination in laminated composites. In “Composite Materials: Fatigue and Fracture (Third Volume)”, pp. 269-286, T. K. O’Brien Ed., ASTM STP 1110, 1991.
- [138] F. CAPPELLO and D. TUMINO. Numerical analysis of composite plates with multiple delaminations subjected to uniaxial buckling load. *Composites Science and Technology*, 66:264–272, 2006.
- [139] I-DEAS 11 Help Library. UGS PLM Solutions Inc.

IDENTIFICATION DE CARTES D'ENDOMMAGEMENT DE PLAQUES COMPOSITES IMPACTÉES PAR LA MÉTHODE DES CHAMPS VIRTUELS

RÉSUMÉ : La présente étude a pour objectif d'identifier non seulement la position mais également la réduction locale de rigidité au sein d'une zone endommagée d'une plaque mince composite. Pour cela, des mesures de champs de pentes par déflectométrie sont couplées à une technique d'identification inverse dédiée au traitement des mesures de champs : la méthode des champs virtuels. Cette méthode se base sur l'écriture de l'équilibre global via le principe des travaux virtuels. Elle a été adaptée ici pour identifier des rigidités spatialement variables. Deux paramétrisations ont été étudiées : discrète (par morceaux) et continue (polynômes). Dans ce document, la procédure est décrite en détail, validée sur des simulations puis testée expérimentalement. Les résultats confirment le potentiel de la méthode dans différents cas. Néanmoins, elle est mise en défaut lorsque l'hypothèse de distribution linéaire des déformations dans l'épaisseur n'est plus vérifiée, ce qui est le cas d'un délaminage unique sur le plan moyen de la plaque, par exemple. Ce cas de figure est heureusement assez éloigné d'un endommagement par impact réel et un premier résultat sur plaque impactée le confirme.

Mots-clés : *méthode des champs virtuels, mesures de champs, déflectométrie, réduction locale de rigidité, détection de l'endommagement*

IDENTIFICATION OF THE LOCAL STIFFNESS REDUCTION OF A DAMAGED COMPOSITE PLATE USING THE VIRTUAL FIELDS METHOD

ABSTRACT: The present study aims at taking advantage of the availability of full-field measurements and adapted inverse identification procedures in order to not only locate the damage but also to identify the local stiffness reduction of a damaged composite plate. To do so, full-field heterogeneous curvature fields are obtained through a deflectometry technique. The virtual fields method (VFM) is used as an inverse procedure to process curvatures for the identification of the local loss of stiffness. The VFM is based on a relevant use of the equilibrium equations through the principle of virtual work. It has been adapted to the case of a plate with stiffnesses varying with the space variables. Two parameterization methods for the stiffness reduction were developed: discrete (piecewise) and continuous (polynomial). In this study, the procedure is described, validated on simulated measurements and several experimental results are given. The method not only picks up the location of the damage but also provides a fairly good estimate of the stiffness reduction in the damaged area when through-the-thickness displacement distribution in the damaged region is linear. However, the current methodology shows unsatisfactory identification if the distribution is not linear, which is the case for a single mid-plane delamination.

Key-words : *Virtual Fields Method, Full-field measurement, Deflectometry, Local stiffness reduction, Damage detection*

